Synthesis and characterisation of proton conducting composite materials resilient to dehydration at elevated temperatures.

by

Jonathan Patrick Turley

Dissertation Submitted in Partial Fulfillment

of the Requirements for the Degree of

Doctor of Philosophy

University of South Wales/Prifysgol De Cymru

December 2015

Abstract

The optimal operating temperature range for a low temperature polymer exchange membrane fuel cell begins at 80 °C. At this temperature water will begin to leave the system as steam and any membrane that relies on water to transport protons will dehydrate and thus, the proton conductivity of the membrane will start to degrade. Here the development of a new proton conducting material that is resilient to dehydration is presented. The exploitation of the oxide surface of the *ca.* 20 Å pore walls of a mesoporous transition metal oxide (mX_2O_5) as a means of anchoring sulfonate groups and suppressing moisture loss to encourage proton conduction pathways in the naphthalene sulfonate formaldehyde (NSF) impregnated analogues is conceived and studied. Composites of mX_2O_5 doped with H_2SO_4 and subsequently impregnated with NSF or having NSF oligomerised *in situ* of the mX_2O_5 pores were synthesised, characterised and had their proton conductivity recorded over a range of temperatures. Initially six mesoporous Ti oxide composites of NSF were made. The most promising sample displayed a proton conductivity of 1.837 mS cm^{-1} at 100 °C. This surpasses that of a pellet of Nafion 117 (1.143 mS cm^{-1}) whilst having a greater conductivity than pure hydrated NSF (0.122 mS cm^{-1}), confirming a synergistic interaction between the NSF and the oxide mesostructure. Next a series of mX_2O_5-NSF composites were synthesised with C_6, C_{12}, and C_{18} templates. Here the most promising sample displayed a conductivity of 21.96 mS cm^{-1} at 100 °C, surpassing the literature value for a Nafion 117 film (ca. 8 mS cm^{-1}). Finally, studies were performed on a series of mNb_2O_5 composites with NSF resin polymerised within the pores. The most promising sample displayed a conductivity of

21.77 mS cm^{-1} at 80 °C. Subsequent thermal durability tests demonstrated that this composite maintains superior conductivity to Nafion 117 at 80 °C for the length of the study (24 h). These observations were subsequently rationalised by in depth solid-state NMR studies.

For Ieuan, Siân and Celyn

Acknowledgments

I would like to thank several people who have contributed enormously towards my PH.D study and my time within the Antonelli group at the University of South Wales.

First and foremost, I would like to extend my utmost gratitude to Professor David Antonelli for not only the opportunity he has given me these past few years, but also for his expert guidance, council and his faith in my ability to manage and complete this project.

I would also like to extend this gratitude to all members of the Antonelli group that I have had the pleasure of working with. Special thanks go to Luke Smith, Dr Leah Morris and Dr Peter Jenkins for not only their guidance but for making my time at the university very enjoyable.

I also offer thanks to the Sustainable Energy Research Centre for the opportunity to do research at the University of South Wales and for the use of their facilities, and to the EPSRC for their funding.

This project has been in collaboration with a number of people without whom the work would not have been possible. I express my thanks and gratitude to Dr Michel Trudeau for his work on the materials characterisation and for taking the time to visit our group whilst in the UK and during my time in Boston; to Dr John Hanna and Frederik Romer for their work and guidance on all things NMR in this thesis and for their visits to the University; to Professor Mark Smith for his collaboration with the manuscripts and guidance; and to Professor Marcos Dias for the NSF to start the project and his guidance.

Last but by no means least; I wish to thank my family. To my Mum (Susan), Dad (Stephen), Alison and Louise, thank you for your support and encouragement during my university life and before. Finally, we get to my loved ones, Siân, Ieuan and Celyn. Every day you are there, with your love, support and encouragement. This thesis is for you and I hope I have made you proud.

Table of Contents

List of Tables

List of Figures

Declaration of Previous Publication

This thesis contains three papers that have been previously published in peer reviewed journals. They are as follows:

Thesis Chapter	Article Title/Citation
2	J. P. Turley, F. Romer, M. L. Trudeau, M. L. Dias, M. E. Smith, J. V. Hanna, D. M. Antonelli, *Microporous Mesoporous Mater.* **2014**, *190*, 284.
3	J. P. Turley, F. Romer, M. L. Trudeau, M. L. Dias, M. E. Smith, J. V. Hanna, D. M. Antonelli, *ChemSusChem.* **2015**, *8*, 301.
4	J. P. Turley, F. Romer, M. L. Trudeau, M. E. Smith, J. V. Hanna, D. M. Antonelli, *ChemNanoMat.* **2015**, *1*, 430.

Chapter 1: Introduction to the Study

Introduction

With each passing day, interest grows in the so-called green technologies market. Companies and governments look towards environmentally friendly methods for power generation such as fuel cells as a replacement for fossil-fueled installations, but without having to sacrifice availability, efficiency and performance. This thesis describes attempts to build on established protocol for mesoporous transition metal oxides and to understand and control the formation of proton conducting pathways within its porous system. This approach allows for proton conduction that is not dictated by dehydration rates and thus, has potential applications for fuel cells.

This chapter begins by defining the fuel cell and describing the basic properties of each type. From there, it will move on to the specifics of one particularly relevant variant and why improvements are necessary. The next section will introduce mesoporous oxides, outline how they are synthesised and what their potential is. This will lead into a section about polymers and how they can be used in conjunction with mesoporous materials to form composites, in particular ones which can be used to transport protons. Finally, the work presented in this thesis will be outlined.

Fuel Cells

The first experimental realisation of a fuel cell was by William Grove in the mid eighteenth Century.[1] He used a combination of zinc in dilute sulfuric acid, platinum in concentrated nitric acid, and a porous ceramic pot to produce *ca.* 1.9 volts of energy. A year later, Christian Friedrich Schönbein discussed the first crude fuel cell whereby

current was generated from hydrogen and oxygen dissolved in water.[2] Thus began the myriad research into the fuel cell.

In 1939, British engineer Francis Thomas Bacon successfully developed a 5 kW stationary fuel cell.[3] In 1955, W. Thomas Grubb, a chemist working for the General Electric Company (GE), further modified the original fuel cell design by using a sulphonated polystyrene ion-exchange membrane as the electrolyte.[4] Three years later another GE chemist, Leonard Niedrach, devised a way of depositing platinum onto the membrane, which served as catalyst for the necessary hydrogen oxidation and oxygen reduction reactions. This became known as the "Grubb-Niedrach fuel cell".[5] GE went on to develop this technology with NASA and McDonnell Aircraft, leading to its use during Project Gemini.[6] This was the first commercial use of a fuel cell. In 1959, a team led by Harry Ihrig built a 15 kW fuel cell tractor for Allis-Chalmers and his system used potassium hydroxide as the electrolyte and compressed hydrogen and oxygen as the reactants.[7] Later in 1959, Bacon and his colleagues demonstrated a practical five-kilowatt unit capable of powering a welding machine.[8] In the 1960s, Pratt and Whitney licensed Bacon's U.S. patents for use in the U.S. space program to supply electricity and drinking water (hydrogen and oxygen being readily available from the spacecraft tanks). In 1991, the first hydrogen fuel cell automobile was developed by Roger Billings.

Since then, the research has come on leaps and bounds with the development of a many different kinds of fuel cell tailored to specific needs. For instance, in 2011, UTC Power was the first company to manufacture and commercialise a large, stationary fuel

cell system for use as a co-generation power plant in hospitals, universities and large office buildings.[64]

In short, a fuel cell is a device that converts the chemical energy from a fuel into electricity through a chemical reaction of positively charged hydrogen ions with oxygen or another oxidising agent. Fuel cells come in many different varieties; each are developed with a specific task in mind and the most common types are described below.

Types of Fuel Cells

Fuel cells come in many varieties;[65] yet they all work in the same general manner. They are comprised of three adjacent segments: the anode, the electrolyte, and the cathode; and at each segment, two chemical reactions occur at each interface. The net result of the two reactions is that fuel is consumed, water or carbon dioxide is formed, and an electric current is created, which can be used to power electrical devices, normally referred to as the load.

At the anode a catalyst oxidises the fuel, usually hydrogen, turning the fuel into a positively charged ion and a negatively charged electron. The electrolyte is a substance specifically designed so ions can pass through it, but the electrons cannot. The freed electrons travel through a wire creating the electric current. The ions travel through the electrolyte to the cathode. Once reaching the cathode, the ions are reunited with the electrons and the two undergo a reduction reaction with a third chemical, usually oxygen, to create water or carbon dioxide. The overarching reaction is a redox reaction and is as follows:

Anode side:

$2H_2 \Rightarrow 4H^+ + 4e^-$

Cathode side:

$O_2 + 4H^+ + 4e^- \Rightarrow 2H_2O$

Net reaction:

$2H_2 + O_2 \Rightarrow 2H_2O$

Four features have to be taken into consideration when designing a fuel cell.[65] The first is the electrolyte substance. It is this which defines the style, type and usage of fuel cell. The type of fuel used is the second parameter to contemplate as this will allow for the fuel cell to be tailored towards a specific use. The anode catalyst is where the fuel is broken down into its constituent protons and electrons. Often made from a very fine platinum powder, the cost, thickness and longevity of the material is the third feature that requires scrutiny. Finally, the cathodic catalyst material is the fourth feature. Often made up of nickel or a nanomaterial-based material, it converts the waste ions chemicals into water or carbon dioxide. Again, cost, longevity and thickness play a major part in the design process. A typical fuel cell design is shown in Figure 1.1.

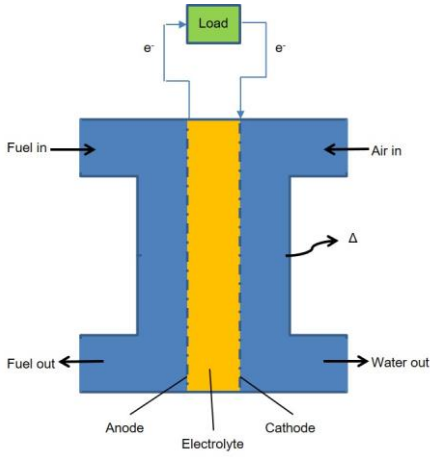

Figure 1.1**:** A schematic illustration of a generic fuel cell

A typical fuel cell produces a voltage from 0.6 V to 0.7 V at full rated load. Voltage decreases as current increases, due to several factors: activation loss, ohmic loss (due in part to the resistance of the cell components and interconnections) and mass transport loss (i.e. depletion of reactants at the catalyst sites under high loads). To deliver the desired amount of energy, the fuel cells can be combined in series to yield a higher voltage, and in parallel to allow a higher current to be supplied. Such a design is called a fuel cell stack. (Figures 1.2 and 1.3) The cell surface area can also be increased, to allow higher current from each cell. Within the stack, reactant gases must be distributed uniformly over each of the cells to maximise the power output.

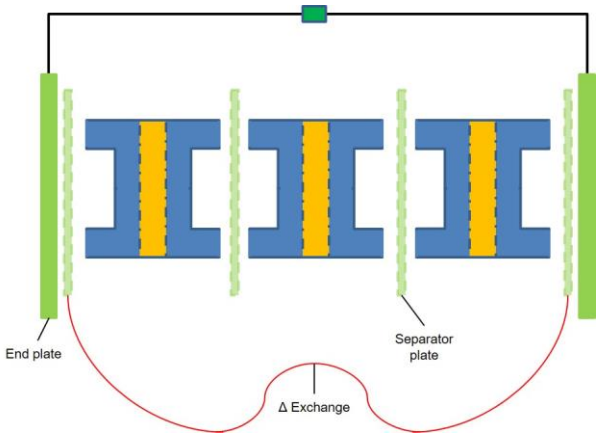

Figure 1.2: A fuel cell stack: series arrangement

In reality, a fuel cell system is comprised of both series and parallel fuel cell stacks in order to optimise efficiency. The system is completed with a fuel processor, a DC/DC converter or AC/DC inverter, a fan to drive air into the system, and the Balance of Plant Components. These are a collection of materials which essentially drive the cost, durability and efficiency of the system.

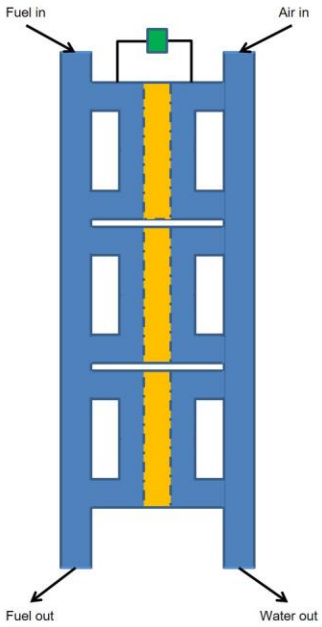

Figure 1.3**:** A fuel cell stack: parallel arrangement

There are many different types of fuel cell that operate in the low temperature and high temperature region. The most common are described below.

Alkaline fuel cells. Alkaline fuel cells (AFCs) were one of the first fuel cell technologies developed, with their use primarily being in the U.S. space program to produce electrical energy and water on-board spacecraft.[66] These fuel cells use a solution of potassium hydroxide in water as the electrolyte and can use a variety of non-precious metals as a catalyst at the anode and cathode.[65] High-temperature AFCs operate at temperatures between 100 °C and 250 °C,[67] while newer AFC designs operate at lower temperatures of roughly 23° C to 70° C.[68] In recent years, novel AFCs that use a polymer membrane as the electrolyte have been developed.[69,70] These fuel cells are closely related to conventional polymer exchange membrane fuel cells (PEMFCs), except that they use

an alkaline membrane instead of an acid membrane. The high performance of AFCs is due to the rate at which electro-chemical reactions take place in the cell. They have also demonstrated efficiencies above 60% in space applications.[9]

The main disadvantage of the AFC is that it is easily poisoned by carbon dioxide, so much so that even the smallest amount will see a large drop in efficiency.[71,72] Therefore, it is necessary to purify the fuels used in the cell and this adds to the cost of the system – something which has resulted in other types of fuel being trialed.[57] Susceptibility to poisoning also affects the cell's lifetime, further adding to cost. Alkaline membrane cells have lower susceptibility to CO_2 poisoning than liquid-electrolyte AFCs do, but performance still suffers as a result of CO_2 that dissolves into the membrane.[73] For the moment, AFCs are used in remote locations where cost isn't such a factor but in order to receive more mainstream use, their operating times have to be in excess of 40,000 hours[67] – a feat which will not happen until durability challenges of the material have been overcome.

Direct methanol fuel cells. NASA's Jet Propulsion Laboratory first made direct methanol fuel cells (DMFCs) in 1992.[74] Unlike many fuel cells, DMFCs are powered by pure methanol that is mixed with water and fed into the system at the anode. Despite this leading to a decrease in efficiency, the methanol used is between 1 and 3 M as more concentrated solutions tend to diffuse through the membrane (dubbed the methanol crossover effect).[10]

As a fuel in a fuel cell system, methanol offers many advantages.[67] It is inexpensive, has a relatively high energy density, and can be easily transported and

stored. It can be supplied to the fuel cell unit from a liquid reservoir which can be kept topped up, or in cartridges which can be quickly changed out when spent. Thus, the need for a fuel reformer is eliminated which drives the cost down. DMFCs have an operating temperature 60 °C to 130 °C which sees them compete with PEMFCs and whilst potentially cheaper, the high permeability of Nafion to methanol counteracts this.[75] Their lightweight nature means that DMFCs are often used to provide power for portable fuel cell applications such as cell phones or laptop computers.[76]

Closely related to these cells are the direct ethanol fuel cell[56] which works in a similar manner, and the indirect methanol/ethanol[77,78] fuel cell which requires the fuel to be reformed before it enters the cell.

Phosphoric acid fuel cells. Designed and introduced in 1961 by G. V. Elmore and H. A. Tanner,[11] the phosphoric acid fuel cell (PAFC) is considered the "first generation" of modern fuel cells. It is one of the most mature cell types and the first to be used commercially resulting in the PAFC being the most sold fuel cell system up until the turn of the millennium.

Phosphoric acid, the electrolyte used in PAFCs, is a non-conductive liquid acid which forces electrons to travel from anode to cathode through an external electrical circuit. Since the hydrogen ion production rate on the porous carbon anode is small, platinum is used as catalyst to increase this ionisation rate. A key disadvantage of these cells is the use of an acidic electrolyte.[79] This increases the oxidation of components exposed and in a bid to minimise this, the electrolyte is pasted onto a Teflon-bonded silicon carbide matrix.[80]

PAFCs commonly operate in temperatures of 150 °C to 200 °C with the heat generated used in cogeneration to enhance the efficiency of the cell from 40–50 % to about 80 %.[81] At lower temperatures phosphoric acid is a poor ionic conductor, and carbon monoxide poisoning of the platinum electro-catalyst in the anode becomes severe. However, they are much less sensitive to carbon monoxide than PEMFCs and AFCs.

Given the same weight and volume, PAFCs are less powerful than other fuel cells, and as a result, they are typically large and heavy. PAFCs are also expensive as they require much higher loadings of the platinum catalyst than other types of fuel cells do and as such, methods are being sought to change this.[82,83] This type of fuel cell is typically used for stationary power generation, but some PAFCs have been used to power large vehicles such as city buses.

Solid oxide fuel cells. Solid oxide fuel cells (SOFCs) use a solid material, most commonly the non-porous ceramic material yttria-stabilised zirconia (YSZ), as the electrolyte. Made entirely of solid materials, they are not limited to the flat plane configuration of other types of fuel cells and are often designed as rolled tubes.[84]

Due to the physical properties of YSZ, they require high operating temperatures (800–1000 °C) as anything lower sees the ionic conductivity of the electrolyte (and thus the fuel cell's efficiency) decrease.[84] These higher operating temperatures result in challenges that need to be overcome. One such challenge is that carbon dust builds up on the anode which leads to a loss of performance, with one viable solution being to use a heat-resistant composite of ceramic and metal (a "cermic"), but this isn't a cheap option.[12] Another disadvantage of SOFC systems is slow start-up time, making SOFCs

less useful for mobile applications. Despite these disadvantages, the high operating temperatures required provide an advantage by removing the need for a precious metal catalyst like platinum, thereby reducing cost.[85] Additionally, waste heat from SOFC systems may be captured and reused which allows SOFCs to reform fuels internally. This enables the use of a variety of fuels and reduces the cost associated with adding a reformer to the system.[86] SOFCs are around 60 % efficient at converting fuel to electricity but in those designed to capture and utilize the system's waste heat (co-generation), overall fuel use efficiencies could top 85 %.[13]

SOFCs are unique in that negatively charged oxygen ions travel from the cathode to the anode instead of positively charged hydrogen ions travelling from the anode to the cathode, as is the case in all other types of fuel cells. Oxygen gas is fed through the cathode, where it absorbs electrons to create oxygen ions. The oxygen ions then travel through the electrolyte to react with hydrogen gas at the anode. The reaction at the anode produces electricity and water as by-products. Carbon dioxide may also be a by-product depending on the fuel, but the carbon emissions from an SOFC system are less than those from a fossil fuel combustion plant.[86]

Research exploring the potential for SOFCs operating at or below 700°C is currently underway,[87,88] but despite there being fewer durability problems and a decreased cost associated, these SOFCs have not yet matched the performance of the higher temperature systems due to the stack materials that function in this lower temperature range still undergoing development. Additionally, the lower operating

temperature allows them to use stainless steel instead of ceramic as the cell substrate, which further reduces the cost and start-up time of the system.[89]

Hydrogen-oxygen fuel cell. Otherwise known as the Bacon cell, the hydrogen-oxygen fuel cell was designed in 1959[14] and was used as a primary source of electrical energy in the Apollo space program.[15] The cell consists of two porous carbon electrodes impregnated with a platinum catalyst. The space between the two electrodes is filled with a concentrated solution of potassium or sodium hydroxide which serves as an electrolyte and to this; hydrogen and oxygen gases are bubbled in where they combine to form water. The cell runs continuously until the reactant's supply is exhausted. This type of cell operates efficiently in the temperature range 70–140 °C and provides a potential of about 0.9 V.

Molten carbonate fuel cells. Molten carbonate fuel cells (MCFCs) are high temperature fuel cells that use lithium potassium carbonate salt as an electrolyte, which is suspended in a porous, chemically inert ceramic lithium aluminium oxide matrix. At high temperatures this salt liquefies which permits movement of charge (in this instance, carbonate anions) within the cell. Hydrogen enters the cell via the fuel used and this reacts with carbonate ions from the electrolyte to produce water, carbon dioxide, electrons and small amounts of other chemicals. The electrons travel through an external circuit creating electricity and return to the cathode. There, oxygen from the air and carbon dioxide recycled from the anode react with the electrons to form carbonate ions that replenish the electrolyte, completing the circuit.[90,91]

The operating temperature for the MCFC is 650 °C and as with the SOFCs, such high temperatures come with their own challenges. Whilst immune to carbon build up on the anode, both the anode and cathode are subject to corrosion from the electrolyte itself which decreases the cell's durability and lifetime.[92] High temperatures also lead to slow start up times, which result in the fuel cells being restricted to stationary purposes, such as power plants for utility,[93] industrial[94] and even military applications.[94] However, outgoing costs can be recovered as non-precious metals can be used as catalysts at the anode and cathode.[95]

Improved efficiency is another reason MCFCs offer significant cost reductions over rivalling fuel cell systems such as PAFCs. MCFCs, when coupled with a turbine, can reach efficiencies approaching 65 %,[96] considerably higher than the 37–42 % efficiencies of a PAFC system. Furthermore, when the waste heat is captured and used, overall fuel efficiencies can be over 85 %.[97] Unlike AFCs, PAFCs, and PEMFCs, MCFCs do not require an external reformer to convert fuels such as natural gas and biogas to hydrogen. At the high temperatures at which MCFCs operate, methane and other light hydrocarbons in these fuels are converted to hydrogen within the fuel cell itself by a process called internal reforming, which also reduces cost.

Reversible fuel cells. Reversible fuel cells (also called regenerative fuel cells; RFCs) produce electricity from hydrogen and oxygen and generate heat and water as by-products, just like other fuel cells. However, RFC systems can also use electricity from solar power, wind power, or other sources to split water into oxygen and hydrogen fuel through a process called electrolysis.[98] Thus, RFCs can provide power when needed, but

during times of high power production from other technologies (such as when high winds lead to an excess of available wind power), they are able to store the excess energy in the form of hydrogen and this has seen commercial success.[99] This energy storage capability could be a key enabler for intermittent renewable energy technologies.

When the fuel cell is operated in regenerative mode, the anode for the electricity production mode (fuel cell mode) becomes the cathode in the hydrogen generation mode (reverse fuel cell mode), and vice versa. When an external voltage is applied, water at the cathode side will undergo electrolysis to form hydrogen and oxide ions; oxide ions will be transported through the electrolyte to anode where it can be oxidised to form oxygen. In this reverse mode, the polarity of the cell is opposite to that for the fuel cell mode.[98]

One example of RFC is the solid oxide regenerative fuel cell (SORFC).[16] Generic SOFCs operate at high temperatures with high fuel to electricity conversion ratios which makes them a good candidate for high temperature electrolysis. Recent research[100] has shown that ceria-based composite electrolytes - where both proton and oxide ion conductions exist - produce high current outputs for fuel cell operation and high hydrogen outputs for electrolysis operation. Zirconia doped with scandia and ceria has also been investigated as a potential electrolyte in SORFC for hydrogen production at intermediate temperatures (500-750 °C).[101]

Since high frequency corresponds to electrolyte activities and low frequency corresponds to electrode processes, it can be deduced that only a small fraction of the overall resistance is from the electrolyte and most resistance comes from anode and

cathode. Hence, developing high performance electrodes are essential for high efficiency SORFC.

Proton Exchange Membrane Fuel Cells

Originally known as a solid polymer electrolyte fuel cell before the proton exchange mechanism was fully understood, the PEMFC (or polymer electrolyte membrane fuel cell) is one of the more common varieties of low temperature fuel cells available.

PEMFCs deliver high power density and offer the advantages of low weight and volume compared with other fuel cells.[102] Whilst they need only hydrogen, oxygen from the air, and water to operate, they are typically fuelled with pure hydrogen supplied from storage tanks or reformers.[54,55] Due to their fast start-up time and favourable power-to-weight ratio, PEMFCs are primarily used for transportation applications and some stationary applications, with particular use in passenger vehicles, such as cars and buses.[103] PEMFCs operate at relatively low temperatures, around 80°C. This low-temperature operation allows them to start quickly (less warm-up time) and results in less wear on system components, resulting in better durability. However, it requires that a noble-metal catalyst (typically platinum) be used to separate the hydrogen's electrons and protons, adding to system cost.[59-61,63] The platinum catalyst is also extremely sensitive to carbon monoxide poisoning, making it necessary to employ an additional reactor to reduce carbon monoxide in the fuel gas if the hydrogen is derived from a hydrocarbon fuel. This reactor also adds cost.[104]

In the archetypical hydrogen–oxide PEMFC design (Figure 1.4), a proton-conducting polymer membrane separates the anode and cathode sides. On the anode side, hydrogen diffuses to the anode catalyst where it later dissociates into protons and electrons. These protons often react with oxidants causing them to become what are commonly referred to as multi-facilitated proton membranes. The protons are conducted through the membrane to the cathode, but the electrons are forced to travel in an external circuit because the membrane is electrically insulating. On the cathode catalyst, oxygen molecules react with the newly arrived electrons and protons to form water. In addition to this pure hydrogen type, there are hydrocarbon fuels for fuel cells, including diesel, methanol and chemical hydrides. The waste products with these types of fuel are carbon dioxide and water.[105,106]

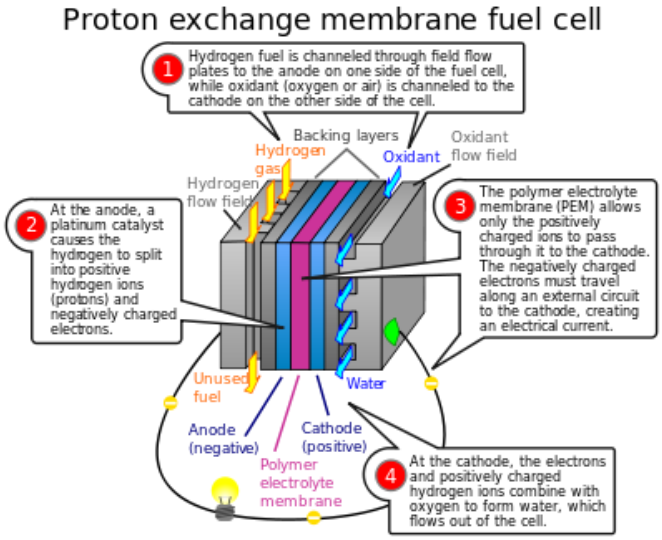

Figure 1.4**:** Construction of a PEMFC: Bipolar plate as electrode with in-milled gas channel structure, fabricated from conductive composites; Porous carbon papers; reactive layer; polymer membrane. Reprinted with permission from[17] Copyright (2007) American Chemical Society

When hydrogen is used as fuel, this is produced when CO_2 is released from the combination of natural gas (methane) with steam, in a process called steam methane reforming. This can take place in a different location to the fuel cell, potentially allowing the hydrogen fuel cell to be used indoors.[58]

The materials used for different parts of the fuel cells differ by type. The bipolar plates may be made of different types of materials, such as, metal, coated metal, graphite, flexible graphite, C–C composite, carbon–polymer composites, etc. The membrane electrode assembly (MEA) is referred as the heart of the PEMFC and is usually made of a proton exchange membrane sandwiched between two catalyst-coated carbon papers. Platinum and/or a similar category of noble metals are usually used as the catalyst for fuel cell system. The electrolyte is often a polymer membrane.

PEMFCs still have a lot of challenges to overcome. Poisoning of the cathode by carbon monoxide is a major concern with research looking into more resistive materials (like peridot).[18] Many companies are working on techniques to reduce cost in a variety of ways, with the main focus being on reducing the amount of platinum needed in each individual cell whilst not being detrimental to performance.[19,63] Catalysts prepared from colloidal particle suspensions,[107] enhanced with carbon silk to reduce platinum usage,[20] or using non-precious metals as a cathode[108] are one of the many avenues explored so far. The membrane must be hydrated, requiring water to be evaporated at precisely the same rate that it is produced. If water is evaporated too quickly, the membrane dries, resistance across it increases, and eventually it will crack, creating a gas "short circuit" where hydrogen and oxygen combine directly, generating heat that will damage the fuel cell. If

the water is evaporated too slowly, the electrodes will flood, preventing the reactants from reaching the catalyst and stopping the reaction. Finding the right balance can be quite the conundrum,[109] as maintaining the same temperature throughout the cell in order to prevent destruction of the cell through thermal loading. This is particularly challenging as the $2H_2 + O_2- > 2H_2O$ reaction is highly exothermic, so a large quantity of heat is generated within the fuel cell. Finally, there's the durability factor. Stationary fuel cell applications typically require more than 40,000 hours of reliable operation at a temperature of −35 °C to 40 °C while automotive fuel cells require a 5,000-hour lifespan (the equivalent of 150 miles) under extreme temperatures. Current service life is 2,500 hours (about 75,000 miles). Automotive engines must also be able to start reliably at −30 °C and have a high power-to-volume ratio (typically 2.5 kW per litre).[110] With the US Department of Energy's targets for PEMFCs ever increasing,[113] research into reaching these has stemmed into, but not restricted to, thinning and tweaking the platinum catalyst,[111,112] improving the carbon support of the platinum cathode,[114,115] and trying different MEAs as an alternative to Nafion (see below).

Nafion. Nafion is a sulfonated tetrafluoroethylene based fluoropolymer-copolymer discovered in the late 1960s by Walther Grot of DuPont,[21] the structure of which is shown in Figure 1.5. The unique ionic properties associated with Nafion are a result of incorporating perfluorovinyl ether groups terminated with sulfonate groups onto a tetrafluoroethylene backbone. Nafion has received a considerable amount of attention as a proton conductor for PEMFCs because of its excellent thermal[22] and mechanical stability.[23]

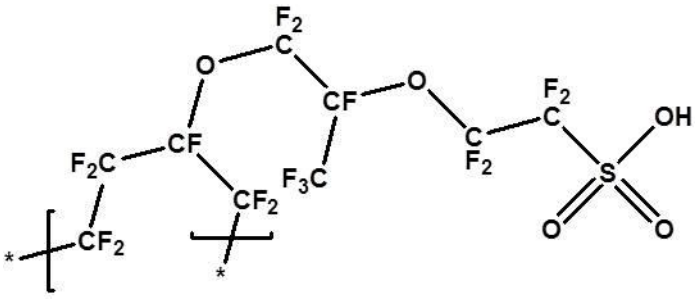

Figure 1.5: Repeat unit of Nafion

Nafion derivatives are first synthesised by the copolymerisation of tetrafluoroethylene and a derivative of a perfluoro (alkyl vinyl ether) with sulfonyl acid fluoride. The resulting product is an -SO_2F-containing thermoplastic that is extruded into films. Hot aqueous NaOH converts these sulfonyl fluoride groups into sulfonate groups. This form of Nafion, referred to as the neutral or salt form, is finally converted to the acid form containing the sulfonic acid groups. Nafion can be cast into thin films by heating in aqueous alcohol at 250 °C in an autoclave. By this process, Nafion can be used to generate composite films, coat electrodes, or repair damaged membranes.

The combination of the stable Teflon backbone with the acidic sulfonic groups gives Nafion a set of specific and extremely preferably characteristics;[116] it is highly conductive to cations, making it suitable for many membrane applications in fuel cells, and it resists chemical attack, with only alkali metals (particularly sodium)[117] and hydrogen peroxide[118] being capable of degrading Nafion under normal temperatures and pressures. Both of these characteristics make Nafion extremely versatile and desirable. Furthermore, the Teflon backbone is interlaced with the ionic sulfonate groups to provide Nafion with a high operating temperature (*ca.* 190 °C), however, in membrane form, this

is not possible due to the loss of water and mechanical strength.[119,120] Nafion is classified as a superacid catalyst: the combination of fluorinated backbone, sulfonic acid groups, and the stabilising effect of the polymer matrix make Nafion a very strong acid, with pK_a ~ -6. In this respect Nafion resembles the trifluoromethanesulfonic acid, CF_3SO_3H, although Nafion is a weaker acid by at least three orders of magnitude; finally, it is selectively and highly permeable to water.

The morphology of Nafion membranes is a matter of continuing study to allow for greater control of its properties. Other properties such as water management, hydration stability at high temperatures, electro-osmotic drag, as well as the mechanical, thermal, and oxidative stability, are affected by the Nafion structure.

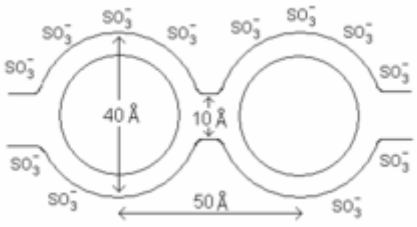

Figure 1.6: Cluster network model of Nafion. Reprinted with permission from[24] Copyright (1981) John Wiley and Sons

The first model for Nafion, called the cluster-channel or cluster-network model,[24] (Figure 1.6) consisted of an equal distribution of sulfonate ion clusters (also described as "inverted micelles") with a 40 Å diameter held within a continuous fluorocarbon lattice. Narrow channels about 10 Å in diameter interconnect the clusters, which explain the transport properties. However, the difficulty in determining the exact structure of Nafion stems from inconsistent solubility and crystalline structure among its various derivatives. Advanced morphological models have included a core-shell model[122] where the ion-rich

core is surrounded by an ion poor shell,[121] a lamellar model,[123] a rod model where the sulfonic groups arrange into crystal-like rods,[124] and a sandwich model where the polymer forms two layers whose sulfonic groups attract across an aqueous layer where transport occurs.[125] Consistency between the models includes a network of ionic clusters; the models differ in the cluster geometry and distribution. Although no model has yet been determined fully correct, some scientists have demonstrated that as the membrane hydrates, Nafion's morphology transforms from the Cluster-Channel model to a rod-like model.

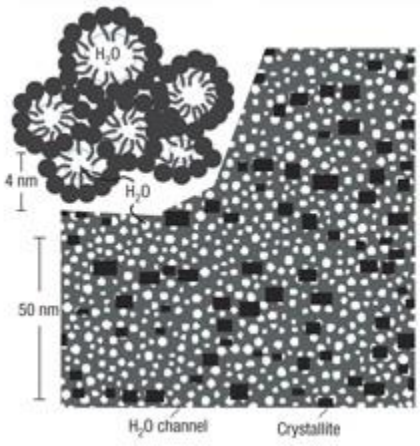

Figure 1.7: Water channel model of Nafion. Reprinted with permission from[25] Copyright (2008) Nature Publishing Group

A more recent water channel model[25] (Figure 1.7) was proposed based on simulations of small-angle X-ray scattering data and solid state nuclear magnetic resonance studies. In this model, the sulfonic acid functional groups self-organize into arrays of hydrophilic water channels, each ~ 2.5 nm in diameter, through which small ions can be easily transported. Interspersed between the hydrophilic channels are hydrophobic polymer backbones which provide the observed mechanical stability and it

is for these reasons why Nafion has become and remains the commercially viable membrane for PEMFCs. However, at temperatures above 80 °C operation becomes difficult as the conductivity of Nafion decreases due to dehydration of the membrane's matrix[133-135] and this, coupled with high cost and high methanol permeability[136-138] results in Nafion falling short of the strictest performance demands in a PEMFC.[139,140] Of late, a lot of research has gone into improving the performance of the Nafion membrane. Methods include doping the membrane with sulfonated silica clusters[126] or nanoparticles,[127] forming composite membranes be it organic[128] or sulfonated inorganic[129] based, looking at reducing the methanol crossover effect,[130] improving water retention,[131] or the *in situ* filling of the membrane with proton conducting macromolecules during the preparation stage.[132] However, whilst these do inprove the efficiency, none of them have becomes commercially viable replacements yet.

Metal-organic Frameworks

A new era in inclusion chemistry began with the discovery of periodic mesoporous materials by Beck *et al.* in 1992 at the Mobil Corporation.[26] MCM-41 (hexagonally packed mesoporous silicate alumino silicate materials) was synthesised with uniformly sized pores and surfaces areas approaching 1400 M^2 g^{-1}. Since then a wide variety of new materials have been synthesised that exploit the ability of these substrates to act as hosts for a broad range of inorganic[141,142] and organic[143,144] guest species too large to be included in the smaller pores of microporous zeolites. The encapsulation of organic and inorganic species within the pores of such a material can lead to different physical properties than those observed for the bulk guest species. Such

porous host guest metal organic composites eventually inspired the synthesis of a new class of crystalline porous network materials which are called metal organic frameworks MOFs and are described below.

As a rule, MOFs are compounds consisting of metal ions or clusters coordinated to organic molecules to form one-, two-, or three-dimensional structures that are often porous in nature. Known as a coordination network, this coordination compound extends through repeating coordination entities in 1 dimension, but with cross-links between two or more individual chains, loops, or spiro-links. Alternatively, it may extend through repeating coordination entities in 2 or 3 dimensions or form a polymer whereby a compound with repeating coordination entities extends through all three dimensions. Generally MOFs are composed of two major components: a metal ion or cluster of metal ions and an organic molecule called a linker. The organic units are typically mono-, di-, tri-, or tetravalent ligands. The choice of metal and linker dictates the structure and hence properties of the MOF. For example, the metal's coordination preference influences the size and shape of pores by dictating how many ligands can bind to the metal and in which orientation.[145]

Developed from the study of zeolites, MOFs are produced almost exclusively by hydrothermal or solvothermal techniques[146] but unlike the former, MOFs are constructed from bridging organic ligands that remain intact throughout the synthesis. Synthesis often makes use of a template and in MOFs, the framework is templated by the secondary building unit and the organic ligands. A templating approach that is useful for MOFs intended for gas storage is the use of metal-binding solvents such as N,N-

diethylformamide and water. In these cases, metal sites are exposed when the solvent is evacuated, allowing hydrogen to bind at these sites. Post-synthetic modification of MOFs opens up possibilities that might not be achieved by conventional synthesis.[147] Of potential relevance to hydrogen storage are MOFs with exposed metal sites.[148] Such sites have been generated by post-synthetic coordination of additional metal ions to sites on the bridging ligands, and addition and removal of metal atoms to the metal site.

Since ligands in MOFs typically bind reversibly, the slow growth of crystals often allows defects to be re-dissolved, resulting in a material with millimetre-scale crystals and a near-equilibrium defect density. Solvothermal synthesis is useful for growing crystals suitable to structure determination, because crystals grow over the course of hours to days.[146] However, the use of MOFs as storage materials for consumer products demands an immense scale-up of their synthesis. Scale-up of MOFs has not been widely studied, though several groups have demonstrated that microwaves can be used to nucleate MOF crystals rapidly from solution. This technique, termed "microwave-assisted solvothermal synthesis", is widely used in the zeolite literature, and produces micron-scale crystals in a matter of seconds to minutes, in yields similar to the slow growth methods.[149,150]

Another approach to increasing adsorption in MOFs is to alter the system in such a way that chemisorption becomes possible. This functionality has been introduced by making a composite material, which contains a MOF and a complex of platinum with activated carbon. In an effect known as hydrogen spillover, H_2 can bind to the platinum surface through a dissociative mechanism which cleaves the hydrogen molecule into two

hydrogen atoms and enables them to travel down the activated carbon onto the surface of the MOF.[151] This innovation produced a threefold increase in the room-temperature storage capacity of a MOF; however, desorption can take upwards of 12 hours, and reversible desorption is sometimes observed for only two cycles. The relationship between hydrogen spillover and hydrogen storage properties in MOFs is not well understood but may prove relevant to hydrogen storage.[152]

As an alternative, researchers suggested the use of MOFs as proton conductors because of high chemical and thermal stability and diverse topological architecture with tuneable functionality. MOFs modified with sulphonate and phosphate anions[27,28] or sulfate nanoparticales[153] have shown some promise in a bid to mimic the proton conducting pathways of Nafion, while anhydrous proton conduction has also been observed in crystalline MOFs.[29,154] However to date, most MOFs do not show high proton conductivity, long-term stability, durability in moisture, or are not yet developed enough[155] to be commercially viable.

Mesoporous materials. Porous materials are classified into several kinds by their size. According to IUPAC notation,[30] microporous materials have pore diameters of less than 2 nm and macroporous materials have pore diameters of greater than 50 nm; the mesoporous category thus lies in the middle. Typical mesoporous materials include a variety of silica and alumina that have similarly-sized fine mesopores. Mesoporous oxides of niobium,[36] tantalum,[35] titanium,[156] zirconium,[157] cerium[158] and tin[159] have also been reported, all of which can have disordered or ordered mesopores within a mesostructure.

A procedure for producing mesoporous materials (silica) was patented around 1970.[31–33] It went almost unnoticed and was reproduced in 1997.[34] Early MCM structures were mesoporous in nature and these were synthesised using the liquid crystal templating mechanism, (otherwise known as the surfactant templating mechanism) whereby surfactants are used which bond with the precursors to form micelles. These micelles rearrange into hexagonal rods and subsequently calcine which enables the silanol groups to form silicon-oxygen bridges into shape around the now cylindrical micelles.[35] (Figure 1.8) During the calcination process the organic template becomes oxidised and is removed to leave a hollow crystalline structure with well-formed pores, a narrow distribution of pore sizes, and very high surface areas ($\geq$1500 m^2 g^{-1}).

Following the research into mesoporous silica, the focus moved towards the development of similar materials using transition metal oxides. The advantages offered by the variable oxidation states in addition to the their unique optical and electronic properties could afford a healthy degree of customisation as each material could potentially be tailor made to suit each individual need. Using niobium ethoxide, Antonelli and Ying in 1996[36] made the first high surface area mesoporous transition metal oxide that was stable after template removal. Following this success, research expanded into high surface area mesoporous transition metal oxides made using Ti, Ta, Mo, Mn and Zr.[37–40] A main deviation from the mesoporous silica procedure is the inability to calcine the sample due to the instability of the material's mesostructure above certain temperatures. The remedy was to age the as-synthesised gel slowly by increasing the temperature incrementally until the peak temperature is achieved, thereby permitting the

remove of the organic template by protonolysis and subsequent washing. The final material is a highly porous amorphous transition metal oxide with very high surface area (>1000 m^2 g^{-1}). Subsequently, altering the template size was shown to change the properties of the material, which further allows for customisation of the material towards certain needs.

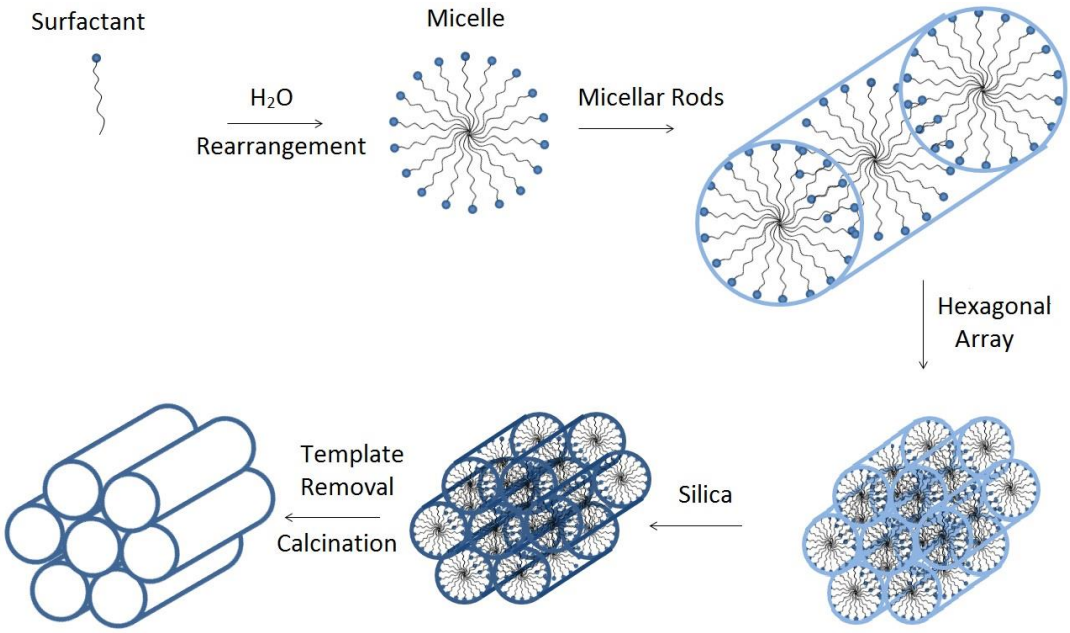

Figure 1.8: Scheme depicting the synthesis procedure of MCM 41[35]

In the years following, research in this field has steadily grown. Notable examples of prospective applications for these materials are catalysis, sorption, gas sensing, ion exchange, optics, and photovoltaics. That said, a lot of focus currently centres on Ti oxide due to its high surface area (*ca.* 1100 m^2 g^{-1}) photocatalytic activity and use in catalytic oxidation. Similarly Nb and Ta oxides (surface areas *ca.* 800 m^2 g^{-1} and 700 m^2 g^{-1} respectively) exhibit special properties such as high stability, variable oxidation states

useful in tailoring catalytic properties, as well as variable acidic properties crucial to acid catalysed reactions. On their own, mesoporous oxides have not shown a high proton conductivity but they have been used as a dopant in Nafion to suppress dehydration of the matrix,[41,42] while they have also been used as blends with zeolites[43] and nanoparticles[41] to encourage conductivity in the same manner.

Polymers

Originally coined in 1833 by Jöns Jacob Berzelius, the modern concept for the term "polymer" was proposed by Hermann Staudinger in 1920.[160] It refers to a molecule whose structure is composed of multiple repeating units, from which originates a characteristic of high relative molecular mass and attendant properties. Thus, a polymer is a large molecule, or macromolecule, composed of many repeated subunits. Polymers range from familiar synthetic plastics such as polystyrene to natural biopolymers such as DNA and proteins that are fundamental to biological structure and function. Polymers, both natural and synthetic, are created via polymerisation of many small molecules, known as monomers. Their consequently large molecular mass relative to small molecule compounds produces unique physical properties, including toughness, viscoelasticity, and a tendency to form glasses and semi-crystalline structures rather than crystals. Monomers tend to derive from molecules of low relative molecular mass. The identity of the repeat units comprising a polymer is its first and most important attribute. Polymer nomenclature is generally based upon the type of monomer residues comprising the polymer. Polymers that contain only a single type of repeat unit are known as

homopolymers, while polymers containing a mixture of repeat units are known as copolymers.

Laboratory synthetic methods are generally divided into two categories, step-growth polymerisation and chain-growth polymerisation. The essential difference between the two is that in chain growth polymerisation, monomers are added to the chain one at a time only, such as in polyethylene, whereas in step-growth polymerisation chains of monomers may combine with one another directly, such as in polyester. However, some newer methods such as plasma polymerisation[44] do not fit neatly into either category.

Polymer properties are broadly divided into several classes based on the scale at which the property is defined as well as upon its physical basis.[161] The most basic property of a polymer is the identity of its constituent monomers. A second set of properties, known as microstructure, essentially describe the arrangement of these monomers within the polymer at the scale of a single chain. These basic structural properties play a major role in determining bulk physical properties of the polymer, which describe how the polymer behaves as a continuous macroscopic material. Chemical properties, at the nanoscale, describe how the chains interact through various physical forces. At the macro-scale, they describe how the bulk polymer interacts with other chemicals and solvents.

The microstructure or configuration of a polymer relates to the physical arrangement of monomer residues along the backbone of the chain. These are the elements of polymer structure that require the breaking of a covalent bond in order to

change. Structure has a strong influence on the other properties of a polymer. An important microstructural feature of a polymer is its architecture and shape, which relates to the way branch points lead to a deviation from a simple linear chain. A branched polymer molecule is composed of a main chain with one or more substituent side chains or branches. Types of branched polymers include star polymers, comb polymers, brush polymers, dendronised polymers, and dendrimers. Two-dimensional polymers also exist which are composed of topologically planar repeat units and many common structures can be seen in Figure 1.9.[162]

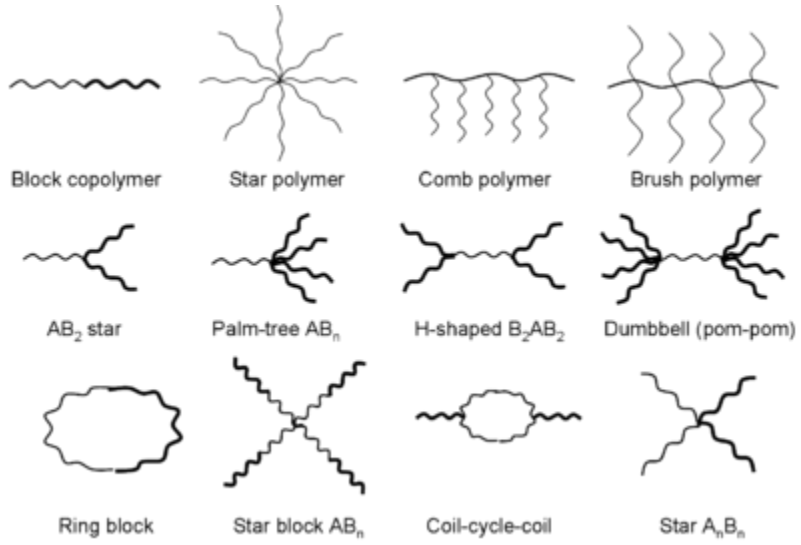

Figure 1.9: Various polymer architectures

A polymer's architecture affects many of its physical properties including, but not limited to, solution viscosity, melt viscosity, solubility in various solvents, glass transition temperature and the size of individual polymer coils in solution.

The physical properties of a polymer are strongly dependent on the size or length of the polymer chain. Impact resistance also tends to increase with chain length, as does

the viscosity, or resistance to flow, of the polymer in its melt state. Increasing chain length furthermore tends to decrease chain mobility, increase strength and toughness, and increase the glass transition temperature. This is a result of the increase in chain interactions such as Van der Waals attractions and entanglements that come with increased chain length. These interactions tend to fix the individual chains more strongly in position and resist deformations and matrix breakup, both at higher stresses and higher temperatures. A common means of expressing the length of a chain is the degree of polymerisation, which quantifies the number of monomers incorporated into the chain. As with other molecules, a polymer's size may also be expressed in terms of molecular weight. Since synthetic polymerisation techniques typically yield a polymer product including a range of molecular weights, the weight is often expressed statistically to describe the distribution of chain lengths present in the same. Common examples are the number average molecular weight and weight average molecular weight. The ratio of these two values is the polydispersity index, commonly used to express the "width" of the molecular weight distribution. A final measurement is contour length, which can be understood as the length of the chain backbone in its fully extended state.

Polymerisation is a process of reacting monomer molecules together in a chemical reaction to form polymer chains or three-dimensional networks. There are many forms of polymerisation and different systems exist to categorise them. Molecules made of a small number of monomer units, up to a few dozen, are called oligomers. An oligomer is molecule of intermediate relative molecular mass; the structure of which essentially comprises a small plurality of units derived, actually or conceptually, from molecules of

lower relative molecular mass. The term multimer is used with a meaning similar to that of oligomer in the context of proteins (although technical restrictions of word sense may exist). Many oils are oligomeric, such as liquid paraffin. Plasticisers are oligomeric esters widely used to soften thermoplastics such as PVC. They may be made from monomers by linking them together, or by separation from the higher fractions of crude oil. Polybutene is an oligomeric oil used to make putty. Greek prefixes are often used to designate the number of monomer units in the oligomer, for example a tetramer being composed of four units and a hexamer of six. Oligomerisation is a chemical process that converts monomers to macromolecular complexes through a finite degree of polymerisation. The actual figure for degree of polymerisation is a matter of debate, often a value between 10 and 100. When an oligomer forms as a result of chain transfer the oligomer is called a telomer and the process telomerisation. Of late, research has stemmed into using sulphated polymers for exploiting their proton conducting nature in a bid to find cheaper alternatives and this has so far yielded proming results.[163,164]

Naphthalene Sulfonate Formaldehyde. Patented as salts of naphthalene sulfonic acid-formaldehyde condensates,[45] naphthalene sulfonate formaldehyde (NSF) is a polymer used most commonly as a plasticiser in the production of concrete and plasterboard. It is also used as a dispersant in synthetic and natural rubbers, as a dye or syntan in the leather industries, as a pesticide in agricultural formulations and in lead–acid battery plates.

Naphthalene sulfonate polymers are produced by treating naphthalene with sulfuric acid and then polymerising with formaldehyde, often followed by neutralisation

with sodium hydroxide or calcium hydroxide. (Figure 1.10) These products are commercially sold in solution (water) or dry powder form. In the sulfonation step, naphthalene reacts slowly with sulfuric acid alone to give naphthalenesulfonic acid. The reaction starts with the protonation of one molecule of sulfuric acid by another, followed by the loss of a molecule of water.

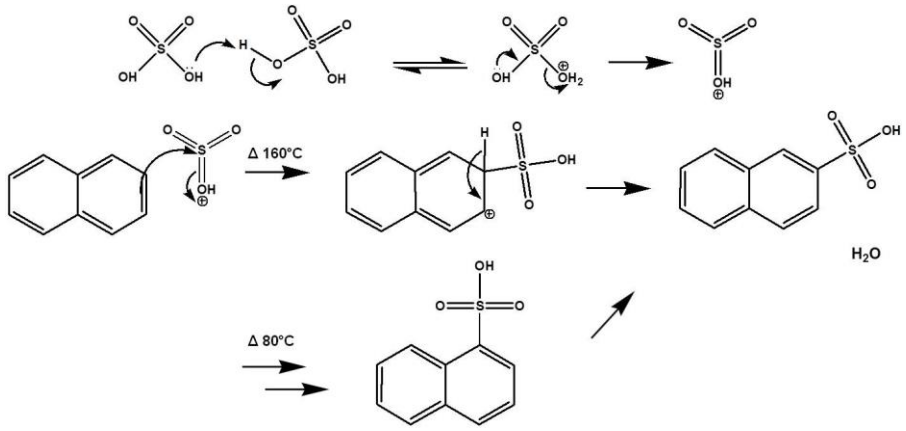

Figure 1.10: Arrow-pushing mechanism for the synthesis of NSF

The cation produced is very reactive and combines with naphthalene via the slow addition to the aromatic π system, followed by rapid loss of a proton to regenerate the aromaticity. To speed up the reaction process, heat is often used and the choice of temperature dictates the isomer formed. At 80 °C, the kinetic product is formed on the alpha position on the aromatic ring; increasing the temperature to 160 °C affords the thermodynamic product on the beta position.

Taking the thermodynamic product, the compound undergoes condensation polymerisation with formaldehyde, in a process catalysed by the compounds inherent acidity. Electrophilic aromatic substitution occurs whereby the naphthalene ring attacks

the formaldehyde molecule at the carbon atom to form an intermediate with the carbocation partially stabilised through resonance which allows the postitive charge to distributed over five carbon other atoms.

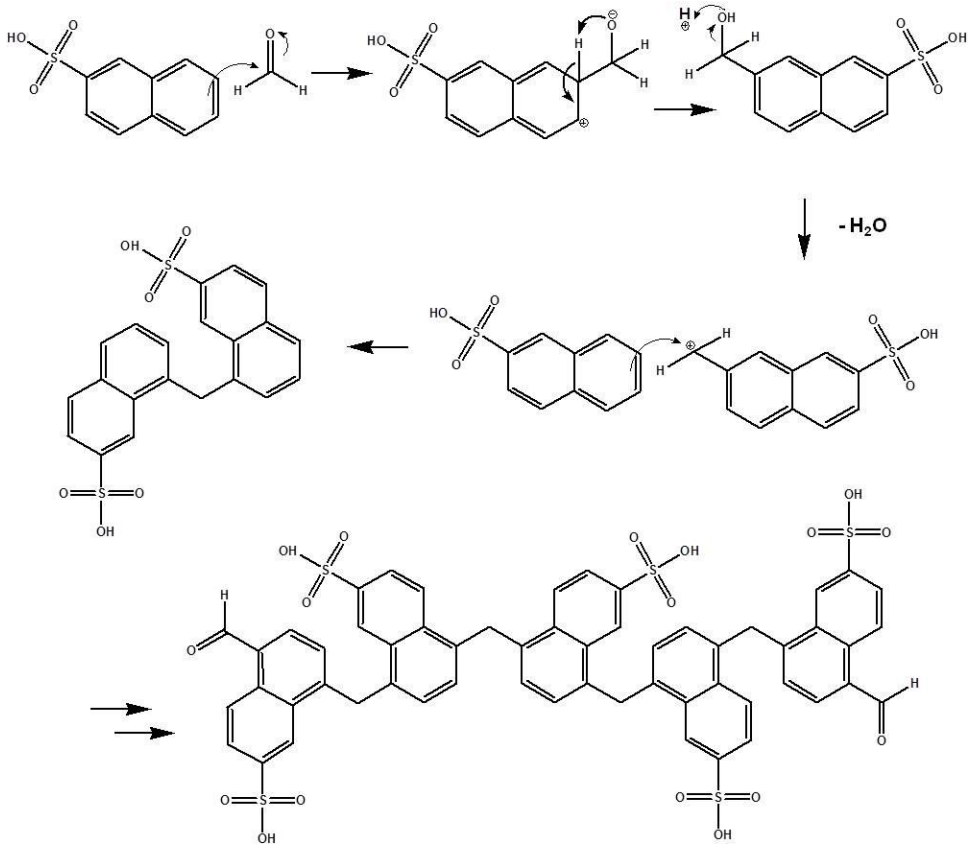

Figure 1.11: Arrow pushing mechanism for the oligermerisation of NSF

In the next stage of the reaction, the negatively charged oxygen molecule acts as a Brønsted base by donating electrons to the hydrogen at the point of the electrophilic attack, with the electrons shared by the hydrogen returning to the π system to regenerate aromaticity. Protonation of the alcohol function group results in a loss of H_2O, which attracts another naphthalenesulfonic acid monomer unit in a step growth polymerisation

mechanism. (Figure 1.11) Once the dimer is formed, further additions of formaldehyde molecules on carbons *meta* to the alkane linkers continues the step growth.

$$C_{10}H_7\text{-}SO_3H\text{-}(C_{10}H_7\text{-}SO_3H)x + H_2SO_4 + 2m\ NaOH \rightarrow C_{10}H_7\text{-}SO_3Na\text{-}(C_{10}H7\text{-}SO_3Na)x + x\ H_2O + Na_2SO_4$$

Oligomers of NSF are often found in units consisting of 4-6 monomers, with a molecular mass between 400 and 1000.[46,47] To form the often seen salts, subsequent neutralisation follows the equation above which proceeds to completely stabilise the polymer and prevent further reaction. Preliminary experiments in our group have explored the proton conducting nature of this oligomer within a mesoporous transition metal oxide scaffold and this has also seen promising results.[53]

Characterisation Techniques

Characterisation is the broad and general process by which a material's structure and properties are probed and measured. This section discusses the main techniques, be it microscopic, spectroscopic or macroscopic, employed thesis-wide to determine and understand the materials and composites created within.

Surface area analysis. The characterisation used in this thesis to confirm the surface area of the as-synthesised materials is comprised of two parts: Brunauer-Emmet-Teller (BET) surface area analysis and Barrett-Joyner-Halenda (BJH) pore size and volume analysis.

BET surface area analysis Originally derived from Langmuir theory and first published in 1938 by Stephen Brunauer, Paul Hugh Emmett, and Edward Teller,[48] BET theory aims to explain the physical adsorption of gas molecules on a solid surface and

serves as the basis for an important analysis technique for the measurement of the specific surface area of ideally, a non-microporous material. It refers to multi-layer adsorption whereby it adopts inert gases (nitrogen, argon) as adsorbates to determine the surface area data. The manner in which these gasses adsorb and desorb with the material enables the assessment of the materials specific surface area and porosity. This initial adsorption of gas onto the surface forms a monolayer which is subsequently followed by supplementary layers until all pores are filled and the saturation pressure is reached. Shown below is the equation for BET Theory, where P is pressure, V_a is the quantity of gas adsorbed at pressure, V_m is the quantity of gas adsorbed when the entire surface is covered in a monomolecular layer, and P_0 is the saturation point of the gas:

$$P/V_a\,(P_0 - P) = (1/V_m)(P/P_0)$$

On a macroscopic scale, the total pore volume and surface area in a material can be determined using a method known as isothermal gas adsorption. By measuring the volume of gas adsorbed onto a material at different pressures, and adsorption isotherm plot can be generated and used to infer several key properties of the material. Initially, the sample must be cooled to 77 K to minimise the effects on the kinetics of desorption. Next, both the reference and sample chambers are evacuated then isolated from each other. The first chamber is filled with a certain pressure of gas, then the chamber is isolated and the pressure is recorded. The valve between the first chamber and sample chamber is opened, and the gas is allowed to reach an equilibrium pressure, which is recorded. Incrementally, pressure is increased until the sample chamber pressure reaches the equilibrium vapor pressure of nitrogen at 77 K, which is 100 kPa. Nitrogen gas is

used to complete the procedure as the ratio of the pressures will be greater by the volume of gas adsorbed to the surface. This adsorbed volume is recorded for a number of equilibrium pressures and plotted as a BET plot, otherwise known as a nitrogen adsorption/desorption isotherm.

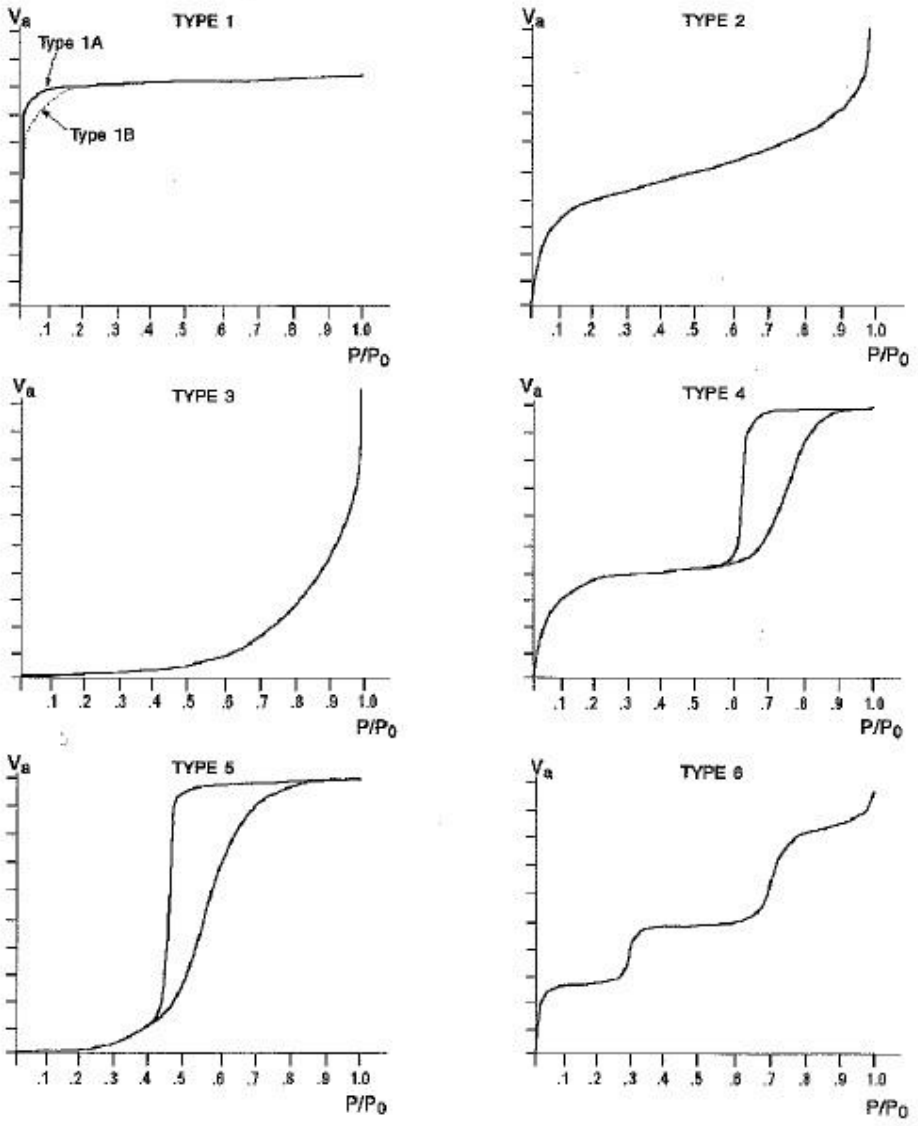

Figure 1.12: The six basic adsorption isotherm types[49] Copyright (2008) Micromeritics

Adsorption isotherms conform to one of following six forms as shown in Figure 1.12: Type 1 is characteristic of adsorbents having small extremely small pores and in this regime, gas adsorbs as a single monolayer until the surface is completely covered, at which time the surface saturates and adsorption rate tapers off. Type 6 is indicative of an irregular isotherm, by which multiple dimensions of pores are present, each reaching saturation incrementally at different total adsorbed volumes, and not having a clear overall saturation level. Types 2 and 4 commonly reflect either nonporous or adsorbents of those with fairly large pores whereby 2 is an adsorption isotherm that indicates a mechanism by which the gas forms a monolayer but continues to adsorb, forming layers several atoms thick while 4 indications of adsorption and condensation into capillary pores that saturate, or fill with essentially a liquid phase of adsorbent. Types 3 and 5 arise in situations where adsorptive molecules have a greater affinity for one another than they do the solid. 3 is an adsorption isotherm which indicates a mechanism by which the gas adsorbs in thick layers prior to or without first forming a single monolayer, while 5 is a direct multilayer adsorption. For mesoporous materials composites synthesised with a pore size within the range of 20 – 30 Å, the expected the isotherm lies between a Type 1 and a Type 4 isotherm. As such, this characterisation is crucial to validating the samples formed. BET analysis has frequently been employed to characterise mesoporous materials in the past[165] and remains a current characterization technique.[166]

BJH pore size and volume analysis. The method of BJH, proposed in 1951,[50] was originally designed for relatively wide-pore adsorbents with a wide pore size distribution.

However, it was repeatedly demonstrated that it can be successfully applied to virtually all types of porous materials. The model is based on the assumption that pores have a cylindrical shape and that pore radius is equal to the sum of the Kelvin radius and the thickness of the film adsorbed on the pore wall. The desorption branch of isotherm in the pressure range is generally used as initial data for BJH calculations (although the use of the adsorption branch is also possible).

BJH analysis can also be employed to determine pore area and specific pore volume using adsorption and desorption techniques.[167] This technique characterises pore size distribution independent of external area due to particle size of the sample and as such, is extremely useful in conjunction with the BET data for analysing mesoporous materials.

Infrared Spectroscopy. Infrared (IR) spectroscopy deals with the IR region of the electromagnetic spectrum where it covers a range of techniques, mostly based on absorption spectroscopy. For a given sample which may be solid, liquid, or gaseous, the method or technique of IR spectroscopy uses an instrument called an IR spectrometer (or spectrophotometer) to produce an IR spectrum. A basic IR spectrum is essentially a graph of infrared light absorbance (or transmittance) on the vertical axis vs. frequency or wavelength on the horizontal axis. Typical units of frequency used in IR spectra are reciprocal centimetres (sometimes called wave numbers), with the symbol cm^{-1}. Units of IR wavelength are commonly given in micrometers (or microns), symbol μm, which are related to wave numbers in a reciprocal way.

The infrared portion of the electromagnetic spectrum is usually divided into three regions; the near-, mid- and far- infrared, named for their relation to the visible spectrum. The higher-energy near-IR, approximately 14000–4000 cm^{-1} can excite overtone or harmonic vibrations. The mid-infrared, approximately 4000–400 cm^{-1} may be used to study the fundamental vibrations and associated rotational-vibrational structure. The far-infrared, approximately 400–10 cm^{-1}, lying adjacent to the microwave region, has low energy and may be used for rotational spectroscopy. The names and classifications of these sub-regions are conventions, and are only loosely based on the relative molecular or electromagnetic properties. This technique exploits the fact that molecules absorb specific frequencies that are characteristic of their structure. These absorptions are resonant frequencies, i.e. the frequency of the absorbed radiation matches the transition energy of the bond or group that vibrates. The energies are determined by the shape of the molecular potential energy surfaces, the masses of the atoms, and the associated vibronic coupling.

Referencing the Born–Oppenheimer and harmonic approximations, the resonant frequencies are associated with the normal modes corresponding to the molecular electronic ground state potential energy surface. The resonant frequencies are also related to the strength of the bond and the mass of the atoms at either end of it. Thus, the frequencies of the vibrations are associated with a particular normal mode of motion and a particular bond type. In order for a vibrational mode in a molecule to be "IR active", it must be associated with changes in the dipole. A permanent dipole is not necessary, as the rule requires only a change in dipole moment.

A molecule can vibrate in many ways, and each way is called a vibrational mode. For molecules with N number of atoms in them, linear molecules have $3N - 5$ degrees of vibrational modes, whereas nonlinear molecules have $3N - 6$ degrees of vibrational modes (also called vibrational degrees of freedom). As an example H_2O, a non-linear molecule, will have $3 \times 3 - 6 = 3$ degrees of vibrational freedom, or modes. Simple diatomic molecules have only one bond and only one vibrational band. If the molecule is symmetrical, e.g. N_2, the band is not observed in the IR spectrum, but only in the Raman spectrum. Asymmetrical diatomic molecules, e.g. CO, absorb in the IR spectrum. More complex molecules have many bonds, and their vibrational spectra are correspondingly more complex, i.e. big molecules have many peaks in their IR spectra. The atoms in a CH_2X_2 group, commonly found in organic compounds and where X can represent any other atom, can vibrate in nine different ways. Six of these involve only the CH_2 portion: symmetric and antisymmetric stretching, scissoring, rocking, wagging and twisting, with each giving rise to a peak on the IR spectra. In practice these spectroscopic techniques are used to readily identify various functional groups in a solid and are thus powerful routine characterisation methods. It remains a current technique for characterisation of mesoporous materials and composites.[168]

Powder X-ray Diffraction. The phenomenon known as elastic scattering sees a regular array of scatterers (often a crystal's electrons) produce a regular array of spherical waves. Although these waves cancel one another out in most directions through destructive interference, they add constructively in a few specific directions, determined by Bragg's law:

$$2d\sin\theta = n\lambda$$

Here *d* is the spacing between diffracting planes, θ is the incident angle, *n* is any integer, and λ is the wavelength of the beam. These specific directions appear as spots on the diffraction pattern called reflections. Thus, X-ray diffraction (XRD) results from an electromagnetic wave impinging on a regular array of scatterers (the repeating arrangement of atoms within the crystal).

X-rays are used to produce the diffraction pattern because their wavelength λ is typically the same order of magnitude (1–100 Å) as the spacing *d* between planes in the crystal. In principle, any wave impinging on a regular array of scatterers produces diffraction, as predicted first by Francesco Maria Grimaldi in 1665. The diffraction of sunlight through a bird's feather was first reported by James Gregory in the later 17th Century while the first artificial diffraction gratings for visible light were constructed by David Rittenhouse in 1787, and Joseph von Fraunhofer in 1821. However, visible light has too long a wavelength (typically, 5500 Å) to observe diffraction from crystals. Prior to the first XRD experiments, the spacings between lattice planes in a crystal were not known with certainty.

The idea that crystals could be used as a diffraction grating for X-rays arose in 1912 following collaboration between Ewald and Von Laue, who realised that electromagnetic radiation of a shorter wavelength was needed to observe such small spacings. Von Laue worked with two technicians, Walter Friedrich and his assistant Paul Knipping, to shine a beam of X-rays through a copper sulfate crystal and record its diffraction on a photographic plate. After being developed, the plate showed a large

number of well-defined spots arranged in a pattern of intersecting circles around the spot produced by the central beam. This enabled Von Laue to develop a law that connects the scattering angles and the size and orientation of the unit-cell spacings in the crystal. As described in the mathematical derivation below, the X-ray scattering is determined by the density of electrons within the crystal. Since the energy of an X-ray is much greater than that of a valence electron, the scattering may be modelled as Thomson scattering, the interaction of an electromagnetic ray with a free electron. This model is generally adopted to describe the polarisation of the scattered radiation.

The intensity of Thomson scattering for one particle with mass *m* and charge *q* is:

$$I_o = I_e \left(\frac{q^4}{m^2 c^4} \right) \frac{1 + \cos^2 2\theta}{2} = I_e 7.94.10^{-26} \frac{1 + \cos^2 2\theta}{2} = I_e f$$

Hence the atomic nuclei, which are much heavier than an electron, contribute negligibly to the scattered X-rays.

It is relatively simple to determine the structure from single crystal diffraction data. However, not all material can provide single crystals and powders are much more common. As a powder contains a very large number of randomly orientated tiny crystals, when placed in the path of a monochromatic X-ray beam, diffraction will occur from planes in those crystallites which happen to be orientated at the correct angle to fulfill the Bragg condition and thus, a reflection will appear. Planes with these *d*-spacings exist in the structure and by assigning *hkl* values to each reflection it is possible to determine the unit cell dimensions – in addition to any other phase changes. That said, full

determination can be problematic as there is less data and thus, it's often only used as a fingerprint technique. A schematic of the XRD process is shown in Figure 1.13.

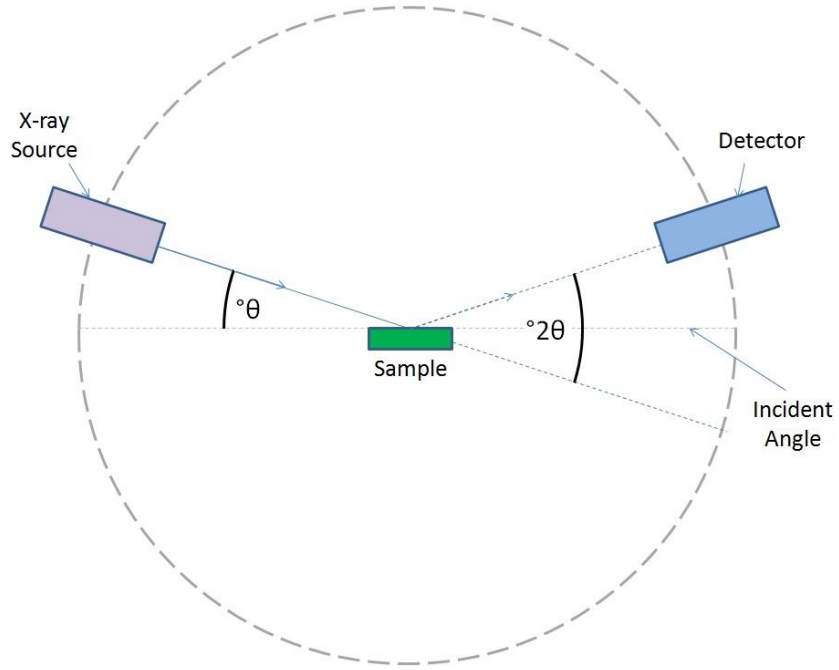

Figure 1.13: Schematic of a XRD analysis

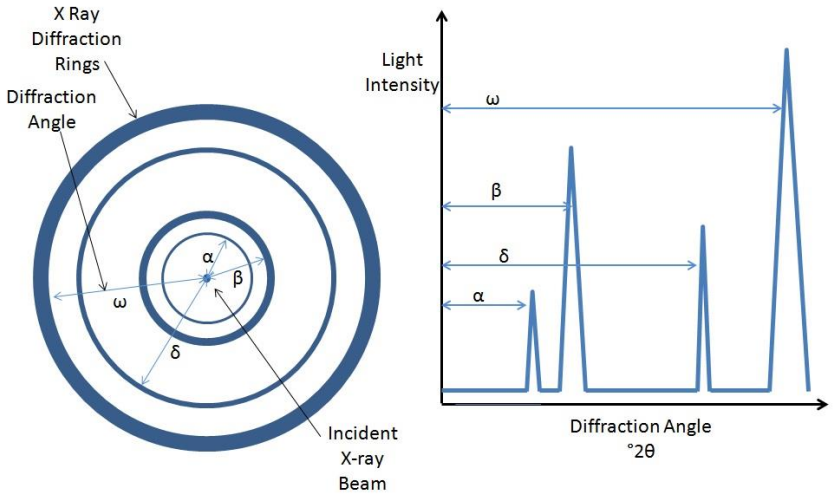

Figure 1.14: An example of a XRD image and plot

In a powder XRD (PXRD) plot the intensity of the reflections produced by the x-rays is diffracted evenly into ring shapes, which results in measurements being recorded in a single direction as this allows the radiation to be averaged and collected from each ring. (Figure 1.14) The gap between ring and the incident beam of x-ray radiation is called the scatter angel (*2θ*). Each of the rings produces a given signal intensity at the set angle, with each reflection representing a lattice parameter. The shape of the peak present in the diffraction pattern indicates the crystallinity of the material. Crystalline materials show high intensity sharp reflections with a narrow base, while amorphous materials show much lower intensities with a wide base to the point where at times they are so low that they are masked by the background noise. (Figure 1.15) In mesoporous materials, the data displays broad reflections to indicate the wormholesque pore structure, with minor reflections to indicate the decree of partial crystallisation within the walls of the structure, hence PXRD being useful for routine characterisation of mesoporous mterials.[169]

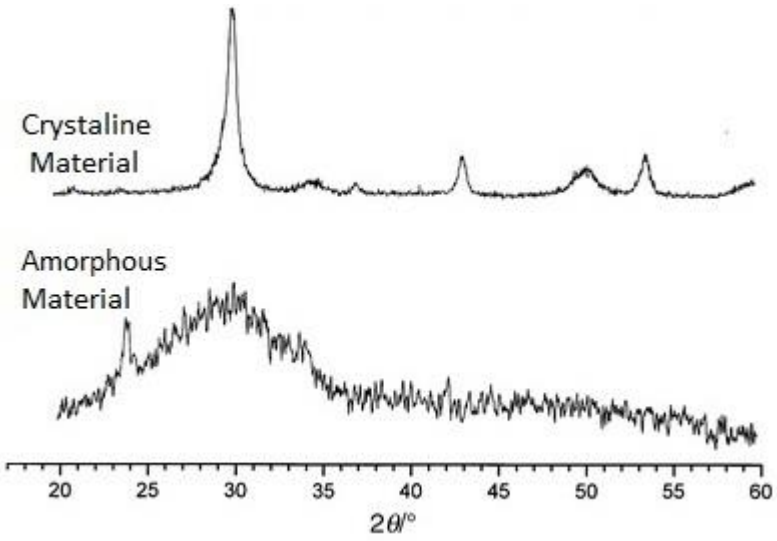

Figure 1.15: PXRD plots for crystalline and amorphous materials

Thermal Analysis. Thermogravimetric (TGA) and differential thermal analysis (DTA) are types of thermal analysis that use the thermal treatment of samples to characterise the materials.

Thermogravimetric Analysis. TGA is a method of thermal analysis in which changes in physical and chemical properties of materials are measured as a function of increasing temperature (with constant heating rate), or as a function of time (with constant temperature and/or constant mass loss). TGA can provide information about physical phenomena, such as second-order phase transitions, including vaporisation, sublimation, absorption, adsorption, and desorption. Likewise, TGA can provide information about chemical phenomena including chemisorptions, desolvation (especially dehydration), decomposition, and solid-gas reactions (e.g., oxidation or reduction).

TGA is commonly used to determine selected characteristics of materials that exhibit either mass loss or gain due to decomposition, oxidation, or loss of volatiles (such as moisture). Common applications of TGA include but are not restricted to; materials characterisation through analysis of characteristic decomposition patterns; studies of degradation mechanisms and reaction kinetics; determination of organic content in a sample; and determination of inorganic (e.g. ash) content in a sample, which may be useful for corroborating predicted material structures or simply used as a chemical analysis. It is an especially useful technique for the study of polymeric materials, including thermoplastics, thermosets, elastomers, composites, plastic films, fibres, coatings and paints. Discussion of the TGA apparatus, methods, and trace analysis will be

elaborated upon below. Thermal stability, oxidation, and combustion, all of which are possible interpretations of TGA traces, will also be discussed.

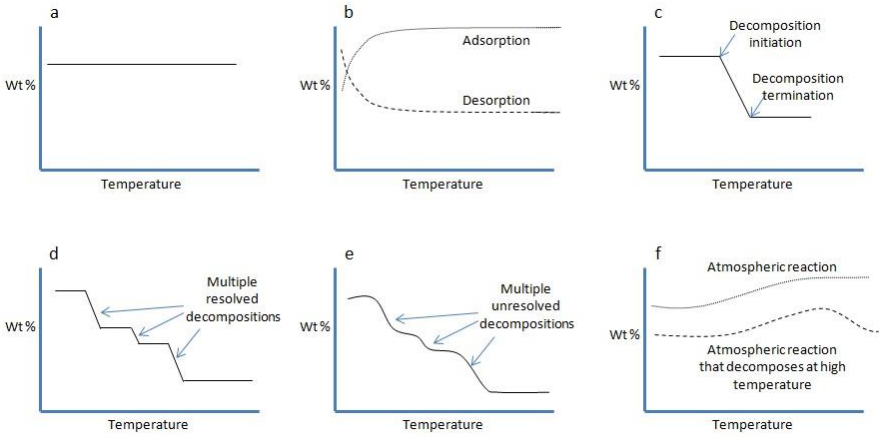

Figure 1.16: Processes types that occur during TGA. A) No change B) adsorption/desorption C) decomposition D) resolved multiple decompositions E) unresolved multiple decompositions F) atmospheric reactions

The TGA instrument continuously weighs a sample as it is heated to temperatures of up to 2000 °C. As the temperature increases, various components of the sample are decomposed and the weight percentage of each resulting mass change can be measured. Results are plotted with temperature on the *X*-axis and mass loss on the *Y*-axis.

If the identity of the product after heating is known, then the ceramic yield can be found from analysis of the ash content. By taking the weight of the known product and dividing it by the initial mass of the starting material, the mass percentage of all inclusions can be found. Knowing the mass of the starting material and the total mass of inclusions, such as ligands, structural defects, or side-products of reaction, which are liberated upon heating, the stoichiometric ratio can be used to calculate the percent mass of the substance in a sample. The results from TGA may be presented by mass versus temperature (or time) curve (or thermogram), or rate of mass loss versus temperature

curve (referred to as the differential thermogram), with the process types shown in Figure 1.16. Simple thermograms generally contain the following features: a horizontal portion or plateau that indicates constant sample weight; a curved portion where the steepness of the curve indicates the rate of mass loss; or an inflection (at which *dw/dt* is a minimum, but not zero).

TGA can be used to evaluate the thermal stability of a material. In a desired temperature range, if a species is thermally stable, there will be no observed mass change. Negligible mass loss corresponds to little or no slope in the TGA trace. TGA also gives the upper use temperature of a material. Beyond this temperature the material will begin to degrade. The three ways a material can lose mass during heating are through chemical reactions, the release of adsorbed species, and decomposition. All of these indicate that the material is no longer thermally stable. As the TGA is performed in air, oxygen reacts with the organic fibers which eventually degrade completely, evidenced by the 100 % mass loss. It is important to link thermal stability to the gas in which the TGA is performed. Oxidative mass losses are the most common observable losses in TGA. Combustion during TGA is identifiable by distinct traces made in the TGA thermograms produced. Due to combustion, a TGA trace can deviate from the normal form of a well-behaved function. This phenomenon arises from a rapid temperature change. When the weight and temperature are plotted versus time, a dramatic slope change in the first derivative plot is concurrent with the mass loss of the sample and the sudden increase in temperature seen by the thermocouple. The mass loss could be the result of particles of

smoke released from burning caused by inconsistencies in the material itself, beyond the oxidation of carbon due to poorly controlled weight loss.

TGA has a wide variety of applications, including analysis of ceramics and thermally stable polymers. Ceramics usually melt before they decompose as they are thermally stable over a large temperature range, thus TGA is mainly used to investigate the thermal stability of polymers. Most polymers melt or degrade before 200 °C. However, there is a class of thermally stable polymers that are able to withstand temperatures of at least 300 °C in air and 500 °C in inert gases without structural changes or strength loss, which can be analysed by TGA.

Differential Thermal Analysis. DTA is a thermoanalytic technique, similar to differential scanning calorimetry. In DTA, the material under study and an inert reference are made to undergo identical thermal cycles, while recording any temperature difference between sample and reference. This differential temperature is then plotted against time, or against temperature (DTA curve, or thermogram). Changes in the sample, either exothermic or endothermic, can be detected relative to the inert reference. Thus, a DTA curve provides data on the transformations that have occurred, such as glass transitions, crystallisation, melting and sublimation. The area under a DTA peak is the enthalpy change and is not affected by the heat capacity of the sample. Used in conjunction with TGA, we can correlate whether or not the changes in mass observed are those of endothermic or exothermic processes. This is essential in order to fully understand the transitions taking places throughout thermal treatment and provide evidence to support conclusions. Together, both TGA and DTA are used for routine characterisation in this

project as they help identify the ratio of mesoporous material to hydrocarbon within the composites.[170,171]

Transmission Electron Microscopy. Transmission electron microscopy (TEM) is a microscopy technique in which a beam of electrons is transmitted through an ultra-thin specimen, interacting with the specimen as it passes through. An image is formed from the interaction of the electrons transmitted through the specimen; the image is magnified and focused onto an imaging device, such as a fluorescent screen, on a layer of photographic film, or to be detected by a sensor such as a charge-coupled device (CCD) camera.

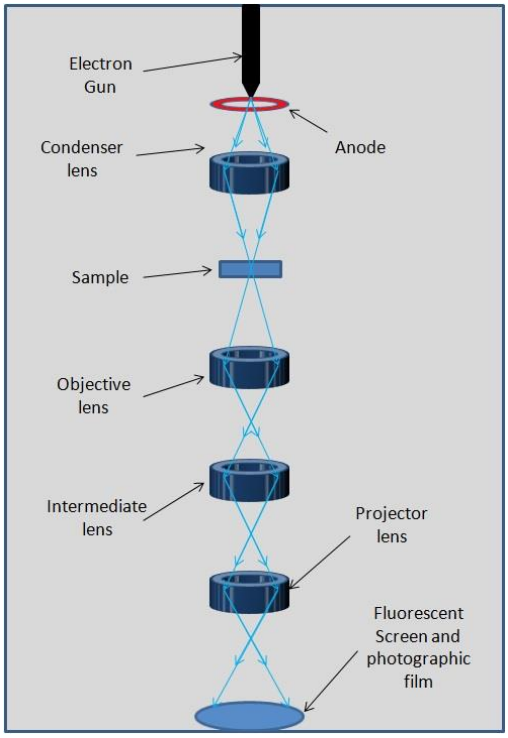

Figure 1.17: Schematic of a TEM analysis

TEMs are capable of imaging at a significantly higher resolution than light microscopes, owing to the small de Broglie wavelength of electrons. This enables the instrument's user to examine fine detail—even as small as a single column of atoms, which is thousands of times smaller than the smallest resolvable object in a light microscope. TEM forms a major analysis method in a range of scientific fields, in both physical and biological sciences. TEMs find application in cancer research, virology, materials science as well as pollution, nanotechnology, and semiconductor research.

At smaller magnifications TEM image contrast is due to absorption of electrons in the material, due to the thickness and composition of the material. At higher magnifications complex wave interactions modulate the intensity of the image, requiring expert analysis of observed images. Alternate modes of use allow for the TEM to observe modulations in chemical identity, crystal orientation, electronic structure and sample induced electron phase shift as well as the regular absorption based imaging.

Electron microscopy involves the use of electrons to create a virtual image of a sample at a significantly higher magnification and resolution than is possible using traditional optical microscopy, and a schematic of a typical TEM is shown in Figure 1.17.

Theoretically, the maximum resolution, *d*, that one can obtain with a light microscope has been limited by the wavelength of the photons that are being used to probe the sample, λ and the numerical aperture of the system, *NA*.

$$d = \frac{\lambda}{2n\sin\alpha} \approx \frac{\lambda}{2\,\mathrm{NA}}$$

Early twentieth Century scientist's theorised ways of getting around the limitations of the relatively large wavelength of visible light (wavelengths of 400–700 nm) by using electrons. Like all matter, electrons have both wave and particle properties (as theorised by de Broglie), and their wave-like properties mean that a beam of electrons can be made to behave like a beam of electromagnetic radiation. The wavelength of electrons is related to their kinetic energy via the de Broglie equation. An additional correction must be made to account for relativistic effects, as in a TEM an electron's velocity approach the speed of light, *c*.

$$\lambda_e \approx \frac{h}{\sqrt{2m_0E\left(1+\frac{E}{2m_0c^2}\right)}}$$

Where, *h* is Planck's constant, m_0 is the rest mass of an electron and *E* is the energy of the accelerated electron. Electrons are usually generated in an electron microscope by a process known as thermionic emission from a filament, usually tungsten, in the same manner as a light bulb, or alternatively by field electron emission. The electrons are then accelerated by an electric potential (measured in volts) and focused by electrostatic and electromagnetic lenses onto the sample. The transmitted beam contains information about electron density, phase and periodicity; this beam is used to form an image.

Other variants of the TEM exist with one such being the scanning transmission electron microscope (STEM). Usually a STEM is a conventional TEM equipped with additional scanning coils, detectors and needed circuitry; however, dedicated STEMs are also manufactured. As with any transmission illumination scheme, the electrons pass

through a sufficiently thin specimen. However, STEM is distinguished from conventional TEMs by focusing the electron beam into a narrow spot which is scanned over the sample in a raster.

The rastering of the beam across the sample makes these microscopes suitable for analysis techniques such as mapping by energy dispersive X-ray (EDX) spectroscopy, electron energy loss spectroscopy (EELS) and annular dark-field imaging (ADF). These signals can be obtained simultaneously, allowing direct correlation of image and quantitative data.

By using a STEM and a high-angle detector, it is possible to form atomic resolution images where the contrast is directly related to the atomic number (z-contrast image). The directly interpretable z-contrast image makes STEM imaging with a high-angle detector appealing. This is in contrast to the conventional high resolution electron microscopy technique, which uses phase-contrast, and therefore produces results which need interpretation by simulation.

In this thesis STEM images are used to routinely characterise the samples by visually identifying the pore structure and lattice of the composites, allowing them to be verified against previous work. Also, TEM imagery remains at the forefront of characterisation for mesoporous materials.[172]

Electrochemical impedance spectroscopy. Electrochemical impedance spectroscopy (EIS) measures the dielectric properties of a medium as a function of frequency. This technique has grown tremendously in stature over the past few years and is now being widely employed in a wide variety of scientific fields such as fuel cell

testing, biomolecular interaction, and microstructural characterisation. Often, EIS reveals information about the reaction mechanism of an electrochemical process: different reaction steps will dominate at certain frequencies, and the frequency response shown by EIS can help identify the rate limiting step of reactions. Impedance is the opposition to the flow of alternating current (AC) in a complex system. A passive complex electrical system comprises both energy dissipater (resistor) and energy storage (capacitor) elements. If the system is purely resistive, then the opposition to AC or direct current (DC) is simply resistance. EIS is used to assess the impedance of a material to electron and ion flow. This is carried out using the more accurate concept of impedance in the place of ideological resistance.

Based on the interaction of an external field with the electric dipole moment of the sample (or permittivity), it is also an experimental method of characterising electrochemical systems. This technique measures the impedance of a system over a range of frequencies, and therefore the frequency response of the system, including the energy storage and dissipation properties, is revealed. Often, data obtained by EIS is expressed graphically in a Bode plot or a Nyquist plot. In traditional electronics resistance is based on the premise that there is a direct relationship between current and potential, (Figure 1.18) which remains unchanged regardless of the frequency used for alternating current. In reality the relationship varies according to frequency following a sinodial relationship as they are not in phase with each other. This phase shift is a parameter of the impedance.

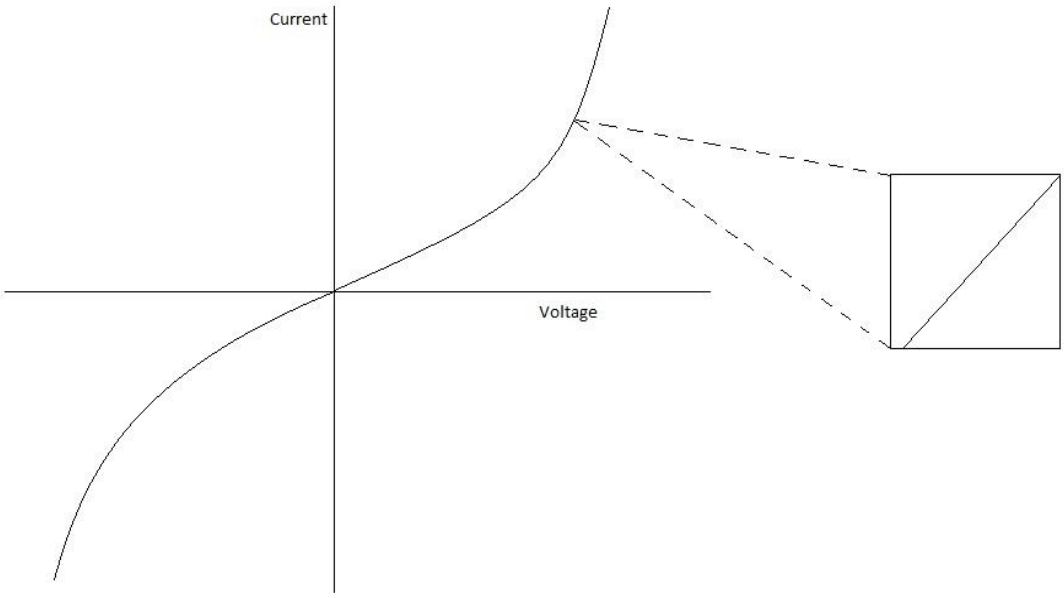

Figure 1.18: Diagram depicting the relationship between current and potential in impedance

The typical plot used in EIS is a Nyquist plot. (Figure 1.19) This consists of real (Z) and imaginary (Z') impedance values, for a range of frequencies. Each point present on the plot represents the impedance values of both parameters at a single frequency. In a potentiostatic system the input is potential and output is current. If we look at only a very small part of the voltage vs. current curve it appears pseudo linear. For this reason, a large number of points are taken using a very small (1-10 mV) AC signal.

Equivalent circuits (Figure 1.19) are used to interpret the Nyquist plot and extract the data from the set of points for a variety of components within the cell. There are a number of essential components present in the standard cell used in the assessment of a lithium ion battery material.

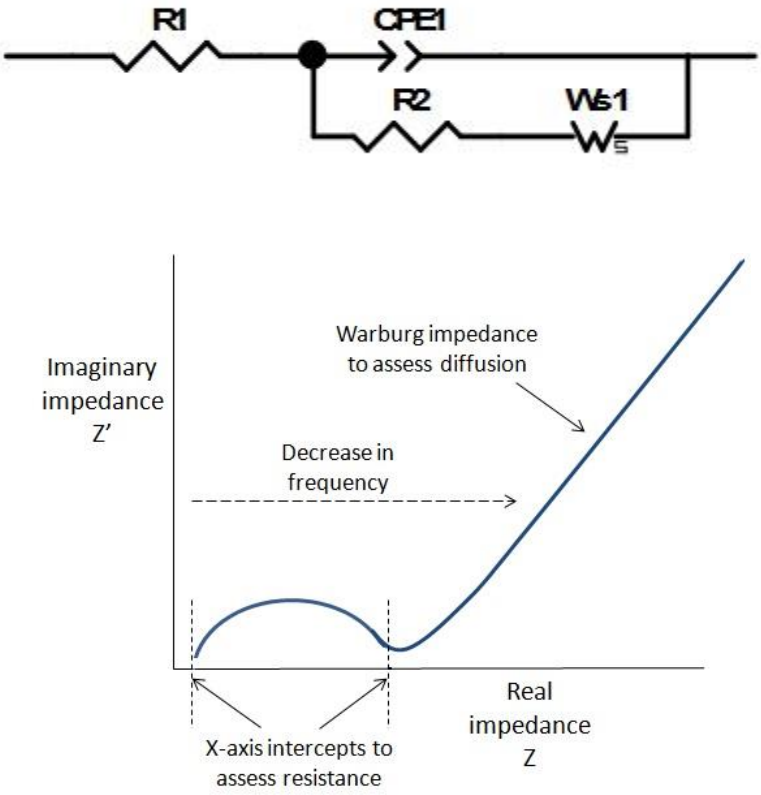

Figure 1.19: Example of a Nyquist plot, with different regions and interpretations, along with the associated equivalent circuit.

Using the equivalent cell and a Nyquist plot it is possible to calculate these parameters. Using the high frequency region to the left of the Nyquist plot, it is possible to determine the R_1 by determining the lowest intercept of the x (real) axis. At lower frequency values the opposite side of the semicircle is used in order to determine the R_2. The intercept at this region is equivalent to $R_2 + R_1$ so by subtracting the value obtained for R_1 this produces value of the R_2 of the redox process taking place. Finally, the line present at lowest frequency region at approximately 45 ° angle represents the Warburg impedance (W_S) and can be used to calculate the diffusions capabilities of the material.

This plot will be used in this project to provide (or where necessary, extrapolate using the Fit Circle function) the data needed to obtain the R_1 for each composite synthesised, which is the most important variable in this project. Increases in conductivity will cause a reduction in R_1 due to the improved charge transport allowing faster reaction kinetics with less resistance. From here, the proton conductivity can be obtained to support the findings of this work, and is determined using Equation 1.1, where σ is the proton conductivity in mS/cm, L is the distance between the two electrodes in cm, A is the area covered by the electrode contact in cm^2 and R is the initial resistance measured where the plot crosses the x-axis on the Nyquist plot. Figure 7.33 shows the typical setup used.

$$\sigma = {}^{L}/_{RA}$$

Equation 1.1: Proton conductivity

Finally, characterisation by EIS remains a strong method for analysing mesoporous materials.[173]

Scope and Outline of this Thesis

Introduction. Fuel cells have attracted a lot of attention in the search for alternative and green energy sources owing to their high efficiencies and low emissions. PEMFCs are a promising candidate as the next generation power sources for transportation, stationary, and portable applications due to low operating temperature, quick start-up time, high current density and easy scale-up. They are also receiving more importance due to the concerns that petroleum resources are depleting and thus needs an

alternate solution as fuel i.e. Hydrogen. Even though the invention of the fuel cell dates back to 1839, the commercialisation has not been fully attained for them. The barriers in the commercialisation are the many, with an efficient membrane material being a prominent concern. Despite research into improvements, the current commercially available incumbent Nafion is still prone to dehydration as the temperatures reach optimal PEMFC working conditions.

Hypothesis. The area of research of this thesis is the impregnation of the mesostructure with proton conducting oligomers, a strategy which has been used most notably by Bein in the synthesis of MCM-41 composites.[51,52] However, the doping of mesoporous transition metal oxides by conducting oligomers remains virtually unexplored. These materials should be particularly interesting because the variable oxidation states and high surface acidities offered by these materials should lead to enhancement of proton and electron conducting properties relative to the mesoporous silica composites. Preliminary results on NSF-doped mesoporous Nb oxide by our research group[53] already suggest that this material is a promising candidate for fuel cell membrane applications. The work presented in this thesis is aimed at the development of a new proton conducting material that is resilient to dehydration. The key idea in the design of the model system was to exploit the oxide surface of the ca. 20 Å pore walls of a mesoporous transition metal oxide as a means of anchoring sulfonate groups and suppressing moisture loss to encourage proton conduction pathways in the NSF impregnated analogues. Thus, a system was conceived and studied consisting of various single mesoporous transition metal oxides doped with H2SO4 and subsequently

impregnated with NSF via direct oligomer impregnation or by the NSF being oligomerised in situ of the mesoporous transition metal oxide's pores.

To achieve the aims of this work, the following objectives are in place:

- Synthesis of a series of sulfated and unsulfated mesoporous Ti, and Nb oxide composites impregnated with an oligomeric resin (NSF)
- Synthesis of a series of sulfated and unsulfated mesoporous Ta oxide composites using different chain length templates, and subsequent impregnation with an oligomeric resin (NSF)
- Characterisation of these composites using surface area analysis (BET and BJH analysis), IR spectroscopy, PXRD, thermal analysis, (DTA and TGA), TEM, and NMR
- Electrochemical characterisation of these composites to obtain the proton conductivity at various temperatures and subsequently, the durability over time
- Rationalising of the findings by in depth solid state NMR studies (1H, 13C, and 17O) to obtain information on the structure of the composites, their inherent proton conducting pathways and to prove the synergistic relationship between the mesoporous support and the sulfonated oligomer resin.

Outline. In this thesis, methods are presented to produce a proton conducting material which is resilient to dehydration at the temperatures needed for optimal PEMFC performance.

The design of the networking proton conducting pathways, along with the preparation, characterisation and functionalisation of the mesoporous titanium oxide

($mTiO_2$) composite is discussed in Chapter 2. It is shown that the mesoporous material can be impregnated with an oligomer and that this increases the proton conductivity over that of the starting material and of pure hydrated NSF, confirming a synergistic interaction between the NSF and the oxide mesostructure in the proton conductivity mechanism.

Chapter 3 describes the optimisation of these pathways using mesoporous niobium oxide (mNb_2O_5) and mesoporous tantalum oxide (mTa_2O_5) composites as the foundations for the system. By changing the pore size and metal of the mX_2O_5 system it is shown that proton conductivity can be increased to greater levels than that offered by Nafion at the working temperatures for PEMFCs.

Chapter 4 describes an alternative method of fabrication, whereby instead of impregnating the NSF into the mesopores, it is grown *in situ*. By tailoring the mX_2O_5 system as thus, we are able to further impregnate the pores of the metal mesostructure. This "one-pot" method is shown to reduce thermal leaching of the system and to encourage mechanical strengthening of the composite structure. With the proton conductivity attained being greater than that of Nafion, these findings are rationalised by conducting subsequent durability tests of the as-synthesised materials over a 24 hour period.

Knowledge of the dynamics of the proton movement is necessary to understand mechanism of the conduction pathways. Therefore, Chapter 5 is devoted to an in depth Solid State NMR analysis of the composites. ^{1}H and ^{13}C solid state NMR studies the NSF

material and the mX_2O_5-NSF composites demonstrate that the oligomeric nature of the NSF is preserved while in contact with the mX_2O_5 surface, thus facilitating conductivity.

Altogether, a viable method to produce a proton conducting material that is resilient to dehydration is presented, one which can be fine tuned through material choice and synthetic procedure.

References

[1] texte A. des sciences (France) A. (1839). *du. Comptes rendus hebdomadaires des séances de l'Académie des sciences / publiés... par MM. les secrétaires perpétuels*. Gallica. Retrieved from http://gallica.bnf.fr/ark:/12148/bpt6k2967c

[2] Wengenmayr, R. & Bührke, T. (2013). *Renewable Energy: Sustainable Energy Concepts for the Energy Change*. John Wiley & Sons.

[3] Williams. K. R., (1994). Francis Thomas Bacon. 21 December 1904-24 May 1992. *Biographical Memoirs of Fellows of the Royal Society*. Retrieved from http://rsbm.royalsocietypublishing.org/content/roybiogmem/39/2.full.pdf

[4] Grubb, J. W. T. (1959). *US2913511 A*. US Patent and Trademark Office.

[5] Niedrach, L. W. (1964). *US3134697 A* US Patent and Trademark Office.

[6] Grimwood. J. M., Hacker. B. C., Vorzimmer P. J., (1968). Prohect Gemini: A chronology. *National Aeronautics and Space Administration*. Retrienved from http://ntrs.nasa.gov/archive/nasa/casi.ntrs.nasa.gov/19690027123.pdf

[7] Ihrig, H. K. (1960). *The fuel cell powerplant for electrically propelled earthmoving machinery*. SAE Technical Paper. Retrieved from http://papers.sae.org/600239/

[8] Kunusch, C., Puleston, P. & Mayosky, M. (2012). *Sliding-mode control of PEM fuel cells*. Springer Science & Business Media.

[9] Types of Fuel Cells | Department of Energy. Retrieved from http://energy.gov/eere/fuelcells/types-fuel-cells#phosphoric

[10] Pivovar. B. S., Bender. G., Davey. J. R., Zelenay. P., (2003). Methanol crossover in direct methanol fuel cell systems. Retrieved from http://permalink.lanl.gov/object/tr?what=info:lanl-repo/lareport/LA-UR-03-0593

[11] Elmore. G. V., Tanner. H. A. (1961). Intermediate temperature fuel cells. *J. Electrochem. Soc*., *108*, 669–671.

[12] Fellet. M., Rossner. W. (2015). Ceramics improve operating conditions of solid-oxide fuel cells – *MRS Bull*. 214-215.

[13] Verda. V., Calí Quaglia. M. (2008). Solid oxide fuel cell systems for distributed power generation and cogeneration. *Int. J. Hydrog. Energy*, *33*, 2087–2096.

[14] Blomen. L. J. M. J., Mugerwa. M. N. (2013) *Fuel Cell Systems*. Springer Science & Business Media.

[15] Warhsay. M., Prokopius. P. R. (1989). *The fuel cell in space: yesterday, today, and tomorrow*. NASA Technical Memorandum. Retrieved online from http://ntrs.nasa.gov/archive/nasa/casi.ntrs.nasa.gov/19900002488.pdf

[16] Laguna-Bercero. M. A., Campana. R., Larrea. A., Kilner. J. A., Orera, V. M. (2011). Performance and aging of microtubular YSZ-based solid oxide regenerative fuel cells. *Fuel Cells*, *11*, 116–123.

[17] Kakati. B. K., Deka. D. (2007). Effect of resin matrix precursor on the properties of graphite composite bipolar plate for PEM fuel cell. *Energy Fuels*, *21*, 1681–1687.

[18] Liivat. A., Thomas. J. (2015). Minerals as a source of novel Li-ion battery electrode materials. *Maced. J. Chem. Chem. Eng.*, *34*, 145–149.

[19] Fernández. J. L., Raghuveer. V., Manthiram. A., Bard. A. J. (2005). Pd−Ti and Pd−Co−Au electrocatalysts as a replacement for platinum for oxygen reduction in proton exchange membrane fuel cells. *J. Am. Chem. Soc*., *127*, 13100–13101.

[19] Yousfi-Steiner. N., Moçotéguy. P., Candusso. D., Hissel, D. (2009). A review on polymer electrolyte membrane fuel cell catalyst degradation and starvation issues: causes, consequences and diagnostic for mitigation. *J. Power Sources*, *194*, 130–145.

[20] Li. H., Knights. S., Shi. Z., Zee. J. W. V., Zhang. J. (2010). *Proton exchange membrane fuel cells:*

contamination and mitigation strategies. CRC Press.

[21] Samms. S. R., Wasmus. S., Savinell. S. R. (1996). Thermal stability of Nafion® in simulated fuel cell environments. *J. Electrochem. Soc*., *143*(5), 1498-1504

[22] Tang. H. L., Pan. Mu., (2008). Synthesis and characterization of a self-assembled Nafion/silica nanocomposite membrane for polymer electrolyte membrane fuel cells. *J. Phys. Chem. C*, *112*(30), 11556–11568.

[23] Gierke. T. D., Munn. G. E., Wilson. F. C. (1981). The morphology in Nafion perfluorinated membrane products, as determined by wide- and small-angle x-ray studies. *J. Polym. Sci. Polym. Phys. Ed.*, *19*, 1687–1704.

[24] Schmidt-Rohr. K., Chen. Q. (2008). Parallel cylindrical water nanochannels in Nafion fuel-cell membranes. *Nat. Mater*., *7*, 75.

[25] Beck. J. S., Vartuli. J. C., Roth. W. J., Leonowicz. M. E., Kresge. C. T., Schmitt. K. D., Chu. C. T. W., Olson. D. H., Sheppard. E. W., McCullen. S. B., Higgins. J. B., Schlenker. J. L. (1992). A new family of mesoporous molecular sieves prepared with liquid crystal templates. *J. Am. Chem. Soc*., *114*(27), 10834–10843.

[26] Stein Sr. E. W., Clearfield. A., Subramanian. M. A. (1996). Conductivity of group IV metal sulfophosphonates and a new class of interstratified metal amine-sulfophosphonates. *Solid State Ionics*, *83*, 113-124.

[27] Goesten. M. G., Juan-Alcanitz. J., Ramos-Fernandez. E. V., Gupta. K. B. S. S., Stavitski. E., van Bekkum, H., Gascon. J., Kapteijn. F. (2011). Sulfation of metal–organic frameworks: opportunities for acid catalysis and proton conductivity. *J. Catal*., *281*(1), 177-187.

[28] Hurd. J. A., Vaidhyanathan. R., Thangadurai. V., Ratcliffe. C. I., Moudrakovski. I. L., Shimizu. G. K. H. (2009). Anhydrous proton conduction at 150 °C in a crystalline metal-organic framework. *Nat. Chem*., *1*, 705.

[29] Rouquerol. J., Avnir. D., Fairbridge. C. W., Everett. D. H., Haynes. J. M., Pernicone. N., Ramsay. J. D. F., Sing. K. S. W., Unger. K. K. (1994). Recommendations for the characterization of porous

solids (technical report). *Pure Appl. Chem*., *66*(8), 1739–1758.

[30] Chiola. V., Ritsko. J. E., Vanderpool. C. D. (1971). *US 3556725 A*. US Patent and Trademark Office.

[31] Hanns. B., Gottfried. K. (1968). *US 3383172 A*. US Patent and Trademark Office.

[32] Le Page. M., Beau. R., Duchene. J. (1970). *US 3493341 A*. US Patent and Trademark Office.

[33] Di Renzo. F., Cambon. H., Dutartre. R. (1997). A 28-year-old synthesis of micelle-templated mesoporous silica. *Microporous Mater*. *10*, 283–286.

[34] Kresge. C. T., Roth. W. J. (2013). The discovery of mesoporous molecular sieves from the twenty-year perspective. *Chem. Soc. Rev*., 42, 3663–3670.

[35] Antonelli. D. M., Ying. J. Y. (1996). Synthesis and characterization of hexagonally packed mesoporous tantalum oxide molecular sieves. *Chem. Mater*., *8*, 874.

[36] Antonelli. D. M., Ying. J. Y. (1996). Synthesis of a stable hexagonally packed mesoporous niobium oxide molecular sieve through a novel ligand-assisted templating mechanism. *Angew. Chem. Int. Ed*., *35*, 426–430.

[37] Antonelli D.M. (1999). Synthesis of phosphorus-free mesoporous titania via templating with amine surfactants. *Microporous Mesoporous Mater*., *30*, 315-319.

[38] Antonelli. D. M. (1999). Synthesis of macro-mesoporous niobium oxide molecular sieves by a ligand-assisted vesicle templating strategy. *Microporous Mesoporous Mater*., *33*, 209-214

[39] Antonelli. D. M. (1999). Hollow ordered zirconia microcage formation by spherical micelle templating with chelating triol surfactants. *Microporous Mesoporous Mater*., *28*, 505–510.

[40] Antonelli. D. M., Trudeau. M. (1999). Phase changes and electronic properties in toroidal mesoporous molybdenum oxides. *Angew. Chem. Int. Ed*., *38*, 1471–1475.

[41] Bentoncello. P., Notargiacomo. A., Nicolini. C. (2005). Langmuir−Schaefer films of Nafion with incorporated TiO_2 nanoparticles. *Langmuir, 21*(1), 172-177.

[42] Liu. P., Bandara. J., Lin. Y., Elgin. D., Allard. L. F., Sun. Y.-P. (2002). Formation of nanocrystalline titanium dioxide in perfluorinated ionomer membrane. *Langmuir, 18*(26), 10398-10401.

[43] Rhee. C. H., Kim, H. K., Chang. K., Lee. J. S. (2005). Nafion/sulfonated montmorillonite composite:

a new concept electrolyte membrane for direct methanol fuel cells. *Chem. Mater*., *17*(7), 1691-1697.

[44] Li. R., Ye. L., Mai. Y.-W. (1997). Application of plasma technologies in fibre-reinforced polymer composites: a review of recent developments. *Composites Part A*, *28*(1), 73-86.

[45] Pieh. S., Werenka. C. (1988) *US4725665 A*. US Patent and Trademark Office.

[46] Bergström. K., Strandberg. C. (2013). *US20130005578 A1*. US Patent and Trademark Office.

[47] Wolf. C., Storm. T., Lange. F. T., Reemtsma. T., Brauch. H.-J., Eberle. S. H., Jekel. M. (2000). Analysis of sulfonated naphthalene−formaldehyde condensates by ion-pair chromatography and their quantitative determination from aqueous environmental samples. *Anal. Chem*., *72*, 5466.

[48] Brunauer. S., Emmett. P. H., Teller. E. (1938). Adsorption of gases in multimolecular layers. *J. Am. Chem. Soc*., *60*, 309–319.

[49] Webb. P., Orr. C. (2008). *Analytical Methods in Fine Particle Technology*. Micromeritics.

[50] Barrett. E. P., Joyner. L. G., Halenda. P. P. (1951). The determination of pore volume and area distributions in porous substances. I. computations from nitrogen isotherms. *J. Am. Chem. Soc*., *73*, 373–380.

[51] Moller. K., Bein. T. (1998). Inclusion chemistry in periodic mesoporous hosts. *Chem. Mater*., *10*(10), 2950.

[52] Spange, S., Gräser. A., Müller. H., Zimmermann. Y., Rehak. P., Jäger. C., Fuess. H., Baehtz. C. (2001). Synthesis of inorganic/organic host−guest hybrid materials by cationic vinyl polymerization within Y zeolites and MCM-41. *Chem. Mater*., *13*(10), 3698-3708.

[53] Santos. A. L. S., Dias. M. L., Antonelli. D. M., (2009). Structure and thermal properties of naphthalene sulfonated resin/mesoporous niobium oxide nanostructured composites. *Chemistry and Chemical Technology*, *3*(3), 177-182.

[54] Srinivas. S. (2006). *Fuel Cells: From Fundamentals to Applications*. United States of America: Springer Science.

[55] Vielstich. W., Lamm. A., Gasteiger. H. A. (2003). *Handbook of fuel cells: fundamentals, technology,*

applications. Wiley: New York

[56] Lamy. C., Lima. A., LeRhun. V., Delime. F., Coutanceau. C., Léger. J.-M. (2002). Recent advances in the development of direct alcohol fuel cells (DAFC). *J. Power Sources*, *105*(2), 283-296.

[57] Verma. A., Basu. S. (2005). Direct use of alcohols and sodium borohydride as fuel in an alkaline fuel cell. *J. Power Sources*, *145*(2), 282-285.

[58] Zhang. J. (2008). *PEM fuel cell electrocatalysts and catalyst layers: fundamentals and fpplications*. Springer.

[59] Bar-On. I., Kirchain. R., Roth. R. (2002). Technical cost analysis for PEM fuel cells. *J. Power Sources*, *109*, 71-75.

[60] Trongchuankij. W., Pruksathorn. K., Hunsom. M. (2011). Preparation of a high performance Pt– Co/C electrocatalyst for oxygen reduction in PEM fuel cell via a combined process of impregnation and seeding. *Appl. Energy*, *88*(3), 974-980.

[61] Sinha. J., Yang. Y. (2010). *Direct Hydrogen PEMFC Manufacturing Cost Estimation for Automotive Applications*. DOE Annual Merit Review. Retireved from https://www1.eere.energy.gov/hydrogenandfuelcells/pdfs/fctt_pemfc_cost_review_0908.pdf

[62] Gasteiger. H. A., Kocha. S. S., Sompalli. B., Wagner. F. T. (2005). Activity benchmarks and requirements for Pt, Pt-alloy, and non-Pt oxygen reduction catalysts for PEMFCs. *Appl. Catal. B*, *56*(1-2), 9-35.

[63] Gasteiger. H.A., Panels. J. E., Yan. S. G. (2004). Dependence of PEM fuel cell performance on catalyst loading. *J. Power Sources*, *127*(1-2), 162-171.

[64] News. (2011, September). UTC Power Fuel Cell to Serve University of Connecticut's Depot Campus. *Fuel Cell Today*. Retrieved from http://www.fuelcelltoday.com/news-archive/2011/september/utc-power-fuel-cell-to-serve-university-of-conneticuts-depot-campus

[65] O'Hayre. R., Cha. S.-W., Coletta. W., Prinz. F. B. (2006). *Fuel cell fundamentals*. Wiley.

[66] Cohn. E. M., Young. G. J., Linden. H. R. (1969), *In fuel cell systems*. American Chemical Society

[67] Blomen. L. J. M. J., Mugerwa. M. N. (1993). *Fuel cell systems*. Springer

[68] Yan. X., Gu. S., He. G., Wu. X., Benziger. J. (2014). Imidazolium-functionalized poly(ether ether ketone) as membrane and electrode ionomer for low-temperature alkaline membrane direct methanol fuel cell. *J. Power Sources, 250,* 90-94.

[69] Qui. B., Liu. B., Qui. L., Yan. F. (2012). Alkaline imidazolium- and quaternary ammonium-functionalized anion exchange membranes for alkaline fuel cell applications. *J. Mater. Chem., 22,* 1040-1045.

[70] Rao. A. H. N., Thankamony. R. L., Kim. H.-J., Nam. S., Kim. T.-H. (2013). Imidazolium-functionalized poly(arylene ether sulfone) block copolymer as an anion exchange membrane for alkaline fuel cell. *Polymer, 54*(1), 111-119.

[71] Yan. J., Hickner. M. A. (2010). Anion exchange membranes by bromination of benzylmethyl-containing poly(sulfone)s. *Macromolecules, 43*(5), 2349-2356.

[72] Yanagi. H., Fukuta. K. (2008). Anion exchange membrane and ionomer for alkaline membrane fuel cells (AMFCs). *ECS Trans., 16*(2), 257-262.

[73] Wang. Y.-J., Qiao. J., Baker. R., Zhang. J. (2013). Alkaline polymer electrolyte membranes for fuel cell applications. *Chem. Soc. Rev., 42,* 5768-5787.

[74] Avadikyan, A., Cohendet. P., Héraud. J.-A. (2003). *The economic dynamics of fuel cell technologies*. Springer.

[75] Thiam. H. S., Daud. W. R. W., Kamarudin. S. K., Mohamad. A. B., Kadhum. A. A. H., Loh. K. S., Majlan. E. H. (2013). Nafion/Pd–SiO_2 nanofiber composite membranes for direct methanol fuel cell applications. *Int. J. Hydrogen Energy, 38*(22), 9474-9483.

[76] Merhoff. H., Helbig. P. (2010). Development and fielding of a direct methanol fuel cell. *ITEA Journal, 31,* 18-21.

[77] Avgouropoulos. G., Paxinou. A., Neophytides. S. (2014). In situ hydrogen utilization in an internal reforming methanol fuel cell. *Int. J. Hydrogen Energy, 39*(31), 18103-18108.

[78] Querioz. A. C., Silva. W. O., Rodrigues. I. A., Lima. F. H. B. (2014). Identification of bimetallic electrocatalysts for ethanol and acetaldehyde oxidation: Probing C_2-pathway and activity for

hydrogen oxidation for indirect hydrogen fuel cells. *Appl. Catal. B, 160*, 423-435.

[79] Cherevko. S., Kulyk. N., Mayrhofer. K. J. J. (2016). Durability of platinum-based fuel cell electrocatalysts: Dissolution of bulk and nanoscale platinum. *Nano Energy*, *29*, 275-298.

[80] Kunusch. C., Puleston. P., Mayosky. M. (2012). *Introducing fuel cells*. Springer

[81] Garche. J., Dyer. C. K., Moseley. P. T., Ogumi. Z., Rand. D. A. J., Scrosati. B. (2009). *Encyclopedia of electrochemical power sources*. Elsevier.

[82] Antolini. E. (2016). Structural parameters of supported fuel cell catalysts: The effect of particle size, inter-particle distance and metal loading on catalytic activity and fuel cell performance. *Appl. Catal. B, 181*, 298-313.

[83] Takahashi. K., Kakinuma. K., Uchida. M. (2016). Improvement of cell performance in low-PT-loading PEFC cathode catalyst layers prepared by the electrospray method. *J. Electrochem. Soc*., *163*(10), F1182-F1188.

[84] Boudghene Stambouli. A., Travesa. E. (2002). Solid oxide fuel cells (SOFCs): a review of an environmentally clean and efficient source of energy. *Renew. Sustainable Energy Rev*., *6*(5), 433-455.

[85] Rossmeisl. J., Bessler. W. G. (2008). Trends in catalytic activity for SOFC anode materials. *Solid State Ionics*, *178*(31), 1694-1700.

[86] Ormerod. R. M. (2003). Solid oxide fuel cells. *Chem. Soc. Rev*., *32*, 17-28.

[87] Van Gestel. T., Sebold. D., Buchkremer. H. P. (2015). Processing of 8YSZ and CGO thin film electrolyte layers for intermediate- and low-temperature SOFCs. *J. Eur. Ceram. Soc*., *35*(5), 1505-1515.

[88] He. Y., Fan. L., Afzal. M., Singh. M., Zhang. W., Zhao. Y., Li. J., Zhu. B. (2016). Cobalt oxides coated commercial $Ba_{0.5}Sr_{0.5}Co_{0.8}Fe_{0.2}O_{3-\delta}$ as high performance cathode for low-temperature SOFCs. *Electochimica Acta*, *191*, 223-229.

[89] Seo. H. S., Yun. D. W., Kim. K. Y. (2013). Oxidation behavior of ferritic stainless steel containing Nb, Nb–Si and Nb–Ti for SOFC interconnect. *Int. J. Hydrogen Energy*, *38*(5), 2432-2442.

[90] Steele. B. C. H., Heinzel. A. (2001). Materials for fuel cell technologies. *Nature*. *414*, 345-352.

[91] Yuh. C., Johnson. R., Faroogue. M., Maru. H. (1995). Status of carbonate fuel cell materials. *J. Power Sources*, *56*(1), 1-10.

[92] Zhu. B., Lindbergh. G., Simonsson. D. (1999). Comparison of electrochemical and surface characterisation methods for investigation of corrosion of bipolar plate materials in molten carbonate fuel cell: Part I. Electrochemical study. *Corros. Sci*., *41*(8), 1497-1513.

[93] Steele. B. C. H. (2001). Material science and engineering: The enabling technology for the commercialisation of fuel cell systems. *J. Mater. Sci.*, *36*(5), 1053-1068.

[94] Bischoff. M. (2006). Molten carbonate fuel cells: A high temperature fuel cell on the edge to commercialization. *J. Power Sources*, *160*(2), 842-845.

[95] Jiang. S. P., Yan. Y. (2013). *Materials for high-temperature fuel cells*. Wiley.

[96] Lunghi. P., Ubertini. S., Desideri. U. (2001). Highly efficient electricity generation through a hybrid molten carbonate fuel cell-closed loop gas turbine plant. *Energ. Convers. Manag.*, *42*(14), 1657-1672.

[97] Wee. J.-H. (2014). Carbon dioxide emission reduction using molten carbonate fuel cell systems. *Renew. Sustainable Energy Rev*., 32, 178-191.

[98] Pettersson. J., Ramsey. B., Harrison. D. (2006). A review of the latest developments in electrodes for unitised regenerative polymer electrolyte fuel cells. *J. Power Sources*, *157*(1), 28-34.

[99] Boeing. News releases/statements. Retrieved from http://boeing.mediaroom.com/2016-02-08-Boeing-Delivers-Reversible-Fuel-Cell-based-Energy-Storage-System-to-U-S-Navy

[100] Badwal. S. P. S., Fini. D., Ciacchi. F. T., Munnings. C., Kimpton. J. A., Drennan. J. (2013). Structural and microstructural stability of ceria – gadolinia electrolyte exposed to reducing environments of high temperature fuel cells. *J. Mater. Chem. A, 1*, 10768-10782.

[101] Hong. J., Kim. H.-J., Park. S.-Y., Lee. J.-H., Park. S.-B., Lee. J.-H., Kim. B.-K., Je. H.-J., Kim. J. Y., Yoon. K. J. (2014). Electrochemical performance and long-term durability of a 200 W-class solid oxide regenerative fuel cell stack. *Int. J. Hydrogen Energy*, *39*(35), 20819-20828.

[102] Larmine. J., Dicks. A., (2003). *Fuel cell systems explained*. Wiley.

[103] Krumpelt. M., Krause. T. R., Carter. J. D., Kopasz. J. P., Ahmed. S. (2002). Fuel processing for fuel cell systems in transportation and portable power applications. *Catal. Today*, *77*(1), 3-16.

[104] Dudfield. C. D., Chen. R., Adcock. P. L. (2001). A carbon monoxide PROX reactor for PEM fuel cell automotive application. *Int. J. Hydrogen Energy*, *26*(7), 763-775.

[105] Sharma. S., Pollet. B. G. (2012). Support materials for PEMFC and DMFC electrocatalysts - A review. *J. Power Sources. 208*(15). 96-119.

[106] Chandan. A., Hattenberger. M., El-kharouf. A., Du. S., Dhir. A., Self. V., Pollet. B. G., Ingram. A., Bujalski. W. (2013). High temperature (HT) polymer electrolyte membrane fuel cells (PEMFC) - A review. *J. Power Sources, 231,* 264-278.

[107] Speder. J., Altmann. L., Roefzaad. M., Bäumer. M., Kirkensgaard. J. J. K., Mortensen. K., Arenz. M. (2013). Pt based PEMFC catalysts prepared from colloidal particle suspensions – a toolbox for model studies. *Phys. Chem. Chem. Phys. 15,* 3602-3608.

[108] Othman. R., Dicks. A. L., Zhu. Z. (2012). Non precious metal catalysts for the PEM fuel cell cathode. *Int. J. Hydrogen Energy*, *37*, 357-372.

[109] Yan. Q., Toghiani. H., Wu. J. (2006). Investigation of water transport through membrane in a PEM fuel cell by water balance experiments. *J. Power Sources*, *158*, 316-325.

[110] von Helmolt. R., Eberle. U. (2007). Fuel cell vehicles: status 2007. *J. Power Sources. 165*(2), 833-843.

[111] Sánchez. M., Pierna. A. R., Lorenzo. A., Del Val. J. J. (2016). Effect of cocatalyst and composition on catalytic performance of amorphous alloys for ethanol electrooxidation and PEMFCs. *Int. J. Hydrogen Energy*, *41*(43), 19749-19755.

[112] Fofana. D., Natarajan. S. K., Hamelin. J., Benard. P. (2014). Low platinum, high limiting current density of the PEMFC (proton exchange membrane fuel cell) based on multilayer cathode catalyst approach. *Energy*, *64*, 398-403.

[113] Office of Energy Efficiency and Renewable Energy. DoE technical targets for polymer electrolyte

membrane fuel cell components. Retrieved from https://energy.gov/eere/fuelcells/doe-technical-targets-polymer-electrolyte-membrane-fuel-cell-components

[114] Shahgaldi. S., Hamelin. J. (2015). Improved carbon nanostructures as a novel catalyst support in the cathode side of PEMFC: a critical review. *Carbon*, *94*, 705-728.

[115] Wang. Y., Jin. J., Yang. S., Li. G., Qiao. J. (2015). Highly active and stable platinum catalyst supported on porous carbon nanofibers for improved performance of PEMFC. *Electrochimica Acta*, *177*, 181-189.

[116] Mauritz. K. A., Moore. R. B. (2004). State of understanding of Nafion. *Chem. Rev.*, *104*, 4535-4585.

[117] Collier. A., Wang. H., Yuan. X. Z., Zhang. J., Wilinkson. D. P. (2006). Degradation of polymer electrolyte membranes. *Int. J. Hydrogen Energy*, *31*(13), 1838-1854.

[118] Kinumoto. T., Inaba. M., Nakayama. Y., Ogata. K., Umebayashi. R., Tasaka. A., Irinyama. Y., Abe. T., Ogumi. Z. (2006). Durability of perfluorinated ionomer membrane against hydrogen peroxide. *J. Power Sources*, *158*(2), 1222-1228.

[119] Choe. Y.-K., Tsuchida. E., Ikeshoji. T., Yamakawa. S. (2009). Nature of proton dynamics in a polymer electrolyte membrane, nafion: a first-principles molecular dynamics study. *Phys. Chem. Chem. Phys.*, 11, 3892-3899.

[120] Yan. Q., Toghiani. H., Wu. J. (2006). Investigation of water transport through membrane in a PEM fuel cell by water balance experiments. *J. Power Sources. 158*, 316-325.

[121] Orfino. F. P., Holdcroft. S. (2000). The morphology of Nafion: are ion clusters bridged by channels or single ionic sites? *J. New Mater. Electrochem. Syst.*, *3*, 287-292.

[122] Fujimura. M., Hashimoto. T., Kawai. H. (1981). Small-angle x-ray scattering study of perfluorinated ionomer membranes. 1. Origin of two scattering maxima. *Macromolecules*, *14*, 1309.

[123] Litt. M. H. (1997). Re-evaluation of Nafion morphology. *Polym. Prepr.*, *38*, 80.

[124] Rubatat, L., Rollet. A.–L., Gebel. G., Diat. O. (2002). Evidence of elongated polymeric aggregates in Nafion. *Macromolecules*, *35*, 4050.

[125] Abroshan. H., Akbarzadeh. H., Taherkhani. F., Parsafar. G. (2011). Effect of water–methanol content

on the structure of Nafion in the sandwich model and solvent dynamics in nano-channels; a molecular dynamics study. *Mol. Phys*., *109*(5), 709-724.

[126] Angioni. S., Millia. L., Bruni. G., Tealdi. C., Mustarelli. P., Quartarone. E. (2016). Improving the performances of Nafion™-based membranes for microbial fuel cells with silica-based, organically-functionalized mesostructured fillers. *J. Power Sources, 334*, 120-127.

[127] Battriola. L. C., Scheider. J. F., Torriani. I. C. L., Tremilioso-Filho. G., Rodrigues-Filho. U. P. (2013). Improvement on direct ethanol fuel cell performance by using doped-Nafion® 117 membranes with Pt and PteRu nanoparticles. *Int. J. Hydrogen Energy, 38*, 12060-12068.

[128] Mokhtarian. N., Ghasemi. M., Daud. W. R. W., Najafpour. G., Alam. J. (2013). Improvement of microbial fuel cell performance by using Nafion polyaniline composite membranes as a separator. *J. Fuel Cell Sci. Technol., 10*, 041008

[129] Chien. H.-C., Tsai. L.-D., Huang. C.-P., Kang. C.-Y., Lin. J.-N., Chang. F.-C. (2013). Sulfonated graphene oxide/Nafion composite membranes for high-performance direct methanol fuel cells. *Int. J. Hydrogen Energy, 38*, 13792-13801.

[130] Mondal. S., Soam. S., Kundu. P. P. (2015). Reduction of methanol crossover and improved electrical efficiency in direct methanol fuel cell by the formation of a thin layer on Nafion 117 membrane: Effect of dip-coating of a blend of sulphonated PVdF-co-HFP and PBI. *J. Membr. Sci., 474*, 140-147.

[131] Lee. S. Y., Shin. D. W., Wang. C., Lee. K. H., Guiver. M. D., Lee. Y. M. (2013). A capillary water retention effect to improve medium-temperature fuel cell performance. *Electrochem. Commun., 31*, 120-124.

[132] Li. J., Fan. K., Cai. W., Ma. L., Xu. G., Xu. S., Ma. L., Cheng. H. (2016). An in-situ nano-scale swelling-filling strategy to improve overall performance of Nafion membrane for direct methanol fuel cell application. *J. Power Sources, 332*, 37-41.

[133] Fang. K., Tang. B., Wu. P. (2015). Does thermal treatment merely make a H2O-saturated Nafion membrane lose its absorbed water at high temperature? *Phys. Chem. Chem. Phys., 17*, 9106-9115.

[134] Jalili. J., Borsacchi. S., Tricoli. V. (2014). Proton conducting membranes in fully anhydrous conditions at elevated temperature: Effect of Nitrilotris(methylenephosphonic acid) incorporation into Nafion- and poly(styrenesulfonic acid). *J. Membr. Sci*., *469*, 162-173.

[135] Si. Y., jiang. R., Lin. J.-C., Kunz. H. R., Fenton. J. M. (2004). CO tolerance of carbon-supported platinum-ruthenium catalyst at elevated temperature and atmospheric pressure in a PEM fuel cell. *J. Electrochem. Soc*., 151(11), A1820-A1824.

[136] Mahajan. C. V., Ganesan. V. (2010). Atomistic simulations of structure of solvated sulfonated poly(ether ether ketone) membranes and their comparisons to Nafion: II. structure and transport properties of water, hydronium ions, and methanol. *J. Phys. Chem. B*, *114*(25), 8367 – 8373.

[137] He. G., He. X., Wang. X., Chang. C., Zhao. J., Li. Z., Wu. H., Jiang. Z. (2016). A highly proton-conducting, methanol-blocking Nafion composite membrane enabled by surface-coating crosslinked sulfonated graphene oxide. *Chem. Commun*., *52*, 2173-2176.

[138] Kreuer. K.-D. (2014). Ion conducting membranes for fuel cells and other electrochemical devices. *Chem. Mater*., *26*, 361-380.

[139] Gasteiger. H. A., Penels. J. E., Yan. S. G. (2004). Dependence of PEM fuel cell performance on catalyst loading. *J. Power Sources*, 127, 162-171.

[140] Zhan. Y. (2014). Current short circuit implementation for performance improvement and lifetime extension of proton exchange membrane fuel cell. *J. Power Sources*, *270*, 183-192.

[141] Luan. Z., Cheng. C.-F., Zhou. W., Klinowski. J. (1995). Mesopore molecular sieve MCM-41 containing framework aluminum. *J. Phys. Chem*., *99*, 1018-1024.

[142] Spange. S., Gräser. A., Müller. H., Zimmermann. Y., Rehak. P., Jäger. C., Guess. H., Baehtz. C. (2001). Synthesis of Inorganic/Organic Host−Guest Hybrid Materials by Cationic Vinyl Polymerization within Y Zeolites and MCM-41. *Chem. Mater*., *13*(10), 3698-3708.

[143] Díaz, J.-P., Balkus Jr. K. J. (1996). Enzyme immobilization in MCM-41 molecular sieve. *J. Mol. Catal. B*: *Enzym*., *2*(2), 115-126

[144] Regi. M. V., Rámila. A., del Real. R. P., Pérez-Pariente. J. (2001). A new property of MCM-41: drug

delivery system. *Chem. Mater*., *13*, 308-311.

[145] Lee. JY., Farha. O. K., Roberts. J., Scheidt. K. A., Nguyen. SB. T., Hupp. J. T. (2009). Metal-organic framework materials as catalysts. *Chem. Soc. Rev*., *38*, 1450-1459.

[146] Kreno. L. E., Leong. K., Farha. O. K., Allendorf. M., Van Duyne. R. P., Hupp. J. T. (2011). Metal-organic framework materials as chemical sensors. *Chem. Rev*., *112*(2), 1105-1125.

[147] Burrows. A. D., Llabres I Xamena. F. X. (ed). (2013) *Metal organic frameworks as heterogeneous catalysts*. RSC Publishing.

[148] Li. B., Zhang. Y., Ma. D., Li. L., Li. G., Li. G., Shi. Z., Feng. S. (2012). A strategy toward constructing a bifunctionalized MOF catalyst: post-synthetic modification of MOFs on organic ligands and coordinatively unsaturated metal sites. *Chem. Commun*., *48*, 6151-6153.

[149] Ni, Z., Masel. R. I. (2006). Rapid production of metal−organic frameworks via microwave-assisted solvothermal synthesis. *J. Am. Chem. Soc*., *128*(38), 12394-12395.

[150] Bux. H., Liang. F., Li. Y., cravillon. J., Wiebcke. M., Caro. J. (2009). Zeolitic imidazolate framework membrane with molecular sieving properties by microwave-assisted solvothermal synthesis. *J. Am. Chem. Soc*., *131*(44), 16000-16001.

[151] Li. Y., Yang. R. T. (2006). Hydrogen storage in metal−organic frameworks by bridged hydrogen spillover. *J. Am. Chem. Soc*., *128*(25), 8136-8137.

[152] Liu. Y.-Y., Zeng. J.-L., Zhang. J., Xu. F., Sun. Li.-X. (2007). Improved hydrogen storage in the modified metal-organic frameworks by hydrogen spillover effect. *Int. J. Hydrogen Energy*. *32*(16), 4005-4010.

[153] Marschall. R., Bannat. I., Feldhoff. A., Wang. L., Lu. G. Q., Wark M. (2009). Nanoparticles of mesoporous SO_3H-functionalized Si-MCM-41 with superior proton conductivity. *Small*, *5*, 854–859

[154] Nagarkar. S. S., Unni. A. M., Sharma. A., Kurungot. S., Ghosh. S. K. (2014). Two-in-one: inherent anhydrous and water-assisted high proton conduction in a 3D metal–organic framework. *Angew. Chem. Int. Ed*., *53*, 2638–2642.

[155] Sadakiyo. M., Yamada. T., Kitagawa. H. (2016). Hydrated proton-conductive metal-organic frameworks. *ChemPlusChem*., *81*, 691.

[156] Antonelli. D. M., Ying. J. Y. (1995). Synthesis of hexagonally packed mesoporous TiO_2 by a modified sol–gel method. *Angew*. *Chem*. *Int. Ed*., *34*, 2014–2017.

[157] Wong. M. S., Antonelli. D. M., Ying. J. Y. (1997). Synthesis and characterization of phosphate mesoporous zirconium oxide. *Nanostruct*. *Mater*., *9*, 165-168.

[158] Laha. S. C., Ryoo. R. (2003). Synthesis of thermally stable mesoporous cerium oxide with nanocrystalline frameworks using mesoporous silica templates. *Chem*. *Commun*., *2003*, 2138-2139.

[159] Chen. F., Liu. M. (1999). Preparation of mesoporous tin oxide for electrochemical applications. *Chem*. *Commun*., *1999*, 1829-1830.

[160] Staudinger. H. (1920). Über Polymerisation. *Eur*. *J*. *Inorg*. *Chem*., *53*, 1073–1085.

[161] Odian. G. (2004). *Principles of polymerization*. Wiley.

[162] Voit. B. I., Lederer. A. (2009). Hyperbranched and highly branched polymer architectures - synthetic strategies and major characterization aspects. *Chem*. *Rev*., *109*, 5924-5973.

[163] Mistri. E. A., Mohanty. A. K., Banerjee. S. (2012). Synthesis and characterization of new fluorinated poly(ether imide) copolymers with controlled degree of sulfonation for proton exchange membranes. *J*. *Membr*. *Sci*., 411, 117-129.

[164] Yang. J., Liu. Y., Li. L., Zhang. C., Liu. T. (2017). Conducting polymer composites: material synthesis and applications in electrochemical capacitive energy storage. *Mater*. *Chem*. *Front*., Retrieved from http://pubs.rsc.org/en/content/articlepdf/2017/qm/c6qm00150e

[165] Inagaki. S., Fukushima. Y., Kuroda. K. (1993). Synthesis of highly ordered mesoporous materials from a layered polysilicate. *J*. *Chem*. *Soc*., *Chem*. *Commun*., *1993*, 680-682.

[166] Sun. S., Wen. Z., Jin. J., Cui. Y., Lu. Y. (2103). Synthesis of ordered mesoporous $CuCo_2O_4$ with different textures as anode material for lithium ion battery. *Microporous Mesoporous Mater*., *169*, 242-247.

[167] Ivanova. I. I., Knyazeva. E. E. (2013). Micro–mesoporous materials obtained by zeolite recrystallization: synthesis, characterization and catalytic applications. *Chem. Soc. Rev., 2013,* 3671-3688.

[168] Ariga. K., Vinu. A., Yamauchi. Y., Ji. Q., Hill. J. P. (2012). Nanoarchitectonics for mesoporous materials. *Bull. Chem. Soc. Jpn., 85,* 1-32.

[169] Li. W., Zhao. D. (2013). An overview of the synthesis of ordered mesoporous materials. *Chem. Commun., 49,* 943-946.

[170] Azizi. S. N., Ghasemi. S., Chiani. E. (2013). Nickel/mesoporous silica (SBA-15) modified electrode: An effective porous material for electrooxidation of methanol. *Electrochimica Acta*, *88,* 463-472.

[171] Nguyen. T. H., Kim. S., Yoon. M., Bae. T.-H. (2016). Hierarchical zeolites with amine-functionalized mesoporous domains for carbon dioxide capture. *ChemSusChem., 9,* 455.

[172] Yamauchi. Y. (2013). Field-Induced alignment controls of one-dimensional mesochannels in mesoporous materials. *J. Ceram. Soc. Jpn., 121,* 831-840.

[173] Walcarius. A. (2013). Mesoporous materials and electrochemistry. *Chem. Soc. Rev., 42,* 4098-4140.

.

Chapter 2: Variable Temperature Proton Conductivity of Mesoporous Titanium Oxides Doped with Naphthalene Sulfonate Formaldehyde Resin

In this Chapter we attempt to synthesise materials resistant to dehydration by exploiting the interaction of sulfonate groups with the hydrophilic surfaces of the inner pore walls of mesoporous titanium oxides to form channels for proton conduction. Thus, six mesoporous titanium oxide composites of NSF were synthesised, fully characterised and formed into pellets for potentiostatic impedance measurements. The most promising sample, a NSF composite of mesoporous TiO_2 ($mTiO_2$), displays a proton conductivity of 1.837 ± 0.14 mS cm^{-1} at 100 °C surpassing that of a pellet of Nafion 117 constructed as a reference under the same conditions (1.143 ± 0.13 mS cm^{-1}). This material also has greater conductivity than pure hydrated NSF (0.122 ± 0.02 mS cm^{-1}), confirming a synergistic interaction between the NSF and the oxide mesostructure in the proton conductivity mechanism.

Introduction

Over the past two decades PEMs have received renewed interest due to their potential applications as a replacement for the combustion engine in the transport industry,[1-3] as a power source for distributed power,[4] and as portable electrical devices.[5] To date the best commercially viable membrane is DuPont's Nafion which offers good thermal and mechanical stability,[6-8] as well as excellent proton conductivity at moderate temperature from a liquid/water humidification process.[9,10] However, at temperatures above 80 °C operation becomes difficult as the conductivity decreases due to water loss

from the Nafion matrix[11,12] and this, coupled with high cost and high methanol permeability[13-15] results in Nafion falling short of the strictest performance demands in a PEMFC.[16,17] Many research groups have looked into improving the efficiency of Nafion. Various approaches include doping the membranes with hydrophilic inorganic materials to maintain high water content and prevent Nafion dehydration at high temperature,[18-20] filling the membrane with mesoporous silica[21,22] or periodic mesoporous organosilicates (PMO),[23,24] incorporating silica and zirconium phosphates into the Nafion water channels by *in situ* chemical reactions in order to increase the working conditions past 100 °C,[25-27] and doping with solid acids (sulfonated zirconium[28,29] or phosphotungstic acid[30,31] or titanium nanoparticles[32,33]) to increase the concentration of acid sites that promote local migration of protons. Research has also focussed on replacing the Nafion membrane altogether with PMOs,[24] MOFs[39,39] and MOFs doped with sulphonates and phosphonates.[40,41] However, none of these alternatives have managed to replace Nafion as the commercially preferred membrane of choice for PEMFCs and thus new approaches to this problem must be explored.

Aim

Using published[38,39] and unpublished work within our research group as a basis, we are attempting to develop new proton conducting materials that are resistant to loss of conductivity on dehydration, with the precursory materials used presented herein. The best of these materials, once identified and optimised, will be fabricated into a membrane at a later stage for further performance and optimisation tests. Our approach is to exploit the oxide surface of the *ca.* 15 Å pore walls of mTiO_2 with *ca.* 20 Å pore size as a means

of anchoring sulfonate groups and suppressing moisture loss to encourage proton conduction pathways that continue to function at higher temperature. The mesostructure will thus be impregnated with oligomeric NSF. With an average molecular mass between 400 and 1000 and consisting of 2-6 units,[40,41] the small size of the resin molecules will ensure facile diffusion into the $mTiO_2$ pore structure. This should result in composites in which the sulphonate groups are in close contact with the Lewis acidic oxide walls, thus offering a channel for proton movement along the interface. This approach is also flexible in that it allows doping of the inorganic walls with species such as sulfate to augment the conductivity properties.

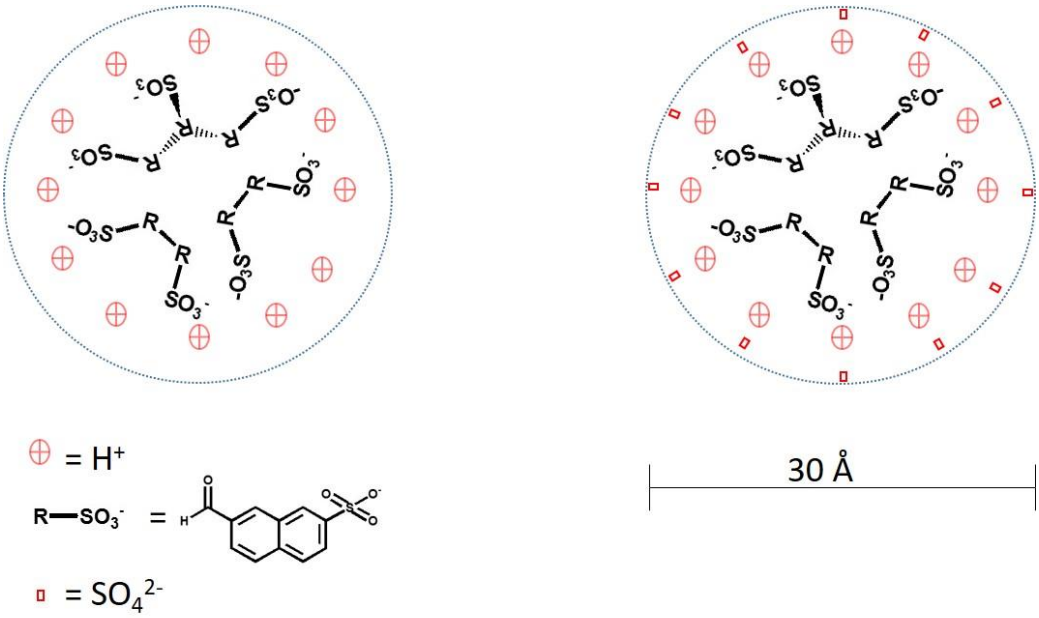

Figure 2.1: From left to right; the first approach showing the expected peripheral arrangement of protons and sulfonated oligomer within a $mTiO_2$ pore; the second approach showing the expected peripheral arrangement of protons, sulfonated oligomer within a $mTiO_2$ pore doped with sulfate anions.

Figure 2.1 outlines the two approaches in the quest to solve the problem that arises from dehydration. In both methods the transition metal-based Lewis acidic sites on

the pore walls function to bind both moisture and sulfonate groups to create proton conduction channels along the walls that should be resistant to thermally induced moisture loss while also potentially creating moisture-free conduction pathways along the sulfonate-oxide interface. These differ from the PMO approach discussed earlier[23,24] whereby the sulfonate groups are self-assembled in the centre of a PMO, preventing any interaction with the oxide walls because of the directionality of the organic tether. These materials are thus reliant on water in the centre channel to sustain the proton conducting network. It also varies greatly from the other major approach to the dehydration concern whereby a Nafion film (or membrane) is dipped into a solution of metal oxide nanoparticles where the nanoparticles self assemble onto the Nafion membrane in a random arrangement.[32,33] In this strategy the nanoparticles function to retain moisture, but the random distribution of the dopant does not guarantee that all water is in contact with the particle surface.

Results and Discussion

In this study six samples were synthesised as per the Experimental section. These include one sample of $mTiO_2$, two composites of $mTiO_2$ impregnated with NSF ($mTiO_2$-NSF) in two different mediums - H_2O and diethyl ether (DEE) – one composite of $mTiO_2$ doped with sulfuric acid ($mTiO_2(SO_4)$) and two composites of $mTiO_2(SO_4)$ impregnated with NSF ($mTiO_2(SO_4)$-NSF), one in H_2O and the other in DEE medium. Each sample was fully characterised using the parameters above and are discussed below.

Surface area analysis. The BET surface area data for the as-synthesised materials is reported in Table 2.1, the nitrogen adsorption-desorption isotherm for

$mTiO_2$–NSF.DEE is shown in Figure 2.2, while the remaining nitrogen adsorption-desorption isotherms are shown in Figures 2.3, 2.4, and 2.5.

Table 2.1

Nitrogen adsorption data for the six as-synthesised materials. N/A: denotes that the surface area was too small to record a pore volume size

Material	BET Surface Area/ m^2g	Pore Volume / $cm^3\ g^{-1}$	BJH Pore Size / Å
$mTiO_2$	1010	0.592	23.42
$mTiO_2$-NSF.H_2O	3.900	0.002	22.06
$mTiO_2$-NSF.DEE	145.3	0.094	26.03
$mTiO_2(SO_4)$	20.90	0.028	53.84
$mTiO_2(SO_4)$-NSF.H_2O	0.900	N/A	N/A
$mTiO_2(SO_4)$-NSF.DEE	3.500	0.007	76.14

In all cases the samples are on the cusp between type I and IV isotherms, as expected for materials with a ca. 20 Å pore size. The $mTiO_2$ sample possesses a high surface area of 1010 m^2g, which decreases when the material is impregnated with NSF to 145.3 m^2g for $mTiO_2$-NSF in DEE and 3.9 m^2g in water. The sulfuric acid doped material possess a surface area of 20.9 m^2g ($mTiO_2(SO_4)$), with further loss of surface area on NSF doping in DEE or water. There is also a loss of pore volume from 0.592 cm^3/g to less than 0.1 cm^3/g in all cases. Impregnation of the pores with NSF is expected to lower the surface area and pore volume on doping, while the loss of surface area on doping with sulfuric acid is consistent with previous work on sulfated mesoporous Ti, Nb, and Ta oxides.[42,43] In both cases, loss of surface area upon NSF impregnation indicates that the pores have been filled with NSF resin. This guarantees -SO_3H sites in the pores to promote the ion conductivity properties of the material(s).

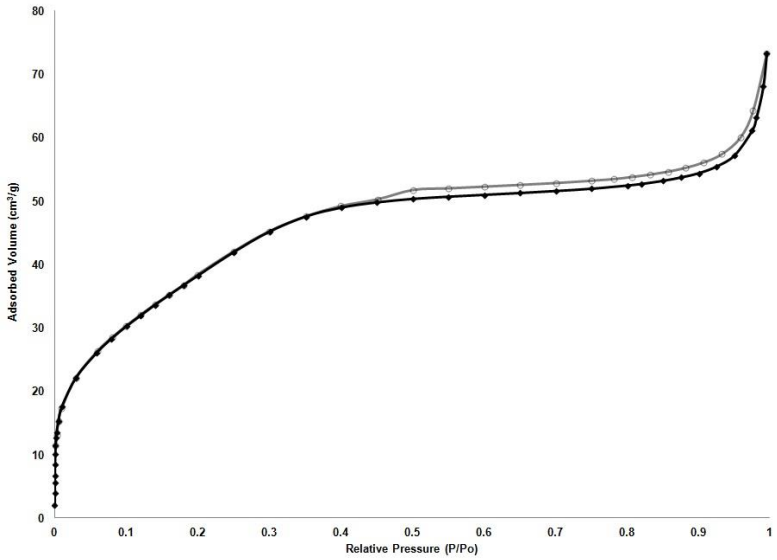

Figure 2.2: Nitrogen adsorption (diamonds)/desorption (circles) isotherm for $mTiO_2$-NSF.DEE

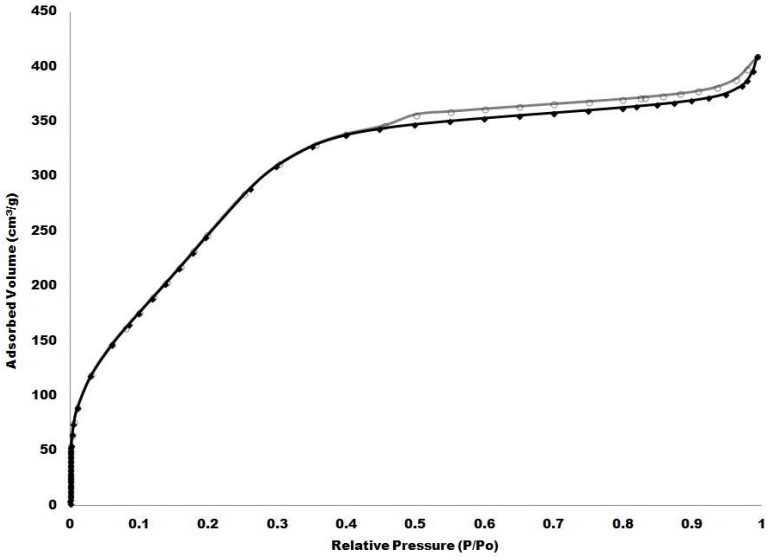

Figure 2.3: Nitrogen adsorption (diamonds)/desorption(circles) isotherm for $mTiO_2$

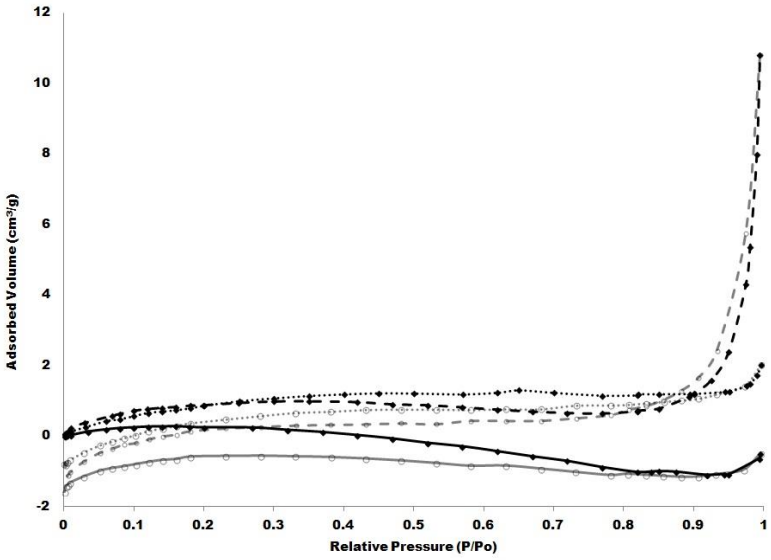

Figure 2.4: Nitrogen adsorption (diamonds)/desorption (circles) isotherms for $mTiO_2$-NSF.H_2O (dots), $mTiO_2(SO_4)$-NSF.H_2O (solid line) and $mTiO_2(SO_4)$-NSF.DEE (dashes). Negative values are an artifact caused by low total adsorption

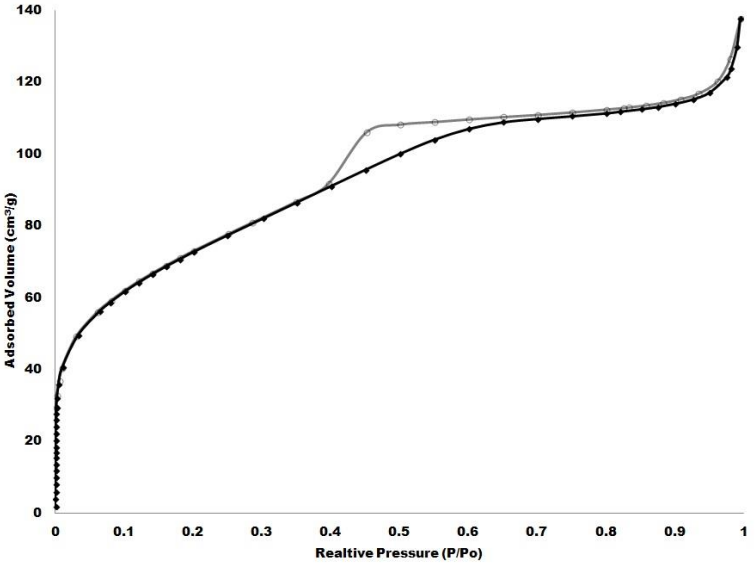

Figure 2.5: Nitrogen adsorption (diamonds)/desorption (circles) isotherms for $mTiO_2(SO_4)$

Infrared Spectroscopy. The IR spectra of the as-synthesised materials are shown in Figure 2.6. The NSF resin gives rise to an aromatic C-H stretch at ν2900 cm^{-1} and

aromatic ring vibration modes at ν1640 cm^{-1}, ν1596 cm^{-1} and ν1507 cm^{-1}. These are apparent in all NSF treated samples. This is also mirrored by the appearance of the NSF SO group and S-phenyl vibrations observed at ν1230 cm^{-1} ν1190 cm^{-1} ν1130 cm^{-1} and ν1040 cm^{-1}. There are also C-H stretches at 2800 cm^{-1} for the NSF methylene protons and trace residual hydrocarbon in the $mTiO_2$.

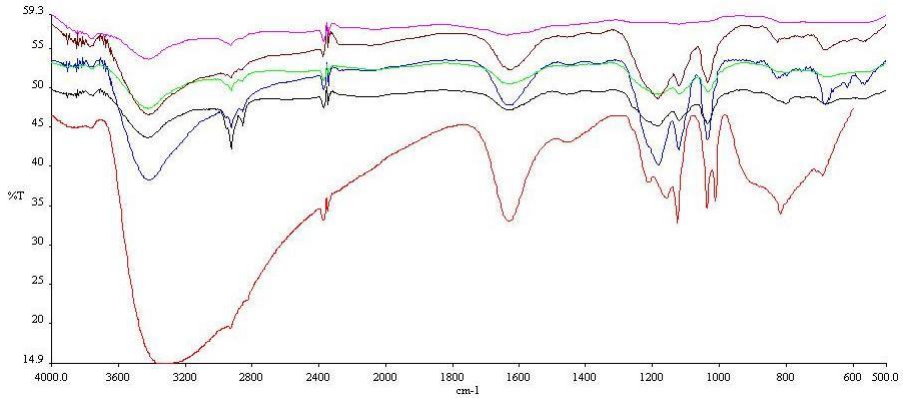

Figure 2.6: IR spectra for $mTiO_2$ (red), $mTiO_2$-NSF.H_2O (black), $mTiO_2$-NSF.DEE (blue), $mTiO_2(SO_4)$-NSF.H_2O (green), $mTiO_2(SO_4)$-NSF.DEE (brown), $mTiO_2(SO_4)$ (purple)

Powder X-ray Diffraction. The PXRD patterns for $mTiO_2$ and the remaining as-synthesised materials are shown in Figures 2.7 and 2.8 respectively. Both spectra show a reflection between 2.4 and 3.2 2θ, indicative of a mesoporous structure and consistent with our previous data.[44] The intensity of this reflection decreases regardless of whether the samples are doped with H_2SO_4 or impregnated with NSF and these findings are consistent with the BET due to partial loss of structure.

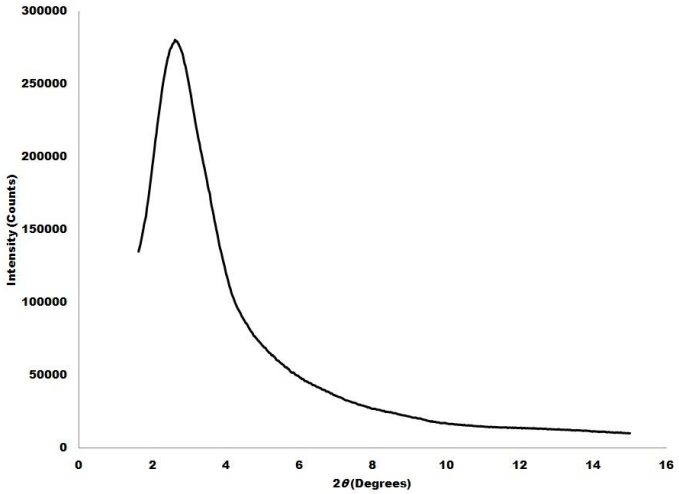

Figure 2.7: PXRD pattern for $mTiO_2$

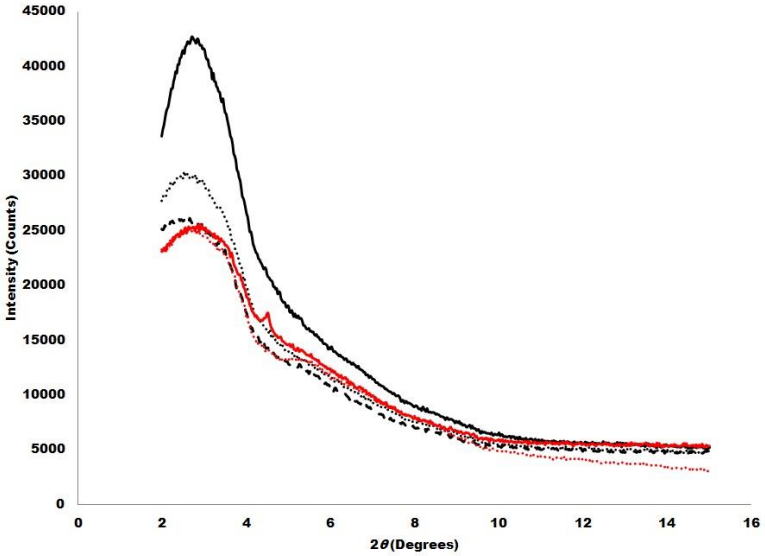

Figure 2.8: PXRD pattern for $mTiO_2$-NSF.H_2O (black dots), $mTiO_2$-NSF.DEE (black line), $mTiO_2(SO_4)$-NSF.H_2O (black dashes), $mTiO_2(SO_4)$-NSF.DEE (red line) and $mTiO_2(SO_4)$ (red dots

X-ray Photoelectron Spectroscopy

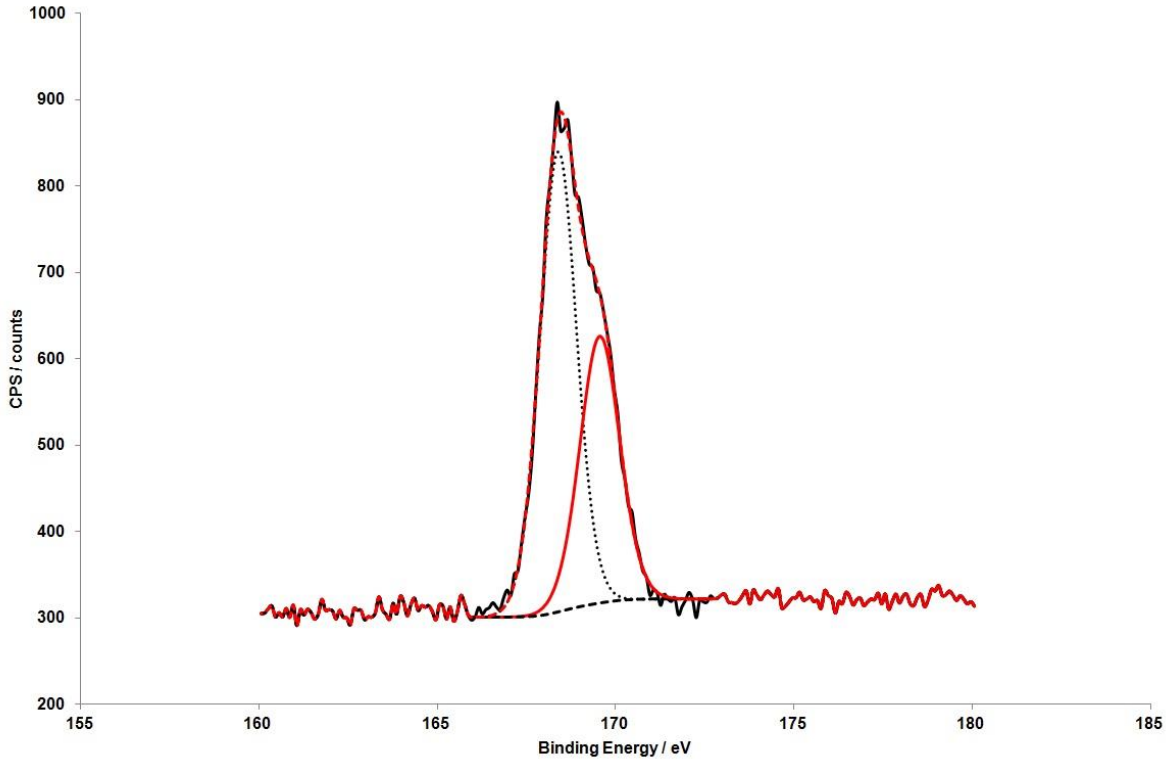

Figure 2.9: XPS peak fitting of the sulphur 2p3 region for $mTiO_2(SO_4)$ showing the raw data (black line) and the simulated fitted peaks

X-ray photoelectron spectroscopy was carried out on the $mTiO_2(SO_4)$ sample and the sulphur 2p region is shown in Figure 2.9. There is a major emission in the $2p_{3/2}$ region at *ca.* 169 eV that is typical of a sulphur containing species. The simulated peak fittings also show a minor emission in the $2p_{1/2}$ region at *ca*. 170 eV which displays the divalent nature of the sulphate anion. The line width of the two S 2p peaks is found to be 0.7 eV and their separation 1.15 eV. The latter value is similar to those reported in the literature for organometallic to indicate that the sulphate anions are succesfully doped into the $mTiO_2$ mesopores.

Thermal analysis. Percentage of hydrocarbon was probed in the as-synthesised samples by TGA and DTA and this is shown in Figures 2.11 through to 2.15 while the composite for $mTiO_2$-NSF.DEE is shown in Figure 2.10. For $mTiO_2$ the thermogravimetric curve shows weight loss of ca. 10 % at 130 °C which is attributed to residual loss of H_2O. At 450 °C there is a weight loss of ca. 5 % which is attributed to the combustion of any residual hydrocarbon from the dodecylamine template or partial collapse of the mesopore structure. This is confirmed by the overlying DTA curve which shows an endothermic peak at 130 °C and two exothermic peaks at 350 °C and 500 °C. $mTiO_2(SO_4)$ has a weight loss of ca. 5 % at 390 °C which is attributed to the SO_3 and NSF is removed from the sample at ca. 485 °C. For the composites $mTiO_2$-NSF.H_2O and $mTiO_2(SO_4)$-NSF.H_2O the weight loss of NSF is ca. 5 % while the weight loss for the composites $mTiO_2$-NSF.DEE and $mTiO_2(SO_4)$-NSF.DEE it is closer to 10 % which indicates that more NSF was impregnated into the sample using DEE than using H_2O. As expected, the water loss in the DEE impregnated samples is also less than in the H_2O samples. The difference in weight loss of NSF between the composites with, and without SO_3 groups is negligible. This is because sulfonation of the pore walls has caused slight degradation of the mesostructure to the crystalline form, as seen by the continued weight loss above ca. 550 °C.

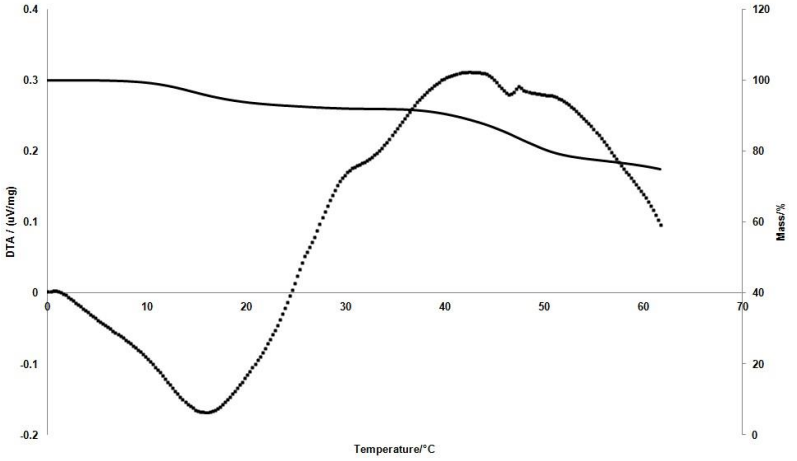

Figure 2.10: TGA (solid line) and DTA (dots) curves for $mTiO_2$-NSF.DEE

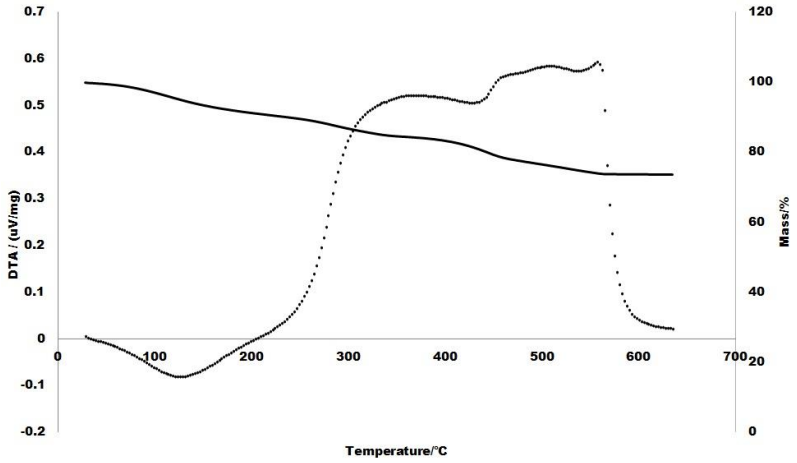

Figure 2.11: TGA (solid line) and DTA (dots) curves for as-synthesised $mTiO_2$

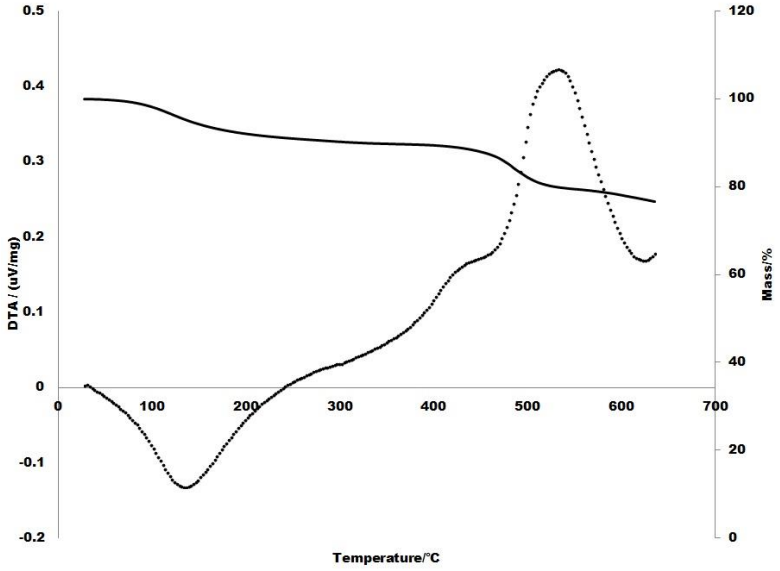

Figure 2.12: TGA (solid line) and DTA (dots) curves for $mTiO_2$.-NSF.H_2O

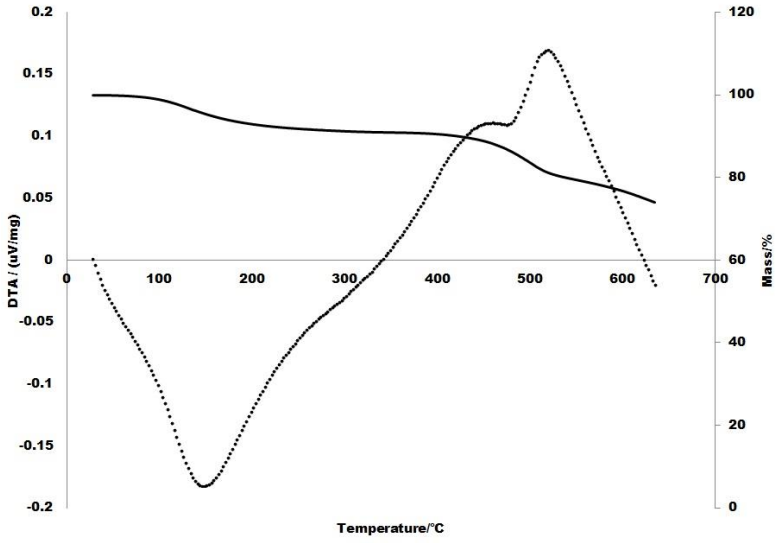

Figure 2.13: TGA (solid line) and DTA (dots) curves for $mTiO_2(SO_4)$-NSF.H_2O

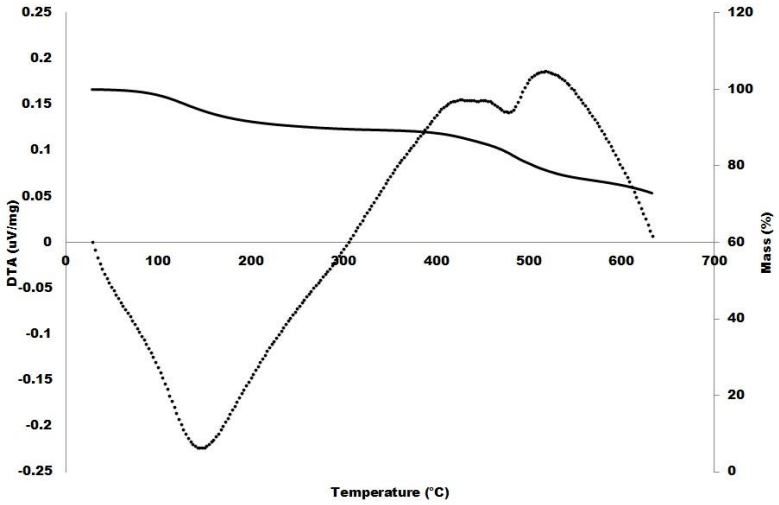

Figure 2.14: TGA (solid line) and DTA (dots) curves for $mTiO_2(SO_4)$-NSF.DEE

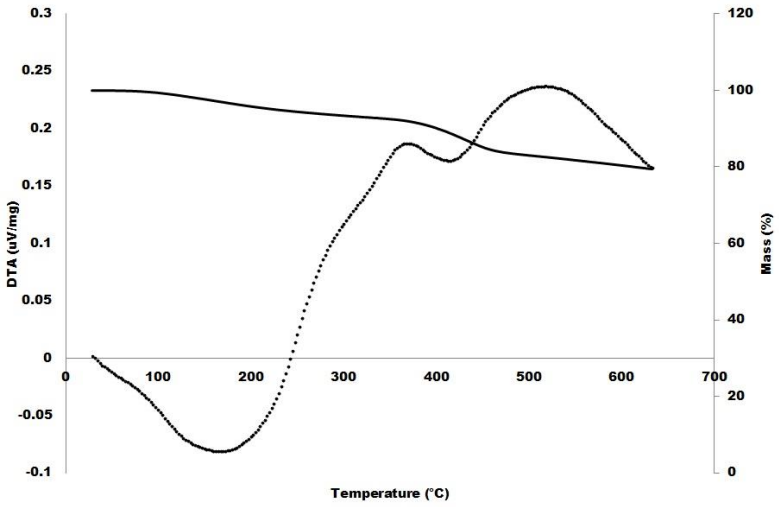

Figure 2.15: TGA (solid line) and DTA (dots) curves for $mTiO_2(SO_4)$

Scanning transmission electron microscopy. To view the pore structure (a) and lattice (b) of the as-synthesised materials, STEM was performed with the images of the as-synthesised material $mTiO_2$-NSF.DEE shown in Figure 2.16 and the remaining images

shown in Figures 2.17-2.21. Each pore structure image, taken at a scale of either 10 or 20 nm, displays a wormhole-like structure that is typical for mesoporous materials. From this we can estimate that the pores are ca. 20 Å in diameter (in agreement with the BET data) and that the pore walls are ca. 20 Å thick, corresponding to what is expected on the basis of the PXRD data and in agreement with previous work.[45] Following impregnation of the pore with NSF and/or doping of the pore wall mesostructure with H_2SO_4 it becomes increasingly difficult to detect either the pores (due to the filling of the pores by the NSF), or the mesostructure (due to pore degradation from the H_2SO_4). Each lattice image, taken at a scale of either 2 or 5 nm, displays a uniform structure, which becomes more apparent in the sample following treatment with NSF and/or H_2SO_4. This is consistent with variable degrees of proton-induced crystallisation of the walls. Both sets of images are consistent with the reported BET data and with previous data using this experimental approach.[41]

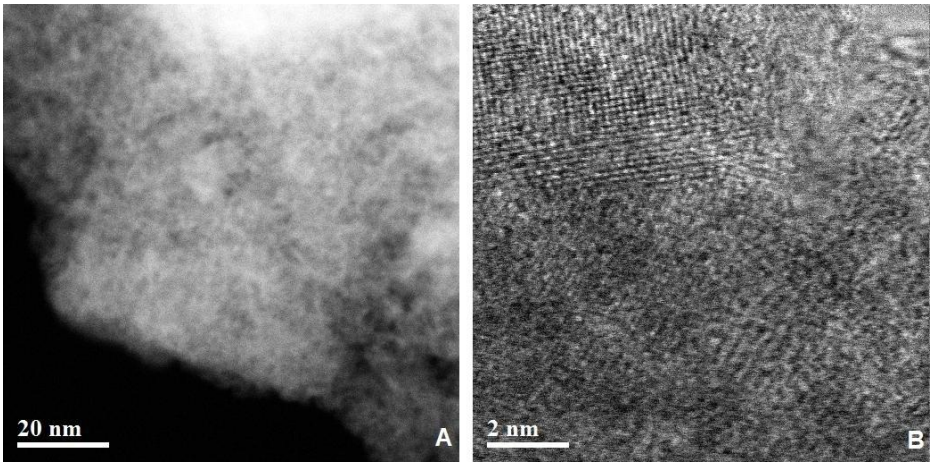

Figure 2.1620: STEM image of the $mTiO_2$-NSF.DEE composite showing, a) the random pore mesostructure; b) a higher magnification of the crystallised regions

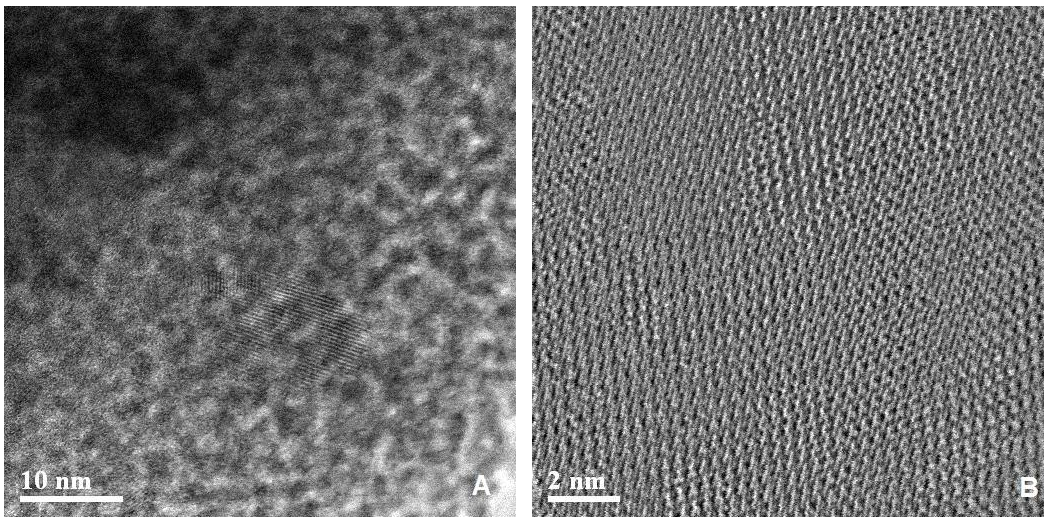

Figure 2.17: STEM image of the as-synthesised $mTiO_2$ showing, a) the random pore mesostructure; b) a higher magnification of the crystallised regions

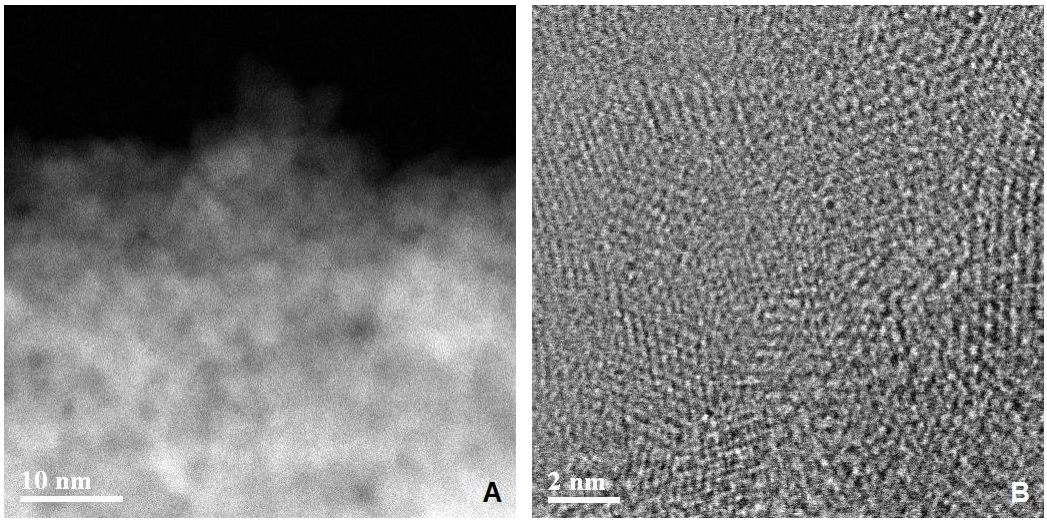

Figure 2.18: STEM image of the $mTiO_2$-NSF.H_2O composite showing, a) the random pore mesostructure; b) a higher magnification of the crystallised regions

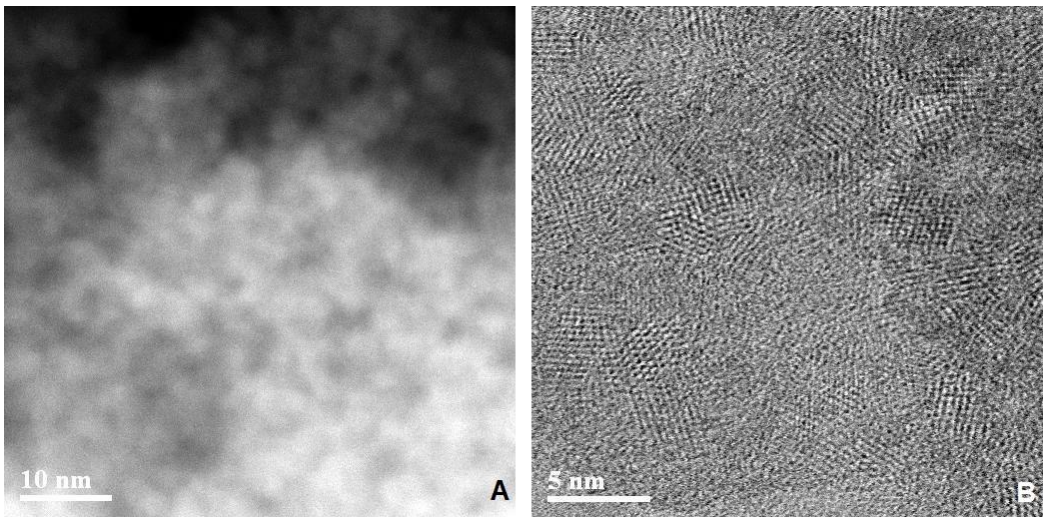

Figure 2.19: STEM image of the as synthesised $mTiO_2(SO_4)$ showing, a) the random pore mesostructure; b) a higher magnification of the crystallised regions

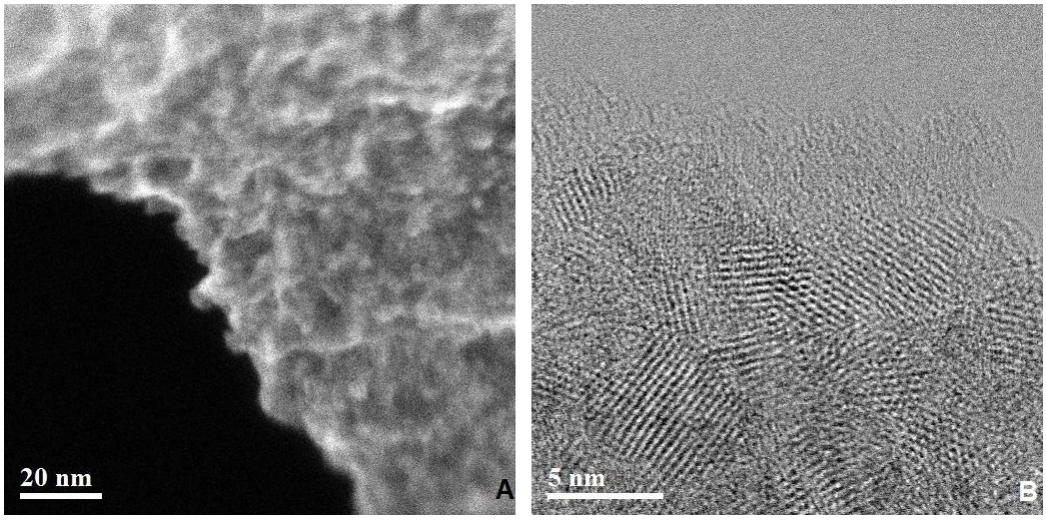

Figure 2.2021: STEM image of the $mTiO_2(SO_4)$-NSF.H_2O composite showing, a) the random pore mesostructure; b) a higher magnification of the crystallised regions

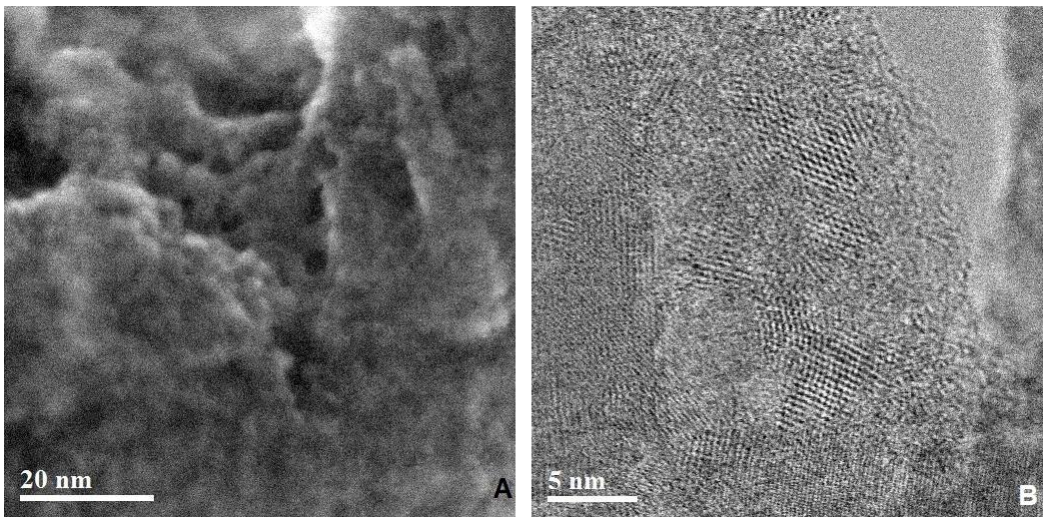

Figure 2.21: STEM image of the $mTiO_2(SO_4)$-NSF.DEE composite showing, a) the random pore mesostructure; b) a higher magnification of the crystallised regions

Electrochemical impedance spectroscopy. As described in the Characterisation Section, each composite was formed into a "cell". Each "cell" had its potentiostatic impedance recorded at room temperature, and pressure at 50% humidity with the results displayed in Figure 2.22. Previous work[46] demonstrated by temperature programmed desorption (TPD) that moisture loss is suppressed by the Lewis acid sites (and/or the sulfonate groups) on the pore walls of sulfate-doped mesoporous Ti, Nb, and Ta oxide and as such, thermal dehydration of the pellet is anticipated to be suppressed compared to that of Nafion 117. As a reference and for equality, a pellet of Nafion 117 was also fabricated and measured under the same conditions, displaying data similar to that previously reported.[47]

Table 2.2

Average proton conductivity and associated error (mS cm^{-1}) of the as-synthesised materials, NSF, and the reference cell, Nafion 117

	25 °C	50 °C	75 °C	100 °C	125 °C	150 °C
$mTiO_2$	0.071±0.01	0.104±0.01	0.488±0.03	0.543±0.08	0.188±0.13	0.056±0.07
$mTiO_2$-NSF.H_2O	0.202±0.01	0.536±0.01	0.458±0.04	0.499±0.04	0.222±0.02	0.127±0.12
$mTiO_2$-NSF.DEE	0.300±0.01	0.764±0.03	1.195±0.02	1.837±0.14	1.084±0.04	0.631±0.09
$mTiO_2(SO_4)$	0.088±0.04	0.268±0.12	0.179±0.09	0.083±0.01	0.034±0.01	0.066±0.01
$mTiO_2(SO_4)$-NSF.H_2O	0.302±0.01	0.391±0.01	0.849±0.07	0.648±0.02	0.165±0.02	0.129±0.01
$mTiO_2(SO_4)$-NSF.DEE	0.231±0.01	0.310±0.02	0.362±0.02	0.490±0.02	0.209±0.04	0.036±0.02
Nafion 117 pellet	1.450±0.16	1.131±0.19	1.013±0.19	1.143±0.12	0.254±0.04	0.126±0.02
NSF pellet	0.508±0.04	0.612±0.03	0.143±0.01	0.122±0.02	0.069±0.02	0.019±0.01

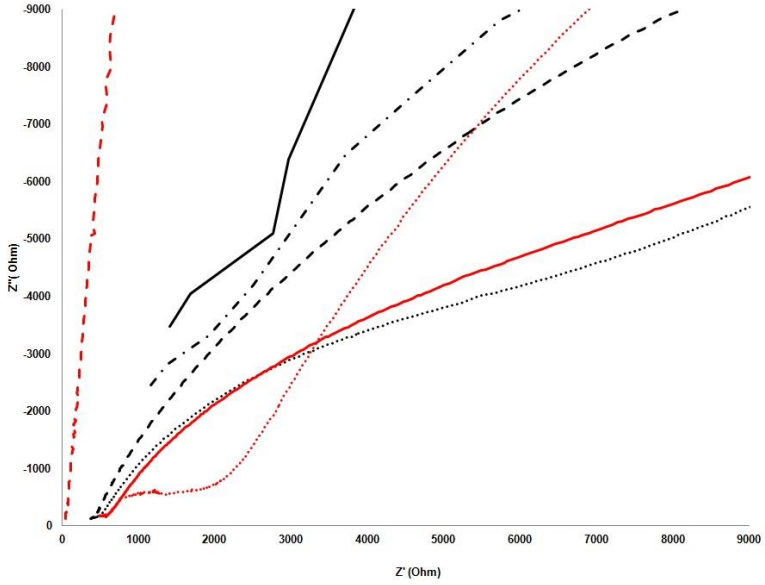

Figure 2.22: Nyquist plot showing the potentiostatic impedance of $mTiO_2$ (black line), mTiO2-NSF.H_2O (black dots), $mTiO_2$-NSF.DEE (black dashes), $mTiO_2(SO_4)$ (black dots and dashes), $mTiO_2(SO_4)$-NSF.H_2O (red line), $mTiO_2(SO_4)$-NSF.DEE (red dots) and Nafion 117 (red dashes) at 25 °C

Next, the temperature was increased to 50 °C, the potentiostatic impedance was measured (Figure 7.1) and subsequently the σ was found. This was repeated at 75 °C (Figure 7.2), 100 °C (Figure 7.3), 125 °C (Figure 7.5) and 150 °C (Figure 7.6) respectively. Figure 7.4 shows a magnified Nyquist Plot of $mTiO_2$-NSF.DEE. at 100 °C. Taken from 7.3, this magnification displays the semi-circular relationship each curve has, followed by the Warburg Tail in the low frequency part of the plot. The average conductivity from all samples at all temperatures, along with the calculated standard error, is shown on Table 2.2 and from this a plot (Figure 2.23) of $\log_{10}\sigma$ versus T was made. The conductivity was derived as per the notes in Chapter 1.

Figure 2.23 shows the average conductivity and associated error of each pellet in relation to Nafion. As displayed above Nafion loses conductivity as the temperature is increased and this is consistent with what we know in the literature.[6] The most promising

material is the $mTiO_2$-NSF.DEE composite (green) in which the conductivity improves with temperature to 100 °C before tailing off towards 150 °C. At 25 °C the proton conductivity was measured at 0.3 ± 0.01 mS cm^{-1} (Nafion 1.450 ± 0.16 mS cm^{-1}) and this rises to 1.195 ± 0.03 mS cm^{-1} at 75 °C by which point it surpasses the Nafion cell (1.013 ± 0.19 mS cm^{-1}).

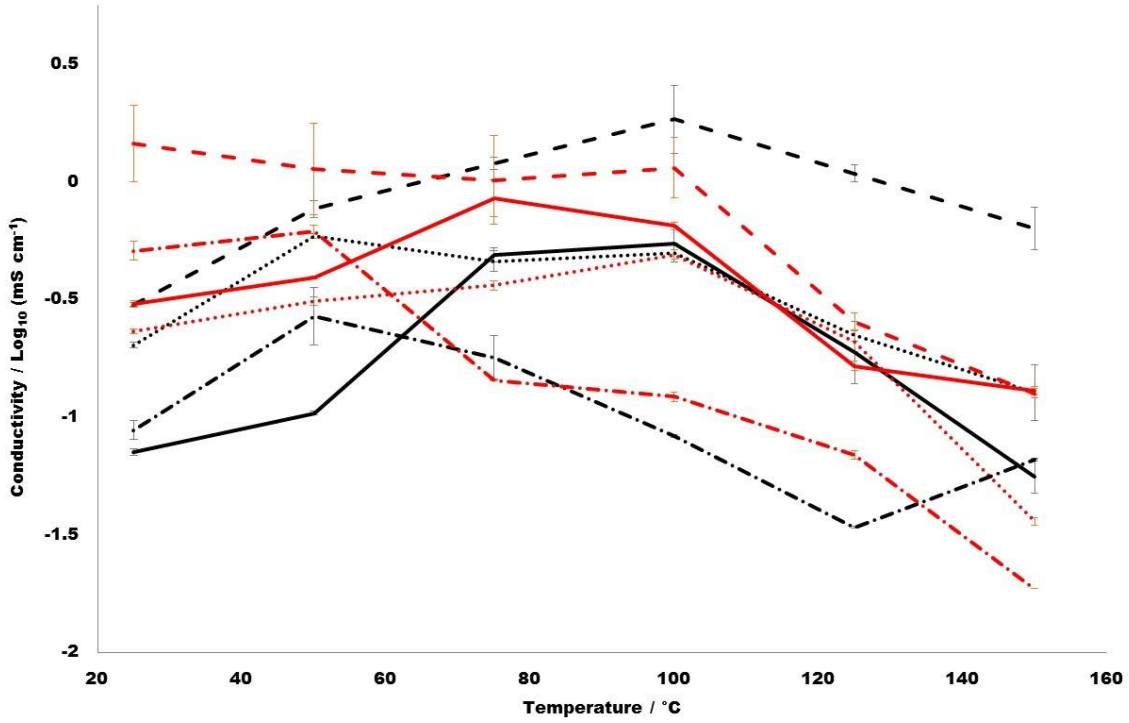

Figure 2.23: Average proton conductivities of $mTiO_2$ (black line), mTiO2-NSF.H_2O (black dots), $mTiO_2$-NSF.DEE (black dashes), $mTiO_2(SO_4)$ (black dots and dashes), $mTiO_2(SO_4)$-NSF.H_2O (red line), $mTiO_2(SO_4)$-NSF.DEE (red dots), Nafion 117 (red dashes) and NSF (red dots and dashes) as a function of temperature

This continues to rise to 1.837 ± 0.14 mS cm^{-1} by 100 °C. By 150 °C the proton conductivity measures 0.631 ± 0.09 mS cm^{-1} and this is still higher than that of Nafion (0.126 ± 0.02 mS cm^{-1}). Whilst these numbers fall short of those published for a Nafion 117 membrane (*ca.* 8 mS cm^{-1} at 50 % humidity at 100 °C),[48] this is because we

deliberately chose to measure the conductivity of Nafion 117 in a powder pellet form with possible grain boundary effects for consistency to most closely mirror the cells fabricated using the composites. Finally, reported error is within acceptable parameters for these experiments and remains consistent throughout.

In subsequent work we plan to explore further improvements in conductivity and deploy our best materials in mechanically robust membranes to compare results to commercial Nafion membranes. For contrasting purposes the combined plots for $mTiO_2$, $mTiO_2(SO_4)$, and NSF can be found on Figures 7.7, 7.8 and 7.9 respectively. The composites $mTiO_2$, $mTiO_2(SO_4)$ afforded the lowest proton conductivity, consistent with more poorly formed proton conducting pathways, while the conductivity of NSF was lower than that of $mTiO_2$-NSF.DEE, suggesting that the synergy between the oxide walls and the organic resin is important in overall performance. Finally, the conductivity measurements were repeated without coating the edges of the pellet with epoxy resin and a similar result was achieved (Figure 7.10). Also, each pellet was, upon cooling back to 25 °C, submitted to the heating cycle again. At each temperature, a decrease in proton conductivity was observed.

Conclusions

With the powder pellet conductivity of the $mTiO_2$-NSF.DEE composite higher than that of Nafion 117 and pure NSF as the optimal temperature for PEMFC operation is approached it appears at this early stage that the approach of doping proton conducting oligomers into mesoporous oxides warrants further study and development. While the best materials slowly degraded with loss of performance over time, the conductivity

results show promise and suggest that use of a more robust mesoporous material (i.e. mesoporous tantalum oxide) or larger less mobile oligomers may lead to further improvements, thus forming the basis of future work.

Experimental Section

All chemicals were purchased from either Sigma Aldrich or Alfa Aesar without further purification. Naphthalene sulphonate formaldehyde condensate was purchased from Specco Industries.

***mTiO$_2$*.** Mesoporous titanium oxide was prepared according to the published procedure using ligand assisted templating.[38] Thus, a 3:1 mixture of titanium isopropoxide (90 g) and dodecylamine (18 g) was created with water (600 ml) to form a white gel and this was left to stand for 24 hours. To this mixture three drops of 12 M HCl were added, and the resultant solution stirred and left to stand for a further 24 hours before being transferred to an oven at 40 °C to begin the ageing process. After 48 hours the temperature was increased to 60 °C whereby the sample was aged for another 48 hours. This was repeated at 80 °C, after which the solid was collected by filtration and placed into a sealed sample tube and returned to the oven at 100 °C for an additional 48 hours. The ageing process was completed at 120 °C for 48 hours and 140 °C for 48 hours, respectively. Removal of the organic template was initiated by combining the material with *p*-toluenesulfonic acid (pTSA) (18 g) in methanol followed by stirring for 24 hours. Following filtration, the material was combined with fresh pTSA (23.4 g) and stirred with methanol for 24 hours. This process was completed with three subsequent filtrations and washings with methanol.

***mTiO$_2$-NSF*.** To a 1:1 mixture of NSF (2.5 g) and water (2.5 g) (alternatively diethyl ether, 2.5 g) was added mTiO$_2$ (1 g). This mixture was stirred for 48 hours and then dried in an oven at 85 °C.

***mTiO$_2$(SO$_4$)-NSF*.** One drop of H_2SO_4 was added to a vial with water (0.5 ml) and left to stand for 5 minutes. To this solution mTiO$_2$ (0.5 g) was added, and the vial sealed and stirred for 48 hours. Finally, the sample was dried in an oven at 85 °C to remove all excess water. After grinding to a fine powder, the (mTiO$_2$(SO$_4$), 0.5 g) was added to a 1:1 mixture of NSF (1.25 g) and water (1.25 g) (alternatively diethyl ether, 1.25 g) and this mixture was stirred for an additional 48 hours and then dried in an oven at 85 °C.

Characterisation section. BET surface area measurements were derived from nitrogen adsorption/desorption data collected on a Micromeritics ASAP 2020. IR spectroscopy was conducted on a Perkin Elmer FT-IR Spectometer Spectrum RX1 using KBr discs and data treated on Spectrum 5.1 software. PXRD was performed on a Bruker DaVinci diffractometer with a Cu Kα radiation (40 kV, 30 mA) source equipped with a VANTEC-1 detector for fast acquisition. The step size was 0.025° and the counting time was 2s for each step and diffraction patterns were recorded in the 2θ range 1.5° - 30°. TGA and DTA were done in a STA 449C analyser from Netzsch under a flow of dried air at 10.00 °C/min up to 650 °C. Argon was also used to protect the balance section. High resolution Transmission Electron Microscopy (HRTEM) was done on a HD-2700 dedicated STEM from Hitachi, with a cold field emitter, equipped with a CEOS Cs corrector and operated at 200 kV. The powder samples were simply deposited dry onto a

Cu grid covered with a carbon film (Quantifoil) having a periodic hole diameter of 1.2 microns. Observation was made in three different modes: Bright Field (BF), High Angle Annular Dark Field (HAADF) and Secondary Electron (SE). The XPS analysis was performed using a PHI-5500 spectrometer using monochromated Al Kα radiation. The positions of the peaks were referenced to surface C-C or C-H bound at 284.8 eV. The powder was placed on the XPS holder inside an Ar glove box and transferred under Ar to the XPS intro chamber without any exposure to air. For insulating materials, an electron-flooding gun was used to compensate the surface charges. The different chemical contributions for each spectrum were obtained using CasaXPS.

EIS was performed with a Princeton Applied Research VersaSTAT 3. A two electrode set-up was constructed and silver wire of length 5 cm was used as the working and counter electrodes and these were attached to each pellet via a silver two part conductive adhesive (figure 7.33). Each pellet was made from a 300 mg of sample, ground and formed into pellets using a 25 tonne manual hydraulic press. The flat sides of this pellet were coated using a silver two part conductive adhesive and for improved structural integrity the edges were partly coated in epoxy resin. Potentiostatic impedance spectra were recorded between 10^6 and 10 Hz using the VersaStudio software and with an amplitude of 100 mV. For analysis the data was exported to ZView. The samples were heated in a sealed sample chamber mounted on an IKA®-Werke GmbH & Co. KG heating mantle with attached temperature probe. Equilibration time at each temperature stage was 20 minutes and the humidity of the sealed sample chamber was held constant throughout at 50%, measured using a humidity controller and probe. Temperature ramp

rate was ca. 5 °C per minute. Pellets of Nafion 117 were created by drying out a sample of Nafion 117 in 5% aliphatic alcohol and water. The resultant film was diced, ground and pressed as described above for the as-synthesised materials. Proton conductivity was derived as obtained in Chapter 1.

References

[1] Yang. Z., Coutinho. D., Feng. F., Ferraris. J. P., Balkus Jr. K. J., (2004). Novel inorganic/organic hybrid electrolyte membranes. *Prepr. Pap.-Am. Chem. Soc., Div. Fuel Chem.*, *49*(2), 600.

[2] Kim. Y. S., Wang. F., Hickner. M., Mccartney. S., Hong.Y. T., Harrison. W., Zawodinski. T. A., Mcgrath. J. E., (2003). Effect of acidification treatment and morphological stability of sulfonated poly(arylene ether sulfone) copolymer proton-exchange membranes for fuel-cell use above 100 °C. *J. Polym. Sci. Part. B, 41*, 2816-2828.

[3] Whittingham. M. S., Savinell. R. F., (2004). Introduction: batteries and fuel cells. *Chem. Rev., 104*(10), 4243–4244.

[4] Park. S., Vohs J. M., Gorte. R. J., (2000). Direct oxidation of hydrocarbons in a solid-oxide fuel cell. *Nature*, *400*, 265-267.

[5] Dyer. C. K. (2002). Fuel cells for portable applications. *Fuel Cells Bull., 2002*(8), 9.

[6] Surowiec. J., Bogoczek. R. (1988). Studies on the thermal stability of the perfluorinated cation-exchange membrane Nafion-417. *J. Therm. Anal. Calorim., 33*(4), 1097-1102.

[7] Samms. S. R., Wasmus. S., Savinell. S. R. (1996). Thermal stability of Nafion® in simulated fuel cell environments. *J. Electrochem. Soc., 143*(5), 1498-1504

[8] Tang. H. L., Pan. Mu., (2008). Synthesis and characterization of a self-assembled Nafion/silica nanocomposite membrane for polymer electrolyte membrane fuel cells. *J. Phys. Chem. C, 112*(30), 11556–11568.

[9] Morris. D. R., Sun. X., (1993). Water-sorption and transport properties of Nafion 117 H. *J. Appl. Polym. Sci., 50*(8), 1445–1452.

[10] Onishi. L. M., Prausnitz. J. M., Newman. J., (2007). Water−Nafion equilibria. absence of Schroeder's paradox. *J. Phys. Chem. B, 111*(34), 10166 – 10173.

[11] Li. Q., Ronghuan. H., Jensen. J. O., Bjerrun. N. J. (2003). Approaches and recent development of polymer electrolyte membranes for fuel cells operating above 100 °C. *Chem. Mater., 15*(26), 4896–4915.

[12] Yang. C., Costamagna. P., Srinivasan. S., Benziger. J., Bocarsly. A. B. (2001). Approaches and technical challenges to high temperature operation of proton exchange membrane fuel cells. *J. Power Sources, 103*(1), 1-9.

[13] Yang. B., Manthiram. A., J. (2003). Sulfonated poly(ether ether ketone) membranes for direct methanol fuel cells. *Electrochem. Soc., 6*(11), A229-A231.

[14] Mahajan. C. V., Ganesan. V. (2010). Atomistic simulations of structure of solvated sulfonated poly(ether ether ketone) membranes and their comparisons to Nafion: II. structure and transport properties of water, hydronium ions, and methanol. *J. Phys. Chem. B, 114*(25), 8367 – 8373.

[15] Dimitrova. P., Friedrich. K. A., Stimming. U., Vogt. B. (2002). Modified Nafion®-based membranes for use in direct methanol fuel cells. *Solid State Ionics, 150*(1-2), 115-122.

[16] Chae. K. J., Choi. M., Ajayi. F. F., Park, W., Chang, I, S., Kim, I, S., (2011). Mass transport through a proton exchange membrane (Nafion) in microbial fuel cells. *Energy Fuels, 22*(1), 169-176.

[17] Nicotera. I., Enotiadis. A., Angjeli. K., Coppola. L., Ranieri. G., Gournis. G., (2011). NMR investigation of the dynamics of confined water in Nafion-based electrolyte membranes at subfreezing temperatures. *J. Phys. Chem. B, 115*(29), 9087-9097.

[18] Chang. J.-K., Park. J. H., Park. G.-G., Kim. C.-S., Park. O. O. (2003). Proton-conducting composite membranes derived from sulfonated hydrocarbon and inorganic materials. *J. Power Sources, 124*(1), 18-25.

[19] Pereira. F., Valle. K., Belleville. P., Morin. A., Lambert. S., Sanchez. C. (2008). Advanced mesostructured hybrid silica−Nafion membranes for high-performance PEM fuel cell. *Chem. Mater., 20*(5), 1710-1718.

[20] Muriithi. B., Loy. D. A. (2012). Processing, morphology, and water uptake of Nafion/*ex situ* Stöber silica nanocomposite membranes as a function of particle size. *ACS Appl*. *Mater*. *Interfaces*, *4*(12), 6766-6773.

[21] Li. J., Tang. H., Chen. L., Chen. R., Pan. M., Jiang. S. P. (2013). Highly ordered and periodic mesoporous Nafion membranes via colloidal silica mediated self-assembly for fuel cells. *Chem. Commun*., *49*, 6537-6539.

[22] Lin. Y.-F., Yen. C.-Y., Ma. C.-C. M., Liao. S.-H., Lee. C.-H., Hsiao. Y.-H., Lin. H.-P. (2007). High proton-conducting Nafion®/–SO_3H functionalized mesoporous silica composite membranes. *J. Power Sources*, *171*(2), 388-395.

[23] Hoffmann. F., Cornelius. M., Morell. J., Froba. M. (2006). Silica-based mesoporous organic-inorganic hybrid materials. *Angew*. *Chem*., *Int*. *Ed*., *45*, 3216-3251.

[24] Sayari. A., Hamoudi. S. (2001). Periodic mesoporous silica-based organic−inorganic nanocomposite materials. *Chem*. *Mater*., *13*, 3151.

[25] Yang. C., Srinivasan. S., Bocarsly. A. B., Tulyani. S., Benziger. J. B., (2004). A comparison of physical properties and fuel cell performance of Nafion and zirconium phosphate/Nafion composite membranes. *J*. *Membr*. *Sci*., *237*(1-2), 145-161.

[26] Costamanga. P., Yang. C., Bocarsly. A. B., Srinivasan. S., (2002). Nafion® 115/zirconium phosphate composite membranes for operation of PEMFCs above 100 °C. *Electrochemica Acta*, *47*(11), 1023-1033.

[27] Yang. C., Srinivasan. S., Arico. A. C., Creti. P., Baglio. V., Antonucci. V., (2001). Composite Nafion/zirconium phosphate membranes for direct methanol fuel cell operation at high temperature. *Electrochem. Solid State Lett*., *4*(4), A31-A34

[28] Rhee. C. H., Kim, H. K., Chang. K., Lee. J. S. (2005). Nafion/sulfonated montmorillonite composite: a new concept electrolyte membrane for direct methanol fuel cells. *Chem*. *Mater*., *17*(7), 1691-1697.

[29] D'Epifanio. A., Navarra, M. A., Weise. F. C., Mechari. B., Farrington. J., Greenbaum. S. (2010).

Composite Nafion/sulfated zirconia membranes: effect of the filler surface properties on proton transport characteristics. *Chem. Mater*., *22*(3), 813-821.

[30] Shao. Z.-G., Joghee. P., Hsing. I.-M. (2004). Preparation and characterization of hybrid Nafion–silica membrane doped with phosphotungstic acid for high temperature operation of proton exchange membrane fuel cells. *J. Membr. Sci*., *229*(1-2), 43-51.

[31] Buzzoni. R., Bordiga. S., Ricchiardi. G., Spoto. G., Zecchina. A. (1995). Interaction of H_2O, CH_3OH, $(CH_3)_2O$, CH_3CN, and pyridine with the superacid perfluorosulfonic membrane nafion: an IR and Raman study. *J. Phys. Chem*., *99*(31), 11937-11951.

[32] Bentoncello. P., Notargiacomo. A., Nicolini. C. (2005). Langmuir−Schaefer films of Nafion with incorporated TiO_2 nanoparticles. *Langmuir*, *21*(1), 172-177.

[33] Liu. P., Bandara. J., Lin. Y., Elgin. D., Allard. L. F., Sun. Y.-P. (2002). Formation of nanocrystalline titanium dioxide in perfluorinated ionomer membrane. *Langmuir*, *18*(26), 10398-10401.

[34] Hurd. J. A., Vaidhyanathan. R., Thangadurai. V., Ratcliffe. C. I., Moudrakovski. I. L., Shimizu. G. K. H. (2009). Anhydrous proton conduction at 150 °C in a crystalline metal-organic framework. *Nat. Chem*., *1*, 705.

[35] Stein Sr. E. W., Clearfield. A., Subramanian. M. A. (1996). Conductivity of group IV metal sulfophosphonates and a new class of interstratified metal amine-sulfophosphonates. *Solid State Ionics*, *83*, 113-124.

[36] Jang. M. Y., Park. Y. S., Yamazaki Y. (2003). Preparation, characterization and proton conductivity of layered cerium sulfophenylphosphonate. *Electrochemistry*, *71*, 691.

[37] Goesten. M. G., Juan-Alcanitz. J., Ramos-Fernandez. E. V., Gupta. K. B. S. S., Stavitski. E., van Bekkum, H., Gascon. J., Kapteijn. F. (2011). Sulfation of metal–organic frameworks: opportunities for acid catalysis and proton conductivity. *J. Catal*., *281*(1), 177-187.

[38] Antonelli D.M. (1999). Synthesis of phosphorus-free mesoporous titania via templating with amine surfactants. *Microporous Mesoporous Mater*., *30*, 315-319.

[39] Santos. A. L. S., Dias. M. L., Antonelli. D. M., (2009). Structure and thermal properties of naphthalene

sulfonated resin/mesoporous niobium oxide nanostructured composites. *Chemistry and Chemical Technology, 3*(3), 177-182

[40] Bergström. K., Strandberg. C. (2013). *US20130005578 A1*. US Patent and Trademark Office.

[41] Wolf. C., Storm. T., Lange. F. T., Reemtsma. T., Brauch. H.-J., Eberle. S. H., Jekel. M. (2000). Analysis of sulfonated naphthalene−formaldehyde condensates by ion-pair chromatography and their quantitative determination from aqueous environmental samples. *Anal. Chem., 72*, 5466.

[42] Rao. Y., Kang. J., Antonelli. D. (2008). 1-hexene isomerization over sulfated mesoporous Ta oxide: the effects of active site and confinement. *J. Am. Chem. Soc., 130*, 394–395.

[43] Rao. Y., Trudeau. M., Antonelli. D. (2006). Sulfated and phosphated mesoporous Nb oxide in the benzylation of anisole and toluene by benzyl alcohol. *J. Am. Chem. Soc., 128*, 13996–13997.

[44] Vettraino. M., Trudeau. M., Lo. A. Y. H., Schurko. R. W., Antonelli. D. (2002). Room-temperature ammonia formation from dinitrogen on a reduced mesoporous titanium oxide surface with metallic properties. *J. Am. Chem. Soc., 124*, 9567.

[45] Antonelli. D. M., Ying. J. Y. (1996). Synthesis and characterization of hexagonally packed mesoporous tantalum oxide molecular sieves. *Chem. Mater., 8*, 874.

[46] Rao. Y., Antonelli. D. M. (2009). Mesoporous transition metal oxides: characterization and applications in heterogeneous catalysis. *J. Mater. Chem., 19*, 1937-1944.

[47] Silva. R. F., De Francesco. M., Pozio. A. (1996). Tangential and normal conductivities of Nafion® membranes used in polymer electrolyte fuel cells. *J. Power Sources, 134*, 18.

[48] Maréchal. M., Souquet. J.-L., Guindet. J., Sanchez. J.-Y. (2007). Solvation of sulphonic acid groups in Nafion® membranes from accurate conductivity measurements. *Electrochem. Commun., 9*, 1023.

Chapter 3: Variable Temperature Proton Conductivity of Mesoporous Niobium and Tantalum Oxide Composites Doped with Naphthalene Sulfonate Formaldehyde Resin

Proton conductivity in a series of mesoporous niobium and tantalum metal oxide (mX_2O_5) composites of NSF resistant to moisture loss at temperatures greater than 50 °C is reported. The investigation focuses on the effect to proton conductivity by changing pore size and metal in the mesostructure of the mX_2O_5 system and thus, a series of mX_2O_5-NSF composites were synthesised with C_6, C_{12}, and C_{18} templates. These were characterised by XRD, TGA, nitrogen adsorption and STEM and then studied using impedance spectroscopy to establish proton conductivity values at various temperatures ranging from 25 °C to 150 °C. The most promising sample displayed a conductivity of 21.96 mS cm^{-1} at 100 °C, surpassing the literature value for Nafion 117 (ca. 8 mS cm^{-1}).

Introduction

For the PEMFC, the most widely used membrane material is DuPont's Nafion, a sulfonated tetrafluoroethylene based fluoropolymer-copolymer. The superior proton conduction properties of this material arise from the incorporation of terminally-bound sulfonate groups on perfluorovinyl ether chains which are anchored onto a perfluorovinyl ether backbone.[1] From the water channel model of Nafion[2] the sulfonic acid functional groups self-assemble into arrays of hydrophilic channels with water molecules bridging the sulfonate units to create a continuous pathway for proton mobility. In its hydrated form the conductivity of Nafion is high[3] and coupled with the high thermal and

mechanical stability[4-6] arising from the polymer backbone, Nafion is often preferred as the membrane of choice. However the main drawback of Nafion is that at temperatures above 80 °C performance deteriorates as the conductivity decreases because of water loss from the Nafion matrix.[7,8] Other concerns such as the high cost involved and also the high methanol permeability (when used in methanol fuel cells),[9-11] means that Nafion falls short of the strictest performance demands in a PEMFC. Recent attempts to improve the efficiency of Nafion at elevated temperatures involve the doping of the Nafion membrane with nanoparticles,[12-14] sulfonated zirconia,[15-17] or phosphotungstic acid[18,19] in order to increase the concentration of the acid sites that promote local migration of protons. Alternative doping methods include employing a blend of polymer, phosphoric acid and Nafion[20] or the use of hydrophilic inorganic materials to maintain high water content and prevent Nafion dehydration at high temperature.[21-24] Further modifications of the Nafion membrane have been explored with mesoporous silica[22,25,26] or PMOs[27,28] being used as a dopant in a bid to maintain a high water content and to prevent dehydration of the Nafion matrix, or with the membrane itself being treated by an electron beam.[29] Research has also focussed on replacing the Nafion membrane altogether with PMOs,[28] MOFs[30] and MOFs doped with sulphonates and phosphonates,[31-33] approaches which have offered varying degrees of promise. However, to date none of these alternatives have yet replaced Nafion as the commercially preferred membrane of choice for PEMFCs and as such, new approaches to this problem must be explored.

Aim

Using previous[34,37] work within our research group as a basis, we are attempting to develop new proton conducting materials resistant to loss of conductivity on dehydration. Our approach is to exploit the oxide surface of the *ca*. 20 Å pore walls of a mesoporous transition metal oxide as a means of anchoring sulfonate groups and suppressing moisture loss to encourage proton conduction pathways in the NSF impregnated analogues, such that operation can continue to function at higher temperature. The best of these materials, once identified and optimised, will be fabricated into membranes at a future date beyond the scope of this study for further performance and optimisation tests. Previous studies in our group using NSF composites of $mTiO_2$[37] demonstrated that proton conductivities higher than pure NSF and Nafion 117 could be obtained at temperatures above 80 °C, but that performance deteriorated above 125 °C with the solid state NMR and PXRD results suggesting that the structure collapses at these temperatures. In this current study we synthesis mesoporous transition metal oxide materials (mX_2O_5 - where X is Ta or Nb) with 15-40 Å pore size with higher thermal stability in smaller or larger pore sizes that might encourage better stability of performance under more demanding operating conditions. The mesoporous Ta and Nb oxide structures are not only more thermally robust[39,40] but previous work has demonstrated higher stability to sulfuric acid treatment of Nb and especially Ta oxides compared to Ti[38] and vastly improved Lewis and Brønsted acidity of the surface of these sulphated materials in solid-acid catalysed reactions.[39]

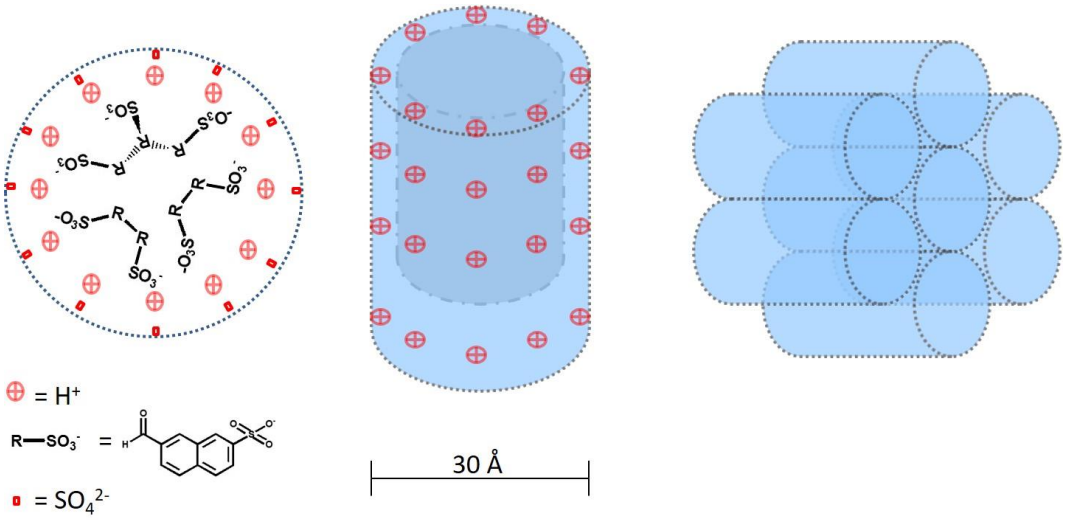

Figure 3.1: Schematic diagram depicting our approach. From left to right; the expected peripheral arrangement of mobile protons, sulfonated oligomer, and sulfate within a mX_2O_5 pore; a 3D representation of the mesopore with the shaded area representing the region in which the oligomer resides; pore alignment within the mX_2O_5 structure.

Since high surface acidity is associated with hydrophilicity and high proton mobility we reasoned that these composites should also have higher proton conductivity, greater stability to moisture loss, as well as the greater thermal stability expected from the Nb and Ta mesostructures.

In this study we have thus prepared and investigated the proton conductivity behaviour of a series of mesoporous sulphated and unsulfated mesoporous Nb, and Ta oxide composites synthesised using C_6, C_{12}, and C_{18} templates impregnated with oligomeric NSF. With an average molecular mass between 400 and 1000 and consisting of 2-6 units,[35,36] the small size of the resin molecules ensure facile diffusion into the mX_2O_5 pore structure. On the basis of our previous results with Ti, this approach results in composites in which the sulphonate groups are in close contact with the Lewis acidic oxide walls, thus offering a channel for proton movement along the interface (Figure 3.1).

Results and Discussion

Previous research from our group[37] demonstrated that $mTiO_2$ synthesized with a dodecylamine template (C_{12}-$mTiO_2$) and then impregnated with NSF in diethyl ether gave rise to an improved proton conductivity over untreated C_{12}-$mTiO_2$ (C_{12}-$mTiO_2$; 0.543 ± 0.08 mS cm^{-1}, C_{12}-$mTiO_2$-NSF.DEE; 1.837 ± 0.14 mS cm^{-1}, both at 100 °C) and diethyl ether gave better results than water as a solvent to conduct the impregnation step (C_{12}-$mTiO_2$-NSF.DEE; 1.837 ± 0.14 mS cm^{-1}, C_{12}-$mTiO_2$-NSF.H_2O; 0.499 ± 0.03 mS cm^{-1}). On the basis of previous work on acid catalysis,[43] doping the structure with sulfate would improve the proton conductivity, however $mTiO_2$ loses its structure when treated with even small (*ca*. 5 %) levels of sulphuric acid.[37] In a more robust mesoporous material doping with sulfuric acid may enhance the proton conducting pathways within the mesopores without degrading the structure when the acid was introduced. Thus, C_{12} mesoporous Ta and Nb oxides, previously shown to be stable to sulphuric acid treatment,[44] were used in the current study in place of Ti and three different pore sizes of the Ta oxide synthesized using templates of differing chain lengths (C_6, C_{12} and C_{18}) were synthesised in order to gauge the effect of changing the metal and/or the pore size on the proton conductivity of the related NSF composites. These four new composites were synthesised as per the Experimental Section and include one sample of C_{12}-mTa_2O_5 doped with sulfuric acid and impregnated with NSF in the presence of diethyl ether medium (C_{12}-$mTa_2O_5(SO_4)$-NSF.DEE) and three analogous composites using C_6-Ta, C_{18}-Ta and C_{12}-Nb respectively. Where appropriate in the text and tables we also list the Ti materials from our previous report, as well as the respective

pristine mesoporous oxides. Data for additional C_{12}-Ta analogues synthesised without sulphate, or with water instead of diethyl ether, can be found within the supporting information, again where appropriate. Each sample was fully characterised using the parameters detailed in the Characterisation section and are discussed below.

Surface area analysis. The BET surface areas for the as-synthesised materials and Ta analogues are reported in Table 3.1 and the nitrogen adsorption-desorption isotherms for C_{12}-mTa_2O_5, C_6-mTa_2O_5, C_{18}-mTa_2O_5 and C_{12}-mNb_2O_5 are shown in Figure 3.2. Figure 3.3 displays the isotherms for C_6-m$Ta_2O_5(SO_4)$-NSF.DEE, C_{18}-m$Ta_2O_5(SO_4)$-NSF.DEE, and C_{12}-m$Ta_2O_5(SO_4)$-NSF.DEE, and Figure 3.4 shows the isotherm for C_{12}-m$Nb_2O_5(SO_4)$-NSF.DEE. In all cases the samples are on the cusp between type I and IV isotherms, as expected for materials with a ca. 25-35 Å pore size. The C_{12}-mTa_2O_5 sample possesses a high surface area of 459 m^2 g^{-1}, which decreases when the material is doped and impregnated to 0.059 m^2 g^{-1}. These changes upon impregnation are also mirrored with the C_6-mTa_2O_5, C_{18}- mTa_2O_5 and C_{12}-mTa_2O_5 systems in which the surface area also drops off significantly with doping. There is also a loss of pore volume by a factor of 100 in all cases and where recorded the pore size notably decreases following treatment.

Table 3.3

Nitrogen adsorption data for the as-synthesised materials. N/A: denotes that the surface area was too small to record a pore volume size

Material	BET Surface Area / m^2g^{-1}	Pore Volume / $cm^3\ g^{-1}$	BJH Pore Size / Å
C_{12}-mTa_2O_5	459	0.324	28.21
C_{12}-$mTa_2O_5(SO_4)$-NSF.DEE	0.959	N/A	N/A
C_6-mTa_2O_5	277	0.239	34.56
C_6-$mTa_2O_5(SO_4)$-NSF.DEE	0.402	N/A	18.59
C_{18}-mTa_2O_5	286	0.282	39.27
C_{18}-$mTa_2O_5(SO_4)$-NSF.DEE	N/A	N/A	N/A
C_{12}-mNb_2O_5	466	0.381	32.67
C_{12}-$mNb_2O_5(SO_4)$-NSF.DEE	4.206	0.003	26.86
C_{12}-mTa_2O_5-NSF.H_2O	20.55	0.0132	25.64
C_{12}-mTa_2O_5-NSF.DEE	11.81	0.0182	N/A
C_{12}-$mTa_2O_5(SO_4)$-NSF.H_2O	22.85	0.00902	N/A
C_{12}-$mTa_2O_5(SO_4)$-NSF.DEE	0.959	0.00048	N/A

Impregnation of the pores with NSF is expected to lower the surface area and pore volume on doping, while the loss of surface area on doping with sulfuric acid is consistent with previous work on sulfated mesoporous Ti, Nb, and Ta oxides.[38,39] In both cases, loss of surface area upon NSF impregnation indicates that the pores have been filled with NSF resin. For comparison, the nitrogen adsorption-desorption isotherms for the Ta analogues can be found on Figure 3.5.

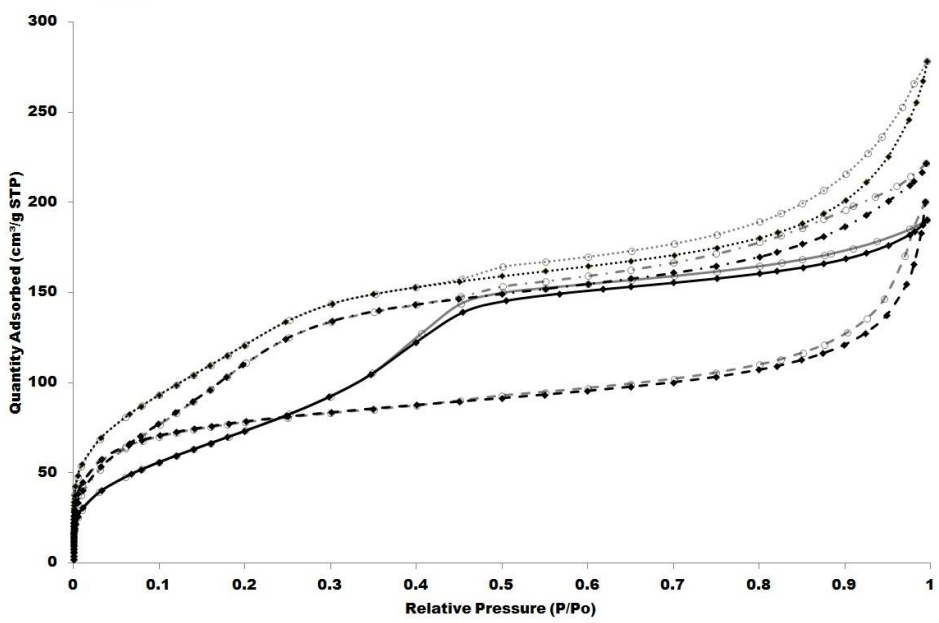

Figure 3.2: Nitrogen adsorption (diamonds)/desorption (circles) isotherms for C_{12}-mTa_2O_5 (dots and dashes), C_6-mTa_2O_5 (dashes), C_{18}-mTa_2O_5 (solid line) and C_{12}-mNb_2O_5 (dots)

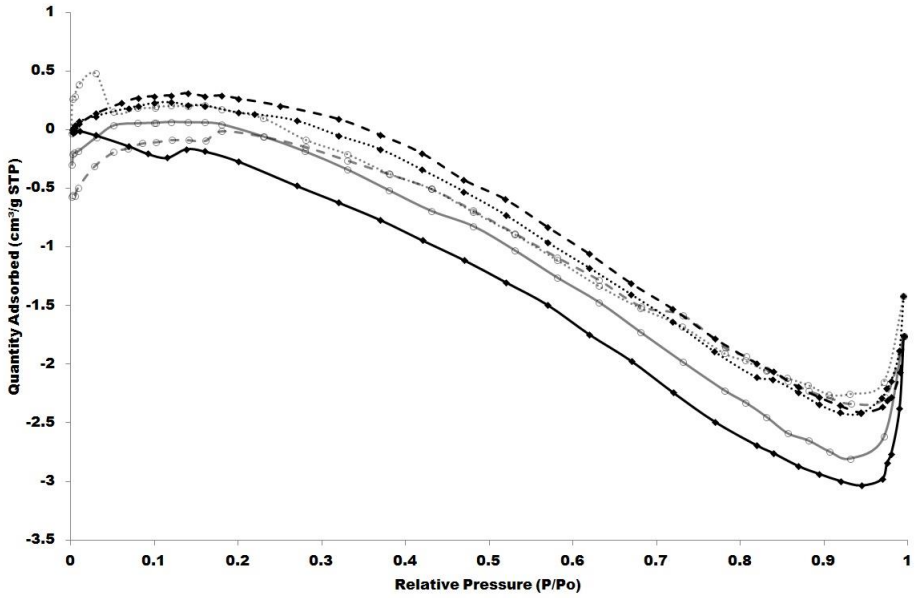

Figure 3.3: Nitrogen adsorption (diamonds)/desorption (circles) isotherms for C_6-$mTa_2O_5(SO_4)$-NSF.DEE (dots), C_{18}-$mTa_2O_5(SO_4)$-NSF.DEE (solid line) and C_{12}-$mTa_2O_5(SO_4)$-NSF.DEE (dashes). Negative values are an artifact caused by low total adsorption due to low surface area and limited size of sample chamber

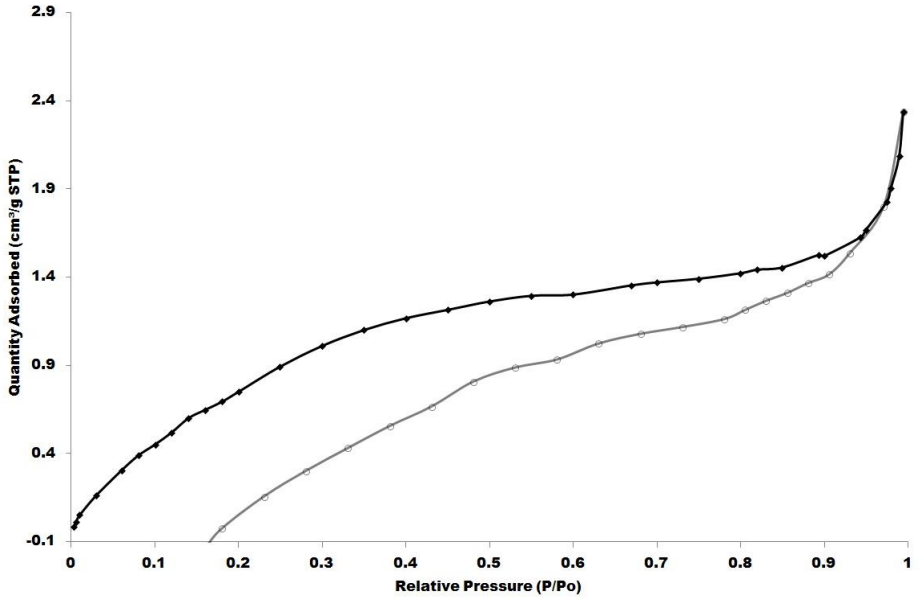

Figure 3.4: Nitrogen adsorption (diamonds)/desorption (circles) isotherms for C_{12}-$mNb_2O_5(SO_4)$-NSF.DEE. Negative values are an artifact caused by low total adsorption due to low surface area and limited size of sample chamber

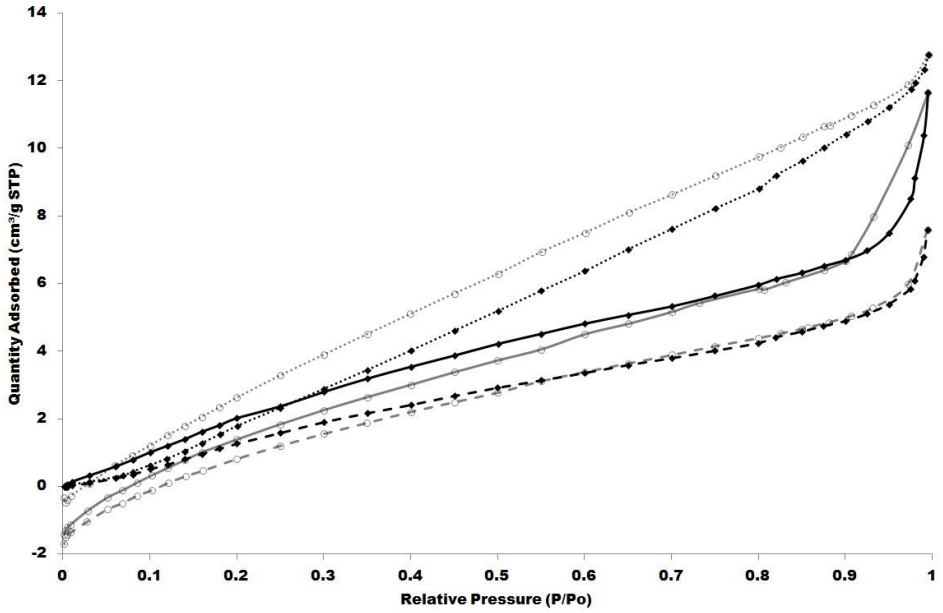

Figure 3.522: Nitrogen adsorption (diamonds)/desorption (circles) isotherms for C_{12}-mTa_2O_5-NSF.DEE (dots), C_{12}-mTa_2O_5-NSF.H_2O (solid line) and C_{12}-$mTa_2O_5(SO_4)$-NSF.H_2O (dashes). Negative values are an artifact caused by low total adsorption due to low surface area and limited size of sample chamber

Infrared spectroscopy. The IR spectra further demonstrate retention of NSF in all cases, with the spectra for the metal oxide composites, metal oxides, and Ta analogues shown on Figures 3.6, 3.7 and 3.8 respectively. Pure NSF resin gives rise to an aromatic C-H stretch at *v*2900 cm^{-1} and aromatic ring vibration modes at *v* 1640 cm^{-1}, *v* 1596 cm^{-1} and *v* 1507 cm^{-1}. These are apparent in all NSF treated samples. This is also mirrored by the appearance of the NSF SO stretch and S-phenyl vibrations observed at *v* 1230 cm^{-1}, *v* 1190 cm^{-1}, *v* 1130 cm^{-1} and *v* 1040 cm^{-1}. There are also C-H stretches at *v* 2800 cm^{-1} for the NSF methylene protons and trace residual hydrocarbon in the mX_2O_5.

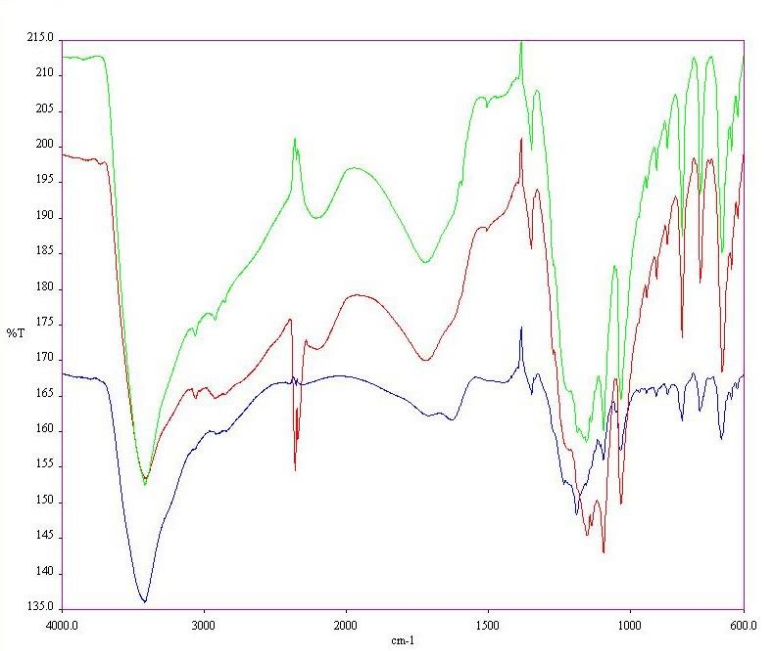

Figure 3.6: IR spectra of C_6-m$Ta_2O_5(SO_4)$-NSF.DEE (blue), C_{18}-m$Ta_2O_5(SO_4)$-NSF.DEE (red) and C_{12}-m$Nb_2O_5(SO_4)$-NSF.DEE (green)

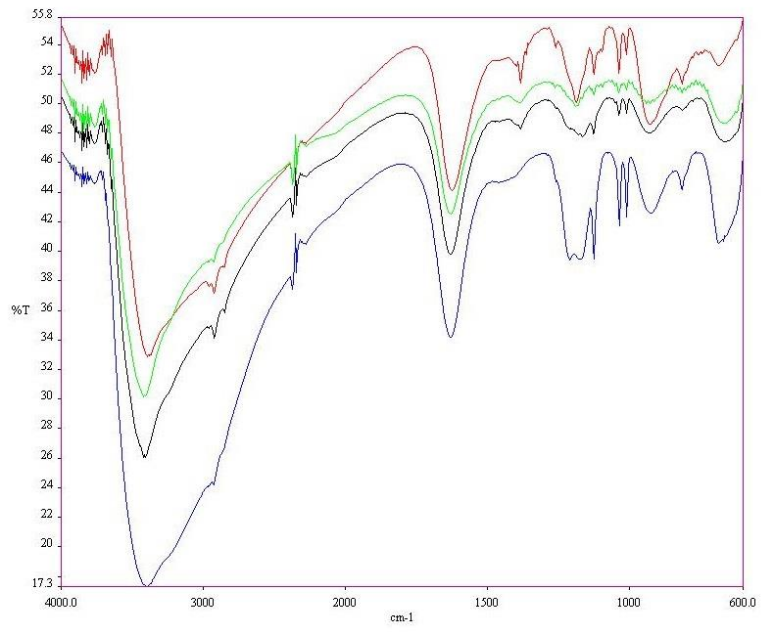

Figure 3.723: IR spectra of C_6-mTa_2O_5 (green), C_{12}-mTa_2O_5 (blue), C_{18}-mTa_2O_5 (black) and C_{12}-mNb_2O_5 (red)

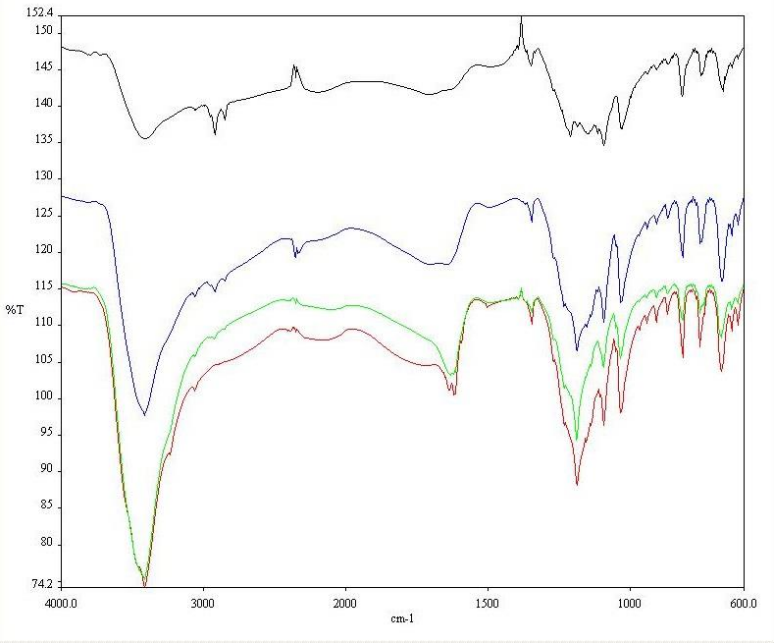

Figure 3.8: IR spectra displaying C_{12}-mTa_2O_5-NSF.H_2O (black), C_{12}-mTa_2O_5-NSF.DEE (blue), C_{12}-m$Ta_2O_5(SO_4)$-NSF.H_2O (red) and C_{12}-m$Ta_2O_5(SO_4)$-NSF.DEE (green)

Powder x-ray diffraction. The PXRD patterns for the as synthesised materials are shown in Figure 3.9. The spectra shows a reflection between 2.4 and 3.2 2θ, indicative of a mesoporous structure and consistent with our previous data.[41] The remaining peaks between 15 and 50 2θ arise from partial crystallisation of the walls in the structure. These reflections are strongest in the Nb sample, demonstrating the greater stability of the amorphous Ta oxide mesostructure over the Nb analogue. Combined with the BET and IR data, these data show that the composite synthesis was completed in all cases.

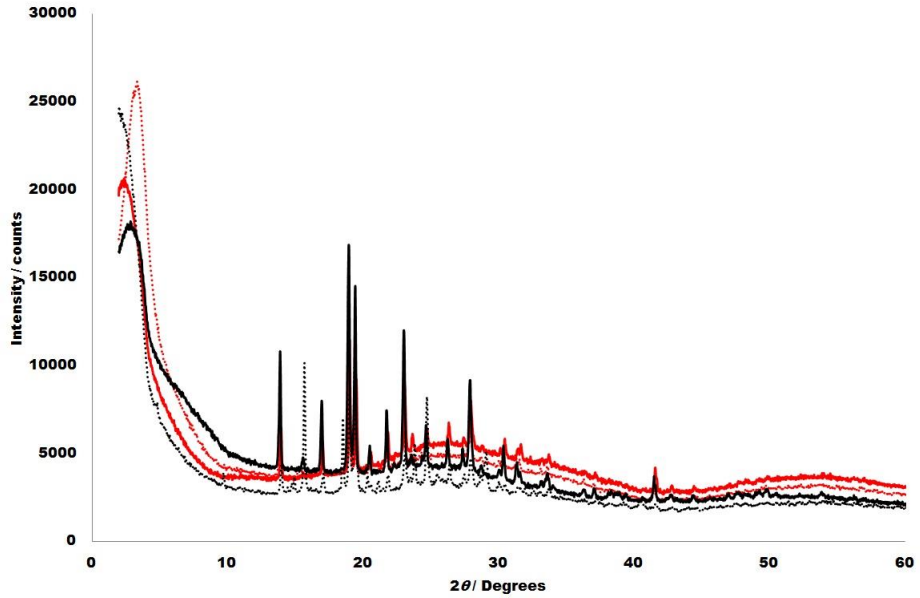

Figure 3.9: PXRD patterns for C_{12}-m$Nb_2O_5(SO_4)$-NSF.DEE (black line), C_6-m$Ta_2O_5(SO_4)$-NSF.DEE (red dots), C_{12}-m$Ta_2O_5(SO_4)$-NSF.DEE (black dots), C_{18}-m$Ta_2O_5(SO_4)$-NSF.DEE (red line).

Thermal analysis. The percentage of hydrocarbon was probed in the as-synthesised samples by TGA and DTA and the trace for these are shown in Figures 3.10 through to 3.13. Each composite has a similar trace to its neighbour whereby firstly, the thermogravimetric curve shows weight loss of ca. 10 % at 130 °C which is attributed to loss of residual H_2O. At 450 °C there is also a weight loss of ca. 5 % which is attributed to the combustion of any residual hydrocarbon from the dodecylamine template or partial collapse of the mesopore structure. This is confirmed by the overlying DTA curve which shows an endothermic peak at 130 °C and two exothermic peaks at 350 and 500 °C. Weight loss of ca 5 % at 390 °C is the loss of the sulfonate groups, whilst NSF is burnt off the sample at 485 °C. Continued weight loss above ca. 550 °C is attributed to a slight degradation to the crystalline form of the oxide itself as the mesostructure begins to

collapse. From the traces the C_6 composite has the least total weight loss at ca. 40 %. Both the C_{12} composites have a total weight loss of ca. 50 %, with the Ta showing a steeper decline than Nb after 485 °C which would indicate more NSF in the Ta sample. The pore size of the Ta sample is greater than that of the Nb, which will also contribute to these observations. The weight loss for the C_6 and the C_{12} composites are expected as more NSF will be impregnated into a sample with larger pore size but intriguingly, the C_{18} composite shows a total weight loss of ca. 45 %. Whilst this is less than expected, the larger pore size could lead to more facile leaching of the NSF from the structure compared to those with a slightly smaller pore size.

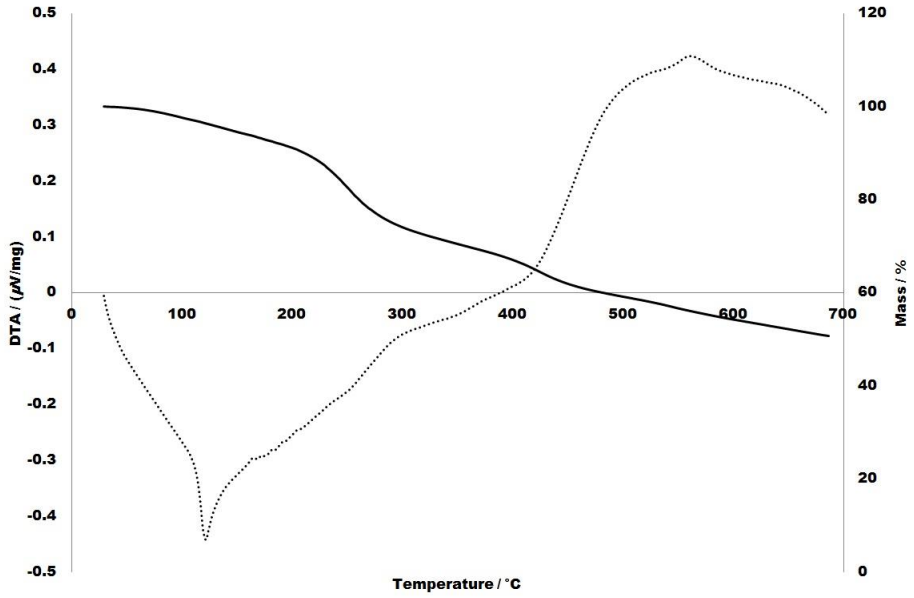

Figure 3.1024: TGA (line) and DTA (dots) trace for C_{12}-m$Nb_2O_5(SO_4)$-NSF.DEE

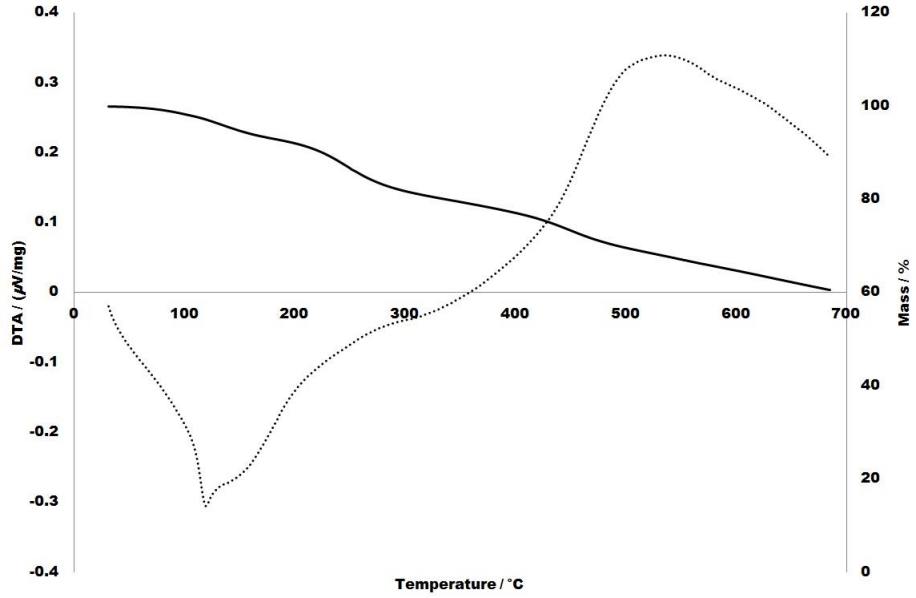

Figure 3.11: TGA (line) and DTA (dots) trace for C_6-m$Ta_2O_5(SO_4)$-NSF.DEE

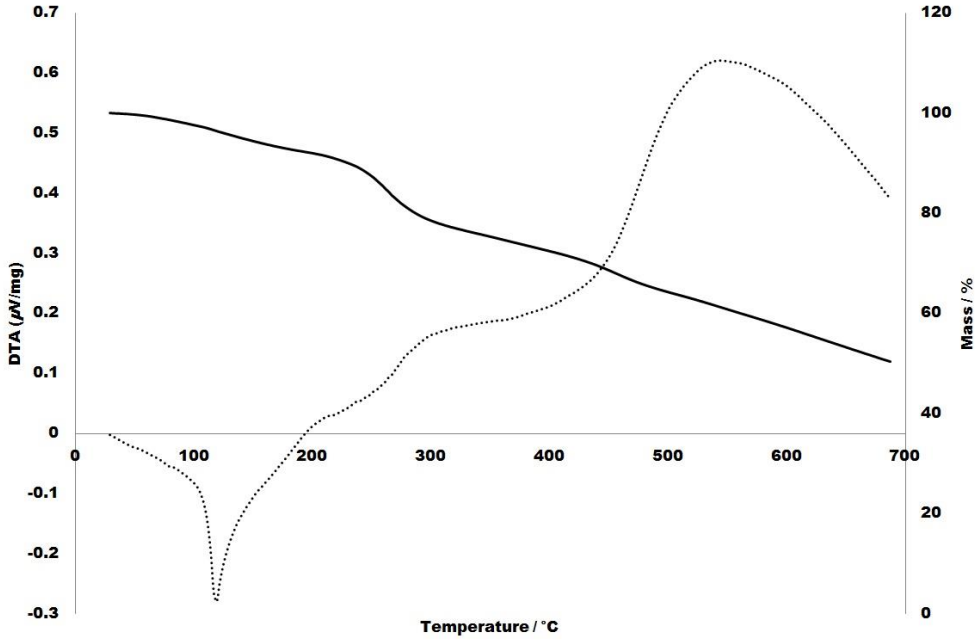

Figure 3.12: TGA (line) and DTA (dots) trace for C_{12}-m$Ta_2O_5(SO_4)$-NSF.DEE

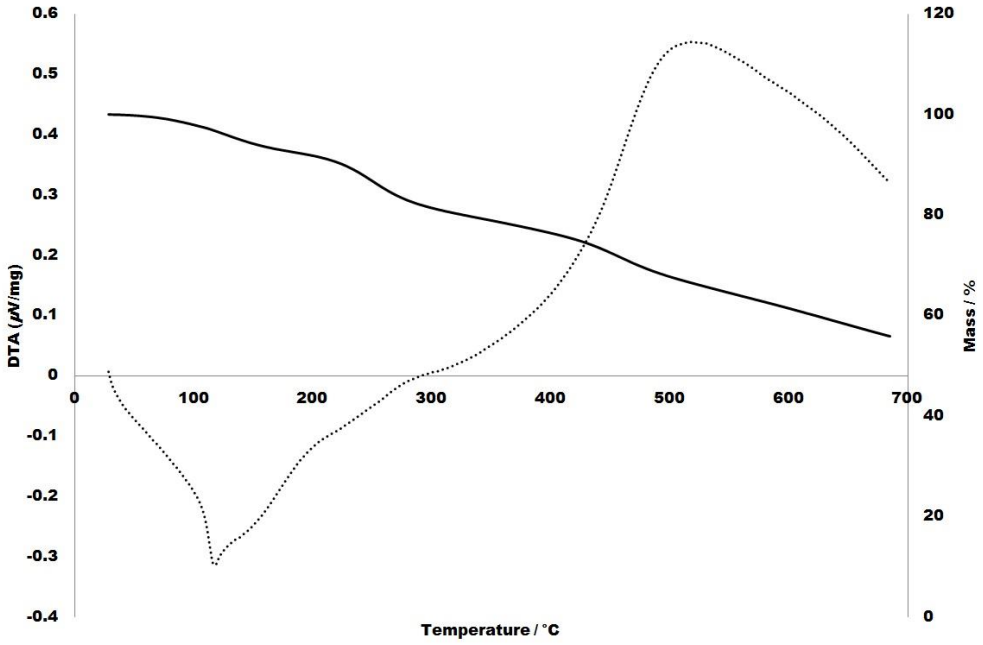

Figure 3.13: TGA (line) and DTA (dots) trace for C_{18}-m$Ta_2O_5(SO_4)$-NSF.DEE

Scanning transmission electron microscopy. To confirm the powder morphology (a) and pore structure (b) of the as-synthesised materials, STEM was performed with the images of the as-synthesised materials shown in Figures 3.14 through to 3.17. Each pore structure image, taken at a scale of either 0.2 or 1 μm, displays a wormhole-like structure that is typical for mesoporous materials synthesised with non-ionic templates. From this, a pore size of ca. 20-30 Å in diameter can be derived (in agreement with the BET data) and that the pore walls are ca. 20 Å thick. This corresponds to what is expected on the basis of the PXRD data and is in agreement with previous work.[42] Following impregnation of the pore with NSF and/or doping of the pore wall mesostructure with H_2SO_4 it becomes increasingly difficult to image either the pores (due to the filling of the pores by the NSF), or the mesostructure (due to pore degradation

from the H_2SO_4). This is further confirmed from our BET surface area and PXRD data. This is consistent with variable degrees of proton-induced crystallisation of the walls. Both sets of images are consistent with the reported BET data and with previous data using this experimental approach.[37]

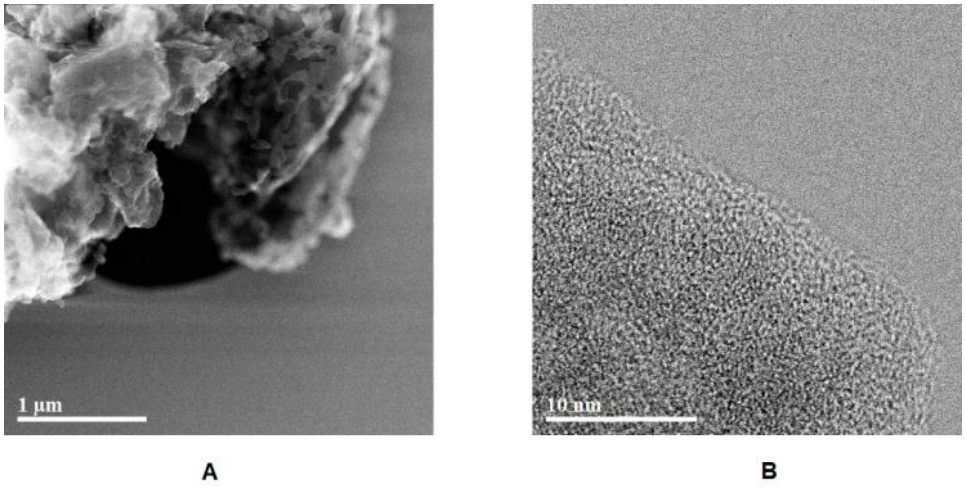

Figure 3.14: STEM images of the $mNb_2O_5(SO_4)$-NSF.DEE composite showing, a) the powder morphology; b) a higher magnification of the pore structure

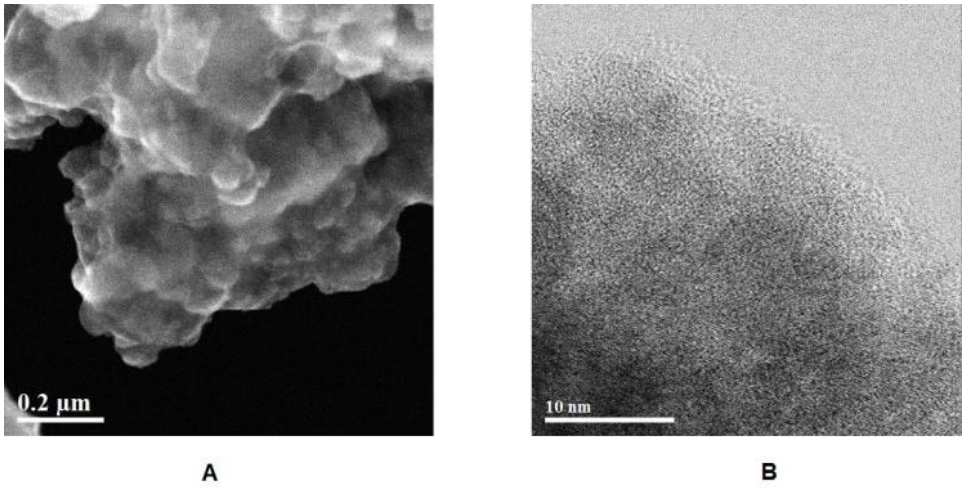

Figure 3.15: STEM images of the C_6-$mTa_2O_5(SO_4)$-NSF.DEE composite showing, a) the powder morphology; b) a higher magnification of the pore structure

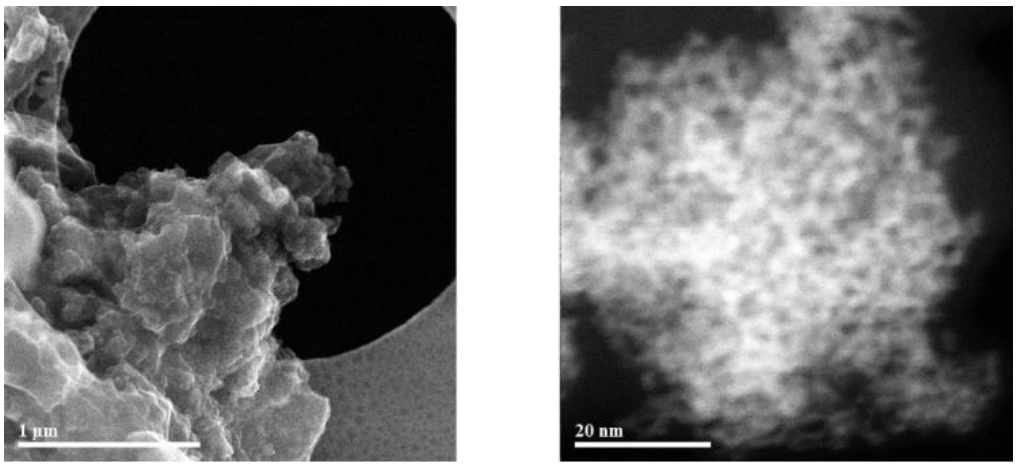

Figure 3.16: STEM images of the C_{12}-m$Ta_2O_5(SO_4)$-NSF.DEE composite showing, a) the powder morphology; b) a higher magnification of the pore structure

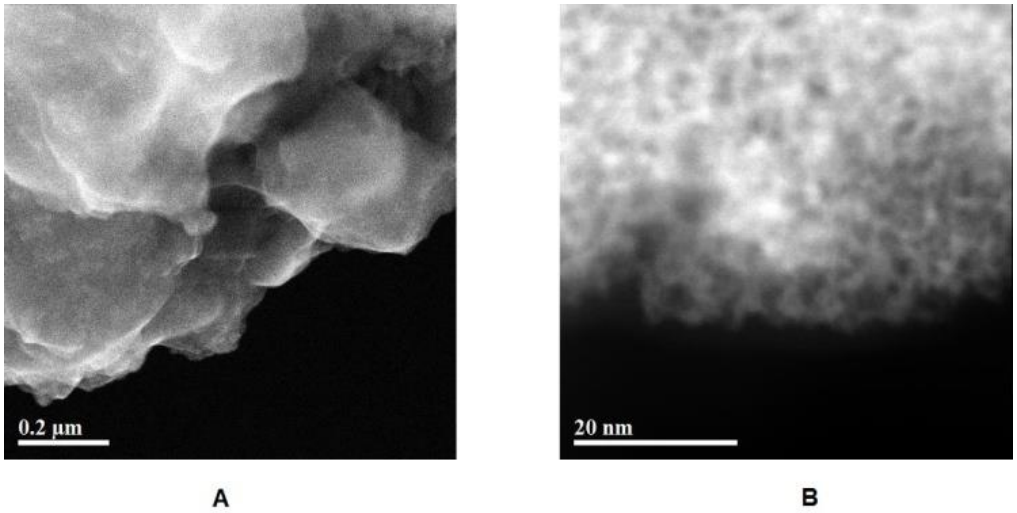

Figure 3.17: STEM images of the C_{18}-m$Ta_2O_5(SO_4)$-NSF.DEE composite showing, a) the powder morphology; b) a higher magnification of the pore structure

As described in the Characterisation Section, each composite was incorporated into a cell. Each cell had its potentiostatic impedance recorded at room temperature, atmospheric pressure and at 50 % humidity with the results (where necessary,

extrapolated as described in the characterisation section) displayed in Figure 18 and Table 2. Previous work[44] demonstrated by TPD that moisture loss is suppressed by the Lewis Acid sites (and/or the sulfonate groups) on the pore walls of sulfate-doped mesoporous Ti, Nb, and Ta oxide and as such, thermal dehydration of the pellet is anticipated to be suppressed compared to that of Nafion 117.

Electrochemical impedence spectroscopy. As a reference and for equality, Nafion 117 was made into a cell (both as a pellet for internal consistency and as a commercially purchased film to compare our measurements with literature values) and measured under the same conditions. Whilst Nyquist plots commonly reveal a complete semi-circle, the straight lines acquired at low resistance in our measurements of Nafion represent portions of a larger semi-circle and are similar in overall appearance to those previously reported for this material.[44] Next, the temperature was increased to 50 °C, the potentiostatic impedance was measured (Figure 7.11) and subsequently the proton conductivity was found. This was repeated at 75 °C (Figure 7.12), 100 °C (Figure 7.13), 125 °C (Figure 7.15) and 150 °C (Figure 7.16) respectively. Figure 7.14 shows a magnified Nyquist Plot of C_{12}-m$Nb_2O_5(SO_4)$-NSF.DEE at 100 °C. Taken from 7.13, this magnification displays the semi-circular relationship of each curve, followed by the Warburg Tail in the low frequency part of the plot. The average conductivity from all samples at all temperatures, along with the calculated standard error, is shown on Table 3.2 and from this a plot (Figure 3.18) of $\log_{10}\sigma$ versus T was made derived as described in the notes in the Experimental Section.

Figure 3.18 also shows the conductivity of each pellet in relation to a Nafion 117 pellet and film formed in a similar fashion to the composites. As shown on the graph, both Nafion 117 cells become more resistive as the temperature is increased and this is consistent with what is reported in the literature for this material.[7,8] A Nyquist plot at 25 °C for the Ta analogues listed in Table 3.2 can be found on Figure 7.17. Initially, proton conductivity for C_{12} Ta analogues was obtained to determine the optimal doping composition for this research and C_{12}-m$Ta_2O_5(SO_4)$-NSF.DEE was selected based on high initial conductivity (2.70 mS cm^{-1}) and the results obtained previously for the Ti analogues.[37]

Whilst this was comparable to the value obtained for C_{12}-m$Ta_2O_5(SO_4)$-NSF.H_2O (2.77 mS cm^{-1}), using DEE as a medium avoids problems with residual moisture in the cell and thus, more control on dehydration when the temperature is raised. (For comparison, the conductivity of the untreated C_{12} Ta at 25 °C is 0.334 mS cm^{-1}.) At 100 °C a conductivity of 13.11 mS cm^{-1} was observed for C_{12}-m$Ta_2O_5(SO_4)$-NSF.DEE, which surpassed the untreated C_{12} Ta (0.461 mS cm^{-1}), our Nafion 117 standards (pellet; 1.143 mS cm^{-1}, film; 0.420 mS cm^{-1}) and the literature value for Nafion 117 at identical humidity (8 mS cm^{-1}).47 At 150 °C, a conductivity of 0.95 mS cm^{-1} was observed for C_{12}-m$Ta_2O_5(SO_4)$-NSF.DEE and despite the conductivity decreasing, it remained higher than that of the untreated sample (0.086 mS cm^{-1}) and the Nafion standards (pellet; 0.126 mS cm^{-1}, film; 0.030 mS cm^{-1}). This is a pattern we observed with the mesoporous Ti system[37] where despite retaining moisture better than Nafion (as evident by the conductivity values measured), NSF leaches out of the composites at 150 °C, which is

consistent with what we observe in the TGA trace at around 130 °C. Next, we changed the pore size of the Ta materials to see if there was a relationship between pore size and conductivity either directly or indirectly through the amount of NSF retained in the pores. At 25 °C, the conductivity was measured for C_6-m$Ta_2O_5(SO_4)$-NSF.DEE (2.89 mS cm^{-1}) and C_{18}-m$Ta_2O_5(SO_4)$-NSF.DEE (6.72 mS cm^{-1}) respectively, both of which surpass their untreated counterparts (C_6 Ta; 0.458 mS cm^{-1}, C_{18} Ta; 0.396 mS $cm^{-1)}$. At 100 °C, these increase to 8.59 mS cm^{-1} and 13.15 mS cm^{-1} respectively, which again surpasses the untreated samples (C_6 Ta; 0.762 mS cm^{-1}, C_{18} Ta; 0.357 mS cm^{-1}) and that of the literature Nafion 117 value (8 mS cm^{-1}). At 150 °C, the performance again tails off to 0.13 mS cm^{-1} (C_6 Ta-NSF) and 0.11 mS cm^{-1} (C_{18} Ta-NSF), which is below that of the Nafion 117 pellet (0.126 mS cm^{-1}), but above that of the Nafion film (0.030 mS cm^{-1}). Intriguingly, both of these composites performed better at 75 °C (C_6 Ta; 18.08 mS cm^{-1}, C_{18} Ta; 22.29 mS cm^{-1}) than at 100 °C. Taking all data into account the pattern established is that the C_{18} material displays higher conductivities than the C_{12} and C_6 samples, but loses performance at elevated temperatures more rapidly than its two congeners.

Table 3.4

Average proton conductivity and associated error (mS cm^{-1}) of the as-synthesised materials, NSF, and the reference cell, Nafion 117

	25 °C	50 °C	75 °C	100 °C	125 °C	150 °C
C_{12}-mTa_2O_5	0.334	0.477	0.233	0.461	0.212	0.086
C_{12}-mTa_2O_5-NSF.H_2O	1.590	N/A	N/A	N/A	N/A	N/A
C_{12}-mTa_2O_5-NSF.DEE	1.030	N/A	N/A	N/A	N/A	N/A
C_{12}-$mTa_2O_5(SO_4)$	0.930	N/A	N/A	N/A	N/A	N/A
C_{12}-$mTa_2O_5(SO_4)$-NSF.H_2O	2.770	N/A	N/A	N/A	N/A	N/A
C_{12}-$mTa_2O_5(SO_4)$-NSF.DEE	2.700±0.01	6.640±0.01	11.12±0.01	13.11±0.01	2.400±0.01	0.950±0.01
C_6-mTa_2O_5	0.458	0.737	0.646	0.762	0.385	0.687
C_6-$mTa_2O_5(SO_4)$-NSF.DEE	2.890±0.01	9.390±0.03	18.08±0.03	8.590±0.03	2.190±0.01	0.110±0.01
C_{18}-mTa_2O_5	0.396	0.268	0.360	0.357	0.284	0.122
C_{18}-$mTa_2O_5(SO_4)$-NSF.DEE	6.720±0.01	6.270±0.02	22.29±0.01	15.35±0.01	0.160±0.12	0.130±0.06
C_{12}-mNb_2O_5	0.373	0.444	0.565	0.469	0.614	0.436
C_{12}-$mNb_2O_5(SO_4)$-NSF.DEE	0.600±0.01	4.88±0.01	13.97±0.02	21.96±0.01	0.780±0.01	0.170±0.01
Nafion 117 (Pellet)	1.450±0.16	1.131±0.19	1.013±0.18	1.143±0.12	0.254±0.04	0.126±0.02
Nafion 117 (Film)	2.570±0.12	1.461±0.11	0.926±0.31	0.420±0.25	0.071±0.04	0.030±0.2
NSF	0.508±0.04	0.612±0.03	0.143±0.01	0.122±0.02	0.069±0.02	0.019±0.01
C_{12}-$mTiO_2$-NSF.DEE	0.300±0.01	0.764±0.03	1.195±0.03	1.837±0.14	1.084±0.04	0.631±0.09

This is consistent with the larger pores allowing for more and deeper penetration by the NSF, which subsequently allows easier leaching of the NSF at elevated temperatures. Next, we kept the pore size constant at C_{12} while changing the metal to Nb to allow a comparison between the C_{12} Ti, Ta and Nb systems and investigate whether or not there is a relationship between the composition of the porous wall and the proton conducting network.

At 25 °C, the conductivity obtained for C_{12}-m$Nb_2O_5(SO_4)$-NSF.DEE was 0.60 ± 0.01 mS cm^{-1}, a value higher than untreated C_{12}-mNb_2O_5 (0.373 mS cm^{-1}) but the lowest of the four composites investigated. At 100 °C, conductivity improves significantly (21.96 ± 0.01 mS cm^{-1}) surpassing that of the untreated sample (0.469 mS cm^{-1}), the literature Nafion value (*ca.* 8 mS cm^{-1}) and all other Ta and Ti composites.

At 150 °C the conductivity decreases to 0.17 ± 0.01 mS cm^{-1} (untreated C_{12} Nb; 0.436 mS cm^{-1}), a pattern observed with the other samples in this study. This demonstrates that the C_{12} Nb system doped with NSF and sulphate in DEE is the optimal proton conducting material in our study. The Nb oxide walls are more robust than those of the Ti system, allowing for greater stability under operating conditions, and a combination of surface area, NSF retention, and or surface acidity properties gives superior proton conducting properties to the Ta system. Finally, reported error is within acceptable parameters for these experiments and remains consistent throughout.

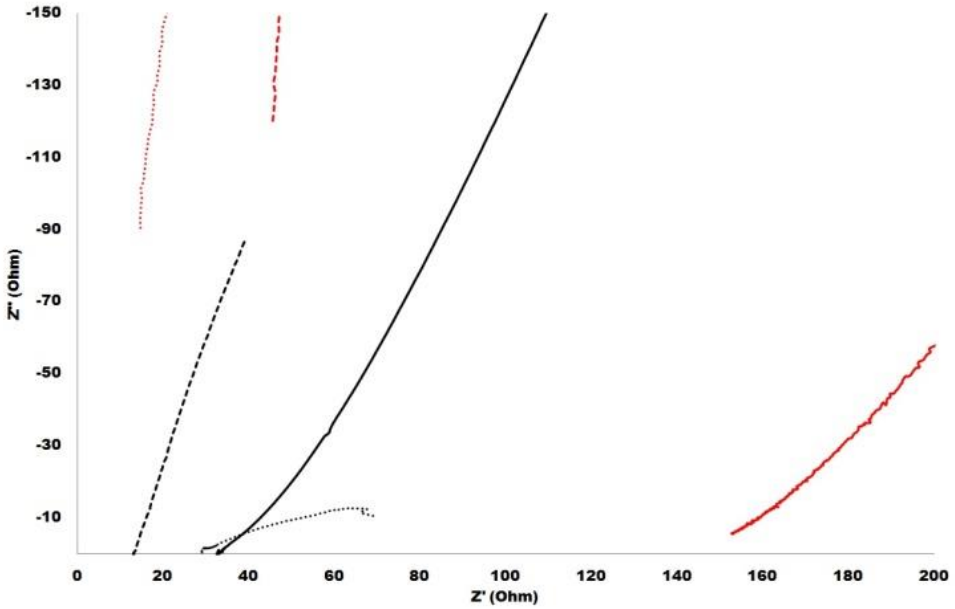

Figure 3.18: Nyquist plot at 25 °C showing the potentiostatic impedance of C_{12}-$mTa_2O_5(SO_4)$-NSF.DEE (black line), C_6-$mTa_2O_5(SO_4)$-NSF.DEE (black dots), C_{18}-$mTa_2O_5(SO_4)$-NSF.DEE (black dashes), C_{12}-$mNb_2O_5(SO_4)$-NSF.DEE (red line), Nafion 117 membrane (red dots) and Nafion 117 pellet (red dashes).

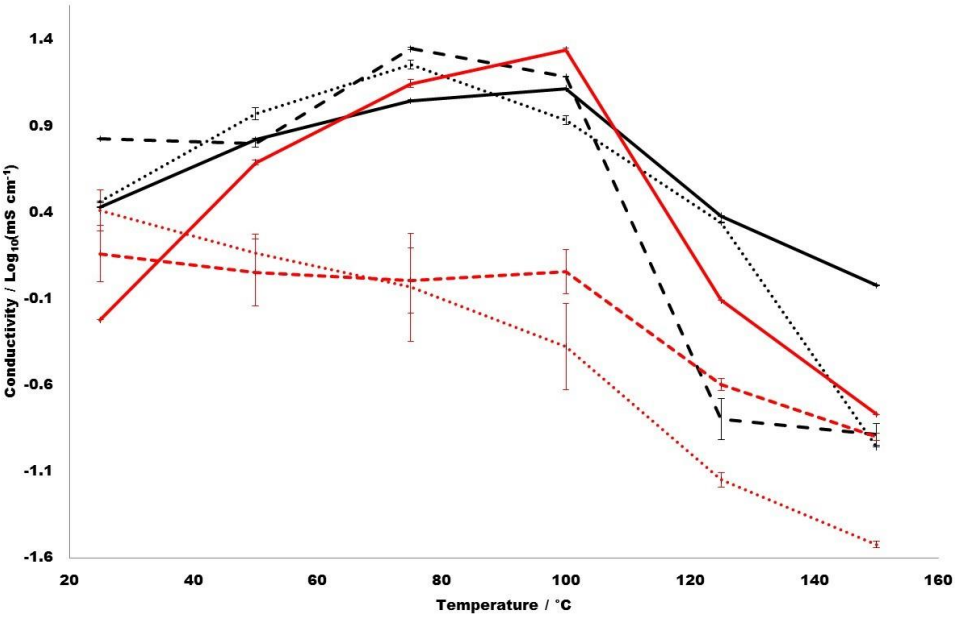

Figure 3.19: Average proton conductivities of C_{12}-$mTa_2O_5(SO_4)$-NSF.DEE (black line), C_6-$mTa_2O_5(SO_4)$-NSF.DEE (black dots), C_{18}-$mTa_2O_5(SO_4)$-NSF.DEE (black dashes), C_{12}-$mNb_2O_5(SO_4)$-NSF.DEE (red line), Nafion 117 membrane (red dots) and Nafion 117 pellet (red dashes) as a function of temperature

Each composite performed better than pure hydrated NSF (Table 3.2), which confirms a synergistic interaction between NSF and the oxide mesostructure in all composites studied. The most promising system is that using C_{12} Nb doping with sulfate as the mesoporous scaffolding. The robust nature of the mesostructure enables optimal augmentation of the proton-conducting network and as such, locks the NSF in the pores at the optimal temperatures for PEMFC operation. However, the NSF is still prone to leaching out of the system once the optimal temperature is surpassed (at temperatures greater than 150 °C the oligomer becomes mobile), which in turn affects the proton conduction network. For this reason, methods of blocking this leaching process by using larger oligomers or condensing the NSF within the pores rather than impregnating with small oligomers, may lead to better results at high temperatures and thus form the basis of future work.

Conclusions

In this paper the synthesis and characterisation of a series of mesoporous Nb and Ta oxide polymer composites has been reported. Each composite (three of Ta with differing pore sizes and one of Nb) was formed into a cell and their proton conductivity was compared against a Nafion 117 standard (literature value for Nafion 117; 100 °C, 8 mS cm^{-1}) over a temperature range of 25 °C and 150 °C. Whilst all composites exhibit conductivities that surpass that of the pure NSF and the Nafion standard, the most promising was the C_{12}-m$Nb_2O_5(SO_4)$-NSF.DEE (21.96 ± 0.01 mS cm^{-1} at 100 °C), although at 150 °C the conductivity drops in all cases, most likely due to leaching of the oligomer. The object of this research was to optimise effects of composition and pore size

on conductivities of these systems and the next steps are to explore methods of blocking the leaching of the polymer while also attempting to fabricate these materials into a membrane whilst preserving the high proton conductivity observed in this current study.

Experimental Section

All chemicals were purchased from either Sigma Aldrich or Alfa Aesar without further purification.

C_{12}-mNb_2O_5. Mesoporous niobium oxide was prepared according to the published procedure using ligand assisted templating.[39] Thus, a 3:1 mixture of niobium (V) ethoxide (10 g) and dodecylamine (6 g) was created with water (75 ml) to form a white gel and this was left to stand for 24 hours. The water was then exchanged for fresh (75 ml) and one drop of 12 M HCl was added, with the resultant solution stirred and left to stand for a further 24 hours before being transferred to an oven at 40 °C to begin the ageing process. After 48 hours the temperature was increased to 60 °C. The sample was then aged for a further 48 hours and this was repeated at 80 °C, after which the solid was collected by filtration, dried for 24 hours at 80 °C, placed into a sealed sample tube and returned to the oven at 100 °C for an additional 48 hours. The ageing process was completed at 120 °C for 48 hours and 140 °C for 48 hours, respectively. Removal of the organic template was initiated by combining of the material with pTSA (6 g) in methanol followed by stirring for 24 hours. Following filtration, the material was combined with fresh pTSA (7.8 g) and stirred with methanol for 24 hours. This process was completed with three subsequent filtrations and washings with methanol.

mTa_2O_5. Mesoporous tantalum oxide was prepared according to the published procedure using ligand assisted templating.[38] The exact method is similar to that described for mNb_2O_5, apart from the starting material being tantalum (v) ethoxide. To obtain the various ligand sizes, C_6-mTa_2O_5 uses hexlyamine, C_{12}-mTa_2O_5 uses dodecylamine and C_{18}-mTa_2O_5 uses octadecylamine.

$C_6/C_{12}/C_{18}$-$mX_2O_5(SO_4)$-NSF. One drop of H_2SO_4 was added to a vial with water (0.5 ml) and left to stand for 5 minutes. To this solution mX_2O_5 (0.5 g) was added, and the vial sealed and stirred for 48 hours. Finally, the sample was dried in an oven at 80 °C to remove all excess water. After grinding to a fine powder, the ($mX_2O_5(SO_4)$, 0.5 g) was added to a 1:1 mixture of NSF (1.25 g) and diethyl ether (DEE, 1.25 g), and this mixture was stirred for an additional 48 hours and then dried in an oven at 80 °C.

***Tantalum Analogues*: C_{12}-mTa_2O_5-NSF**. To a 1:1 mixture of NSF (2.5 g) and water (2.5 g) (alternatively DEE, 2.5 g) was added mTa_2O_5 (1 g). This mixture was stirred for 48 hours and then dried in an oven at 80 °C. *C_{12}-$mTa_2O_5(SO_4)$*: As for C_{12}-$mTa_2O_5(SO_4)$-NSF.DEE but stopping prior to the NSF addition. *C_{12}-$mTa_2O_5(SO_4)$-NSF.H_2O*: As for C_{12}-$mTa_2O_5(SO_4)$-NSF.DEE, but with H_2O (1.25 g) replacing DEE in the final step.

NSF. 6.53 g Naphthalene was melted in a glass flask equipped with a reflux condenser. To this, H_2SO_4 (5 ml) was slowly added and the temperature was kept below 115 °C during the addition. The heat was then increased to 160 °C, kept constant and stirred for eight hours to ensure maximum sulfonation of the naphthalene adduct and afford 2-naphthalene sulfonic acid, with an excess naphthalene removed by filtration.

With the internal temperature raised to 95 °C formaldehyde (0.65 g, 0.9 M) was added along with a few drops of water and this was maintained for eighteen hours. Once cooled this was dissolved in diethyl ether and dried to achieve a free flowing solid.

Characterisation section. BET surface area measurements were derived from nitrogen adsorption/desorption data collected on a Micromeritics ASAP 2020. IR spectroscopy was conducted on a Perkin Elmer FT-IR Spectometer Spectrum RX1 using KBr discs and data processed using Spectrum 5.1 software. PXRD was performed on a Bruker DaVinci diffractometer with a Cu Kα radiation (40 kV, 30 mA) source equipped with a VANTEC-1 detector for fast acquisition. The step size was 0.025° and the counting time was 2s for each step and diffraction patterns were recorded in the 2θ range 1.5 ° - 30 °. TGA and DTA were done in a STA 449C analyser from Netzsch under a flow of dried air at 10.00 °C/min up to 650 °C. Argon was also used to protect the balance section. HRTEM was performed on a HD-2700 dedicated STEM from Hitachi, with a cold field emitter, equipped with a CEOS Cs corrector and operated at 200 kV. The powder samples were simply deposited dry onto a Cu grid covered with a carbon film (Quantifoil) having a periodic hole diameter of 1.2 microns. Observation was made in three different modes: BF, HAADF and SE. Impedance spectroscopy was performed with a Princeton Applied Research VersaSTAT 3. A two electrode set-up was constructed and silver wire of length 5 cm was used as the working and counter electrodes and these were attached to each pellet via a silver two part conductive adhesive. Each pellet was made from a 300 mg of sample, ground and formed into pellets using a 25 tonne manual hydraulic press. The flat sides of this pellet were coated using a

silver two part conductive adhesive and for improved structural integrity the edges were partly coated in epoxy resin. Potentiostatic impedance spectra were recorded between 10^6 and 10 Hz using the VersaStudio software and with an amplitude of 100 mV. For analysis the data was exported to ZView. The samples were heated in a sealed sample chamber mounted on an IKA®-Werke GmbH & Co. KG heating mantle with attached temperature probe. Equilibration time at each temperature stage was 20 minutes and the humidity of the sealed sample chamber was held constant throughout at 50 %, measured using a humidity controller and probe. Temperature ramp rate was ca. 5 °C per minute. Pellets of Nafion 117 were created by drying out a sample of Nafion 117 in 5 % aliphatic alcohol and water. The resultant film was diced, ground and pressed as described above for the as-synthesised materials. Cells of Nafion 117 film were created by cutting a circular disk with the same circumference as the pellets from a sheet of Nafion 117 film. To these, wires were attached in the same manner as used for the pellets to complete the cell. An image of the cell attached to the VersaSTAT3 can be found at Figure 7.33. The proton conductivity of each cell was determined as described in Chapter 1.

References

[1] Li. H., Knights. S., Shi. Z., Van Zee. J. W., Zhang. J. (2010). *Proton exchange membrane fuel cells: contamination and mitigation strategies*. CRC Press.

[2] Schmidt-Rohr. K., Chen. Q. (2008). Parallel cylindrical water nanochannels in Nafion fuel-cell membranes. *Nat. Mater., 7*, 75.

[3] Sone. Y., Ekdunge. P., Simonsson. D., (2006). Proton conductivity of nafion 117 as measured by a four-electrode AC impedance method. *J. Electrochem. Soc., 143*, 1254.

[4] Surowiec. J., Bogoczek. R. (1988). Studies on the thermal stability of the perfluorinated cation-

exchange membrane Nafion-417. *J. Therm. Anal. Calorim.*, *33*(4), 1097-1102

[5] Samms. S. R., Wasmus. S., Savinell. S. R. (1996). Thermal stability of Nafion® in simulated fuel cell environments. *J. Electrochem. Soc.*, *143*(5), 1498-1504

[6] Tang. H. L., Pan. Mu. (2008). Synthesis and characterization of a self-assembled Nafion/silica nanocomposite membrane for polymer electrolyte membrane fuel cells *J. Phys. Chem. C.*, *112*(30), 11556–11568

[7] Li. Q., Ronghuan. H., Jensen. J. O., Bjerrun. N. J. (2003). Approaches and recent development of polymer electrolyte membranes for fuel cells operating above 100 °C. *Chem. Mater.*, *15*(26), 4896–4915

[8] Yang. C., Costamagna. P., Srinivasan. S., Benziger. J., Bocarsly. A. B. (2001). Approaches and technical challenges to high temperature operation of proton exchange membrane fuel cells. *J. Power Sources*, *103*(1), 1-9

[9] Yang. B., Manthiram. A., J. (2003). Sulfonated poly(ether ether ketone) membranes for direct methanol fuel cells. *Electrochem. Soc.*, *6*(11), A229-A231

[10] Mahajan. C. V., Ganesan. V. (2010). Atomistic simulations of structure of solvated sulfonated poly(ether ether ketone) membranes and their comparisons to Nafion: II. structure and transport properties of water, hydronium ions, and methanol. *J. Phys. Chem. B*, *114*(25), 8367 – 8373

[11] Dimitrova. P., Friedrich. K. A., Stimming. U., Vogt. B. (2002). Modified Nafion®-based membranes for use in direct methanol fuel cells. *Solid State Ionics*, *150*(1-2), 115-122

[12] Bentoncello. P., Notargiacomo. A., Nicolini. C. (2005). Langmuir−Schaefer films of Nafion with incorporated TiO_2 nanoparticles. *Langmuir*, *21*(1), 172-177

[13] Liu. P., Bandara. J., Lin. Y., Elgin. D., Allard. L. F., Sun. Y.-P. (2002). Formation of nanocrystalline titanium dioxide in perfluorinated ionomer membrane. *Langmuir*, *18*(26), 10398-10401

[14] Battirola. L. C., Schneider. J. F., Torriani. Í. C. L., Tremiliosi-Filho. G., Rodrigues-Filho. U. P. (2013). Improvement on direct ethanol fuel cell performance by using doped-Nafion® 117 membranes with Pt and Pt–Ru nanoparticles. *Int. J. Hydrog. Energy*, *38*, 12060.

[15] Rhee. C. H., Kim, H. K., Chang. K., Lee. J. S. (2005). Nafion/sulfonated montmorillonite composite: a new concept electrolyte membrane for direct methanol fuel cells. *Chem. Mater*., *17*(7), 1691-1697

[16] D'Epifanio. A., Navarra, M. A., Weise. F. C., Mechari. B., Farrington. J., Greenbaum. S. (2010). Composite Nafion/sulfated zirconia membranes: effect of the filler surface properties on proton transport characteristics. *Chem. Mater*., *22*(3), 813-821.

[17] Navarra. M. A., Croce. F., Scrosati. B. (2007). New, high temperature superacid zirconia-doped Nafion™ composite membranes. *J. Mater. Chem., 17*, 3210-3215

[18] Shao. Z.-G., Joghee. P., Hsing. I.-M. (2004). Preparation and characterization of hybrid Nafion–silica membrane doped with phosphotungstic acid for high temperature operation of proton exchange membrane fuel cells. *J. Membr. Sci*., *229*(1-2), 43-51

[19] Buzzoni. R., Bordiga. S., Ricchiardi. G., Spoto. G., Zecchina. A. (1995). Interaction of H_2O, CH_3OH, $(CH_3)_2O$, CH_3CN, and pyridine with the superacid perfluorosulfonic membrane nafion: an IR and Raman study. *J. Phys. Chem*., *99*(31), 11937-11951

[19] Aili. D., Hansen. M. K., Pan. C., Li. Q., Christensen. E., Jensen. J. O., Bjerrum. N. J. (2011). Phosphoric acid doped membranes based on Nafion®, PBI and their blends – Membrane preparation, characterization and steam electrolysis testing. *Int. J. Hydrogen Energy*, *36*(12), 6985-6993

[20] Chang. J.-K., Park. J. H., Park. G.-G., Kim. C.-S., Park. O. O. (2003). Proton-conducting composite membranes derived from sulfonated hydrocarbon and inorganic materials. *J. Power Sources*, *124*(1), 18-25

[21] Pereira. F., Valle. K., Belleville. P., Morin. A., Lambert. S., Sanchez. C. (2008). Advanced mesostructured hybrid silica−Nafion membranes for high-performance PEM fuel cell. *Chem. Mater*., *20*(5), 1710-1718

[22] Muriithi. B., Loy. D. A. (2012). Processing, morphology, and water uptake of Nafion/*ex situ* Stöber silica nanocomposite membranes as a function of particle size. *ACS Appl. Mater. Interfaces*, *4*(12),

6766-6773

[23] Guo. B., Liu. Z., Hong. L. (2011). Doping Nafion® matrix by p-aramid flakes for a proton transport less reliant on moisture. *J. Mater. Chem.*, *21*, 12414-12421

[24] Lin. Y.-F., Yen. C.-Y., Ma. C.-C. M., Liao. S.-H., Lee. C.-H., Hsiao. Y.-H., Lin. H.-P. (2007). High proton-conducting Nafion®/–SO_3H functionalized mesoporous silica composite membranes. *J. Power Sources*, *171*(2), 388-395

[25] Wang. H., Holmberg. B. A., Huang. L., Wang. Z., Mitra. A., Norbeck. J. M., Tan Y. (2002). Nafion-bifunctional silica composite proton conductive membranes. *J. Mater. Chem.*, *12*, 834-837

[26] Hoffmann. F., Cornelius. M., Morell. J., Froba. M. (2006). Silica-based mesoporous organic-inorganic hybrid materials. *Angew. Chem., Int. Ed.*, *45*, 3216-3251

[27] Sayari. A., Hamoudi. S. (2001). Periodic mesoporous silica-based organic−inorganic nanocomposite materials. *Chem. Mater.*, *13*, 3151.

[28] Hobsen. L. J., Ozu. H., Yamaguchi. M., Hayase. S. (2001). Modified Nafion 117 as an improved polymer electrolyte membrane for direct methanol fuel cells. *J. Electrochem. Soc.*, *148*(10), A1185-A1190

[29] Hurd. J. A., Vaidhyanathan. R., Thangadurai. V., Ratcliffe. C. I., Moudrakovski. I. L., Shimizu. G. K. H. (2009). Anhydrous proton conduction at 150 °C in a crystalline metal-organic framework. *Nat. Chem.*, *1*, 705.

[30] Stein Sr. E. W., Clearfield. A., Subramanian. M. A. (1996). Conductivity of group IV metal sulfophosphonates and a new class of interstratified metal amine-sulfophosphonates. *Solid State Ionics*, *83*, 113-124

[31] Jang. M. Y., Park. Y. S., Yamazaki Y. (2003). Preparation, characterization and proton conductivity of layered cerium sulfophenylphosphonate. *Electrochemistry*, *71*, 691

[32] Goesten. M. G., Juan-Alcanitz. J., Ramos-Fernandez. E. V., Gupta. K. B. S. S., Stavitski. E., van Bekkum, H., Gascon. J., Kapteijn. F. (2011). Sulfation of metal–organic frameworks: opportunities for acid catalysis and proton conductivity. *J. Catal.*, *281*(1), 177-187

[33] Antonelli D.M. (1999). Synthesis of phosphorus-free mesoporous titania via templating with amine surfactants. *Microporous Mesoporous Mater*., *30*, 315-319

[34] Bergström. K., Strandberg. C. (2013). *US20130005578 A1*. US Patent and Trademark Office

[35] Wolf. C., Storm. T., Lange. F. T., Reemtsma. T., Brauch. H.-J., Eberle. S. H., Jekel. M. (2000). Analysis of sulfonated naphthalene−formaldehyde condensates by ion-pair chromatography and their quantitative determination from aqueous environmental samples. *Anal. Chem*., *72*, 5466.

[36] Turley. J. P., Romer. F., Trudeau. M. L., Dias. M. L., Smith. M. E., Hanna. J. V., Antonelli. D. M. (2014). Variable temperature proton conductivity of mesoporous titanium oxides doped with naphthalene sulfonate formaldehyde resin. *Microporous Mesoporous Mater*., *190*, 284.

[37] Rao. Y., Kang. J., Antonelli. D. (2007). 1-hexene iomerization over sulfated mesoporous Ta oxide: The effects of active site and confinement. *J. Am. Chem. Soc*., 130, 394.

[38] Rao. Y., Trudeau. M., Antonelli. D. (2006). Sulfated and phosphated mesoporous Nb oxide in the benzylation of anisole and toluene by benzyl alcohol. *J. Am. Chem. Soc*., *128*, 13996–13997.

[39] Antonelli. D. M. (1999). Synthesis of macro-mesoporous niobium oxide molecular sieves by a ligand-assisted vesicle templating strategy. *Microporous Mesoporous Mater*., *33*, 209-214

[40] Vettraino. M., Trudeau. M., Lo. A. Y. H., Schurko. R. W., Antonelli. D. (2002). Room-temperature ammonia formation from dinitrogen on a reduced mesoporous titanium oxide surface with metallic properties. *J. Am. Chem. Soc*., *124*, 9567.

[41] Antonelli. D. M., Ying. J. Y. (1996). Synthesis and characterization of hexagonally packed mesoporous tantalum oxide molecular sieves. *Chem. Mater*., *8*, 874.

[42] Rao. Y., Antonelli. D. M. (2009). Mesoporous transition metal oxides: characterization and applications in heterogeneous catalysis. *J. Mater. Chem*., *19*, 1937-1944

[43] Silva. R. F., De Francesco. M., Pozio. A. (1996). Tangential and normal conductivities of Nafion® membranes used in polymer electrolyte fuel cells. *J. Power Sources*, *134*, 18.

[44] Maréchal. M., Souquet. J.-L., Guindet. J., Sanchez. J.-Y. (2007). Solvation of sulphonic acid groups in Nafion® membranes from accurate conductivity measurements. *Electrochem. Commun*., *9*, 1023.

Chapter 4: Niobium composite formation via in situ polymerisation techniques

Proton conductivity and thermal durability studies were performed on a series of mesoporous Nb_2O_5 (mNb_2O_5) composites with naphthalene sulfonate formaldehyde resin polymerised within the pores. The proximity of the sulfonate groups of the polymer to the walls of the oxide mesostructure was deliberately tailored to ensure superior dehydration resistance crucial to proton conductivity. Initially characterised by nitrogen adsorption, XRD, TGA and STEM, subsequent study using impedance spectroscopy over a temperature range of 20 - 150 °C established their proton conductivity performance. The most promising sample displayed a conductivity of 21.77 ± 0.01 mS cm^{-1} at 80 °C surpassing the literature value for Nafion 117 (*ca.* 8 mS cm^{-1}) as measured in our labs using the same set up. Subsequent thermal durability tests demonstrated that this composite maintains superior conductivity to Nafion 117 at 80 °C for the length of the study (24 hours).

Introduction

Fuel cell membrane materials are currently being sought with improved physical properties and conductivities able to withstand the operating systems of the fuel cell over a wide humidity range.[1] The temperature window for optimal proton conducting performance in a PEMFC begins at 80 °C and for this reason the membrane material of choice must have a similar working temperature coupled with high durability over as wide a range of conditions as possible.[2] Nafion is the current industrial standard material used for this application, but has certain limitations in this regard. While Nafion conducts

protons at room temperature with high efficiency[3] due to proton hopping along the vast network of water molecules trapped within the Nafion matrix,[4] as the temperature rises, conductivity decreases as the membrane begins to dehydrate, jeopardizing the proton conducting network such that proton mobility becomes increasingly compromised.[5,6] Consequently there have been numerous efforts to stabilize the Nafion structure to water loss at higher temperature. Attempts include the incorporation of silica[7,8] or transition metal oxide[9–11] nanoparticles within the matrix. Alternatively, Nafion has also been doped with heteropolyacids[12,13] or blended with polymers to form composite membranes,[14] with both approaches yielding varied results. Completely replacing Nafion with periodic mesoporous organosilicates,[15,16] mesoporous silica[17,18] metal organic frameworks[19,20] or other polymers[21,22] has yielded encouraging results, but, nothing has yet replaced Nafion as the commercially viable option. In recent years, DuPont have also developed a thinner Nafion membrane with better longevity and tensile strength[23] and whilst this improves efficiency, the primary concerns still remain.

Aim

For these reasons our research group has looked into developing alternatives to Nafion more resilient to dehydration and less reliant on weakly-bound water molecules to transfer protons across the membrane. The systems we have focused on[24, 25] exploit the 700-900 m^2g^{-1} surface area and *ca.* 20 Å pore walls of mesoporous Nb oxide (mNb_2O_5) as a means of anchoring organosulfonate groups to the pore-wall interface, which is inherently resistant to moisture loss because of the high Lewis acidity of the Nb centers, and may also provide an alternative conduction pathway along the Nb-O-Nb backbone

running through the wall. Thus, by impregnating the mNb_2O_5 pores with NSF resin, an oligomer with an average molecular mass between 400 and 1000 g mol^{-1} consisting of 2-6 units,[26,27] we were able to create a new class of composite materials in which proton conduction can be maintained at higher temperatures where dehydration is a problem for Nafion 117. Whilst these NSF-impregnated Nb oxides demonstrated conductivity values at 80 ºC surpassing Nafion 117 (21.96 ± 0.01 mS cm^{-1}),[25] as the temperature approaches 150 ºC the performance drops to 0.170 ± 0.01 mS cm^{-1}. Using solid-state NMR techniques, it was shown that the NSF oligomers become more mobile at higher temperatures due to increasing local motion of the molecules, which leads to pore leaching and subsequent loss of conductivity.

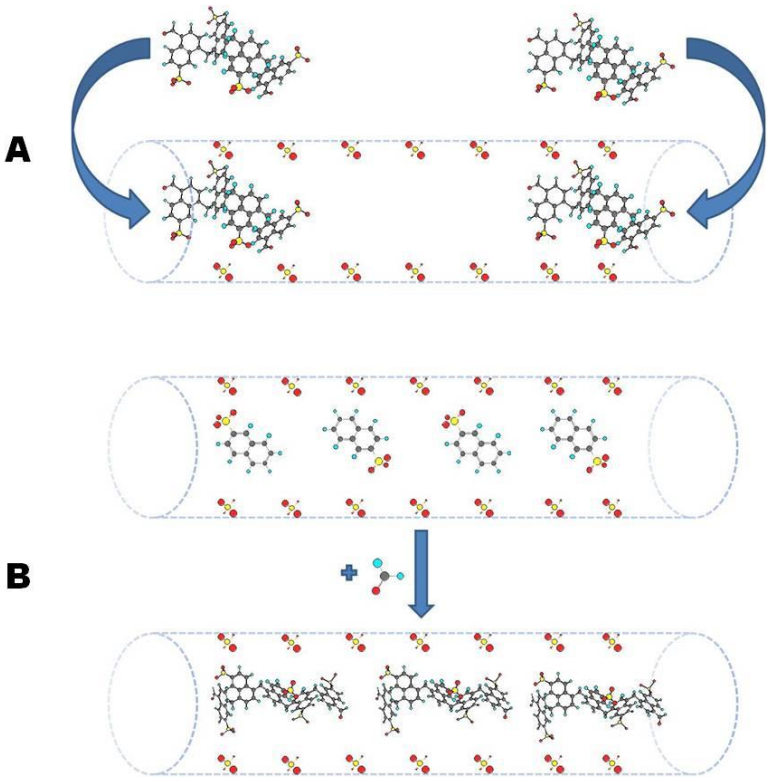

Figure 4.1: From top to bottom: (A) mesopore showing impregnation with NSF oligomer; (B) mesopore showing impregnation with NSA monomer and condensation *in situ* via formaldehyde.

It was also concluded that the oligomer likely does not fully penetrate the pore structure and instead remains close to the pore windows, where it is more prone to thermal leaching. For this reason either a longer oligomer is sought, which would likely be an ineffective strategy due to increased molecular mass leading to further exacerbation of diffusion problems through the small 20 Å pore windows, or a method of initiating polymerisation directly within the mesopores must be developed. This latter method is particularly attractive because the synthesis of NSF can be accomplished in two simple steps from naphthalene: the sulfonation of the fused aromatic followed by the condensation of the naphthalene sulfonic acid product with formaldehyde. By stopping at the second stage and impregnating the pore with the much smaller monomer naphthalene sulfonic acid, we can affect condensation *in situ* of the mesopore to not only ensure maximum penetration, but to lock the polymer in place and decrease the chances of any potential leaching (Figure 4.1B). This strategy should also ensure that the proton network is maintained at higher temperatures for a longer period and thus offer superior conductivity performance at operating temperatures as a function of time.

Results and Discussion

Previous research[25] from our group established that mesoporous niobium oxide doped with sulfuric acid and subsequently impregnated with NSF oligomers possesses an improved proton conductivity (21.96 ± 0.01 mS cm^{-1}) with respect to Nafion 117 at 80 °C (*ca.* 8 mS cm^{-1}) under controlled humidity conditions.[28] However, this composite shows gradual loss of conductivity at temperatures over 80 °C due to leaching of the NSF out of the 20 Å pores. With the goal of fabricating materials with similar proton conductivity,

but improved thermal stability, four new composites were synthesised using the new *in situ* polymerisation technique outlined schematically in Figure 1B. The first two composites ($mNb_2O_5(SO_4)$-NSF and mNb_2O_5-NSF) were synthesised with and without sulfuric acid doping prior to solution impregnation of naphthalene sulfonic acid (NSA) monomer and condensed using two molar equivalents of formaldehyde with respect to NSA *in situ* to drive polymerisation within the pores. The second pair of composites followed the same synthesis pattern, but with an additional 10 % NSA added during the formaldehyde condensation stage ($mNb_2O_5(SO_4)$-NSF(110%) and mNb_2O_5-NSF(110%)). This additional 10% NSA was experimentally determined over a range of 5-50 % as the optimal amount required to further improve proton conductivity and mechanical stability of the composites, possibly by ensuring bridging conductivity pathways throughout the pores and between adjacent grains by cohesion of polymer to external surface sites. These as-synthesized materials were prepared as per the details provided in the Experimental Section and fully characterised using the parameters described below.

Surface analysis. BET surface areas for the as-synthesised materials are reported in Table 4.1. The nitrogen adsorption/desorption isotherms for composites mNb_2O_5-NSF, $mNb_2O_5(SO_4)$-NSF and $mNb_2O_5(SO_4)$-NSF(110%) are shown in Figure 4.3 while that for composite mNb_2O_5-NSF(110%) is displayed in Figure 4.4. For comparison, the isotherm for pristine mNb_2O_5 is displayed in Figure 4.2. In all cases the composites display isotherms on the cusp between type I and IV, as expected for mesoporous composites synthesized from host materials with a *ca.* 20-30 Å pore size, with a sharp rise at high relative pressure in the case of mNb_2O_5-NSF indicative of textural porosity. However, the

negative values and low total adsorption of the composite isotherms due to pore filling suggest low surface areas and limit the degree of useful interpretation from these data. Indeed, the mNb_2O_5 starting material possesses an expected high surface area of 516 $m^2 g^{-1}$, which decreases when the material is doped and impregnated to *ca.* 10.0 $m^2 g^{-1}$ in each of the four composites, suggesting successful impregnation of the mesopores.

Table 4.5

Nitrogen adsorption data for mNb_2O_5 materials

	BET Surface Area / $m^2 g^{-1}$	Pore Volume / $cm^{-3} g^{-1}$	BJH Pore Size / Å
mNb_2O_5	516.9	0.249	24.8
mNb_2O_5-NSF	9.9	0.015	16.9
$mNb_2O_5(SO_4)$-NSF	11.1	0.007	17.7
mNb_2O_5-NSF(110%)	14.3	0.014	17.1
$mNb_2O_5(SO_4)$-NSF(110%)	9.3	0.006	17.1

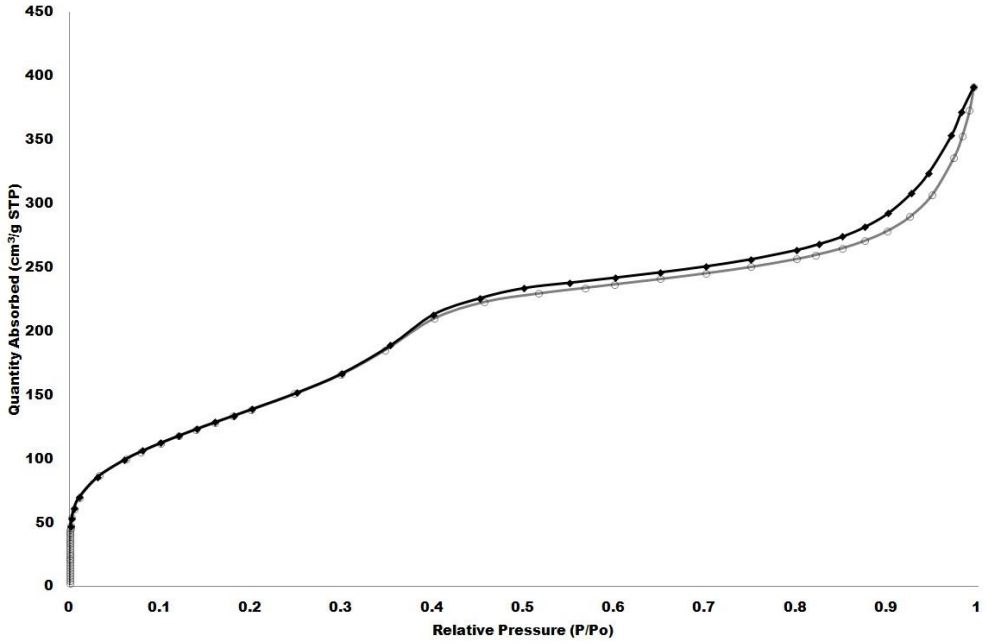

Figure 4.2: Nitrogen adsorption (diamonds)/desorption (circles) isotherms for mNb_2O_5

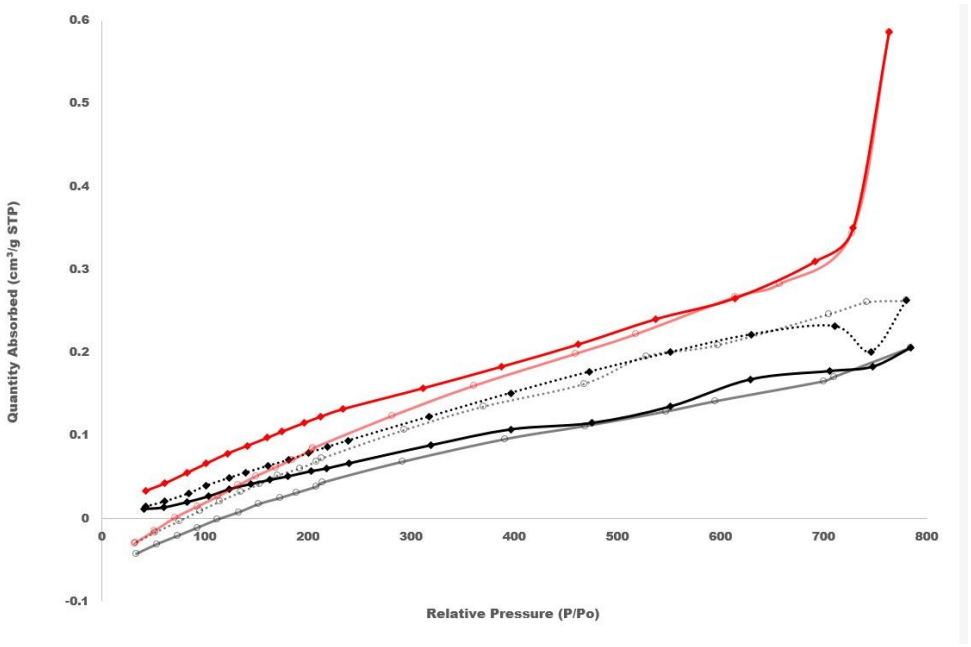

Figure 4.3: Nitrogen adsorption (diamonds)/desorption (circles) isotherms for $mNb_2O_5(SO_4)$-NSF (black), $mNb_2O_5(SO_4)$-NSF(110%) (black dots), mNb_2O_5-NSF (red). Negative values are an artifact caused by low total adsorption due to low surface area and the limited size of the sample chamber.

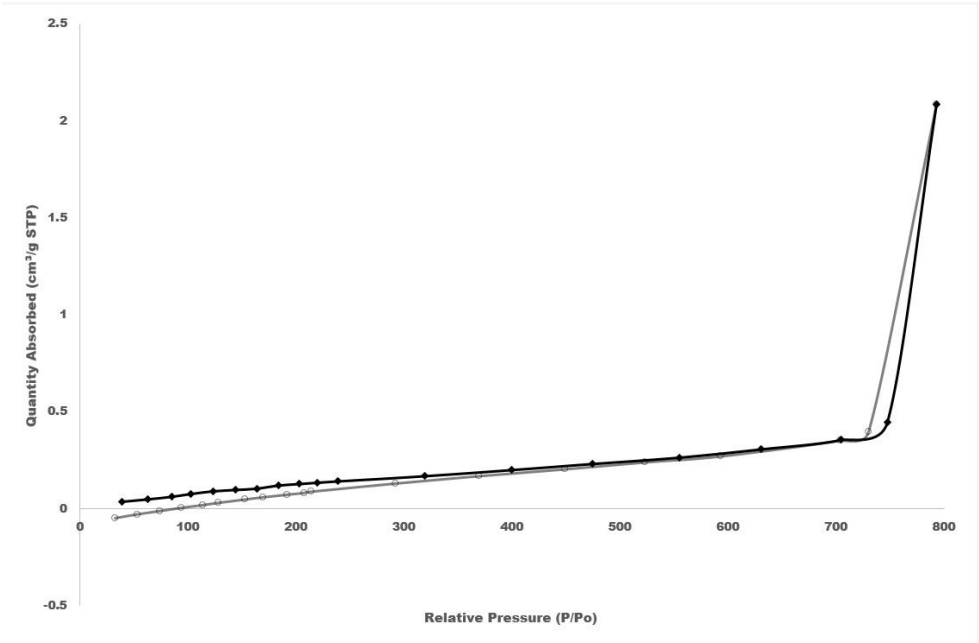

Figure 4.4: Nitrogen adsorption (diamonds)/desorption (circles) isotherms for mNb_2O_5-NSF(110%). Negative values are an artifact caused by low total adsorption due to low surface area and the limited size of the sample chamber.

Infrared spectroscopy. The IR spectra further support impregnation with NSF in all cases, with the spectra for the composites, and pristine mNb_2O_5 shown on Figure 4.5. Pure NSF resin gives rise to an aromatic C-H stretch at *v* 2900 cm^{-1} and aromatic ring vibration modes at *v* 1640 cm^{-1}, *v* 1596 cm^{-1} and *v* 1507 cm^{-1}, which are all apparent in all NSF treated samples. The NSF SO stretch and S-phenyl vibrations observed at *v* 1230 cm^{-1}, *v* 1190 cm^{-1}, *v* 1130 cm^{-1} and *v* 1040 cm^{-1} are also evident in the composites. There are also C-H stretches at *v* 2800 cm^{-1} for the NSF methylene protons and trace amounts of residual hydrocarbon in the mNb_2O_5. The C-H stretches in each material appear at varying intensities, suggesting different loading levels of polymer.

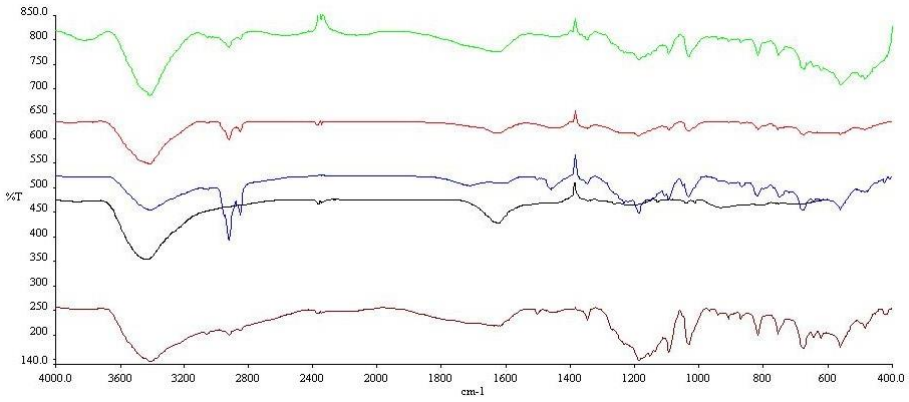

Figure 4.5: IR spectra of mNb_2O_5 (black), mNb_2O_5-NSF (blue), $mNb_2O_5(SO_4)$-NSF (red), $mNb_2O_5(SO_4)$-NSF(110%) (green), mNb_2O_5-NSF(110%) (brown)

Thermal analysis. Since IR intensities can vary due to sample preparation, the percentage of hydrocarbon was further probed by TGA and DTA as shown in Figures 4.6 through to 4.8. For all samples, the thermogravimetric curves show an initial *ca.* 10% weight loss between 100 °C and 150 °C, which can be attributed to a loss of residual water within the system. Further weight loss occurs between *ca.* 250 °C and 450 °C, due

to the combustion of hydrocarbon from the NSA and residual octadecylamine template. This is confirmed by the overlying DTA curve, which displays an endothermic peak at 130 °C assigned to loss of water and two exothermic peaks at 350 and 500 °C attributable to hydrocarbon combustion. Weight loss of *ca.* 5 % at 390 °C is also expected from the loss of the sulfonate groups, whilst NSF hydrocarbon is burnt off the sample at 485 °C. Continued weight loss above *ca.* 550 °C is attributed to further loss of water by condensation of Nb-OH groups as the mesostructure begins to collapse. From the TGA traces composites mNb_2O_5-(SO_4)-NSF and mNb_2O_5-NSF(110%) demonstrate a total weight loss of *ca.* 42 %, while mNb_2O_5(SO_4)-NSF (110%) and mNb_2O_5-NSF show a total weight loss of *ca.* 45 %. These similar amounts of hydrocarbon indicate there is no disparity between the synthetic approach nor the additional NSA added during condensation with regards to total weight. However, the DTA traces display a pattern possibly attributable to moisture retention whereby the composites without sulfate doping exhibit three exothermic peaks below 100 °C, whilst those with sulfate doping exhibit minor endothermic peaks instead.

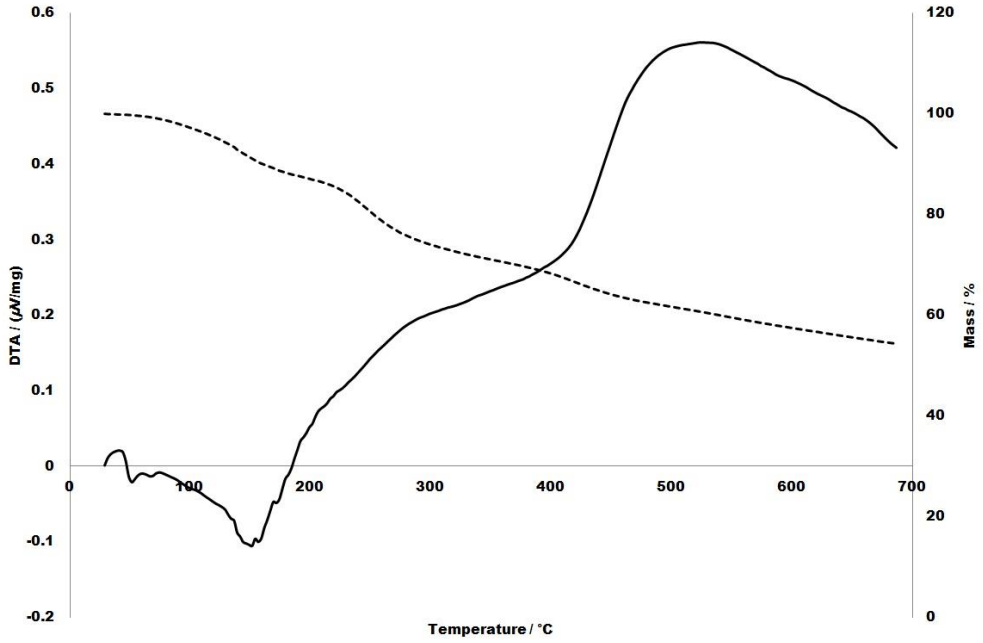

Figure 4.625: TGA (dots) and DTA (line) curve for $mNb_2O_5(SO_4)$-NSF

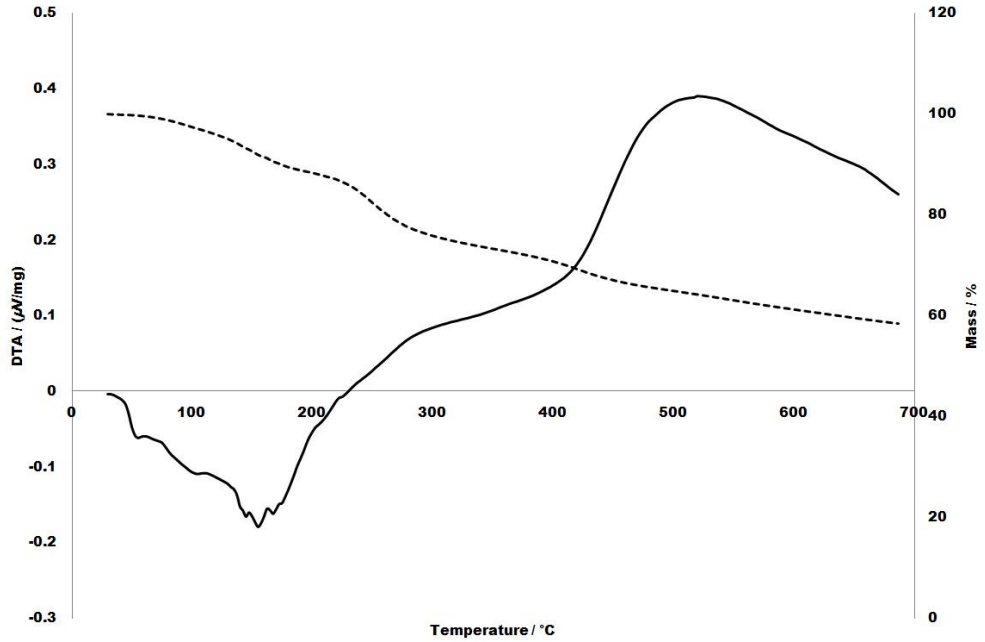

Figure 4.7: TGA (dots) and DTA (line) curve for $mNb_2O_5(SO_4)$-NSF(110%)

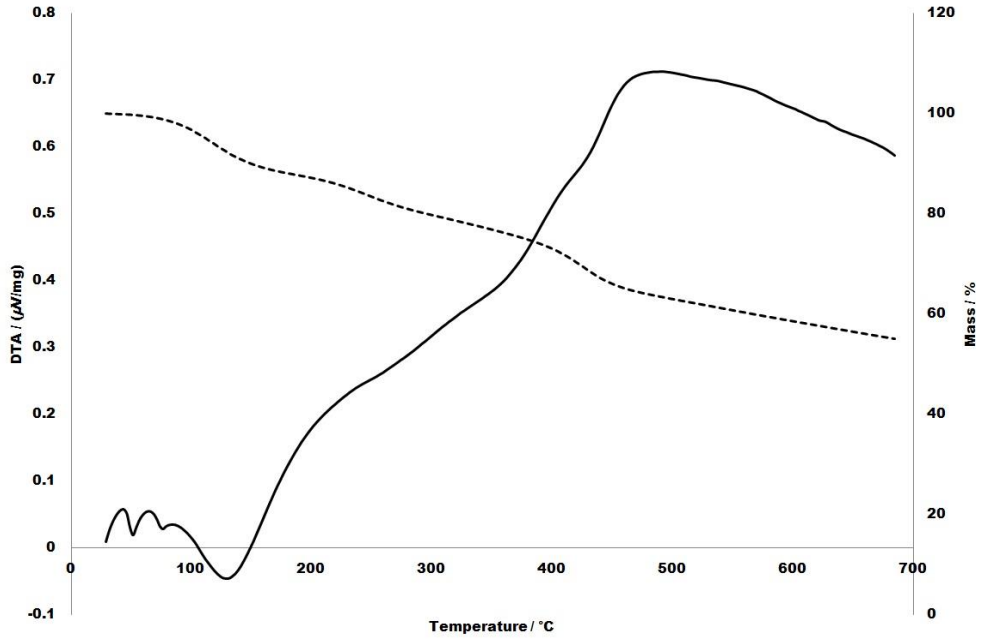

Figure 4.8: TGA (dots) and DTA (line) curve for mNb_2O_5-NSF(110%)

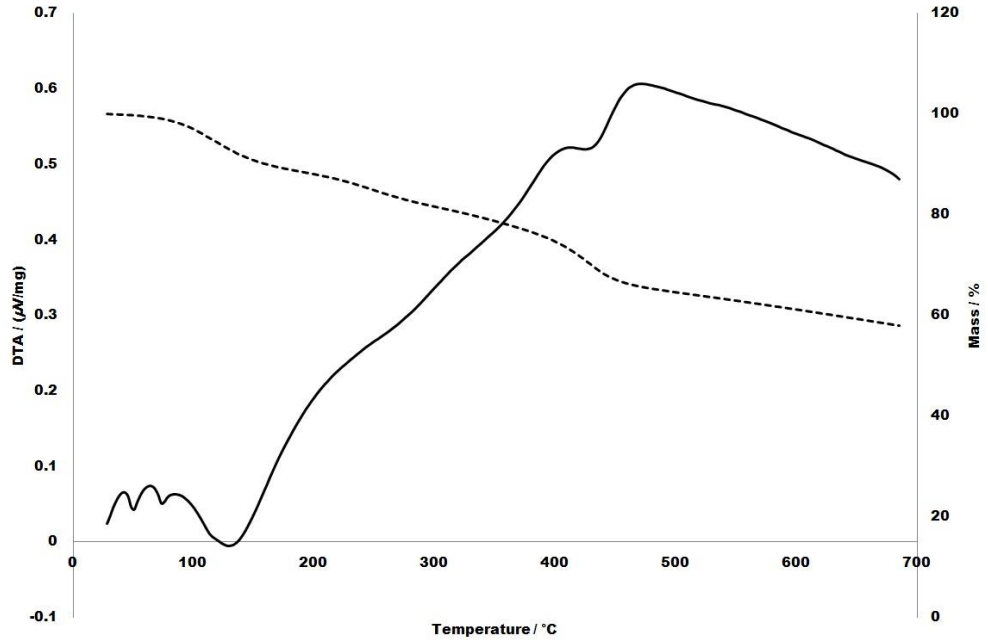

Figure 4.9: TGA (dots) and DTA (line) curve for mNb_2O_5-NSF

Powder x-ray diffraction. The PXRD patterns for the as-synthesised materials are shown in Figure 4.10. All patterns are similar with broad reflections partially obscured by the beam between 2.4° and 3.2° 2θ, indicative of a wormhole mesoporous structure and consistent with our previous data.[29] The remaining reflections between 15° and 35° 2θ arise from partial crystallisation of the walls in the structure.

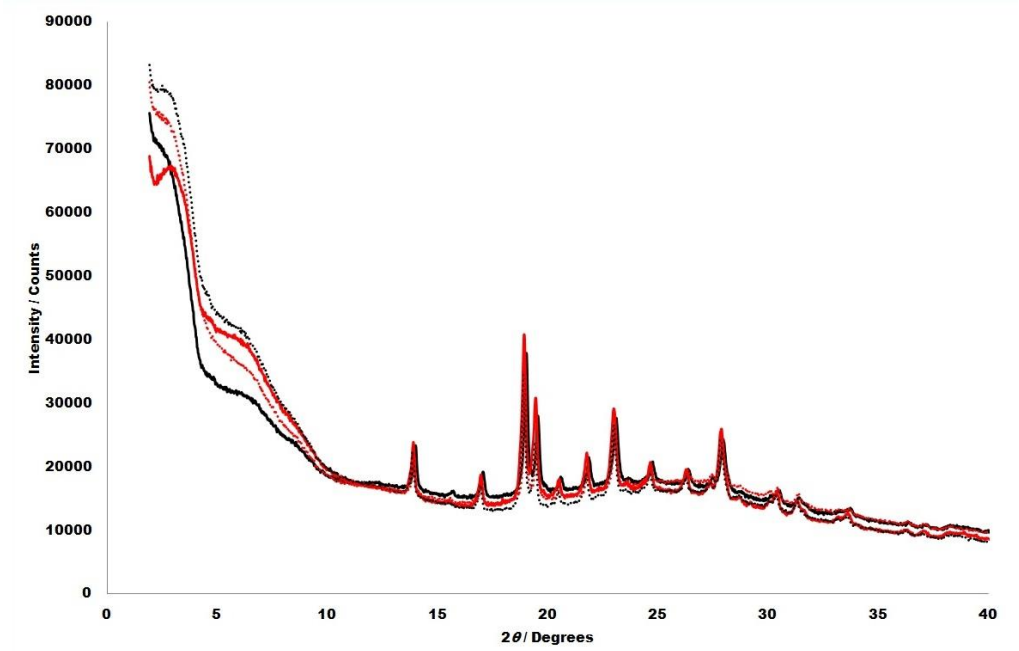

Figure 4.10: PXRD patterns for $mNb_2O_5(SO_4)$-NSF (black line), $mNb_2O_5(SO_4)$-NSF(110%) (red line), mNb_2O_5-NSF(110%) (black dots), mNb_2O_5-NSF (red dots)

Scanning transmission electron microscopy. To further probe the powder morphology and pore structure of the as-synthesised materials, STEM was performed with the images of the as-synthesised materials exhibited in Figures 4.11 through to 4.14. All ihe images were recorded with scale bars between 50 and 10 nm, and show the expected wormhole-like structure typical for mesoporous materials synthesised with non-ionic templates. From this, a pore size of *ca.* 20-30 Å in diameter can be derived, as

expected from the parent mNb_2O_5 host, with pore walls *ca.* 20 Å in thickness. This corresponds to what is expected on the basis of the PXRD data and is in agreement with previous work on amine templated composites.[30] Following impregnation of the pores with NSF and/or doping of the pore wall mesostructure with H_2SO_4 it becomes increasingly difficult to image either the mesopores, possibly due to the filling of the pores by the NSF or mesostructure degradation due to the effect of H_2SO_4 and/or the sulfonate protons on the oxide structure of the walls. This is consistent with the PXRD results, and combined with the BET, IR, and TGA data, these data confirm that the composite synthesis was completed in all cases with at least partial retention of a 20-30 Å amorphous pore structure.

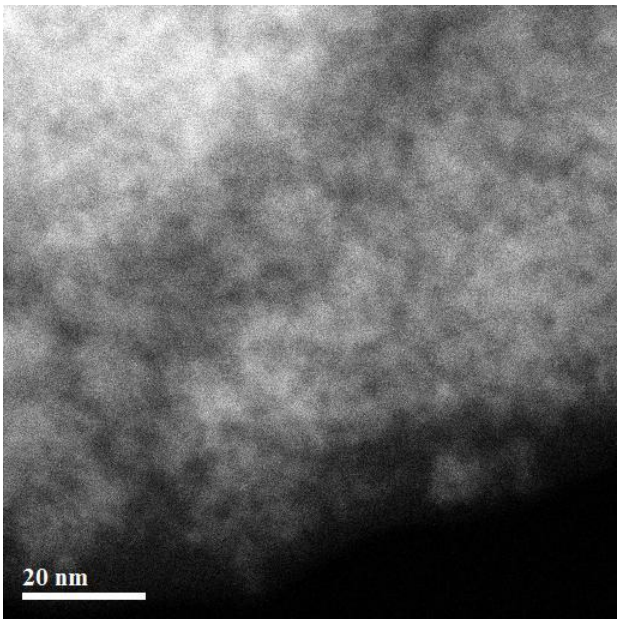

Figure 4.11: STEM image displaying the pore structure of $mNb_2O_5(SO_4)$-NSF

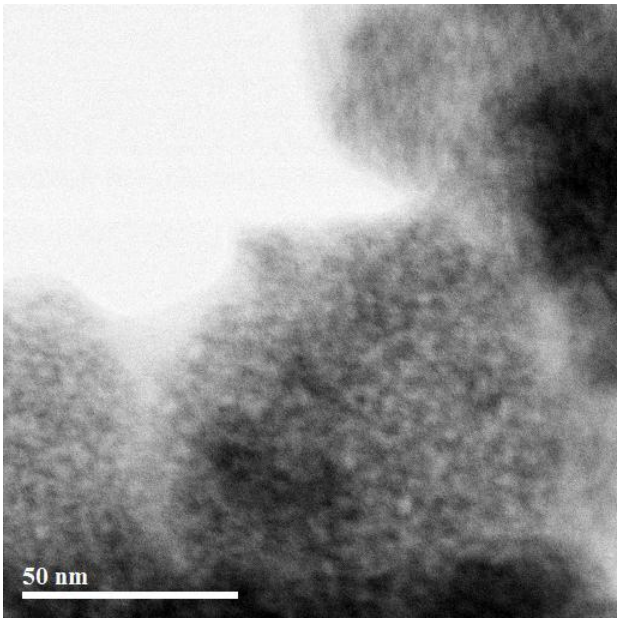

Figure 4.12: STEM image displaying the pore structure of $mNb_2O_5(SO_4)$-NSF(110%)

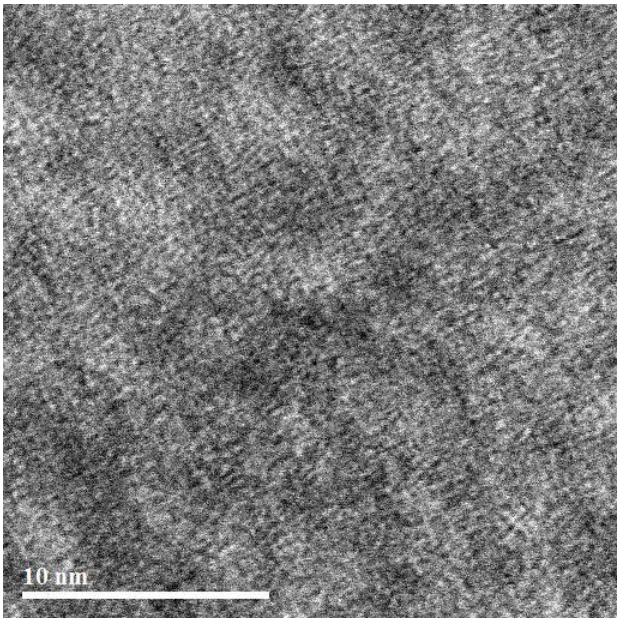

Figure 4.13: STEM image displaying the pore structure of mNb_2O_5-NSF(110%)

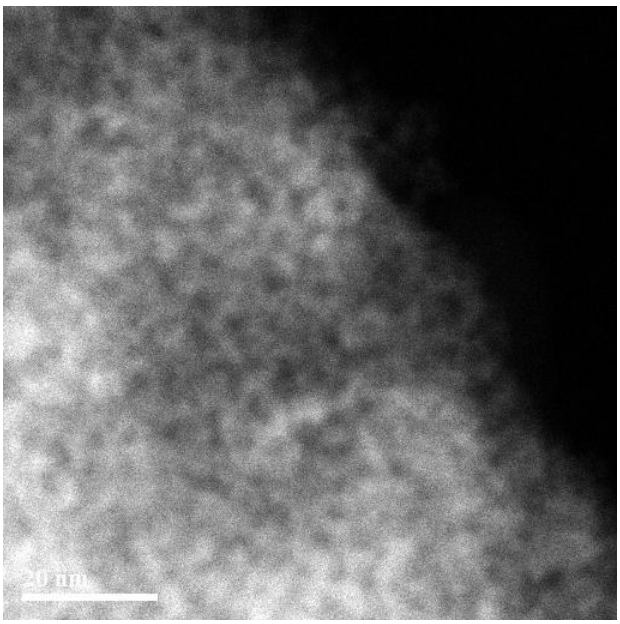

Figure 4.14: STEM image displaying the pore structure of mNb_2O_5-NSF

Electrochemical impedance spectroscopy. As described in the characterisation section, a sample of each composite was made into a cell and the impedance recorded at 20 °C. The measurement was repeated every ten degrees up to 150 °C and compared to a reference commercial film of Nafion 117 prepared as a pellet in analogous form to the composite cells. While Nyquist plots commonly show a complete semi-circle, the straight lines acquired at low resistance in our measurements of Nafion represent portions of a larger semi-circle and are similar in overall appearance to those reported by other groups for this material.[31] The entire suite of the averaged impedance data and calculated standard error is shown in Table 4.2 and the relevant Nyquist plots are displayed in Figures 7.18 through to 7.32. From this data we generated a plot of $Log_{10}\sigma$ versus temperature (Figure 4.15) showing the conductivity of each pellet in relation to both the Nafion 117 film and pellet. While both Nafion samples gradually become more resistive

as temperature increases, with values from the film in close agreement with the literature,[31] the NSF composites becomes more conductive up to a peak at ~80 °C before gradually falling as the temperature is further increased to 150 °C, at which temperature the resistivities are broadly similar to the Nafion samples. This is consistent with our previous data[24,25] and like the previous data, the conductivity of Nafion is surpassed in all cases by the NSF composites at 80 °C, with the new composite $mNb_2O_5(SO_4)$-NSF(110%) displaying the highest performance and thus, being the most promising for further membrane applications (Figure 4.15, black dashes).

Table 4.6

Average proton conductivity and associated error (mS cm^{-1}) of the as-synthesised materials. N/A denotes where the Nyquist Plot is too erratic to derive a proton conductivity.

Temperature / °C	mNb_2O_5-NSF	$mNb_2O_5(SO_4)$-NSF	mNb_2O_5-NSF(110%)	$mNb_2O_5(SO_4)$-NSF(110%)
20	0.076±0.01	0.537±0.01	0.071±0.01	0.316±0.01
25	0.354±0.01	1.647±0.01	0.048±0.01	0.514±0.02
30	0.325±0.01	0.760±0.02	0.076±0.01	0.424±0.04
40	0.439±0.01	0.905±0.02	0.654±0.01	1.372±0.03
50	0.680±0.06	1.525±0.01	1.220±0.07	3.392±0.01
60	0.515±0.03	5.418±0.01	1.034±0.06	8.807±0.01
70	1.652±0.04	6.279±0.12	3.035±0.01	21.81±0.01
80	2.074±0.01	9.324±0.08	4.538±0.01	21.77±0.01
90	1.249±0.01	6.184±0.12	3.834±0.01	13.79±0.01
100	0.405±0.01	4.912±0.01	1.762±0.01	3.260±0.01
110	0.120±0.01	1.773±0.02	0.678±0.01	1.068±0.01
120	0.021±0.01	0.791±0.01	0.236±0.01	0.189±0.02
130	0.013±0.01	0.415±0.07	0.139±0.02	N/A
140	N/A	0.165±0.01	0.157±0.01	0.184±0.01
150	N/A	0.117±0.07	0.040±0.01	N/A

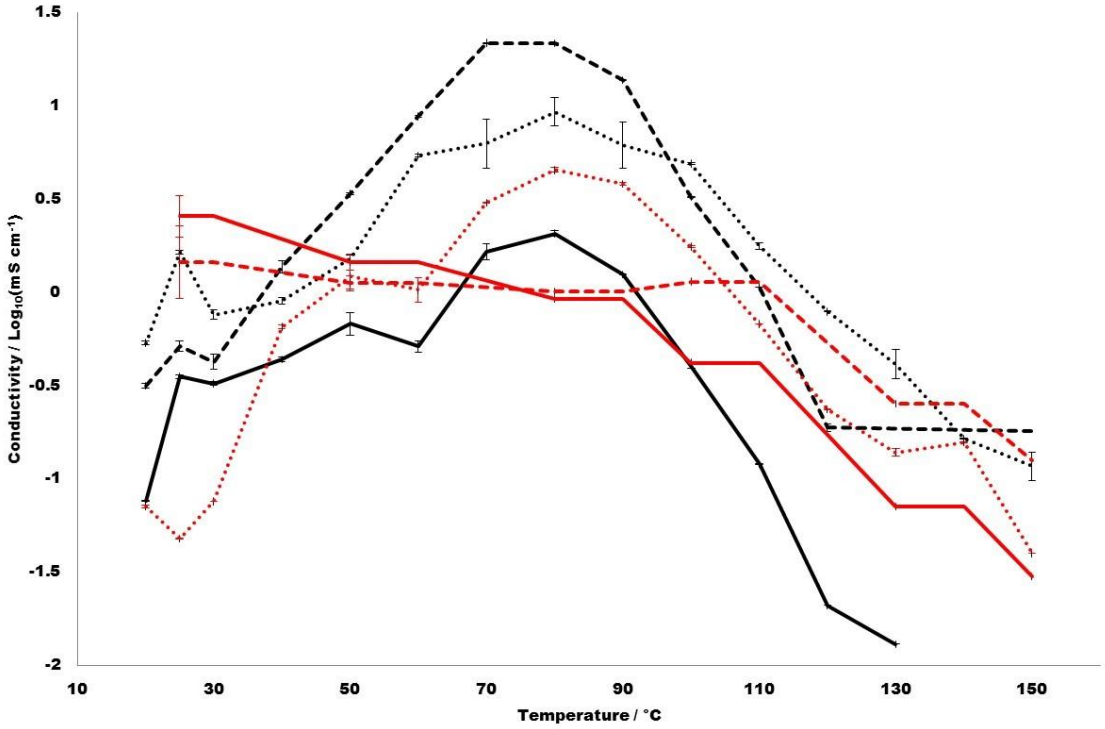

Figure 4.15: Average proton conductivities as a function of temperature of mNb_2O_5-NSF (black line), $mNb_2O_5(SO_4)$-NSF synthesised by *in situ* polymerisation (black dots), $mNb_2O_5(SO_4)$-NSF(110%) (black dashes), mNb_2O_5-NSF(110%) (red dots), Nafion 117 film (red line), Nafion 117 pellet (red dashes).

At 25 °C a proton conductivity of 0.514 ± 0.02 mS cm^{-1} was recorded, which compares to the Nafion 117 film value under these conditions (2.57 ± 0.12 mS cm^{-1}). This increases to 21.77 ± 0.01 mS cm^{-1} at 80 °C before falling to 0.18 ± 0.01 mS cm^{-1} at 150 °C (the Nafion 117 film possesses values of 0.93 ± 0.31 and 0.03 ± 0.02 mS cm^{-1} at 80 °C and 150 °C, respectively). Compared to the C_{12}-$mNb_2O_5(SO_4)$-NSF composite formed via direct polymer impregnation,[25] the differences are negligible and show that the high conductivity has been maintained using the new polymerisation protocol, establishing that effective proton conducting pathways were formed using *in situ* condensation of the polymer.

In order to explore stability of proton conductivity over time at the peak temperature the thermal durability of the best composite prepared by the new method, $mNb_2O_5(SO_4)$-NSF(110%), as well as C_{12}-$mNb_2O_5(SO_4)$-NSF prepared by the previous method of NSF oligomer solution doping, and both Nafion references were explored by heating fresh pellets to 80 °C and then maintaining this temperature for 24 hours (Table 4.1). Impedance was recorded at set times intervals of 0, 1, 2, 4, 8 and 24 hours, with the results compiled and plotted on a graph of $Log_{10}\sigma$ versus time (Figure 4.16) and from this data, we see that the conductivity of each sample decreases at different rates over time. With Nafion 117, at 80 °C the conductivity has already decreased from that at room temperature (8.356 ± 0.11 mS cm^{-1})[31] from dehydration and this trend continues over 24 hours at 80 °C as the matrix further dehydrates. By comparison, $C_{12}mNb_2O_5(SO_4)$-NSF begins with a conductivity of 19.02 ± 0.01 mS cm^{-1}, which drops by more than half after one hour to 8.514 ± 0.04 mS cm^{-1}. After two hours the conductivity has further dropped to 5.96 ± 0.02 mS cm^{-1} and then to 1.34 ± 0.01, 0.22 ± 0.01 and 0.03 ± 0.01 mS cm^{-1} after 4, 8 and 24 hours respectively. Thus, despite a high initial conductivity, after four hours the conductivity falls below that of the Nafion 117 film. This change is consistent with the previous observation, corroborated by solid state NMR, that NSF leaching begins at this temperature,[25] which results in a reduction in the cooperative conductivity-enhancing effect between the oxide walls and the NSF.

In contrast, composite $mNb_2O_5(SO_4)$-NSF(110%) begins with a conductivity of 17.39 ± 0.08 mS cm^{-1} at 80 °C, which only decreases slightly after one hour to 14.02 ± 0.03 mS cm^{-1} and then to 11.15 ± 0.07, 7.314 ± 0.01, 2.717 ± 0.03,

0.272 ± 0.01 mS cm^{-1} for 2, 4, 8 and 24 hours, respectively. Not only does this durability surpass composites synthesized via the direct impregnation technique, but it surpasses both Nafion standards in conductivity over a 24 hour period, maintaining a six fold advantage over the Nafion 117 film for as long as eight hours. This result can be rationalized by the improved penetration and/or oligomer chain length produced by the new protocol resulting in superior stability to leaching, however in order to further establish the underlying reason for this improved performance, or any other hidden structure-property relationships, solid-state NMR studies were conducted. Finally, reported error is within acceptable parameters for these experiments and remains consistent throughout.

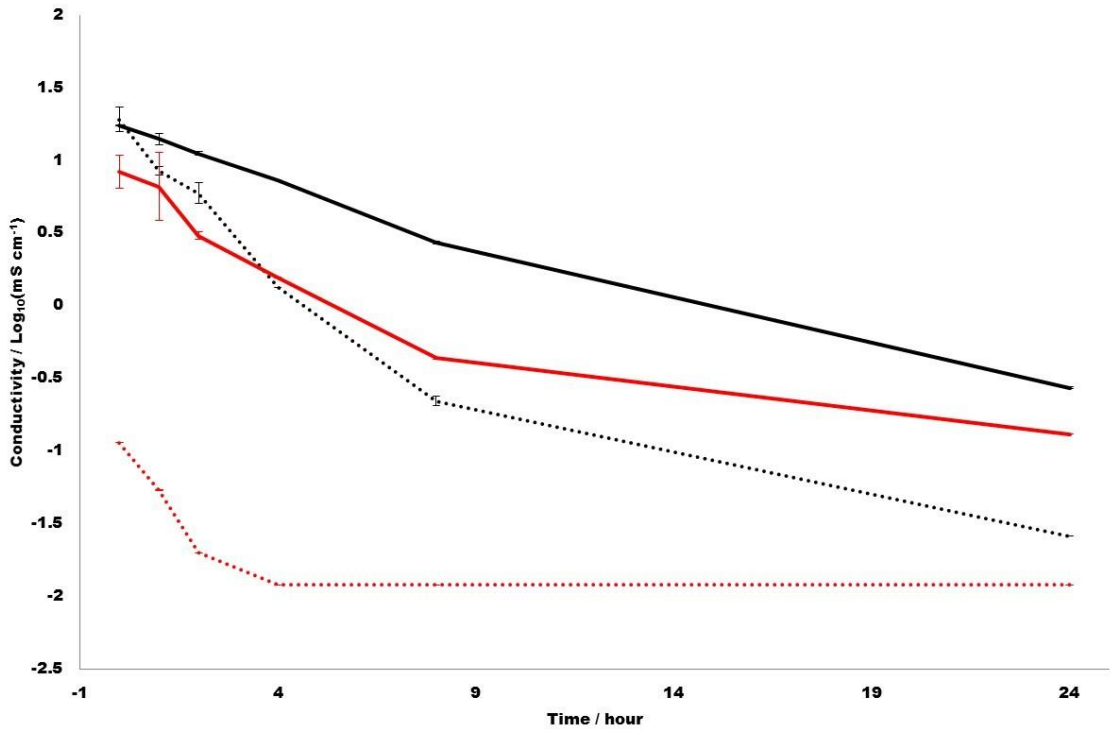

Figure 4.16: Average proton conductivity as a function of time at 80 °C of $mNb_2O_5(SO_4)$-NSF(110%) (black line), C_{12}-$mNb_2O_5(SO_4)$-NSF synthesised by direct oligomer impregnation (black dots), Nafion 117 film (red line) and Nafion 117 pellet (red dots)

Table 4.7

Average proton conductivity and associated error (mS cm^{-1}) of the best-performing composites and Nafion 117 references at 80°C, over a period of 24 hours

Time / hours	C_{12}-m$Nb_2O_5(SO_4)$-NSF	m$Nb_2O_5(SO_4)$-NSF(110%)	Nafion 117 film	Nafion 117 pellet
0	19.02±0.08	17.39±0.01	8.356±0.11	0.114±0.01
1	8.514±0.03	14.02±0.03	6.606±0.24	0.054±0.01
2	5.959±0.07	11.15±0.02	3.030±0.03	0.020±0.01
4	1.336±0.01	7.314±0.01	1.560±0.01	0.012±0.01
8	0.220±0.03	2.717±0.01	0.436±0.01	0.012±0.01
24	0.026±0.01	0.272±0.01	0.131±0.01	0.012±0.01

Conclusions

In this chapter, the *in situ* synthesis of a new series of mesoporous Nb oxide NSF composites is reported. The object of this research was to develop a new method of retarding degradation of proton conductivity through polymer leaching observed in previously studied materials, which otherwise showed promising performance relative to Nafion 117. This was achieved through an *in situ* polymerisation technique, which allows superior penetration of NSF oligomers within the pore structure giving improved thermal durability of conductivity over a larger time span. Thus, the conductivity of all samples were recorded as a function of temperature under controlled humidity and compared versus that of Nafion 117. Whilst all composites surpassed Nafion 117 at the operating temperature for PEMFCs, the most promising sample, m$Nb_2O_5(SO_4)$-NSF(110%) possessed and maintained a much higher conductivity for a longer period than a commercially procured Nafion 117 film, holding a six fold edge in this regard after as long as eight hours, and a two-fold advantage after 24 hours. While these results are extremely encouraging, further research is required to increase the durability and to

fabricate a membrane using this system whilst maintaining the high conductivities presented herein.

Experimental Section

All chemicals were purchased from either Sigma Aldrich or Alfa Aesar and used without further purification.

***m*Nb_2O_5.** Mesoporous niobium oxide was prepared according to the published procedure using ligand assisted amine templating[32] Thus, water (75 ml) was added to a homogeneous 4:1 solution of niobium (V) ethoxide (10 g) and octadecylamine (2.5 g) to form a white gel, which was left to stand for 24 hours. The water was then decanted and a second portion of water (75 ml) was added followed by three drops of 12 M HCl. The resultant solution was stirred and left to stand for 24 hours before transfer to an oven at 40 °C. After 48 hours the temperature was increased to 60 °C, and after an additional 48 hours the temperature was increased again to 80 °C, after which the solid was collected by filtration, air dried for 24 hours at 80 °C, placed into a sealed sample tube and returned to an oven at 100 °C for an additional 48 hours. The ageing process was continued at 120 °C for 48 hours and then at 140 °C for a final 48 hours. Removal of the organic template was initiated by combing the white to beige solid with pTSA (3.2 g) in methanol followed by stirring for 24 hours. After collecting by filtration the material was combined with additional pTSA (2.5 g) and stirred once more with methanol for 24 hours. This process was completed with three subsequent filtrations and washings with methanol.

$mNb_2O_5(SO_4)$. One drop of H_2SO_4 was added to distilled water (0.5 ml) in a vial and left to stand for 5 minutes. To this solution mNb_2O_5 (0.5 g) was added, and the vial sealed and stirred for 48 hours. Finally, the sample was dried in an oven at 80 °C for 24 hours to evaporate the water and dry the solid.

$mNb_2O_5(SO_4)$-NSA/mNb_2O_5-NSA. After grinding to a fine powder, the mesoporous host ($mNb_2O_5(SO_4)$/mNb_2O_5, 0.83 g) was added to a 2:3 mixture of naphthalene sulfonic acid (NSA) (1.25 g) and diethyl ether (DEE, 1.25 g), and this mixture was stirred for an additional 48 hours and then dried in an oven at 80 °C for 24 hours.

$mNb_2O_5(SO_4)$-NSF/mNb_2O_5-NSF. To a sample of $mNb_2O_5(SO_4)$-NSA/mNb_2O_5-NSA (0.25 g), two equivalents of 35 wt% aqueous formaldehyde (0.173 ml, ratio of 0.9 with respect to total NSA) were added to a sealed container for 24 hours. This was subsequently dried at 80 °C for 24 hours.

$mNb_2O_5(SO_4)$-NSF(110%)/mNb_2O_5-NSF(110%). To a sample of $mNb_2O_5(SO_4)$-NSA/mNb_2O_5-NSA (0.25 g), two equivalents of 35 wt% aqueous formaldehyde (0.173 ml, ratio of 0.9 with respect to total NSA) and further NSA (0.015 g, 10 % total NSA content) were added to a sealed container for 24 hours. This was subsequently dried at 80 °C for 24 hours.

Characterisation section. BET surface area data were derived from nitrogen adsorption/desorption data collected on a Micromeritics ASAP 2020. IR spectroscopy was conducted on a Perkin Elmer FT-IR Spectometer Spectrum RX1 using KBr discs and data processed using Spectrum 5.1 software. PXRD was performed on a Bruker DaVinci

diffractometer with a Cu Kα radiation (40 kV, 30 mA) source equipped with a VANTEC-1 detector for fast acquisition. The step size was 0.025° and the counting time was 2 s for each step and diffraction patterns were recorded in the 2θ range 1.5° - 30°. TGA and DTA were performed in a STA 449C analyser from Netzsch under a flow of dried air at 10.00 °C/min up to 650 °C. Argon was also used to protect the balance section. HRTEM was performed on a HD-2700 dedicated STEM from Hitachi, with a cold field emitter, equipped with a CEOS Cs corrector and operated at 200 kV. The powder samples were simply deposited dry onto a Cu grid covered with a carbon film (Quantifoil) having a periodic hole diameter of 1.2 microns. Observation was made in three different modes: BF, HAADF and SE.

EIS was performed with a Princeton Applied Research VersaSTAT 3. A two electrode set-up was constructed and silver wire of length 5 cm was used as the working and counter electrodes and these were attached to each pellet via a silver two part conductive adhesive. Each pellet was made from a 300 mg of sample, ground and formed into pellets using a 25 tonne manual hydraulic press. The flat sides of this pellet were coated using a silver two part conductive adhesive and for improved structural integrity the edges were partly coated in epoxy resin. Potentiostatic impedance spectra were recorded between 106 and 10 Hz using the VersaStudio software and with an amplitude of 100 mV. For analysis the data was exported to ZView. The samples were heated in a sealed sample chamber mounted on an IKA®-Werke GmbH & Co. KG heating mantle with attached temperature probe. Equilibration time at each temperature stage was 20 minutes and the humidity of the sealed sample chamber was held constant throughout

at 50 %, measured using a humidity controller and probe. The temperature ramp rate was *ca*. 5 °C per minute. Pellets of Nafion 117 were created by drying out a sample of Nafion 117 in 5 % aliphatic alcohol and water. The resultant film was diced, ground and pressed as described above for the as-synthesised materials. Cells of Nafion 117 film were created by cutting a circular disk with the same circumference as the pellets from a sheet of Nafion 117 film. To these, wires were attached in the same manner as used for the pellets to complete the cell. An image of the cell attached to the VersaSTAT 3 is shown in Figure 7.33. The proton conductivity of each cell was determined as described in Chapter 1.

References

[1] Neburchilov. V., Martin. J., Wang. H., Zhang. J. (2007). A review of polymer electrolyte membranes for direct methanol fuel cells. *J. Power Sources*, *169*, 221.

[2] Barbir. F. (2013). *PEM Fuel Cells: Theory and Practice*, Academic Press.

[3] Sone. Y., Ekdunge. P., Simonsson. D., (2006). Proton conductivity of nafion 117 as measured by a four-electrode AC impedance method. *J. Electrochem. Soc*., *143*, 1254.

[4] Schmidt-Rohr. K., Chen. Q. (2008). Parallel cylindrical water nanochannels in Nafion fuel-cell membranes. *Nat. Mater*., *7*, 75.

[5] Li. Q., He. R., Jensen J. O., Bjerrum. N. J. (2003). Approaches and recent development of polymer electrolyte membranes for fuel cells operating above 100 °C. *Chem. Mater*., *15*, 4896.

[6] Yang. C., Costamagna. P., Srinivasan. S., Benziger. J., Bocarsly. A. B. (2001). Approaches and technical challenges to high temperature operation of proton exchange membrane fuel cells. *J. Power Sources*, *103*, 1.

[7] Tang. H., Wan. Z., Pan. M., Jiang. S. P. (2007). Self-assembled Nafion–silica nanoparticles for elevated-high temperature polymer electrolyte membrane fuel cells. *Electrochem. Commun.*, *9*,

2003.

[8] Pan. J., Zhang. H., Pan. M. (2008). Self-assembly of Nafion molecules onto silica nanoparticles formed in situ through sol–gel process. *J. Colloid Interface Sci*., *326*, 55.

[9] Bertoncello. P., Notargiacomo. A., Nicolini. C. (2005). Langmuir−Schaefer films of Nafion with incorporated TiO_2 nanoparticles. *Langmuir*, *21*, 172.

[10] Liu. P., Bandara. J., Lin. Y., Elgin. D., Allard. L. F., Sun. Y.-P. (2002). Formation of nanocrystalline titanium dioxide in perfluorinated ionomer membrane. *Langmuir*, *18*, 10398.

[11] Battirola. L. C., Schneider. J. F., Torriani. Í. C. L., Tremiliosi-Filho. G., Rodrigues-Filho. U. P. (2013). Improvement on direct ethanol fuel cell performance by using doped-Nafion® 117 membranes with Pt and Pt–Ru nanoparticles. *Int*. *J*. *Hydrog*. *Energy*, *38*, 12060.

[12] Ramani. V., Kunz. H. R., Fenton. J. M. (2005). Stabilized heteropolyacid/Nafion® composite membranes for elevated temperature/low relative humidity PEFC operation. *Electrochimica Acta*, *50*, 1181.

[13] Staiti. P., Aricò. A. S., Baglio. V., Lufrano. F., Passalacqua. E., Antonucci. V. (2001). Hybrid Nafion–silica membranes doped with heteropolyacids for application in direct methanol fuel cells. *Solid State Ion*., *145*, 101.

[14] Nouel. K. M, Fedkiw. P. S. (1998). Nafion®-based composite polymer electrolyte membranes. *Electrochimica Acta*, *43*, 2381.

[15] Sayari. A., Hamoudi. S. (2001). Periodic mesoporous silica-based organic−inorganic nanocomposite materials. *Chem*. *Mater*., *13*, 3151.

[16] Hoffmann. F., Cornelius. M., Morell. J., Fröba. M. (2006). Silica-based mesoporous organic-inorganic hybrid materials. *Angew*. *Chem*. *Int*. *Ed*., *45*, 3216.

[17] Wang. H., Holmberg. B. A., Huang. L., Wang. Z., Mitra. A., Norbeck. J. M., Yan. Y. (2002). Nafion-bifunctional silica composite proton conductive membranes. *J*. *Mater*. *Chem*., *12*, 834.

[18] Lin. Y.-F., Yen. C.-Y., Ma. C.-C. M., Liao. S.-H., Lee. C.-H., Hsiao. Y.-H., Lin. H.-P. (2007). High proton-conducting Nafion®/–SO_3H functionalized mesoporous silica composite membranes. *J*.

Power Sources, *171*, 388.

[19] Liang. X., Zhang. F., Feng. W., Zou. X., Zhao. C., Na. H., Liu. C., Sun. F., Zhu. G. (2013). From metal–organic framework (MOF) to MOF–polymer composite membrane: enhancement of low-humidity proton conductivity. *Chem. Sci*., *4*, 983.

[20] Hurd. J. A., Vaidhyanathan. R., Thangadurai. V., Ratcliffe. C. I., Moudrakovski. I. L., Shimizu. G. K. H. (2009). Anhydrous proton conduction at 150 °C in a crystalline metal-organic framework. *Nat. Chem*., *1*, 705.

[21] Nunes. S. P., Ruffmann. B., Rikowski. E., Vetter. S., Richau. K. (2002). Inorganic modification of proton conductive polymer membranes for direct methanol fuel cells. *J. Membr. Sci*., *203*, 215.

[22] Soboleva. T., Xie. Z., Shi. Z., Tsang. E., Navessin. T., Holdcroft. S. (2008). Investigation of the through-plane impedance technique for evaluation of anisotropy of proton conducting polymer membranes. *J. Electroanal. Chem*., *622*, 145.

[23] Roelofs. M. G., Choudhury. B., Siddiqui. J. A., Banerjee. S. (2012). *WO2012174463 A1*. US Patent and Trademark Office

[24] Turley. J. P., Romer. F., Trudeau. M. L., Dias. M. L., Smith. M. E., Hanna. J. V., Antonelli. D. M. (2014). Variable temperature proton conductivity of mesoporous titanium oxides doped with naphthalene sulfonate formaldehyde resin. *Microporous Mesoporous Mater*., *190*, 284.

[25] Turley. J. P., Romer. F., Trudeau. M. L., Dias. M. L., Smith. M. E., Hanna. J. V., Antonelli. D. M. (2015). Proton conductivity of naphthalene sulfonate formaldehyde resin-doped mesoporous niobium and tantalum oxide composites. *ChemSusChem*., *8*, 301.

[26] Wolf. C., Storm. T., Lange. F. T., Reemtsma. T., Brauch. H.-J., Eberle. S. H., Jekel. M. (2000). Analysis of sulfonated naphthalene−formaldehyde condensates by ion-pair chromatography and their quantitative determination from aqueous environmental samples. *Anal. Chem*., *72*, 5466.

[27] Bergström. K., Strandberg. C. (2013). *US20130005578 A1*. US Patent and Trademark Office

[28] Maréchal. M., Souquet. J.-L., Guindet. J., Sanchez. J.-Y. (2007). Solvation of sulphonic acid groups in Nafion® membranes from accurate conductivity measurements. *Electrochem. Commun*., *9*, 1023.

[29] Vettraino. M., Trudeau. M., Lo. A. Y. H., Schurko. R. W., Antonelli. D. (2002). Room-temperature ammonia formation from dinitrogen on a reduced mesoporous titanium oxide surface with metallic properties. *J. Am. Chem. Soc*., *124*, 9567.

[30] Antonelli. D. M., Ying. J. Y. (1996). Synthesis and characterization of hexagonally packed mesoporous tantalum oxide molecular sieves. *Chem. Mater*., *8*, 874.

[31] Silva. R. F., De Francesco. M., Pozio. A. (1996). Tangential and normal conductivities of Nafion® membranes used in polymer electrolyte fuel cells. *J. Power Sources*, *134*, 18.

[32] Rao. Y., Kang. J., Antonelli. D. (2007). 1-hexene iomerization over sulfated mesoporous Ta oxide: The effects of active site and confinement. *J. Am. Chem. Soc*., 130, 394.

[33] Schuster. M., Kreuer. K. D., Steininger. H., Maier. J. (2008). Proton conductivity and diffusion study of molten phosphonic acid H_3PO_3. *Solid State Ionics*, *179*, 523.

Chapter 5: Analysis of Structure and Proton Conducting Pathways via Solid State NMR

With the synthesis of the composite system and its proton conducting properties established, a number of questions still remain unanswered. This chapter focuses on in depth solid state nuclear magnetic resonance (NMR) experiments which were used to characterise, investigate, and rationalise the physical properties of the composites discussed in the previous chapters.

Introduction

Solid state NMR spectroscopy is an extremely useful and informative tool in identifying and characterising local environments in materials, even in those that lack long-range order.[1] As such, it has been widely applied in modern fundamental and applied science, medicine, and industry. Its role is particularly valuable in materials chemistry due to the capability of solid state NMR to rapidly solve tasks connected with structural descriptions of complex systems on macro and/or molecular levels, and the identification of the dynamics often responsible for the mechanical properties of complex systems. The analysis uses electron spin interactions with an applied electromagnetic field, with the proximity, orientation and types of bond present within the structure all producing specific types of interactions. In many cases, NMR is a uniquely applicable method for measurement of porosity, particularly for porous systems containing partially filled pores or for dual-phase systems. Studies of solids by NMR relaxation experiments can be summed up with the following general statements: 1) the experimental decay of macroscopic transverse or longitudinal magnetisation follows the exponential law for

complete domination of the spin-diffusion mechanism, with a single relaxation time to characterise all of the nuclei in rigid solids (even those that are not chemically or structurally equivalent); 2) the spin-diffusion mechanism is typical of systems with nuclei experiencing strong dipolar interactions (protons, fluorine or phosphorous nuclei at relatively small concentrations of paramagnetic centres); 3) or other nuclei with weak dipolar coupling and/or at high concentration of paramagnetic centers, relaxation tends to be non-exponential.

In the more condensed solid phase, the NMR spectra of a certain material are much less clear then for respective gas and liquid samples. They typically experience the following three types of interactions: 1) chemical shift anisotropy, 2) quadropolar, and 3) dipolar interactions. These lead to the broadening of spectra making them harder to interpret and lower the resolution High resolution images of solid state NMR spectra are often achieved using magic angle spinning (MAS) NMR. These experiments enhance the mobility of the nuclei and facilitate the averaging of interactions observed providing a clearer picture of the interactions taking place. This gives a better report on the chemical shift of the interactions taking place, and the local environment for each resonance. A typical ^{13}C cross polarised (CP) MAS NMR spectrum will contain resonances with an average width of 0.5 – 2 ppm. Quadrupolar interactions can produce line widths of up to 1000 ppm, but these types of interactions are very well suppressed by the effects of MAS. Solid state NMR can also provide useful information concerning proton mobility within conducting polymers on the molecular level[2,3] because it is able to probe the local chemical environments. Such information is helpful to give a deeper understanding of the

observed differences in proton conductivity in various materials. MAS is used routinely to achieve high resolution of ^{1}H NMR spectra in the solid state. Since dipolar interactions can reveal the relative mobility, methods which can retrieve information about the dipolar interaction removed by magic angle spinning are desirable.

Oxygen is a key chemical element and solid state ^{17}O NMR can provide unique insight into the local environment and its structural role in a wide range of materials and molecules.[4–6] The large chemical shift range of ^{17}O produces high sensitivity to even subtle differences in the structure. The major problem with ^{17}O NMR is the low natural abundance of the NMR-active ^{17}O isotope (0.037 %) and subsequent poor sensitivity, which can be overcome by even modest enrichment of the material (e.g., using 20 % in the precursor material).[4,5] In the compounds where solid state NMR was originally observed (namely zeolites and ceramic superconductors), ^{17}O tends to have quite large quadrupole interactions (C_Q) so that even fast MAS only causes partial narrowing of the resonances. More recent studies have shown that resolution between different sites is often easier for other materials as ^{17}O actually has a very wide chemical shift range.[7,8] Hence, MAS causes significant line narrowing, producing very high resolution spectra which are extremely sensitive to the local structure. To overcome this, a new technique was developed in 1995. Multiple quantum (MQ) MAS, in which experiments are performed on the half-integer quadrupole spin, is an echo experiment involving transitions between non-consecutive energy levels during the excitation of the spin system by the first pulse. This method has proved applicable for the study of natural samples, where isotopic enrichment is impossible, or for materials where enrichment may

be difficult is envisaged.[9] A recent ^{17}O NMR study on Nb-TMS1[10] showed its walls are exclusively constructed of ONb_2 linkages, which is very unusual as all other ^{17}O NMR data reported on niobia have shown a mixture of ONb_2 and ONb_3 environments.[10,11] This suggests that the amine template may play a role in suppressing the formation of ONb_3 units, which would represent an unprecedented example of a structure directing agent not only templating the formation of a pore structure, but also the discrete local structure.

Characterisation

The ^{1}H MAS NMR data for the Ti analogues are shown on Figure 5.1. The ^{1}H MAS NMR data from NSF is characterised by a prominent narrow resonance observed at δ 3-4 ppm which is attributed to the mobile/loosely attached solvated sulfonic acid proton (henceforth referred to as the mobile proton species), and much broader resonances found in the δ 6-8 ppm region which are associated with the more immobile and dipolar bound naphthalene protons.

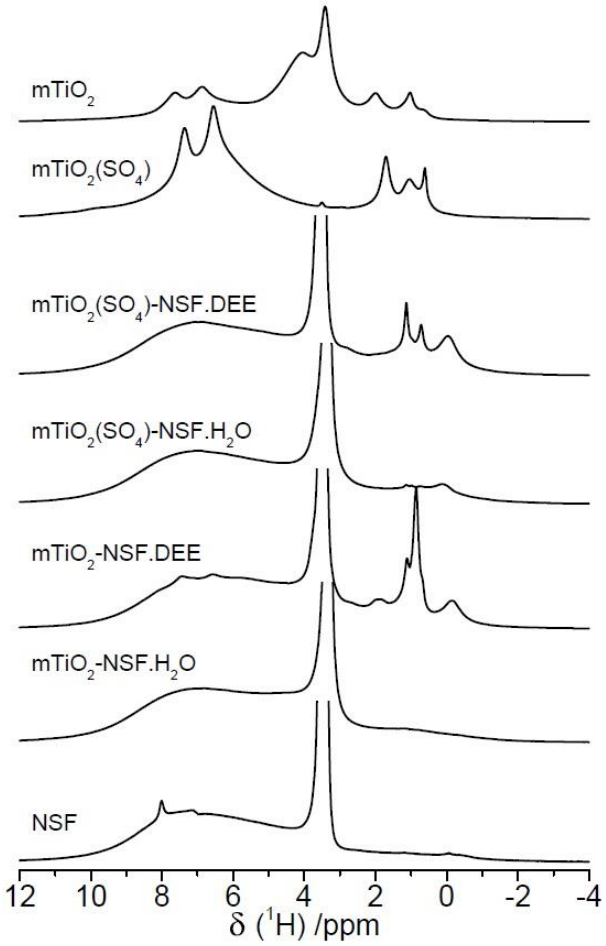

Figure 5.1: ^{1}H MAS NMR data for the commercially acquired NSF and the Ti analogues

These characteristic ^{1}H resonances are also observed in the range of $mTiO_2$ composites, which indicates that NSF has been successfully impregnated within the framework surfaces of these mesoporous systems. The $mTiO_2$ sample doped with sulphuric acid ($mTiO_2(SO_4)$) lacks all forms of mobile proton species and is particularly devoid of surface adsorbed water and hydroxyl species, although some aliphatic (δ 0 – 2 ppm) and aromatic (δ 6 – 8 ppm) resonances are observed due to the residual presence of template in the structure. In contrast, the $mTiO_2$ spectrum exhibits a variety of both

surface hydroxyl and water moieties in addition to those resonances associated with the template. The corresponding ^{13}C CPMAS NMR data for the Ti analogues are shown in Figure 5.2.

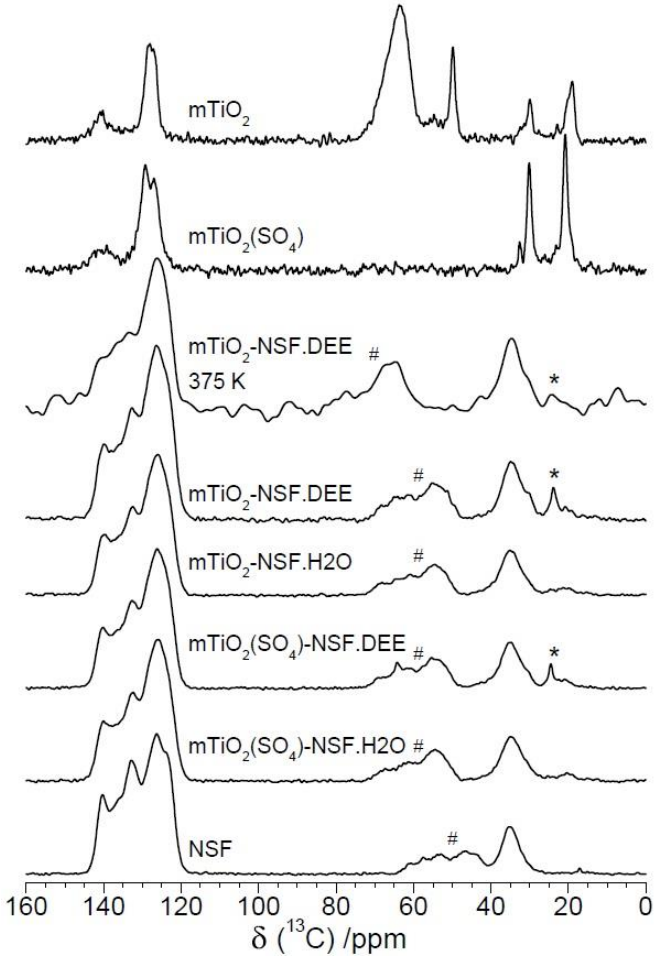

Figure 5.2: ^{13}C CPMAS NMR data for the commercially acquired NSF and Ti analogues

In analogous fashion to the ^{1}H MAS NMR data, the ^{13}C CPMAS NMR data clearly demonstrates that the NSF speciation remains unchanged throughout its incorporation within the different composite systems, and in particular the reproducibility of the δ 35 ppm bridging methylene resonance establishes that the degree of

polymerisation remains intact throughout. The resonances at δ 25 ppm and δ 30 ppm show evidence of some residual DEE solvation from the preparative routes for the $mTiO_2$-NSF.DEE and $mTiO_2(SO_4)$-NSF.DEE preparations. In marked contrast, the resonances observed in the ^{13}C CPMAS NMR data from the $mTiO_2$ and $mTiO_2(SO_4)$ composite originate from residual dodecylamine template and pTSA.

As depicted in Figure 5.3, the ^{1}H MAS NMR data acquired at ambient/room temperature (ca. 20 °C) and at 115 °C of NSF inserted into mTa_2O_5 and mNb_2O_5 metal oxide frameworks have common features. The group of resonances spanning the δ ~6 – 8 ppm range is consistent with NSF aromatic protons possibly engaged in a weak hydrogen bonding arrangement. The resonances at δ ~1 ppm represent aliphatic hydrogen species presumably associated with the methylene linkage, while the narrow resonance at δ ~5 ppm in the room temperature spectra is consistent with physisorbed H_2O; this is noticeably absent in the 115 °C data due to sample dehydration at this temperature. A close inspection of these ^{1}H MAS NMR data shows that the ^{1}H linewidths are extremely temperature dependent, with significantly narrowed resonances being measured at higher temperatures.

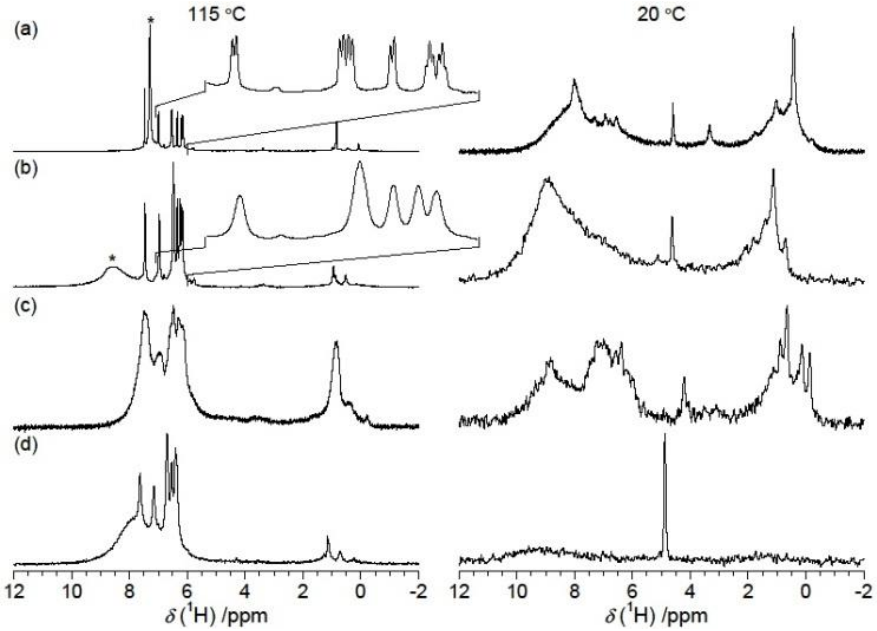

Figure 5.3: ^{1}H MAS NMR data at a) 115 °C and b) 25 °C for C_6-m$Ta_2O_5(SO_4)$-NSF.DEE (A), C_{12}-m$Ta_2O_5(SO_4)$-NSF.DEE (B), C_{18}-m$Ta_2O_5(SO_4)$-NSF.DEE (C) and C_{12}-m$Nb_2O_5(SO_4)$-NSF.DEE (D)

Furthermore, the degree of temperature-driven line narrowing is also influenced by the metal oxide pore size. The C_{12}-mTa_2O_5-NSF system possesses the smallest average pore size of ca. 28 Å (because the composite pore sizes are inaccurate due to the low BET surface areas, the pore sizes stated in this section are those of the precursor metal oxides; i.e., C_{12}-mTa_2O_5 in this case from Table 3.1. From the PXRD data in this study, the pore structure is not destroyed in these more robust systems upon composite formation and the 115 °C data shown in Figure 3a exhibits extremely narrow aromatic ^{1}H resonances within the δ ~6 – 8 ppm region which possess linewidths of <4 Hz. This degree of resolution has allowed $^{1}J(^{1}H,^{1}H)$ and some $^{2}J(^{1}H,^{1}H)$ multiplet structure to be observed. In this region an additional narrowed resonance at δ 7.2 ppm (marked with an asterisk) is observed which exhibits a linewidth of $\Delta\nu$ = 25 Hz; this resonance is assigned

to the mobile sulfonate proton species responsible for initiating ^{1}H conduction. The corresponding room temperature data for this system (Figure 5.3b) shows that all resonances have become broadened due to the lack of ^{1}H motion facilitating exchange that induces this line narrowing.

As the metal oxide pore size increases the fast conduction properties become diminished as evidenced by the ^{1}H MAS NMR data of Figure 3b. The C_6-mTa_2O_5-NSF system possesses an increased pore size of ca. 34 Å (C_6-mTa_2O_5, Table 3.1) and the reduced ^{1}H conduction properties at high temperature (115 °C) are subsequently manifest by increased ^{1}H linewidths for all species. In addition, the resonance assigned to the mobile sulfonate proton species has become significantly broadened by approximately a factor of >10 to a linewidth of $\Delta\nu$ = 300 Hz, and it has shifted downfield to δ 8.5 ppm. This apparent deshielding of the sulfonate proton suggests that the average residence time of this ^{1}H species is increasingly displaced from the notional –SO_3H moiety, thus becoming increasingly delocalised on the mTa_2O_5 pore surface. Furthermore, the other NSF aromatic and aliphatic proton species will also be contributing to the conduction process, with the overall ^{1}H conduction mechanism being defined by a complex interplay between the –SO_3H moiety, the NSF aromatic and aliphatic proton species, and the mTa_2O_5 pore characteristics. The C_{18}-mTa_2O_5-NSF system is consistent with this trend; it possesses the largest pore size of ca. 39 Å (C_{18}-mTa_2O_5, Table 3.1) however the observed motional narrowing is minimal and the sulfonate ^{1}H resonance has become exchange broadened beyond detection. This implies that the larger mTa_2O_5-NSF distance

hinders/slows the proton motional exchange rate to the point where the exchange frequency is now on the order of the ^{1}H NMR experiment.

The C_{12}-mNb_2O_5-NSF system depicts an extreme example of this exchange broadening phenomenon (pore size ca. 32 Å; C_{12}-mNb_2O_5, Table 3.1). At 115 °C the ^{1}H MAS NMR linewidths are comparable to that of the C_6-mTa_2O_5-NSF system with a large exchange broadened resonance at δ ~7.8 ppm (marked with an asterisk) able to be observed. However, the corresponding 20 °C data shows that all ^{1}H resonances are completely exchanged broadened, thus suggesting that all proton species participate (directly or indirectly) in the conduction process.

The corresponding ^{13}C CPMAS NMR data acquired at 20 °C from these mTa_2O_5-NSF and mNb_2O_5-NSF systems is shown in Figure 5.4. Here, the data is very similar to that of pure NSF implying that it doesn't undergo significant structural alteration upon incorporation into the mX_2O_5 frameworks. The resonances in the range δ 120 – 150 ppm are assigned to the aromatic carbons in naphthalene ring comprising the NSF structure. In the pure NSF and mTa_2O_5-NSF samples there is an additional low intensity resonance at δ 35 ppm, which is assigned to the methylene bridge linking the naphthalene rings.

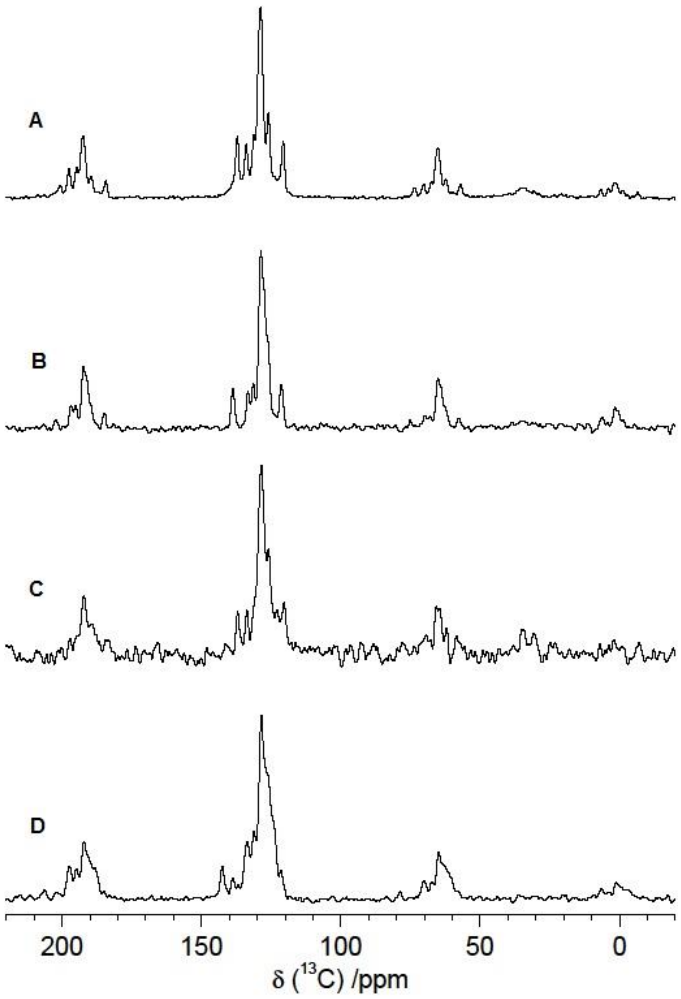

Figure 5.4: ^{13}C CPMAS NMR data at 25 °C for C_6-$mTa_2O_5(SO_4)$-NSF.DEE (A), C_{12}-$mTa_2O_5(SO_4)$-NSF.DEE (B), C_{18}-$mTa_2O_5(SO_4)$-NSF.DEE (C) and C_{12}-$mNb_2O_5(SO_4)$-NSF.DEE (D)

Figure 5.5 shows the ^{1}H MAS and ^{13}C CPMAS NMR data acquired at 25 °C for the C_{18}-Nb composites in relation to the C_{12}-$mNb_2O_5(SO_4)$-NSF composite from Chapter Three. The ^{13}C CPMAS NMR data (Figure 5, right) exhibit seven resolved ^{13}C resonances which are observed in the range δ 120 – 140 ppm and this is characteristic of the aromatic NSF species. In addition, there are indications of low intensity resonances at δ 30 and 20 ppm which are particularly evident in the spectra of Figures 5b (mNb_2O_5-

NSF) and 5c (mNb_2O_5-NSF(110%)). These resonances are consistent with methylene linkers and methyl end caps, respectively. Although there are ten aromatic C species comprising the naphthalene moiety, the additional break in symmetry induced by the presence of the methylene linker facilitates seven of the ten C positions to be consistently observed in each ^{13}C CPMAS NMR spectrum. The well resolved ^{13}C CPMAS NMR data suggests that NSF is not a highly polymerized backbone chain of naphthalene units as the chemical shift dispersion induced in large molecular weight networks is expected to result in much broader and less-resolved ^{13}C resonances. The very low intensity of the resonance of methylene linker resonance(s) at δ 30 and 20 ppm compared to the aromatic naphthalene resonances support this conclusion. If all the NSF moieties were dimers of naphthalene units the expected intensity of the methylene resonance would be half that of the aromatic resonances; i.e. as the polymer chain becomes longer it is expected that the intensity of the methylene resonance would approach the intensity of its aromatic counterparts. Since the relative intensities of the ^{13}C resonances due to carbon with one or more protons attached is normally expected to be ~20 % of each other, these ^{13}C NMR data are consistent with a mixture of low molecular weight oligomers with some residual monomer. As the intensities of the resonances comprising the ^{13}C CPMAS data are only semi-quantitative, it is difficult to assign actual chain-length values and compare to those obtained from the spectra of NSF composites made previously using direct impregnation. Although there is a marked lack of resolution in comparison to the ^{13}C CPMAS NMR data, some information from three broader ^{1}H spectral regions can be elucidated from the corresponding ^{1}H MAS NMR data (Figure 5.5, left). The ^{1}H resonances in the range δ 0 –

2 ppm are typical of protons attached to sp^3 hybridised carbon and these are assigned to the proton on the methylene linker. Other ^1H resonances are observed in the δ 6 - 8 ppm range which are typical of protons attached to aromatic carbon, and at $\delta > 8$ ppm which are characteristic of H-bonded protons. All systems exhibit the presence of the $\delta > 8$ ppm H-bonded species except the mNb_2O_5-NSF(110%) (Figure 5.5c) preparation. It is noted that the intensity of the ^1H resonance(s) in the δ 0 – 2 ppm range are comparable to that of the ^1H resonances of aromatic and H-bonded shift regions. This is in sharp contrast to the ^{13}C CPMAS data where sp^3 hybridised carbon resonances are much less intense than those of the aromatic resonances.

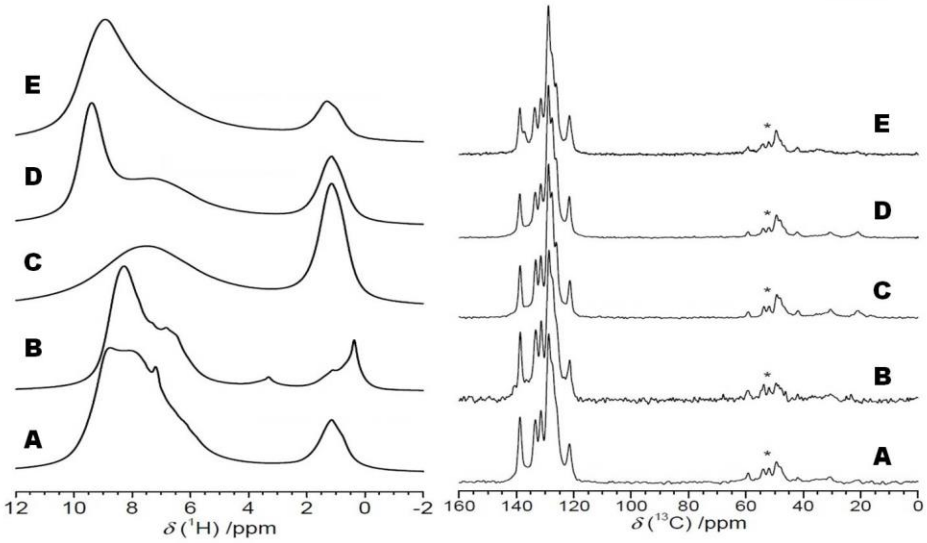

Figure 5.5: ^1H spin echo MAS (left) and ^{13}C CPMAS (right) NMR spectra for C_{18}-$mNb_2O_5(SO_4)$-NSF (A), C_{18}-$mNb_2O_5(SO_4)$-NSF(110%) (B), C_{18}-mNb_2O_5-NSF(110%) (C), C_{18}-mNb_2O_5-NSF (D) and C_{12}-$mNb_2O_5(SO_4)$-NSF (E) at 25 °C

There are two possible explanations for this observation. The first is that the resonance is due to aliphatic protons, which are also associated to the metal oxide. The second is that the aromatic and acidic protons appear to have a lower intensity in the

NMR spectra than would be expected because of a relatively large inhomogeneous loss of coherence in the echo experiment due to strong dipolar coupling. Both explain the relative lack of aliphatic ^{13}C resonances.

Variable Temperature Experiments

To account for the observations seen during the Variable Temperature (VT) EIS experiments, the structural changes on heating were investigated by NMR. VT ^{1}H MAS NMR data for the mobile proton species for the mTiO_2-NSF.DEE system is shown in Figures 5.8 and 5.9. Here it is evident that over the 20-100 °C VT range studied the ^{1}H linewidth becomes motionally narrowed and remains in a most narrowed condition over the ~50-100 °C temperature range leading up to maximum conductivity.

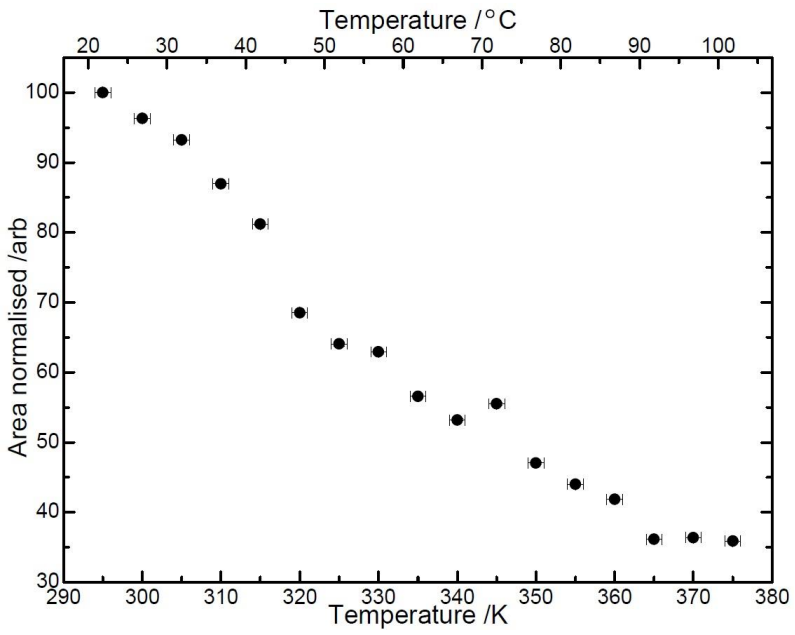

Figure 5.6: Area normalisation data for mTiO_2-NSF.DEE

More importantly, from Figure 5.6 the normalised integrated intensity of this ^{1}H resonance is shown to monotonically decrease to a value of ~35 % leading up to

maximum conductivity at 100 °C. This result suggests that the majority of this species is not being observed in this experiment, and that this proportion is probably exchange broadened by a co-existing process with a correlation time on a different timescale, which suggests that more than one motional mechanism is contributing to the overall conductivity phenomenon. Furthermore, from Figure 5.7 and 5.8 the ^{1}H chemical shift for the observable mobile proton component exhibits a marked upfield trend to increased shielding, and hence a greater association with the $mTiO_2$-NSF.DEE network.

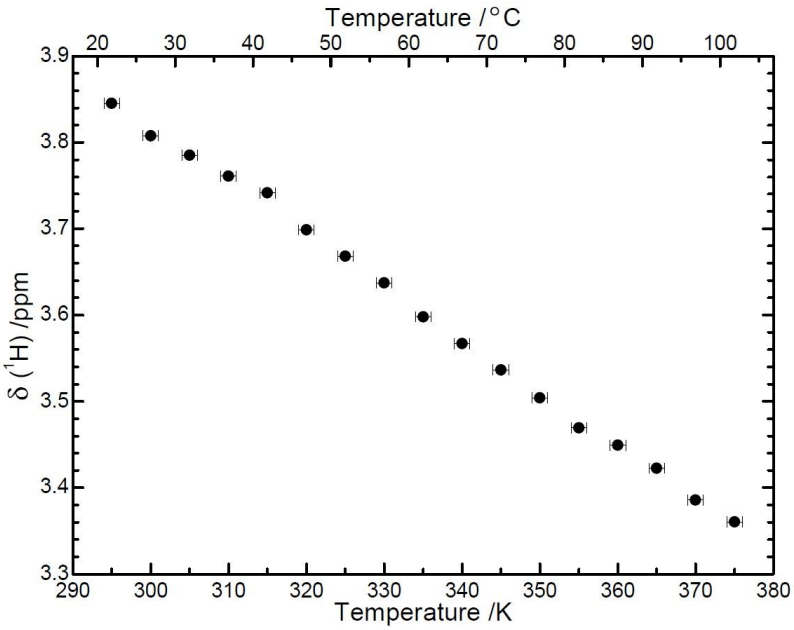

Figure 5.7: Chemical shift data for $mTiO_2$-NSF.DEE

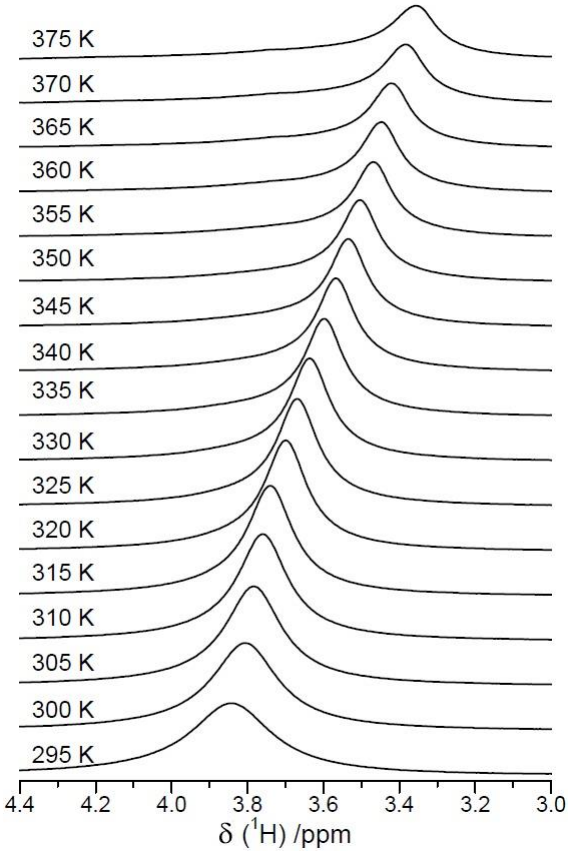

Figure 5.8: Variable Temperature (VT) ^{1}H MAS NMR data for mTiO_2-NSF.DEE tracking the mobile proton species

The upfield movement of the H-bonded shifts shown in Figure 5.8 further indicates that the strength of the H-bond network is weakening as the temperature rises. The mobility of the mobile proton species, which is evident from the ^{1}H MAS NMR data (Figure 5.5), allows the NSF moieties to migrate and rearrange to configurations within the Ti oxide network and this occures more frequently at higher temperatures. This ties in with the Ti oxide EIS data (Figure 2.23) whereby an increasingly mobile mobile proton species coincides with an increase in proton conduction between 20 and 100 °C. The VT ^{1}H MAS and ^{13}C CPMAS NMR measurements on thermally cycled pellets shows that

this is an insignificant perturbation on the speciation of the $mTiO_2$-NSF.DEE system and the polymerisation of the NSF resin; it can be inferred that the reduced conductivity behaviour is due to collapse of the pore walls resulting in a change of environment for the NSF material. (Figure 5.10). Whilst the weakening of the H-bonded network appears to be needed to provide proton movement and thus, to enchance conductivity, the degredation of the pore walls in the Ti oxide system cause the conductivity to tail off which supports the need for a more robust framework.

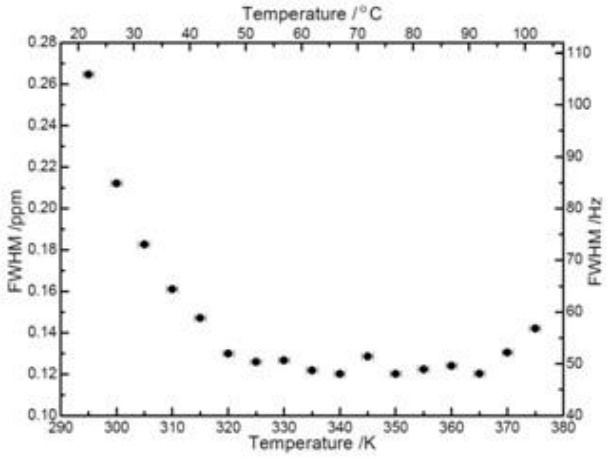

Figure 5.9: VT data for $mTiO_2$-NSF.DEE tracking the mobile proton species

This degradation is confirmed by the nitrogen adsorption data and the increased amount of crystallisation apparent on the STEM images following NSF or sulphuric acid addition as the more lattice visible, the more amorphous the pore structure has become. Composite $mTiO_2$-NSF.DEE again shows the highest proton conductivity and is higher than pure NSF. This confirms the underlying hypothesis of our approach by suggesting that there is a synergistic relationship between the mesoporous support and the sulfonated resin and a greater dependency on NSF loading rather than H_2O concentration in the

pores, an observation confirmed by the TGA data as it is the one that contains the most NSF. A lower conductivity was also observed with the Nafion and this is likely due to the dehydration of the pellet.

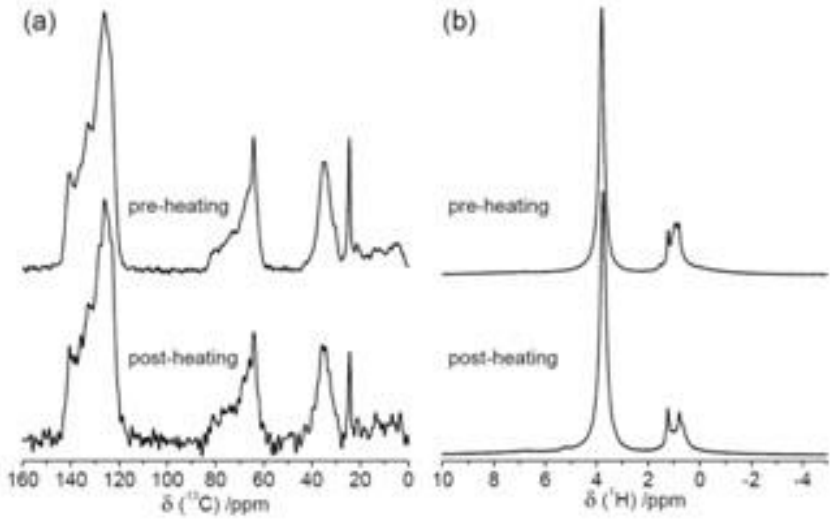

Figure 5.1026: Exerts of VT ^{13}C CPMAS NMR and ^{1}H MAS NMR data for $mTiO_2$-NSF.DEE before and after heating to 150 °C

Figure 5.11 shows that remarkably high resolution data can be observed from the mesoporous Nb composite systems synthesised from the different techniques when ^{1}H MAS NMR measurements are recorded at 80 °C. These data exhibit seven well-resolved aromatic ^{1}H resonances in which ^{3}J vicinal coupling can be observed from six of these; the most downfield resonance(s) at $\delta \sim 7.8$ ppm is assigned to the H-bonded protons which have shifted down below $\delta \sim 8.0$ ppm with increasing temperature. The methylene ^{1}H resonances in the δ 0 - 2 ppm range observed at 25 °C have completely disappeared at 80 °C probably through exchange broadening. The ^{1}H connectivity described by the ^{3}J vicinal coupling patterns allows an unambiguous assignment of these resonances which can be seen in Figure 5.13. With these assignments supporting a

structure involving a single naphthalene moiety with one attached sulfonate functional group (Figure 4.1).

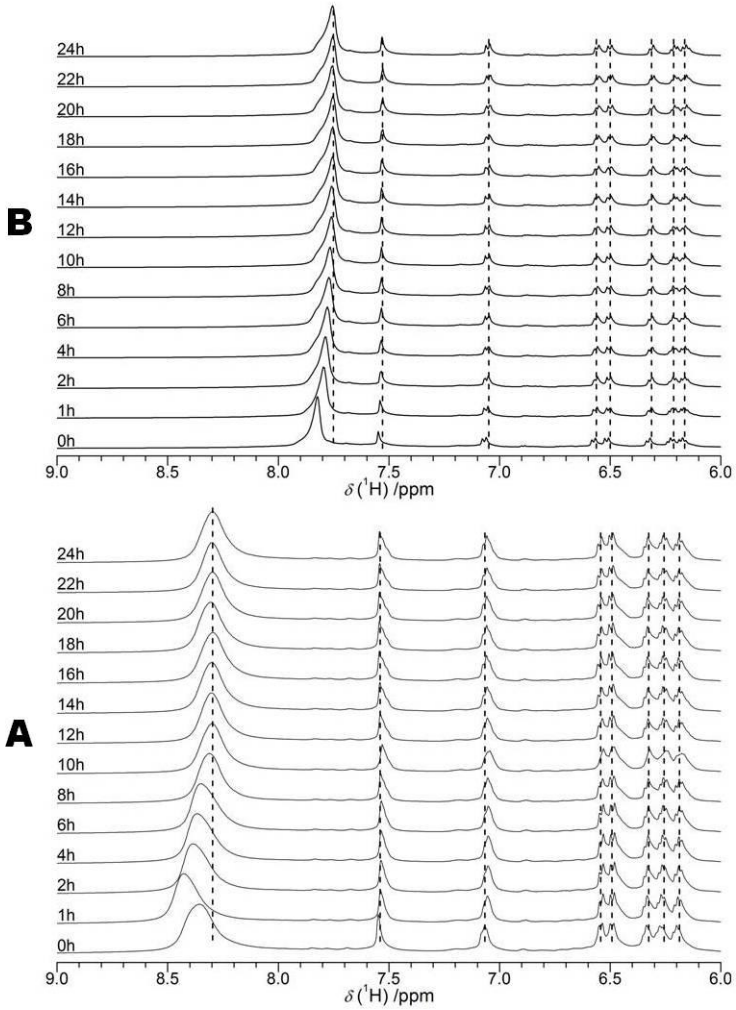

Figure 5.11: The ^{1}H MAS NMR spectra of C_{12}-$mNb_2O_5(SO_4)$-NSF synthesised by direct oligomer impregnation (A) and C_{18}-$mNb_2O_5(SO_4)$-NSF(110%) (B)

This is consistent with the ^{13}C CPMAS NMR data (Figure 5.5) where the aromatic resonances exhibit narrow linewidths, indicating that the attached protons are highly mobile species which facilitates the reduction the ^{1}H-^{1}H homonuclear dipolar coupling sufficiently to narrow these resonances. The H-bonded protons could achieve

such mobility by jumping between H-bonded positions, however, the narrow aromatic resonances suggests that molecular mobility is also present.

A closer inspection of the narrow aromatic ^{1}H resonances shows that they collectively appear to be located on top of a much broader resonance. This indicates that not all NSF is mobile enough to give rise to narrow resonances; the most likely cause is that some NSF oligomers are too large to be highly mobile. The chemical shift evolution of the H-bonded proton resonance is shown for the mesoporous Nb composite systems held at 80 °C over a 24 hour period (Figure 5.12). In both cases the chemical shift of the H-bonded resonances moves upfield (to lower ppm), while the ^{1}H chemical shift of all other species remain relatively constant.

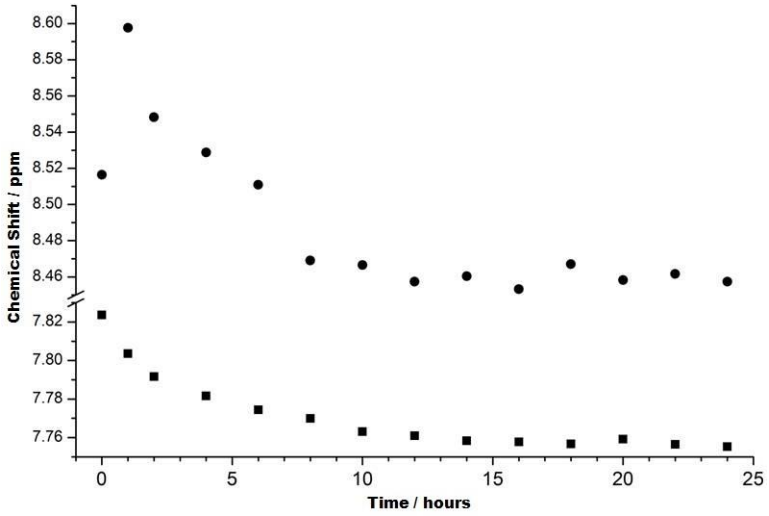

Figure 5.12: The chemical shift change with time of the NSF OH^{1} resonance for C_{18}-$mNb_2O_5(SO_4)$-NSF(110%) (squares) and C_{12}-$mNb_2O_5(SO_4)$-NSF synthesised by direct oligomer impregnation (circles) over a period of 24 hours.

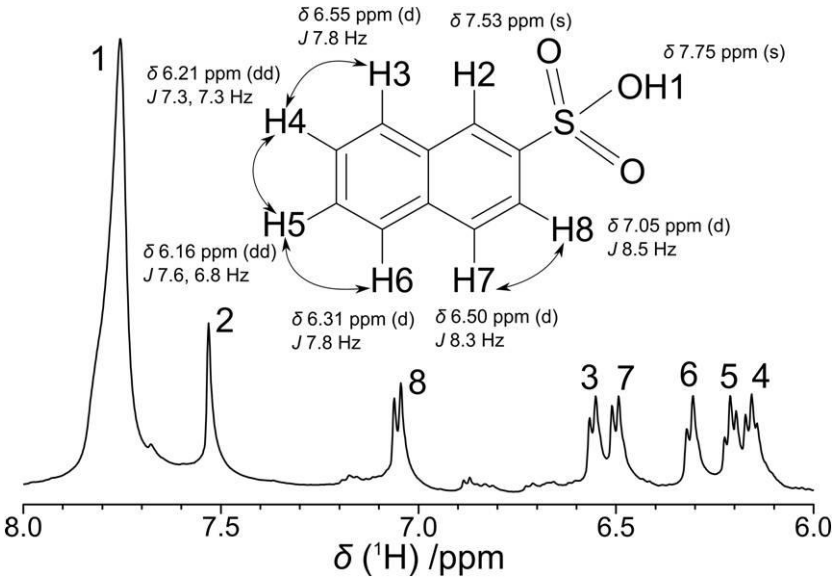

Figure 5.13: Assignment of the ^{1}H spin echo MAS NMR spectra C_{18}-m$Nb_2O_5(SO_4)$-NSF(110%) after 24 hours at 80 °C

This upfield movement of the H-bonded shifts indicates that the strength of the H-bond is weakening with time, and indicates that the mobility which is evident from the ^{1}H MAS NMR data allows the NSF moieties to migrate and rearrange to configurations within the Nb oxide network which thus decreases the strength of the H-bonded network. A strong H-bonding network has often been demonstrated to be beneficial to proton conductivity systems[12] and the time evolution of the ^{1}H shifts describing a weakening of the H-bonding systems corroborates the decrease in conductivity derived from impedance measurements undertaken under the same temperature and time conditions. The average shift of this resonance is *ca.* 1 pmm less shifted in the case of the composite synthesised by the new technique. Although from a hydrogen bond strength argument this might suggest lower conductivities, the reverse of what is observed, there are several other factors that might contribute to the net shift between different structures (as opposed to

the same structure changing with temperature). Since there is no significant difference in NSF chain lengths between the two systems as estimated by NMR, it would lead one to infer that the greater conductivity for the *in situ* polymerised samples is due to deeper penetration and continuity of the NSF units into the pore structure using the new method. This observation suggests that further gains in stability could be achieved by developing methods to increase the polymer chain length deep within the pore structure to lock the NSF into place and block the leaching process which leads to decereased performance.

^{17}O Measurements

Figures 5.14(a), 5.14(b), 5.14(c) and 5.14(d) show the ^{17}O solid echo MAS NMR data from the C_6, C_{12}, and C_{18}-mNb_2O_5-NSF systems, as well as C_{12}-mTa_2O_5-NSF system, respectively. In the 1D data for C_6-mNb_2O_5-NSF two broad ^{17}O resonances are observed at 127 and 560 ppm (Figure 5.14a). In contrast, the 1D data for C_{12}-mNb_2O_5-NSF and C_{18}-mNb_2O_5-NSF exhibit increased resolution and thus more expansive O speciation with four resonances (551, 385, 147 and 62 ppm; Figure 5.14b) and five/six resonances (549, 383 ppm, manifold of three/four resonances in the 80 - 170 ppm range; Figure 5.14c) being observed for these systems, respectively. The 1D data from the C_{12}-mTa_2O_5-NSF system (Figure 5.14d) reveals quite different O speciation with three well-resolved ^{17}O resonances at 457, 163 and 26 ppm being measured.

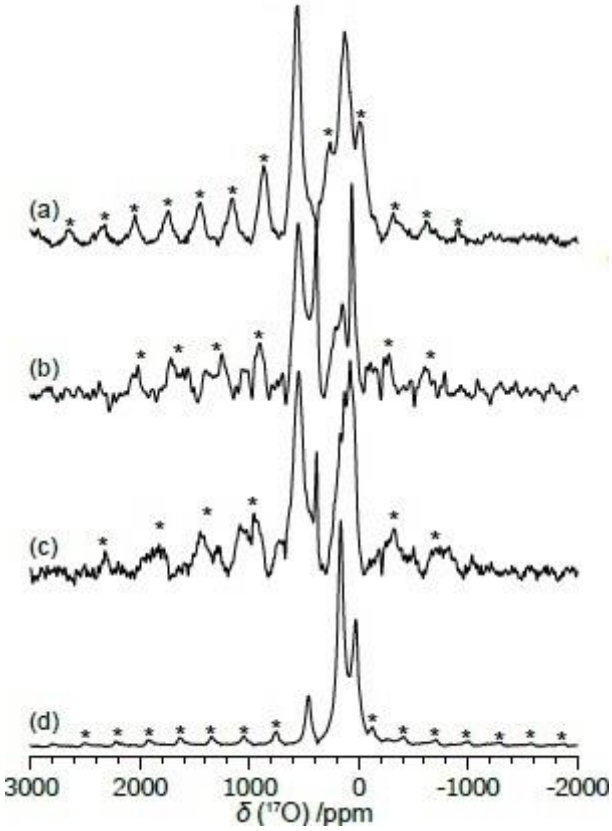

Figure 5.14: ^{17}O MAS 1D NMR spectra for mX_2O_5 material

From the 1D data from the C_6, C_{12}, and C_{18}-mNb_2O_5-NSF systems shown on Figure 5.14 the observed ^{17}O resonances at ~550 and ~380 ppm are assigned to $^{17}ONb_2$ and $^{17}ONb_3$ environments in the mNb_2O_5 framework, respectively, as previously reported.[13] The ONb_3 resonance linewidth is significantly narrower than that of the ONb_2 resonance suggesting that the higher point symmetry of the ONb_3 position results in a reduced electric field gradient at the O position, and thus a smaller quadrupole coupling constant (C_Q). In contrast to the C_{12}, and C_{18}-mNb_2O_5-NSF systems, only the ~550 ppm resonance can be observed from C_6-mNb_2O_5-NSF which is unambiguously identifies to

the $^{17}ONb_2$ position. Similar to the C_6-mNb_2O_5-NSF, the C_{12}-mTa_2O_5-NSF system exhibits only one observable ^{17}O resonance from the tantalum oxide framework which is observed at 450 ppm; this is attributed to the $^{17}OTa_2$ environment.[10] These parallel observations suggest that the H exchange phenomenon (and hence the overall conductivity pathway) from the NSF to the mesoporous metal (Nb and Ta) oxide surface occurs selectively through the ONb_3 moieties, with the associated $^{17}ONb_3$ resonances becoming completely exchange broadened. Further evidence of this occurrence is given in the 1D ^{17}O solid echo MAS NMR data from C_{12}, and C_{18}-mNb_2O_5-NSF; these data show that the overall integrated intensity of the ONb_3 resonance is much reduced in comparison to its ONb_2 counterpart (from the expected stoichiometric 1:1 ratio) thus suggesting that a large component of the ONb_3 (but not all) is unobservable due to the same exchange broadening phenomenon.

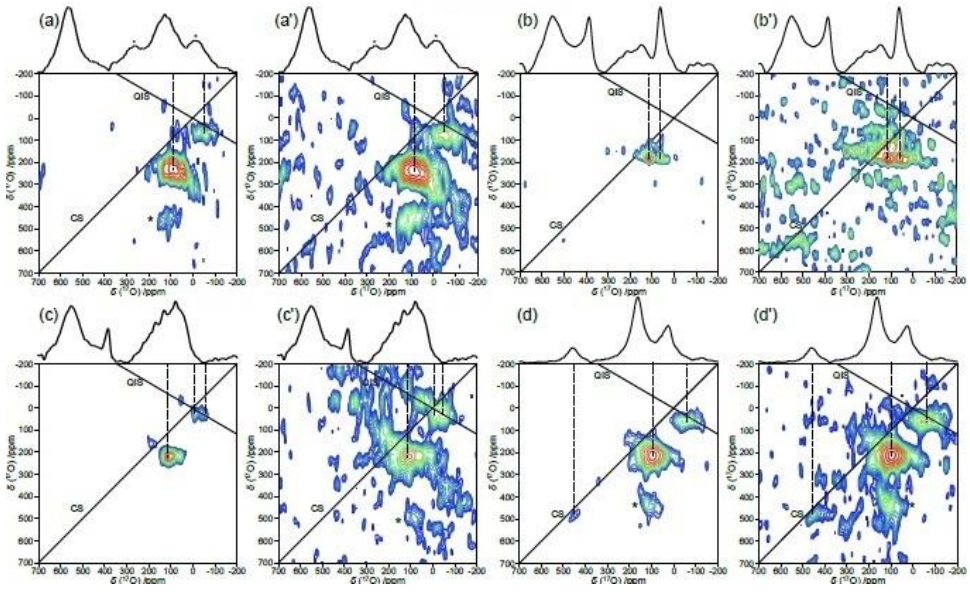

Figure 5.15: ^{17}O MQMAS 2D NMR spectra for the mX_2O_5 system

Furthermore, evidence of a broad unresolved signal bridging between these two characteristic framework resonances further suggests that an additional process may also exist where the H exchange may extend from the ONb_3 to the ONb_2 positions, subsequently establishing a secondary process between these moieties. The remaining ^{17}O resonances observed from Figure 5.14 fall into two categories. Resonances in the ~140 – 170 ppm range represent O position in the SO_3^{2-} functionality which has been previously established by Marker *et al*[14] to occur at shifts up to >170 ppm. From the C_6-mNb_2O_5-NSF system data only a single broad SO_3^{2-} resonance is observed, while the increased resolution from the corresponding C_{12} and C_{18}-mNb_2O_5-NSF data indicates that multiple resonances are present. It can thus be inferred that the pore size has a significant effect on the quantity and number of different sulfonate environments residing in the channel structure associated with each framework. The remaining resonances in the ~20 – 80 ppm range are probably free OH^- species released from any polymerisation processes that have occurred in the channels.

The corresponding 2D ^{17}O MQMAS NMR data is shown in Figures 5.15a - d for the C_6, C_{12}, C_{18}-mNb_2O_5-NSF systems and the C_{12}-mTa_2O_5-NSF system, respectively. Figures 5.15a' - d' represent a magnified view of the same data with a lower contour threshold level. From initial inspection it is evident that a number of resonances have not survived the filtering and timescale of the MQMAS experiment. The most obvious resonances absent from the data emanating from this experiment are those identifying the ONb_2 and ONb_3 moieties in the Figures 5.15a - c and Figures 5.15a' - c'. In this case, the very short T_1 andT_2 relaxation times of these O species caused by the rapid H exchange

from the sulphonate to the metal oxide framework induces a complete loss of coherence on the timescale of the MQMAS experiment. This T_1/T_2 relaxation phenomenon is not as short for the C_{12}-mTa_2O_5-NSF system since some residual multiple quantum magnetisation survives to indicate reduced evidence of the OTa_2 species (Figures 5.15d and 5.15d'). In addition, while some OH species are represented in these MQMAS data (Figures 5.15b and 5.15b' for C_{12}-mNb_2O_5-NSF), most sulphonate O species have been similarly affected by the same extremely short T_1/T_2 phenomenon since they also participate in the same exchange process; hence, these associated contours are also noticeably absent. The resulting MQMAS data exhibits residual resonances identifying minor species that do not participate significantly in the H conduction pathway depicted by very low intensity contours at *ca.*100 and *ca.*−30 ppm.

Conclusions

In summary, it has been shown by these comprehensive NMR experiments that there is a synergistic relationship between the mesoporous support, the sulfonated resin, as well as a greater dependency of conductivity on NSF loading rather than H_2O concentration in the pores. It has also been shown that there is no significant structural alteration of NSF upon incorporation into the mX_2O_5 frameworks, and that the proton conductivity of the composites can be influenced by changing the pore size of the metal oxide. It is also clear that the NSF remains an oligomer inside the pores, supporting the theory allowing for deeper penetration of the NSF and prolonged conductivity. Furthermore, it has been established that both the NSF aromatic and aliphatic proton species are contributing to the conduction process, with the overall ^{1}H conduction

mechanism being defined by a complex interplay between the $–SO_3H$ moiety, the NSF aromatic and aliphatic proton species, and the mX_2O_5 pore characteristics. The solid state NMR experiments have thus confirmed the findings of chapters 2-4 and where necessary, explained the proton conducting pathways through these composite materials.

Experimental Section

All chemicals were purchased from either Sigma Aldrich or Alfa Aesar and used without further purification.

The Ti analogues and composites were synthesised as described in Chapter two. The Ta composites and C_{12}-mNb composites were synthesised as described in Chapter three. The remaining Nb composites were synthesised as described in Chapter four.

^{17}O-labelled mNb_2O_5. mNb_2O_5 is added to a Schlenk tube under the presence of nitrogen. To this, twice the weight amount of ^{17}O-enriched H_2O is added, sealed, and placed into an oven for 48 hours. This is subsequently dried *in vacuo* and backfilled.

^{17}O-labelled NSF. H_2SO_4 (18 M, 5 ml) is placed into a Shlenk tube and back filled with nitrogen. Once inside a glove box $^{17}OH_2$ (40 % enrichment, 5 ml) is added and the Shlenk tube shaken briefly, before removal to an oven set at 80 ^{0}C for four days. Next, the excess water is removed *in vacuo* to give ~5 ml of ^{17}O-labelled H_2SO_4. Finally, this is back filled with nitrogen and the NSF synthesis proceeds as per Chapter three and four, using ^{17}O-labelled H_2SO_4 in place of regular H_2SO_4.

Characterisation section. The ^{1}H spin echo MAS and ^{13}C CPMAS NMR of the mesoporous Ti, Ta and Nb composites were acquired on a Bruker Avance III 500 Spectrometer operating at 500.09 MHz and 125.76 MHz respectively. Each ^{1}H MAS

NMR spectrum was acquired using a Bruker 2.5 mm triple channel HXY probe (operating in double channel mode) in which rotational frequencies (νr) of 31.25 kHz were achieved. These ^{1}H data were obtained using a rotor-synchronised spin echo ($\pi/2$ - τ - π - τ - acq.) experiment which used a $\pi/2$ excitation and π refocusing pulses of 2.5 and 5.0 μs duration, respectively, a rotor-synchronised τ delay of 32 μs (for νr = 31.25 kHz), and a recycle delay of 3 s. All ^{1}H chemical shifts are referenced to TMS (δ 0.0 ppm) via an alanine secondary solid reference, which exhibited shifts at δ 1.1, 3.5 and 8.4 ppm. The ^{13}C CPMAS NMR spectra were acquired using a Bruker 4 mm triple resonance (HXY) probe operating in double resonance mode and a spinning frequency of 8 kHz. The initial ^{1}H $\pi/2$ excitation pulse duration was 2.5 μs, the Hartmann-Hahn contact period was 1 ms and the recycle delay was 3 s. The SPINAL64 sequence of ^{1}H decoupling using 5 μs pulses was implemented during data acquisition. All ^{13}C chemical shifts are referenced to TMS (δ 0.0 ppm) via an alanine secondary solid reference which exhibited shifts at δ 20.5, 51.0 and 177.8 ppm. Corresponding variable temperature ^{1}H MAS NMR measurements were conducted at 9.4T using a Bruker DSX-400 spectrometer and a Bruker 4mm VT MAS probe which enabled MAS frequencies of 15 kHz and an elevated temperature range up to 100 °C, or via a Bruker 3.2 mm double resonance (HX) probe in which a spinning frequency at 7 kHz was achieved. These ^{1}H data were also obtained using a rotor-synchronised spin echo ($\pi/2$ - τ - π - τ - acq.) experiment which used a $\pi/2$ excitation and π refocusing pulses of 2.5 and 5.0 μs duration, respectively, a rotor-synchronised τ delay of 66.7 μs (for νr = 15 kHz). The recycle delay was 3 s, and the dephasing and refocussing times were $\tau = 1/\nu_r$ = 142 μs (making the two echo times

(MAS and spin) coincident). The temperature calibration of these measurements was achieved using lead nitrate located within the rotor volume.[15] Samples of C_6, C_{12} and C_{18}-Nb_2O_5 as well as C_{12}-Ta_2O_5 were studied using ^{17}O 1D solid echo MAS and 2D MQMAS NMR measurements. These data were acquired at 11.75 T using a Bruker Avance III-500 spectrometer operating at a ^{17}O Larmor frequency of ω_0 = 67.75 MHz. These experiments were implemented using a Bruker 3.2 mm HXY probe operating in double channel mode which enabled a MAS frequency of 20 kHz in all cases. Each solid echo measurement was undertaken using a θ - τ - θ - τ - acquire experiment (with $\theta = \pi/4$) with $\pi/4$ pulse lengths of length 1 μs duration, and a short recycle delay of 100 ms. This short recycle delay was compared against similar experiments with much longer recycle delays of up to 5 s to ascertain the true quantitative nature of the data. The 2D MQMAS measurements used the four pulse z-filtered $3\pi/2$ - $t1$ - $\pi/2$ – ($\pi/2$ - τ - $\pi/2$) experiment where the final two $\pi/2$ pulses constitute the soft z-filter. This experiment utilised hard $3\pi/2$ triple quantum excitation pulses and $\pi/2$ conversion pulses of 3.6 and 1.2 μs length, respectively, in addition to the selective (soft) z-filter $\pi/2$ pulses of 12 μs duration, and a recycle delay 100 ms. All ^{17}O chemical shifts were referenced to the ^{17}O primary reference H_2O at δ_{iso} 0.0 ppm.

References

[1] Mackenzie. K., Smith. M. E. (2002) *Multinuclear solid-state nuclear magnetic resonance of inorganic materials. Volume 6 (1st Edition)*. Elsevier.

[2] Graf. R., Demco. D. E., Hafner. S., Spiess. H. W. (1998). Selective residual dipolar couplings in cross-linked elastomers by 1H double-quantum NMR spectroscopy. *Solid State Nucl. Magn. Reson., 12*, 139–152.

[3] Hickman. B. S., Mascal. M., Titman. J. J., Wood. I. G. (1999). Protonic conduction in imidazole: a solid-state ^{15}N NMR study. *J. Am. Chem. Soc.*, *121*(49), 11486-11490

[4] Ashbrook. S. E., Smith. M. E. (2006). Solid state ^{17}O NMR—an introduction to the background principles and applications to inorganic materials. *Chem. Soc. Rev.*, 35, 718–735.

[5] Lemaître. V., Smith. M. E., Watts. A. (2004). A review of oxygen-17 solid-state NMR of organic materials - towards biological applications. *Solid State Nucl. Magn. Reson.*, *26*, 215–235.

[6] Wu. G. (2008). Solid-state ^{17}O NMR studies of organic and biological molecules. *Prog. Nucl. Magn. Reson. Spectrosc.*, *52*, 118–169.

[7] Oldfield. E. (1989). ^{17}O nuclear-magnetic-resonance spectroscopic study of high-Tc superconductors. *Phys. Rev. B*, *40*, 6832–6849.

[8] Bastow. T. J., Stuart. S. N. (1990). ^{17}O NMR in simple oxides. *Chem. Phys.*, *143*, 459–467.

[9] van Eck. E. R. H., Smith. M. E., Kohn. S. C. (1999). Observation of hydroxyl groups by 17O solid-state multiple quantum MAS NMR in sol–gel-produced silica. *Solid State Nucl. Magn. Reson.*, *15*, 181–188.

[10] Skadtchenko. B. O. (2007). A solid-state ^{17}O NMR study of local order and crystallinity in amine-templated mesoporous Nb oxide. *Angew. Chem. Int. Ed.*, *46*, 2635–2638.

[11] Julián. B. (2003). Synthesis and characterization of transparent PDMS−metal-oxo based organic−inorganic nanocomposites. *Chem. Mater.*, *15*, 3026–3034.

[12] Schuster. M., Kreuer. K.-D., Steininger. H., Maier. J. (2008). Proton conductivity and diffusion study of molten phosphonic acid H_3PO_3. *Solid State Ion.*, *179*, 523–528.

[13] Rao. Y., Kemp. T. F., Trudeau. M., Smith. M. E., Antonelli. D. M. (2008). ^{17}O and ^{15}N solid state NMR studies on ligand-assisted templating and oxygen coordination in the walls of mesoporous Nb, Ta and Ti oxides. *J. Am. Chem. Soc.*, *130*, 15726–15731.

[14] Marker. A., Roy. A. B. (1983). The use of ^{17}O-NMR in the study of bond cleavage during the hydrolysis of sulphate esters. *Biochim. Biophys. Acta BBA - Protein Struct. Mol. Enzymol. 742*, 446–451.

[15] van Gorkom. L. C. M., Hook. J. M., Logan. M. B., Hanna. J. V., Wasylishen. R. E. (1995). Solid-state lead-207 NMR of lead(II) nitrate: localized heating effects at high magic angle spinning speeds. *Magn*. *Reson*. *Chem*., *33*, 791–795.

Chapter 6: Conclusions, Summaries and Perspectives

Introduction

An increasing desire for energy without the need for fossil fuels has led to a concomitant increase in the usage and development of fuel cells in recent years. Of the many types of fuel cells to arise, the PEMFC is one which holds the greatest degree of promise in regards to replacing the combustion engine inside automobiles,[1] or towards an improved power source for portable electronic devices.[2] Built around a membrane electrode assembly (consisting of electrodes, electrolyte, catalyst, and gas diffusion layers), any material selected for use in a PEMFC must be able to perform admirably at the designated operating temperatures over a prolonged period. For a PEMFC, the optimal working temperature begins at 80 °C as this forces the water in the membrane to become steam which further drives the system and aids proton transfer. In a PEMFC, the electrolyte is a thin membrane and this needs to adhere to the strict operating whilst maintaining a high proton conductivity. Currently, the best commercially available membrane is DuPont's Nafion. Nafion (of which there are many forms) is a sulfonated tetrafluoroethylene-based fluoropolymer-copolymer which boasts excellent mechanical and thermal stability.[3] In addion, Nafion has superior proton conduction properties, which arise from terminally-bound sulphonate groups achored to the molecule's ether backbone. It is these sulphonate groups which cause Nafion to self assemble into arrays of hydrophilic channels with water molecules bridging the sulfonate units to create a continuous pathway for proton mobility. However, as the optimal temperature for

PEMFC function is approached, performance deteriorates as the conductivity decreases due to dehydration of the Nafion matrix.[4] To improve on Nafion, research groups have attempted to dope the Nafion matrix,[5,6] or to replace it outright[7,8], however, to date none of these alternatives have yet replaced Nafion as the commercially preferred membrane of choice for PEMFCs and as such, new approaches to this problem must be explored.

The work presented in this thesis was aimed at the development of a new proton conducting material that is resilient to dehydration. The key idea in the design of the model system was to exploit the oxide surface of the ca. 20 Å pore walls of a mesoporous transition metal oxide as a means of anchoring sulfonate groups and suppressing moisture loss to encourage proton conduction pathways in the NSF impregnated analogues. Thus, a system was conceived and studied consisting of various single mesoporous transition metal oxides doped with H_2SO_4 and subsequently impregnated with NSF via direct oligomer impregnation or by the NSF being oligomerised *in situ* of the mesoporous transition metal oxide's pores.

Research Conclusions

In Chapter two the proton conducting pathway was constructed by synthesising a series of NSF composites of mesoporous Ti oxide. Initial experiments centred on obtaining the optimal loading of the NSF oligomer into a typically sized mesoporous Ti mesopore by using a wide range of solvents. This was also repeated by doping the mesoporous Ti with H_2SO_4. With the optimal loading confirmed, the composites were fully characterised, formed into pellets and their inherent proton conductivity recorded over a range of temperatures via variable temperature EIS. The data was subsequently

compared with a similarly formed pellet of Nafion 117. As the temperature approached the optimal condition PEMFC operation, the best composite for proton conduction was that which saw the mesoporous Ti doped with H_2SO_4 and impregnated with a mixture of NSF in a medium of diethyl ether (designated $mTiO_2$-NSF.DEE). At 25 °C the proton conductivity was measured at 0.3 mS cm^{-1} (Nafion 1.450 mS cm^{-1}) and this rises to 1.195 mS cm^{-1} at 75 °C by which point it surpassed the Nafion cell (1.013 mS cm^{-1}). This continued to rise to 1.837 mS cm^{-1} by 100 °C. By 150 °C the proton conductivity measured 0.631 mS cm^{-1} and this was still higher than that of Nafion (0.126 mS cm^{-1}). While the best materials slowly degraded with loss of performance over time, the conductivity results showed promise and suggested that use of a more robust mesoporous material was required in order to resist any pore degradation. It was also noted how the samples doped with H_2SO_4 had an increased proton conductivity over the un-doped samples which implied a positive contribution to the proton conducting network.

From previous work, mesoporous Nb and mesoporous Ta had already been used in conjunction with H_2SO_4 doping[9,10] for catalytic purposes and thus, these represented ideal candidates for the exploration of improved proton conductivity and durability in Chapter three. Pore size was also varied during the synthesis stage as this was anticipated to invoke a higher thermal stability in smaller or larger pore sizes that might encourage better stability of performance under more demanding operating conditions. As arguably the most robust, three batches of mesoporous Ta oxide were templated using one of three different ligand sizes (C_6, C_{12} and C_{18}), while a batch of C_{12} mesoporous Nb oxide was synthesised for comparison. For each composite formed the optimal NSF loading was

determined (again, found to be a sample doped with H_2SO_4 and impregnated with a solution of NSF in a diethyl ether medium), fully characterised and formed into pellets so that their proton conductivity could be determined via EIS over a range of temperatures. This time, they were compared with a Nafion 117 film with a literature value of 8 mS cm^{-1} at 100 °C. Whilst all composites exhibited conductivities that surpassed that of the pure NSF and the Nafion standard, the most promising was the C_{12}-m$Nb_2O_5(SO_4)$-NSF.DEE (21.96 mS cm^{-1} at 100 °C). However, by 150 °C the conductivity dropped off in all cases, with thermal leaching of the oligomer being the likely cause. With the system optimised the next course of action was to attempt to lock the oligomer within the mesopore. We thus hypothesised that the NSF could be condensed and polymerised within the pores rather than doped into them by impregnation, which should allow for a deeper penetration of the polymer and less susceptibility to thermal leaching.

This *in situ* technique was developed to replace the direct impregnation technique and this was described in Chapter four. This new method was particularly attractive because the synthesis of NSF can be accomplished in two simple steps from naphthalene: the sulfonation of the fused aromatic followed by the condensation of the naphthalene sulfonic acid product with formaldehyde. By stopping at the second stage and impregnating the pore with the much smaller monomer naphthalene sulfonic acid, we were able to induce condensation *in situ* of the mesopore to not only ensure maximum penetration, but to lock the polymer in place and decrease the chances of any potential leaching. Since formaldehyde is a small molecule we believed that it should readily diffuse through the pores during the second synthesis step to the adsorbed NSA sites and

induce polymerisation with minimal loss of the organic to leaching. This strategy was expected to ensure that the proton network was maintained at higher temperatures for a longer period, thus offering superior conductivity performance at operating temperatures as a function of time. Of the three mesoporous Ta composites in Chapter three, the best performing sample was derived from that which had been synthesised with a C_{18} template. As mesoporous Nb outperformed this, it was postulated that a mesoporous Nb composite constructed with a C_{18} template would afford not only good proton conductivity but also that the larger pore size would allow for a deeper penetration of the NSA monomner. Initial work went into acquiring the optimal loading of NSA and in turn, to attain the optimal loading of formaldehyde. It was here that we also added an additional amount of NSA to the mix. Experimentally determined over a range of 5 - 50 %, this was added as the optimal amount (10 %) required to further improve proton conductivity and mechanical stability of the composites. With this determined, the conductivity of all samples were recorded as a function of temperature under controlled humidity and compared versus that of a Nafion 117 film and the C_{12}-m$Nb_2O_5(SO_4)$-NSF.DEE composite from Chapter three. Whilst all composites surpassed Nafion at the operating temperature for PEMFCs, the most promising sample, m$Nb_2O_5(SO_4)$-NSF(110%) possessed and maintained a much higher conductivity for a longer period than Nafion, holding a six fold edge in this regard after as long as eight hours, and a two-fold advantage after 24 hours. Similarly it outperformed the C_{12}-m$Nb_2O_5(SO_4)$-NSF.DEE composite to reinforce the belief that the *in situ* method retards degradation of proton conductivity through the polymer leaching observed in Chapters two and three.

Attempts to understanding the proton conducting pathway was discussed in Chapter five, where the focus was on solid state NMR studies of the all mesoporous materials and composites synthesised within this thesis. By performing comprehensive NMR experiments, the synergistic relationship between the sulphated mesoporous host and oligomer resin towards improved proton conductivity was demonstrated, and how this can be controlled by variation of the pore size during construction of the host material. Through peak assignments in this Chapter we have been able to determine that the structure of the oligomer remains intact (and an oligomer) within the pores to support the hypothesis that the NSF has penetrated deep within to influence proton conductivity. Furthermore, it was established that both the NSF aromatic and aliphatic proton species are contributing to the conduction process, with the overall ^{1}H conduction mechanism being defined by a complex interplay between the $–SO_3H$ moiety, the NSF aromatic and aliphatic proton species, and the mesoporous transition metal oxide pore walls.

In summary, the goal of this thesis was to create a material that sulfonate groups to build a proton-conducting network, using the walls of the oxide channel to suppress moisture loss or possibly even replace water entirely, with the potential for use within a membrane electrode assembly. The best material was resilient to decreased conductivity due to dehydration of the membrane as the temperatures approached the optimal working conditions for a low temperature fuel cell. By creating a proton conducting network that is more resistant to degradation through moisture loss, and one which surpasses the proton conductivity of the commercially available Nafion in many membrane electrode assemblies, we can say that the goal may have been achieved.

Future Work

As this project unfolded, there were many avenues that could have been explored would there have been more time and resources to enable this. In Chapter two it was established that diethyl ether was to be the solvent of choice, but research could have explored the impregnation of NSF using a different medium such as toluene, petroleum ether or hexane. By expanding the solvents used, a study on how the polarity of the medium affects the weight percentage, and subsequently the proton conductivity, could help with the understanding of why diethyl ether was the most effective solvent for this project. In Chapter three the pore size was systematically altered in a series of mesoporous Ta oxides. However, from a completionist point of view, composites of C_6, C_{18} templated mesoporous Ti and Nb oxides could have been synthesised and subsequently subjected to variable temperature EIS to record their proton conductivity. By opening the research up in such a way to encompass all the alternatives, it helps build an overall picture of the processes at hand. Chapter four focused on synthesis of the most promising composite via a new in-situ polymerization approach. However, research into a further eight composites (C_6, C_{12}, C_{18} Ti, Ta and C_6, C_{12} Nb) using the *in situ* technique still remains unexplored. Whilst performing research in this area may not necessarily yield improved results, I believe it would cement the findings of Chapter four, by optimising all samples for the next stage, and to fully bring this part of the project to a close by completing the story.

Naturally, there are further alternatives. Previous work[10] has seen mesoporous transition metal oxides doped with phosphate anions. By treating a mesoporous transition

metal oxide in this manner one creates a solid acid catalyst with high ratio of Lewis acidity to Brønsted acidity. While phosphates may well give similar results to sulphate, it is a good start point due to the familiarity of the process. From here, the work can be expanded with various other dopants and a study of changing the composite ratios to record the effects on proton conductivity can be undertaken. Substituting the NSF for a similarly small oligomer resin is another path to go down and one such example is melamine sulphonate resin. Melamine sulfonate formaldehyde oligomers are of interest towards this project because the resin itself can be further cross linked with more formaldehyde, so after doping into the pores adding more formaldehyde could potentially "lock" them in. Doing this is likely to stop (or at least suppress) the thermal leaching of the resin at higher temperatures, but the unknown factor is how this will affect the proton conductivity of this new system. Similarly, solid state NMR studies would be applicable here to determine and track the mobile proton species, in addition to confirming whether or not synergistic relationships between mesoporous transition metal materials and oligomeric resins are an isolated phenomenon.

In the past, researchers have synthesised mesoporous transitions metal oxides from all of the suitable transition metals and characterised them to the point where doping them with small amounts of other metals is routine practice. However, mixed metal composites could possibly show potential as they do in solar cell research.[11–13] Here it is seen that doping TiO_2 structures with Ta can improve cell efficiency and it is possible that this can be applied to mesoporous transition metal oxides, either by enhancing the inexpensive mesoporous Ti composites or by adding mesoporous Ta to mesoporous Nb

(or any other metal on the periodic table) at the other end of the scale to find the optimal amounts needed to boost conductivity. On the other hand, doping mesoporous silica with a mesoporous transition metal could yield some interesting results in terms of stabilising the structure as mesoporous silicas are more stable than those constructed with transition metals. Finally, there remains the ultimate test of this material: the formation of a membrane and consequent testing of said membrane. Membrane fabrication is often done by the solution casting and solvent evaporation technique,[14,15] but for this to occur and suitably binder is required the composite and it is likely that this would need to be experimentally determined. Leading candidates for this include more formaldehyde, Cashew's reagent, or even a small chloropolymer, however, each binder runs the risk of diluting the conductivity of the composite by potentially breaking up the network between individual pores, and thus a lot of work may be needed to remedy this.

References

[1] Cao. Y., Liu. K., Riley. J. T., Pan W.-P. (2004). Application of a circulating fluidized-bed process for the chemical looping combustion of solid fuels. *Prepr. Pap.-Am. Chem. Soc., Div. Fuel. Chem.*, *49*(2), 815

[2] Dyer. C. K. (2002). Fuel cells for portable applications. *Fuel Cells Bull.*, *2002*(8), 9.

[3] Tang. H. L., Pan. M. (2008). Synthesis and characterization of a self-assembled Nafion/silica nanocomposite membrane for polymer electrolyte membrane fuel cells. *J. Phys. Chem. C, 112,* 11556–11568.

[4] Li. Q., He. R., Jensen. J. O., Bjerrum. N. J. (2003). Approaches and recent development of polymer electrolyte membranes for fuel cells operating above 100 °C. *Chem. Mater., 15,* 4896–4915.

[5] Bertoncello. P., Notargiacomo. A., Nicolini. C. (2005). Langmuir−Schaefer films of nafion with incorporated TiO_2 nanoparticles. *Langmiur*, *21*(1), 172-177

[6] Rhee. C. H., Kim. H. K., Chang. H., Lee. J. S. (2005). Nafion/sulfonated montmorillonite composite: a new concept electrolyte membrane for direct methanol fuel cells. *Chem. Mater*., *17*, 1691–1697.

[7] Sayari. A., Hamoudi. S. (2001). Periodic mesoporous silica-based organic−inorganic nanocomposite materials. *Chem. Mater*., *13*, 3151–3168.

[8] Stein Sr. E. W., Clearfield. A., Subramanian. M. A. (1996). Conductivity of group IV metal sulfophosphonates and a new class of interstratified metal amine-sulfophosphonates. *Solid State Ionics*, *83*, 113-124

[9] Rao. Y., Kang. J., Antonelli. D. (2008). 1-hexene isomerization over sulfated mesoporous Ta oxide: the effects of active site and confinement. *J. Am. Chem. Soc*., *130*, 394–395.

[10] Rao. Y., Trudeau. M., Antonelli. D. (2006). Sulfated and phosphated mesoporous Nb oxide in the benzylation of anisole and toluene by benzyl alcohol. *J. Am. Chem. Soc*., *128*, 13996–13997.

[11] Ghosh. R. (2012). Increasing photocurrents in dye sensitized solar cells with tantalum-doped titanium oxide photoanodes obtained by laser ablation. *ACS Appl. Mater. Interfaces*, *4*, 4566–4570.

[12] Feng. X., Shankar. K., Paulose. M., Grimes. C. A. (2009). Tantalum-doped titanium dioxide nanowire arrays for dye-sensitized solar cells with high open-circuit voltage. *Angew. Chem. Int. Ed*., *48*, 8095–8098.

[13] Liu. J., Yang. H., Tan. W., Zhou. X., Lin. Y. (2010) Photovoltaic performance improvement of dye-sensitized solar cells based on tantalum-doped TiO_2 thin films. *Electochimica Acta*, *56*, 396-400

[14] Smitha. B., Sridhar. S. & Khan. A. A. (2003). Synthesis and characterization of proton conducting polymer membranes for fuel cells. *J. Membr. Sci*., *225*, 63–76.

[15] Sankir. M., Harrison. W. L., Wiles. K. B., Li. Y., McGrath. J. E. (2004). Proton exchange membrane fuel cells: I. synthesis and characterization of disulfonated poly (arylene ether benzonitrile) copolymers. *Prepr. Pap.-Am. Chem. Soc., Div. Fuel Chem*., *49*(2), 526.

Chapter 7: Appendices

Appendix 1: Supporting Information for Chapter 2

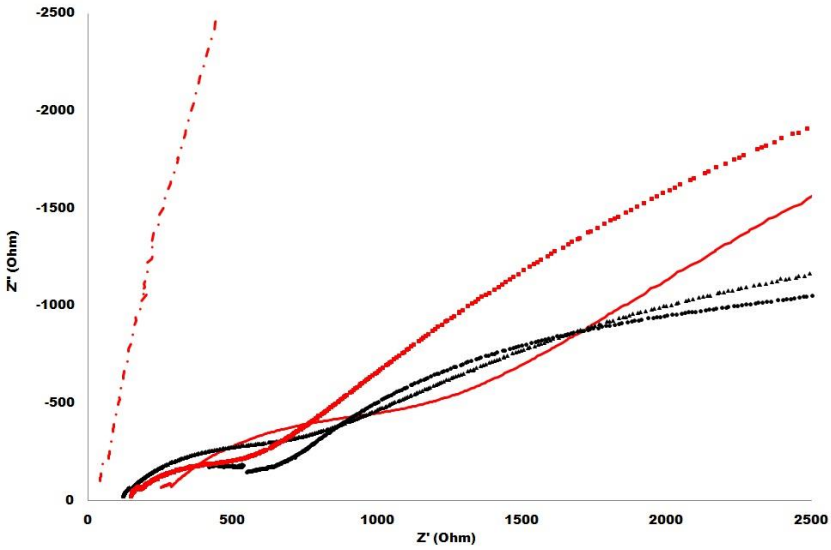

Figure 7.1: Nyquist plot showing the potentiostatic impedance of $mTiO_2$-NSF.H_2O (red squares), $mTiO_2$-NSF.DEE (black triangles), $mTiO_2(SO_4)$-NSF.H_2O (red line), $mTiO_2(SO_4)$-NSF.DEE (black dots) and Nafion 117 (red dots and dashes) at 50 °C

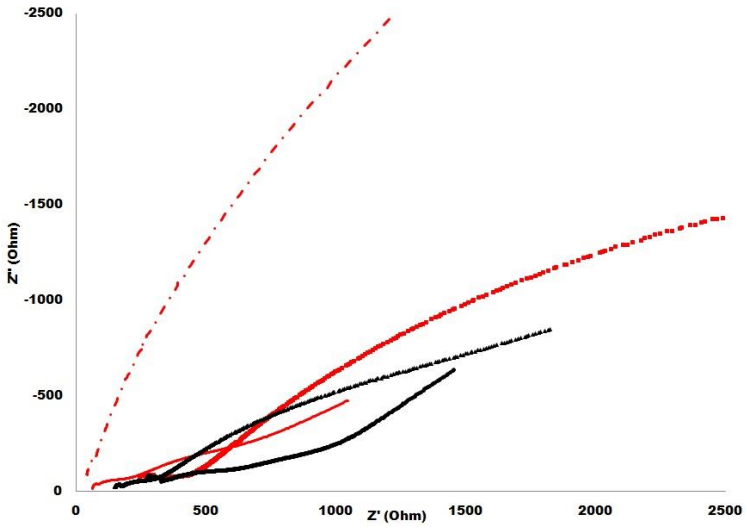

Figure 7.2: Nyquist plot showing the potentiostatic impedance of $mTiO_2$-NSF.H_2O (red squares), $mTiO_2$-NSF.DEE (black triangles), $mTiO_2(SO_4)$-NSF.H_2O (red line), $mTiO_2(SO_4)$-NSF.DEE (black dots) and Nafion 117 (red dots and dashes) at 75 °C

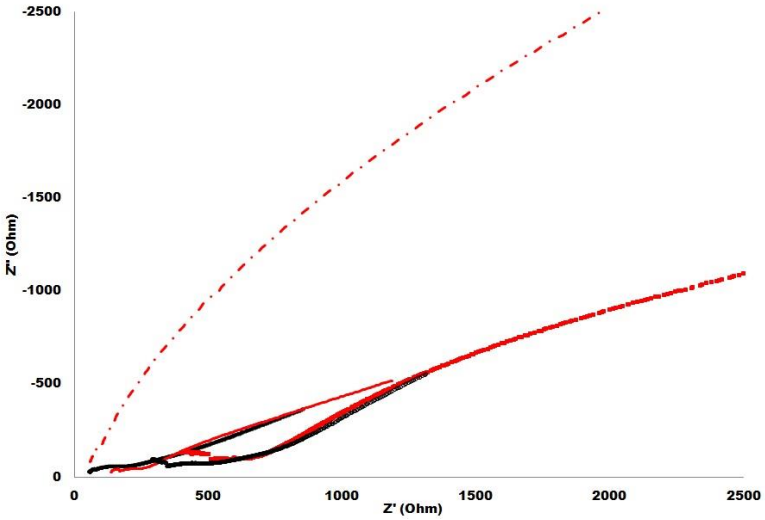

Figure 7.3: Nyquist plot showing the potentiostatic impedance of $mTiO_2$-NSF.H_2O (red squares), $mTiO_2$-NSF.DEE (black triangles), $mTiO_2(SO_4)$-NSF.H_2O (red line), $mTiO_2(SO_4)$-NSF.DEE (black dots) and Nafion 117 (red dots and dashes) at 100 °C

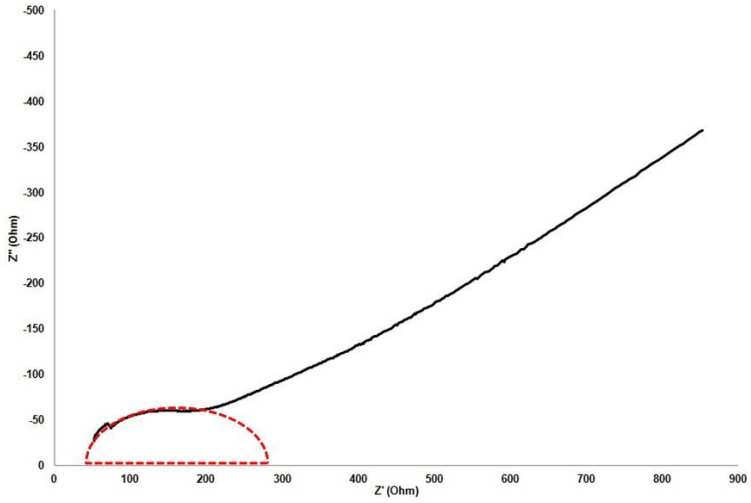

Figure7.4: Magnified Nyquist plot of $mTiO_2$-NSF.DEE at 100 °C (Figure 7.3, black triangle) displaying a semi circular relationship before a Warburg Tail

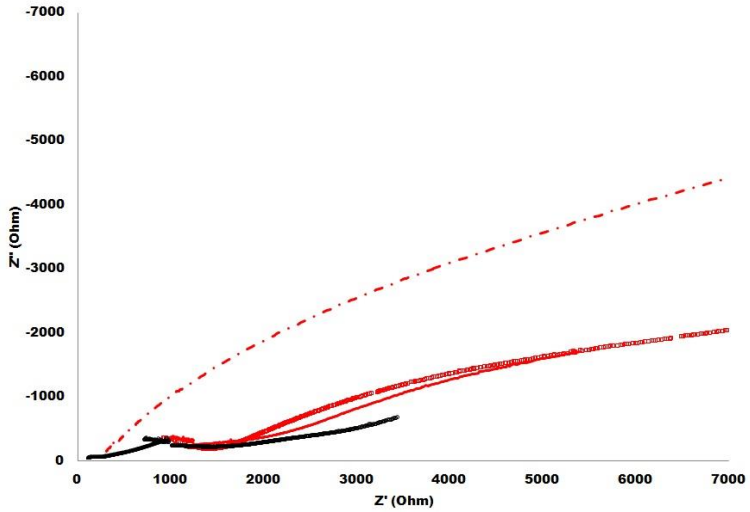

Figure 7.5: Nyquist plot showing the potentiostatic impedance of $mTiO_2$-NSF.H_2O (red squares), $mTiO_2$-NSF.DEE (black triangles), $mTiO_2(SO_4)$-NSF.H_2O (red line), $mTiO_2(SO_4)$-NSF.DEE (black dots) and Nafion 117 (red dots and dashes) at 125 °C

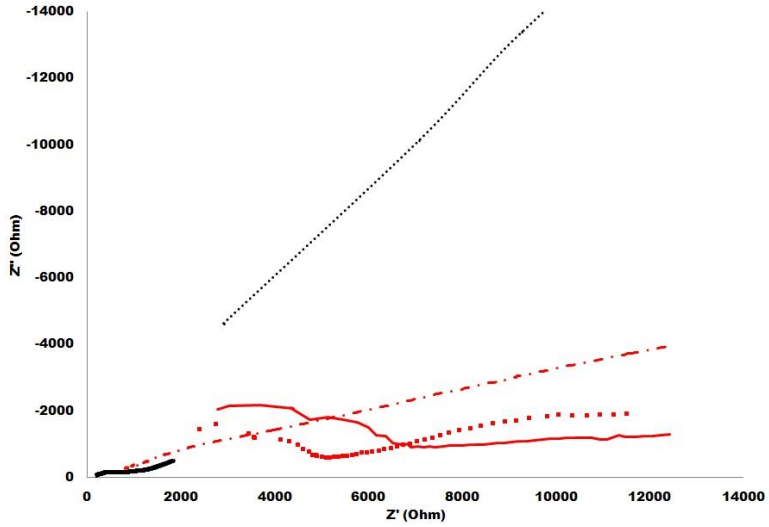

Figure 7.6: Nyquist plot showing the potentiostatic impedance of $mTiO_2$-NSF.H_2O (red squares), $mTiO_2$-NSF.DEE (black triangles), $mTiO_2(SO_4)$-NSF.H_2O (red line), $mTiO_2(SO_4)$-NSF.DEE (black dots) and Nafion 117 (red dots and dashes) at 150 °C

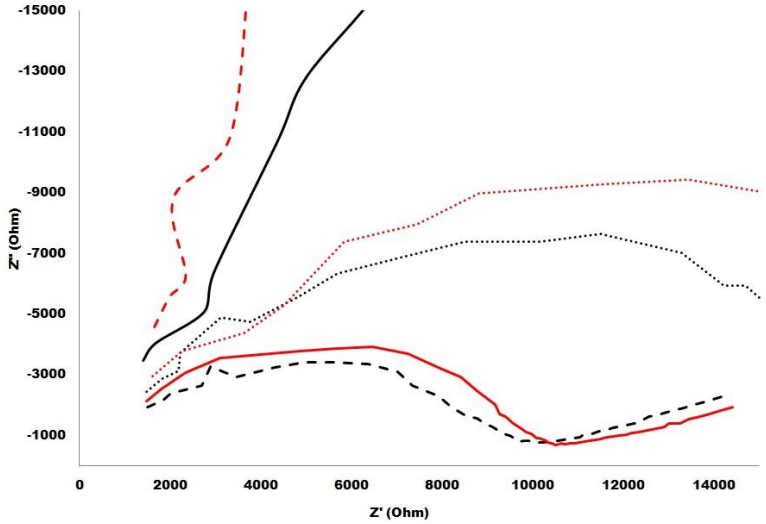

Figure 7.7: Nyquist plot for $mTiO_2$ at 25 °C (black line), 50 °C (black dots), 75 °C (black dashes), 100 °C (red line), 125 °C (red dots), 150 °C (red dashes)

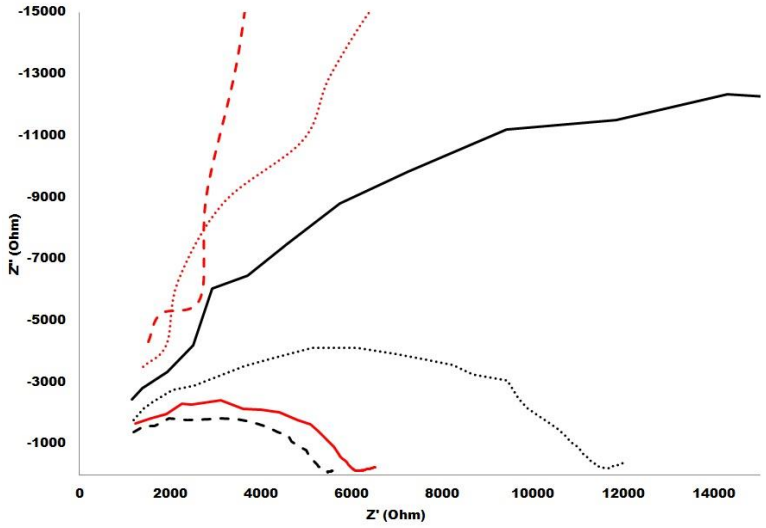

Figure 7.8: Nyquist plot for $mTiO_2(SO_4)$ at 25 °C (black line), 50 °C (black dots), 75 °C (black dashes), 100 °C (red line), 125 °C (red dots), 150 °C (red dashes)

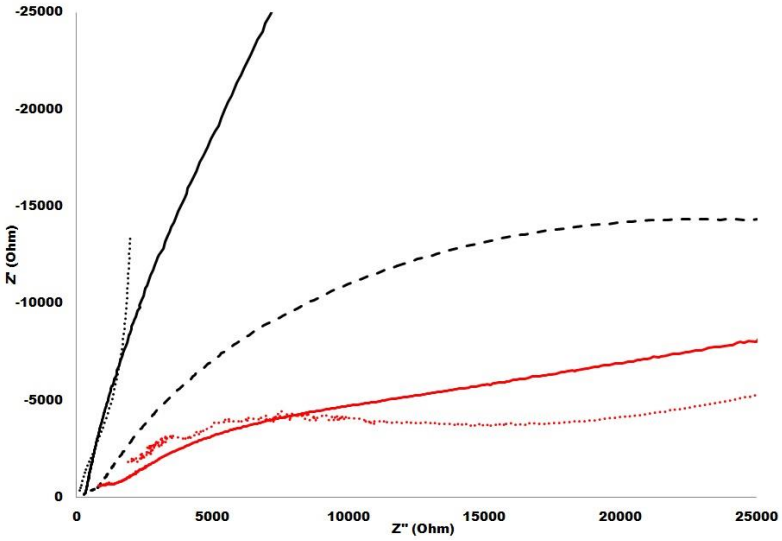

Figure 7.9: Nyquist plot for NSF at 25 °C (black line), 50 °C (black dots), 75 °C (black dashes), 100 °C (red line), 125 °C (red dots)

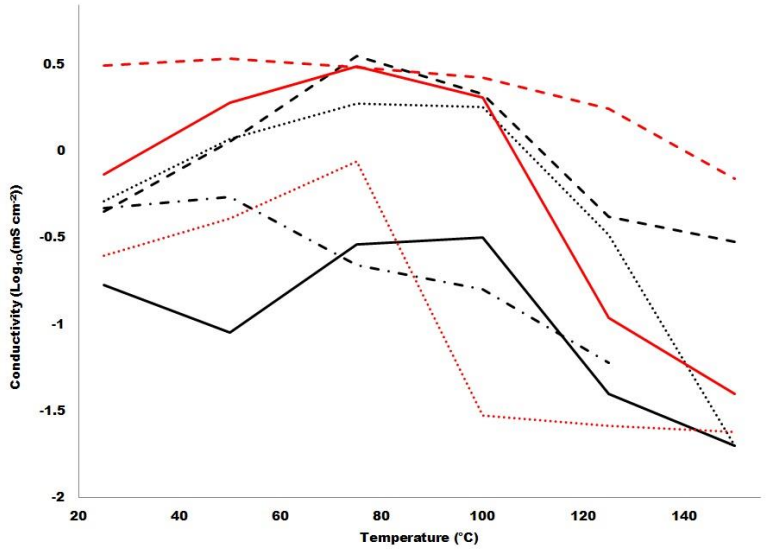

Figure 7.10: Proton conductivities of $mTiO_2$ (black line), mTiO2-NSF.H_2O (black dots), $mTiO_2$-NSF.DEE (black dashes), $mTiO_2(SO_4)$ (black dots and dashes), $mTiO_2(SO_4)$-NSF.H_2O (red line), $mTiO_2(SO_4)$-NSF.DEE (red dots) and Nafion 117 (red dashes) as a function of temperature

Appendix 2: Supporting Information for Chapter 3

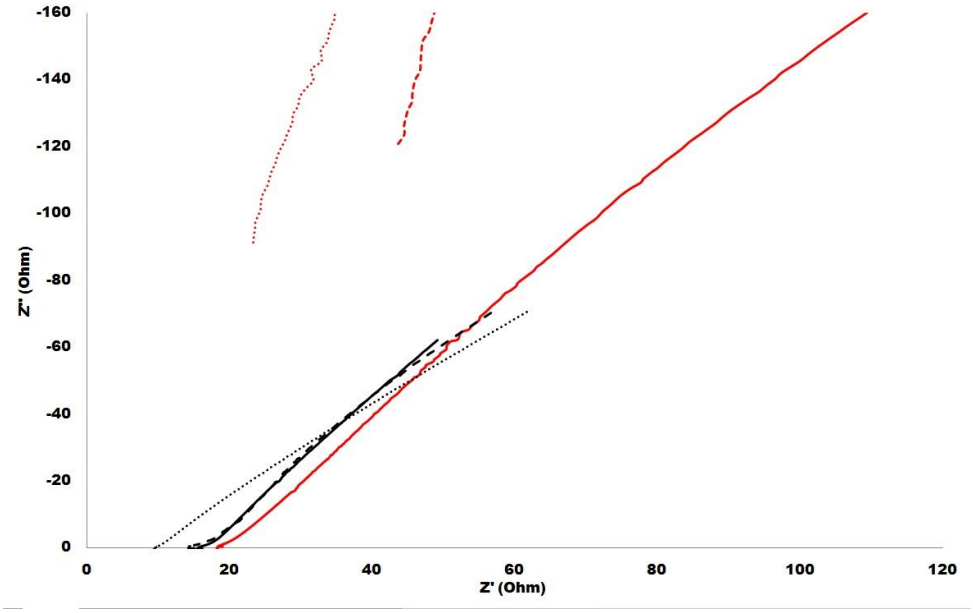

Figure 7.11: Nyquist plot at 50 °C showing the potentiostatic impedance of C_{12}-m$Ta_2O_5(SO_4)$-NSF.DEE (black line), C_6-m$Ta_2O_5(SO_4)$-NSF.DEE (black dots), C_{18}-m$Ta_2O_5(SO_4)$-NSF.DEE (black dashes), C_{12}-m$Nb_2O_5(SO_4)$-NSF.DEE (red line), Nafion 117 film (red dots) and Nafion 117 pellet (red dashes)

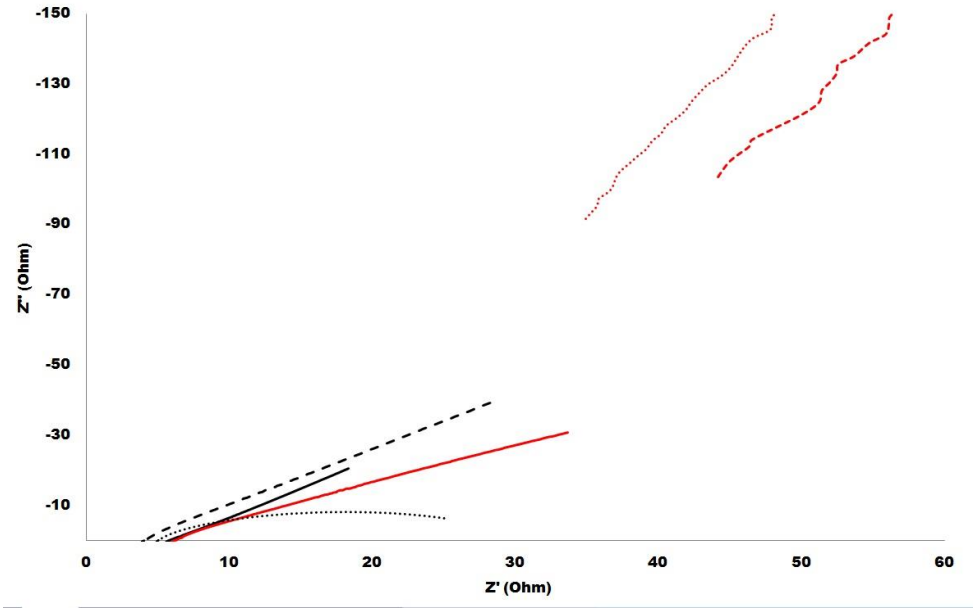

Figure 7.12: Nyquist plot at 75 °C showing the potentiostatic impedance of C_{12}-m$Ta_2O_5(SO_4)$-NSF.DEE (black line), C_6-m$Ta_2O_5(SO_4)$-NSF.DEE (black dots), C_{18}-m$Ta_2O_5(SO_4)$-NSF.DEE (black dashes), C_{12}-m$Nb_2O_5(SO_4)$-NSF.DEE (red line), Nafion 117 film (red dots) and Nafion 117 pellet (red dashes)

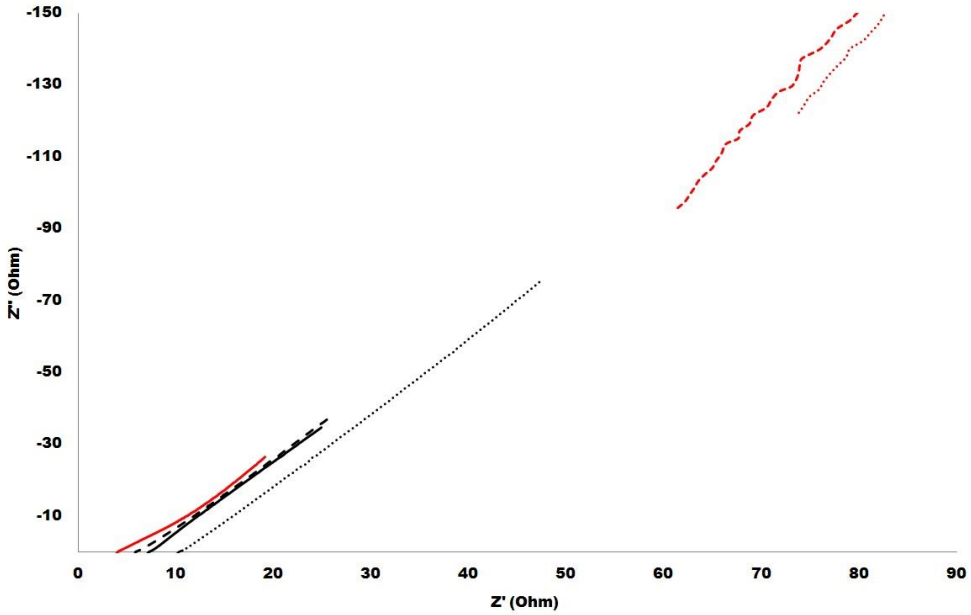

Figure 7.13: Nyquist plot at 100 °C showing the potentiostatic impedance of C_{12}-$mTa_2O_5(SO_4)$-NSF.DEE (black line), C_6-$mTa_2O_5(SO_4)$-NSF.DEE (black dots), C_{18}-$mTa_2O_5(SO_4)$-NSF.DEE (black dashes), C_{12}-$mNb_2O_5(SO_4)$-NSF.DEE (red line), Nafion 117 film (red dots) and Nafion 117 pellet (red dashes)

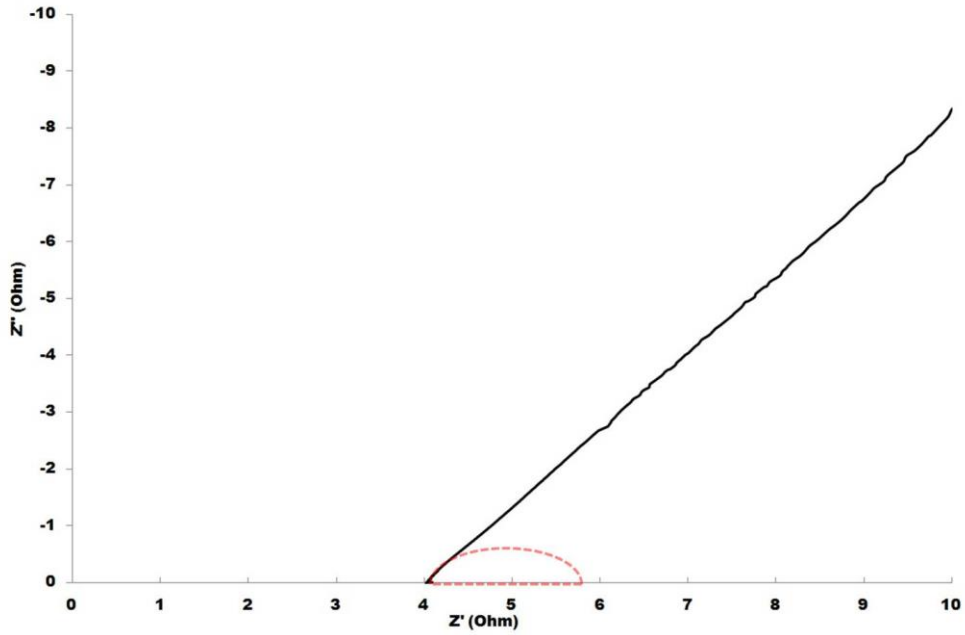

Figure 7.14: Magnified Nyquist plot of C_{12}-$mTa_2O_5(SO_4)$-NSF.DEE at 100 °C (Figure S15, black line) displaying a semi circular relationship before a Warburg Tail.

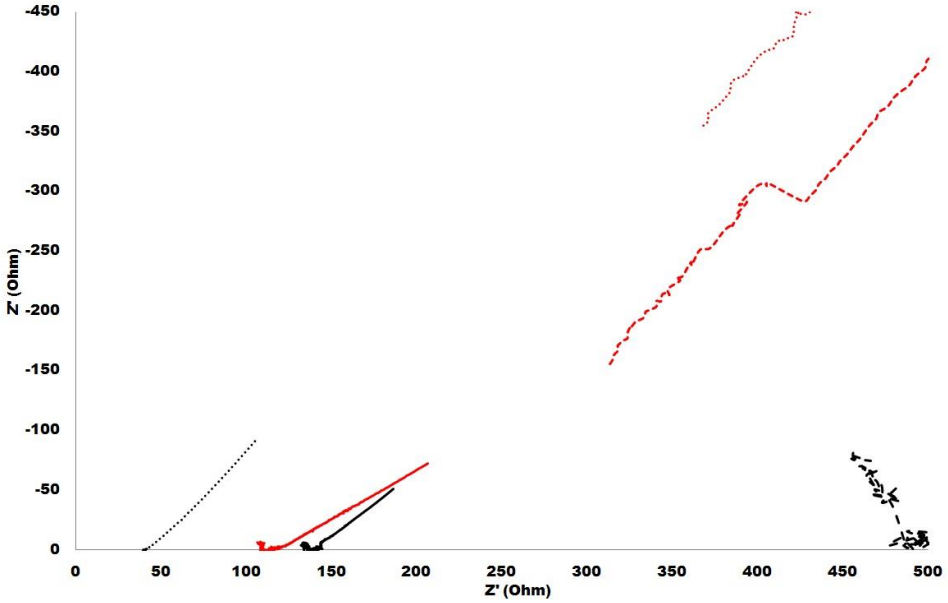

Figure 7.15: Nyquist plot at 125 °C showing the potentiostatic impedance of C_{12}-$mTa_2O_5(SO_4)$-NSF.DEE (black line), C_6-$mTa_2O_5(SO_4)$-NSF.DEE (black dots), C_{18}-$mTa_2O_5(SO_4)$-NSF.DEE (black dashes), C_{12}-$mNb_2O_5(SO_4)$-NSF.DEE (red line), Nafion 117 film (red dots) and Nafion 117 pellet (red dashes)

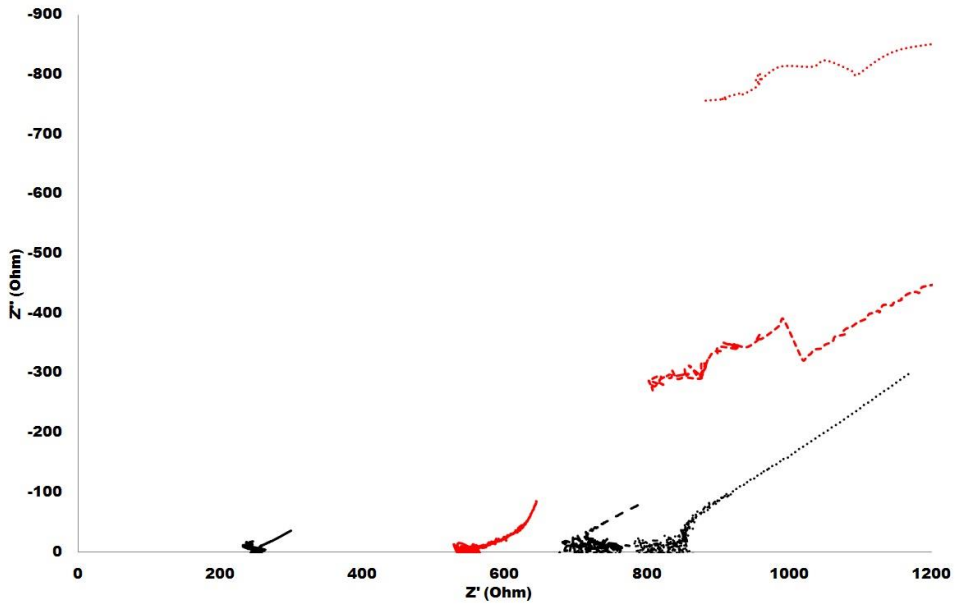

Figure 7.16: Nyquist plot at 150 °C showing the potentiostatic impedance of C_{12}-$mTa_2O_5(SO_4)$-NSF.DEE (black line), C_6-$mTa_2O_5(SO_4)$-NSF.DEE (black dots), C_{18}-$mTa_2O_5(SO_4)$-NSF.DEE (black dashes), C_{12}-$mNb_2O_5(SO_4)$-NSF.DEE (red line), Nafion 117 film (red dots) and Nafion 117 pellet (red dashes)

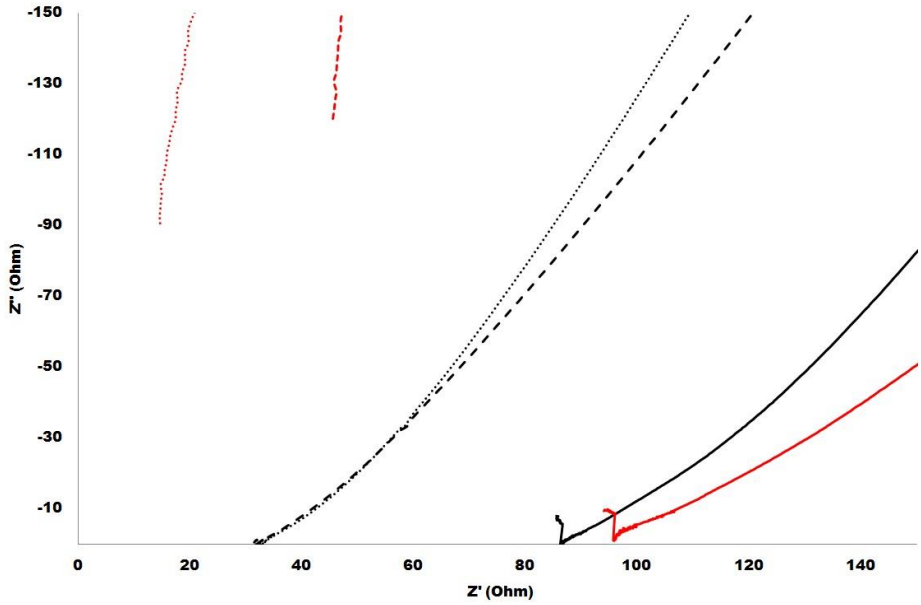

Figure 7.17: Nyquist plot at 25 °C showing the potentiostatic impedance of C_{12}-mTa_2O_5-NSF.H_2O (black line), C_{12}-mTa_2O_5-NSF.DEE (red line), C_{12}-$mTa_2O_5(SO_4)$-NSF.H_2O (black dashes), C_{12}-$mTa_2O_5(SO_4)$-NSF.DEE (black dots), Nafion 117 film (red dots) and Nafion 117 pellet (red dashes)

Appendix 3: Supporting Information for Chapter 4

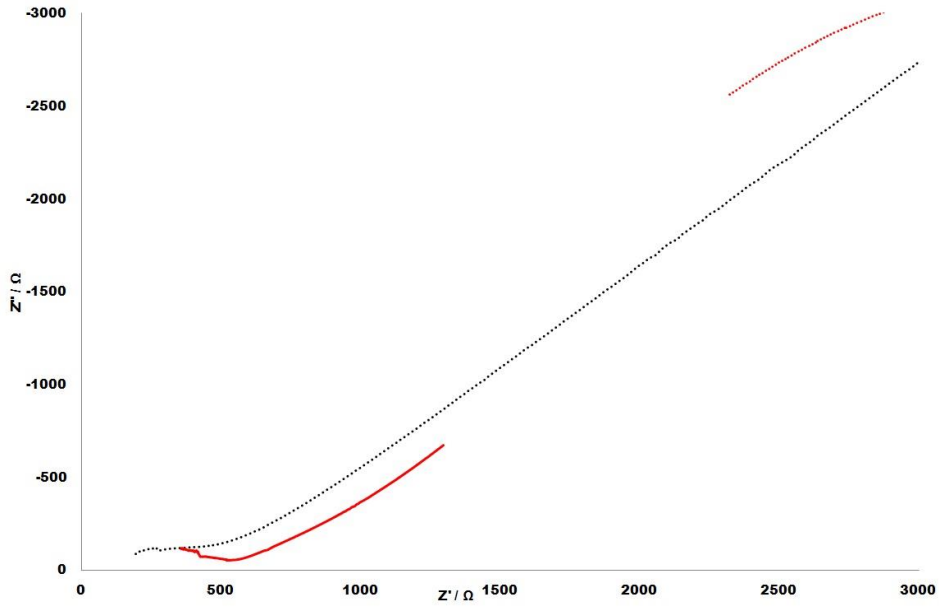

Figure 7.18: Nyquist plots at 20 °C showing the potentiostatic impedance spectrum of $mNb_2O_5(SO_4)$-NSF (black dots), $mNb_2O_5(SO_4)$-NSF(110%) (red line), mNb_2O_5-NSF(110%) (red dots)

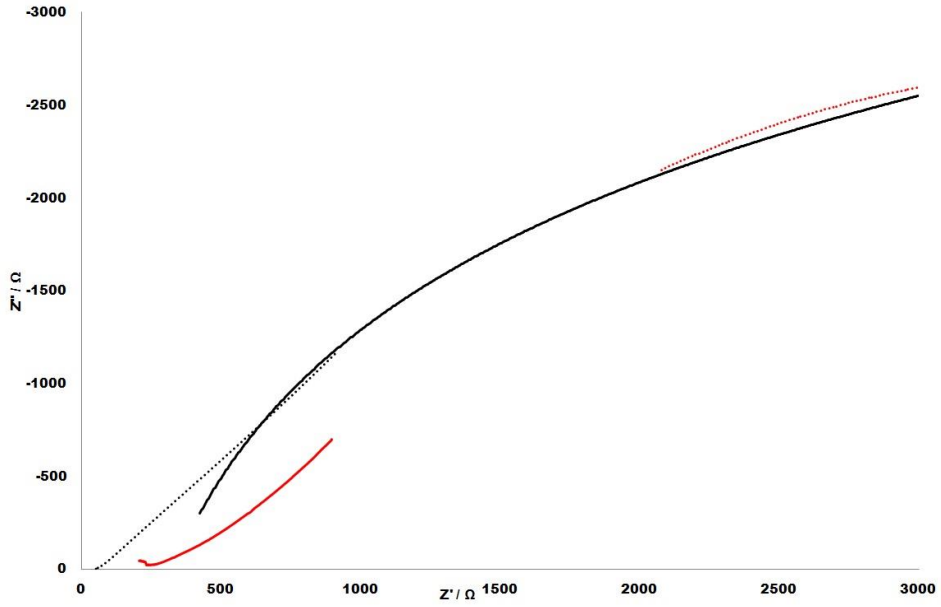

Figure 7.19: Nyquist plots at 25 °C showing the potentiostatic impedance spectrum of mNb_2O_5-NSF (black line), $mNb_2O_5(SO_4)$-NSF (black dots), $mNb_2O_5(SO_4)$-NSF(110%) (red line), mNb_2O_5-NSF(110%) (red dots)

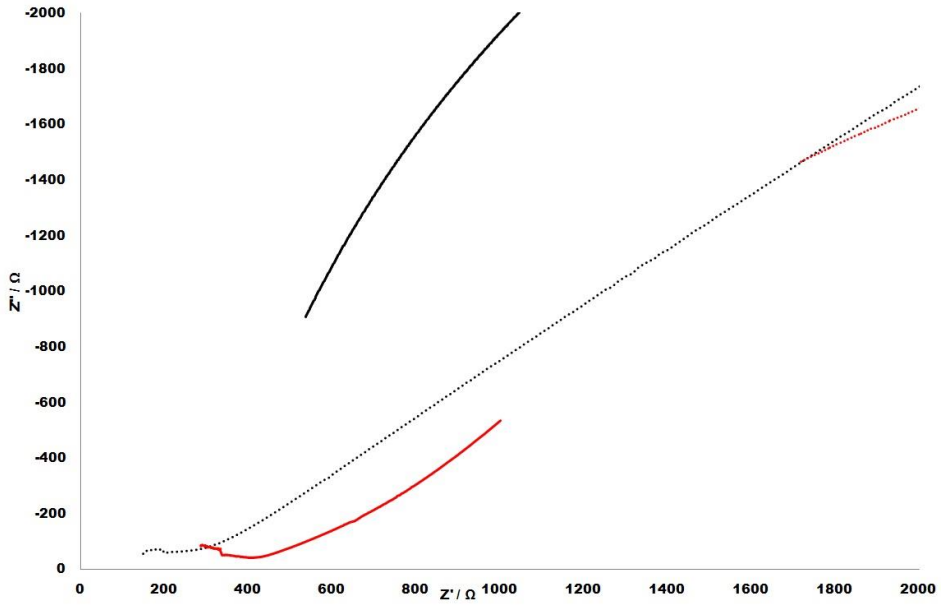

Figure 7.20: Nyquist plots at 30 °C showing the potentiostatic impedance spectrum of mNb_2O_5-NSF (black line), $mNb_2O_5(SO_4)$-NSF (black dots), $mNb_2O_5(SO_4)$-NSF(110%) (red line), mNb_2O_5-NSF(110%) (red dots)

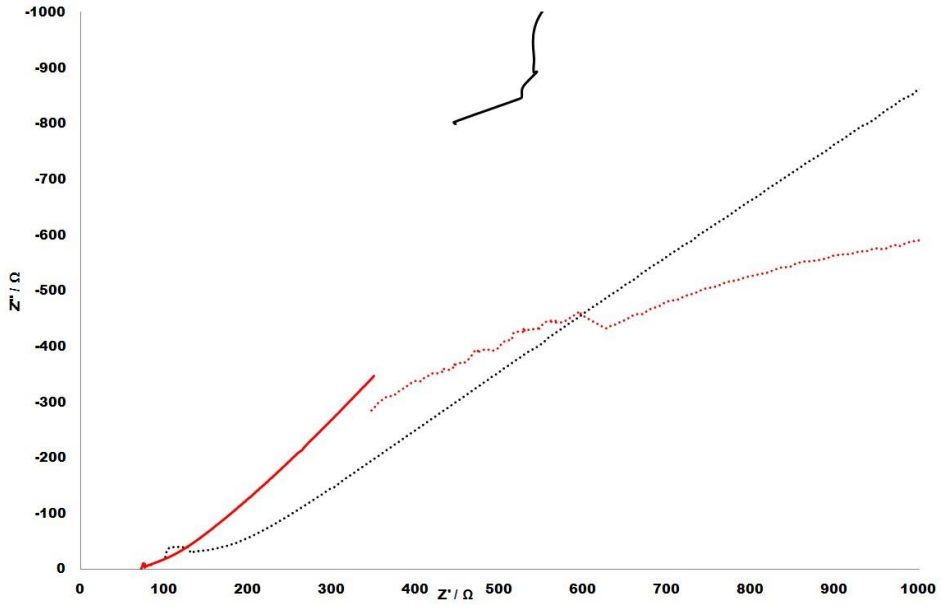

Figure 7.21: Nyquist plots at 40 °C showing the potentiostatic impedance spectrum of mNb_2O_5-NSF (black line), $mNb_2O_5(SO_4)$-NSF (black dots), $mNb_2O_5(SO_4)$-NSF(110%) (red line), mNb_2O_5-NSF(110%) (red dots)

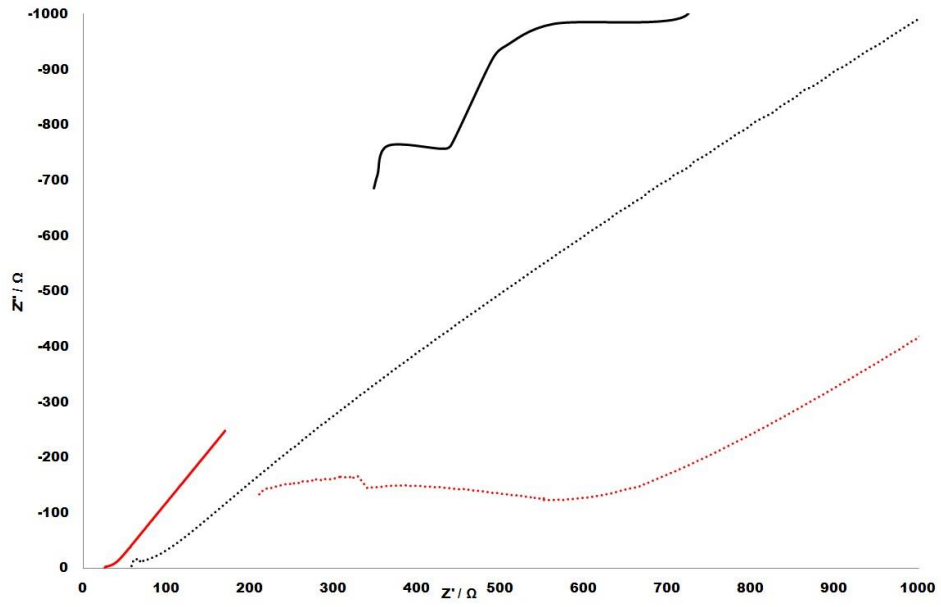

Figure 7.22: Nyquist plots at 50 °C showing the potentiostatic impedance spectrum of mNb_2O_5-NSF (black line), $mNb_2O_5(SO_4)$-NSF (black dots), $mNb_2O_5(SO_4)$-NSF(110%) (red line), mNb_2O_5-NSF(110%) (red dots)

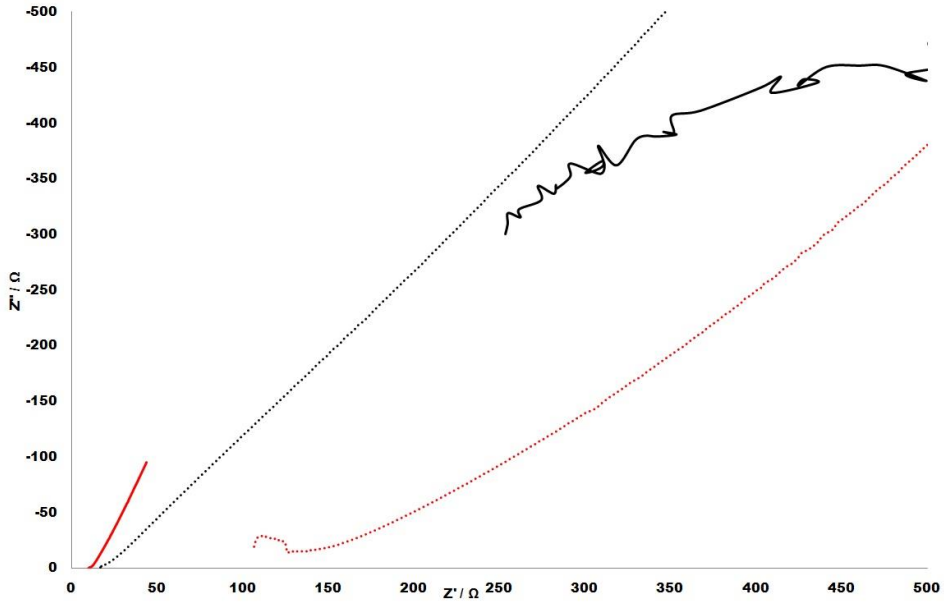

Figure 7.23: Nyquist plots at 60 °C showing the potentiostatic impedance spectrum of mNb_2O_5-NSF (black line), $mNb_2O_5(SO_4)$-NSF (black dots), $mNb_2O_5(SO_4)$-NSF(110%) (red line), mNb_2O_5-NSF(110%) (red dots)

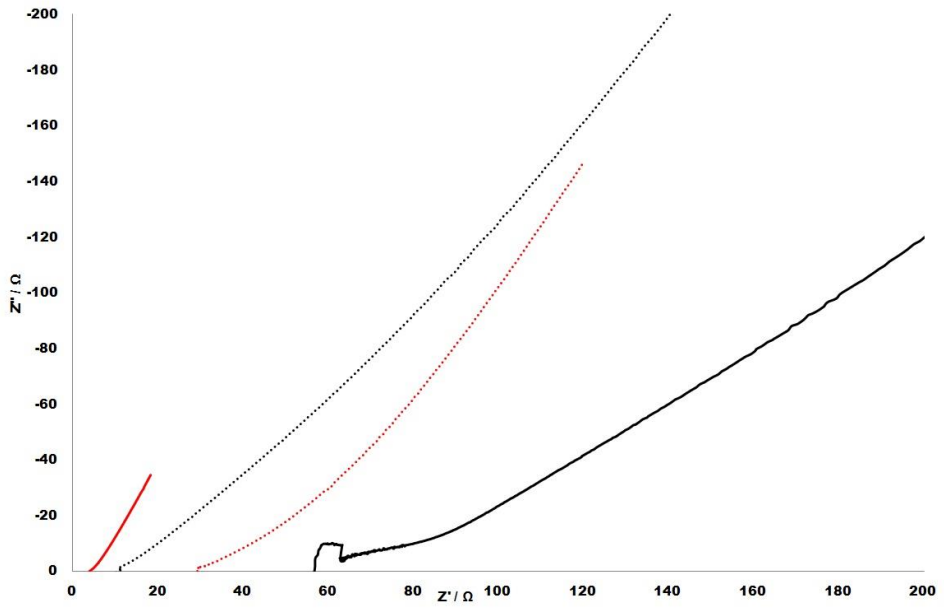

Figure 7.24: Nyquist plots at 70 °C showing the potentiostatic impedance spectrum of mNb_2O_5-NSF (black line), $mNb_2O_5(SO_4)$-NSF (black dots), $mNb_2O_5(SO_4)$-NSF(110%) (red line), mNb_2O_5-NSF(110%) (red dots)

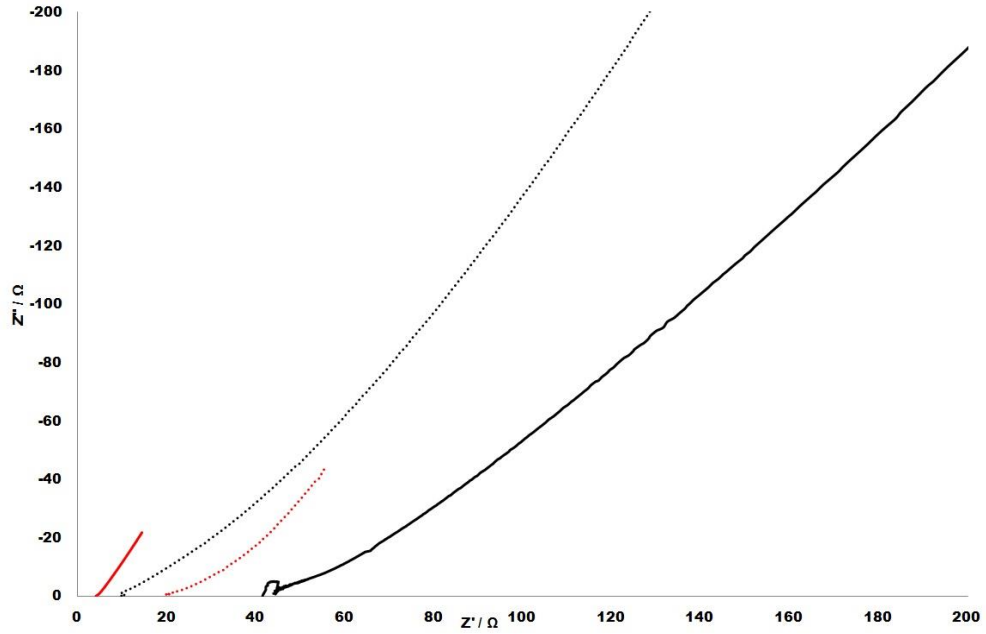

Figure 7.25: Nyquist plots at 80 °C showing the potentiostatic impedance spectrum of mNb_2O_5-NSF (black line), $mNb_2O_5(SO_4)$-NSF (black dots), $mNb_2O_5(SO_4)$-NSF(110%) (red line), mNb_2O_5-NSF(110%) (red dots)

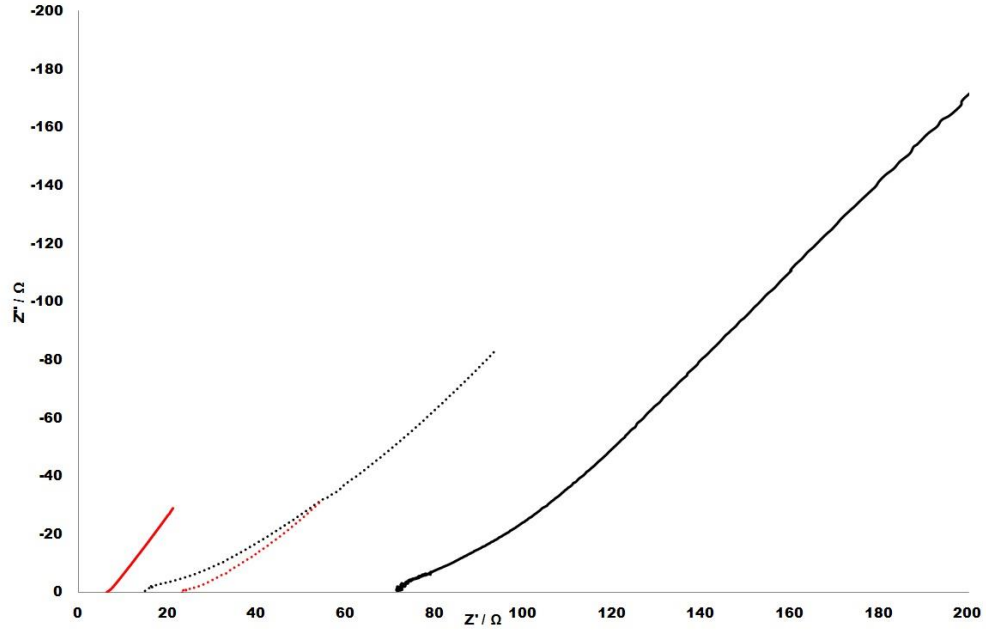

Figure 7.26: Nyquist plots at 90 °C showing the potentiostatic impedance spectrum of mNb_2O_5-NSF (black line), $mNb_2O_5(SO_4)$-NSF (black dots), $mNb_2O_5(SO_4)$-NSF(110%) (red line), mNb_2O_5-NSF(110%) (red dots)

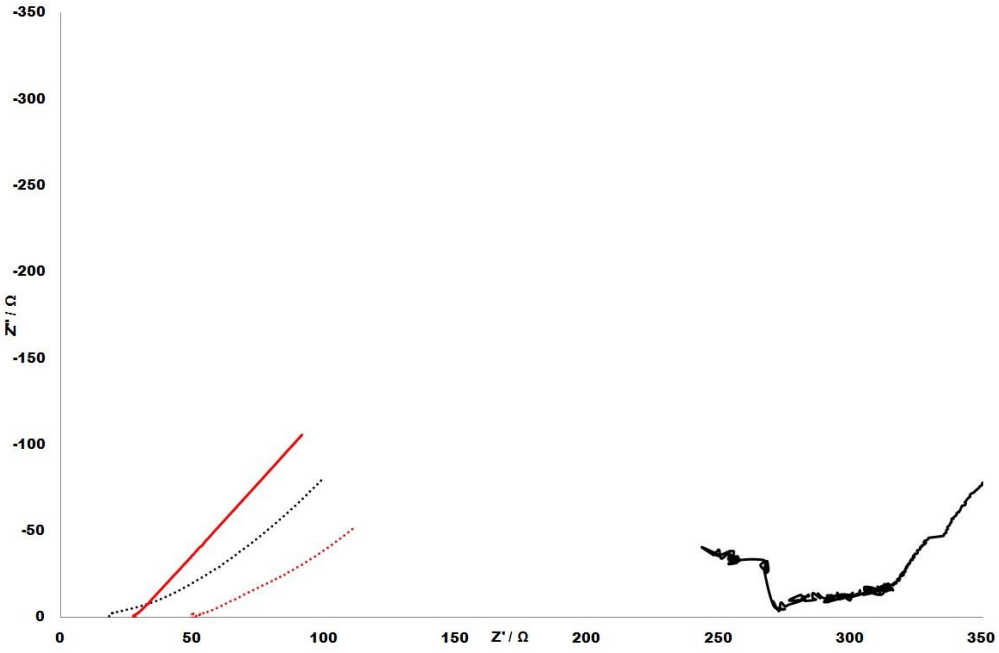

Figure 7.27: Nyquist plots at 100 °C showing the potentiostatic impedance of mNb_2O_5-NSF (black line), $mNb_2O_5(SO_4)$-NSF (black dots), $mNb_2O_5(SO_4)$-NSF(110%) (red line), mNb_2O_5-NSF(110%) (red dots)

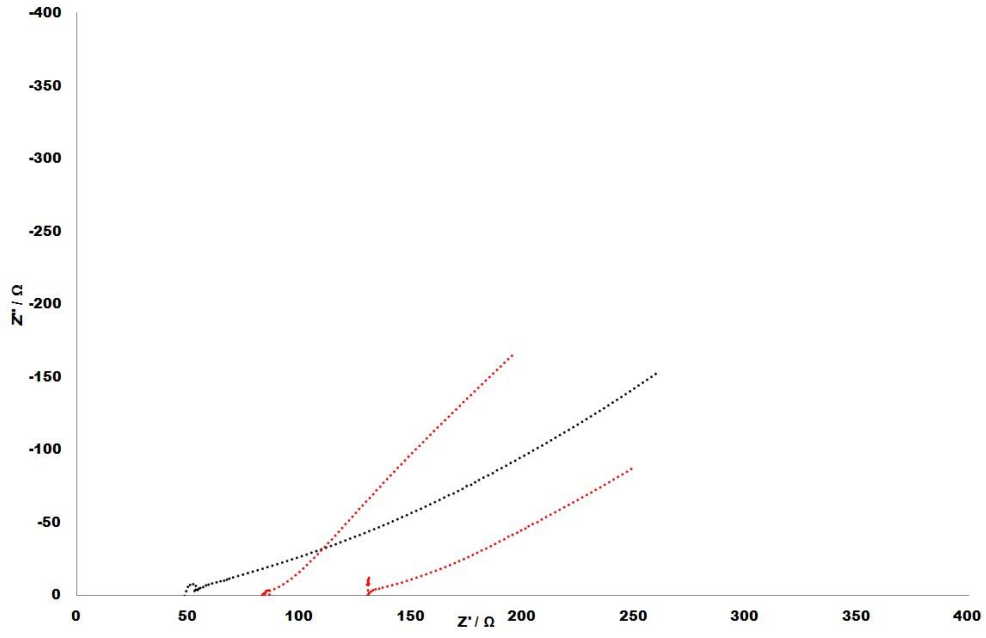

Figure 7.28: Nyquist plots at 110 °C showing the potentiostatic impedance spectrum of $mNb_2O_5(SO_4)$-NSF (black dots), $mNb_2O_5(SO_4)$-NSF(110%) (red line), mNb_2O_5-NSF(110%) (red dots)

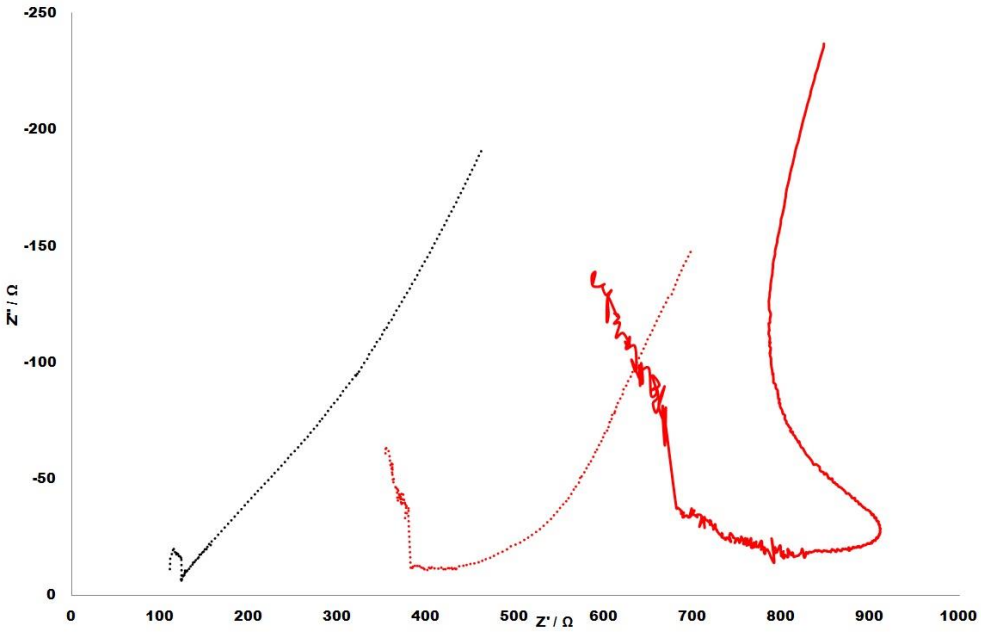

Figure 7.29: Nyquist plots at 120 °C showing the potentiostatic impedance spectrum of m$Nb_2O_5(SO_4)$-NSF (black dots), m$Nb_2O_5(SO_4)$-NSF(110%) (red line), mNb_2O_5-NSF(110%) (red dots)

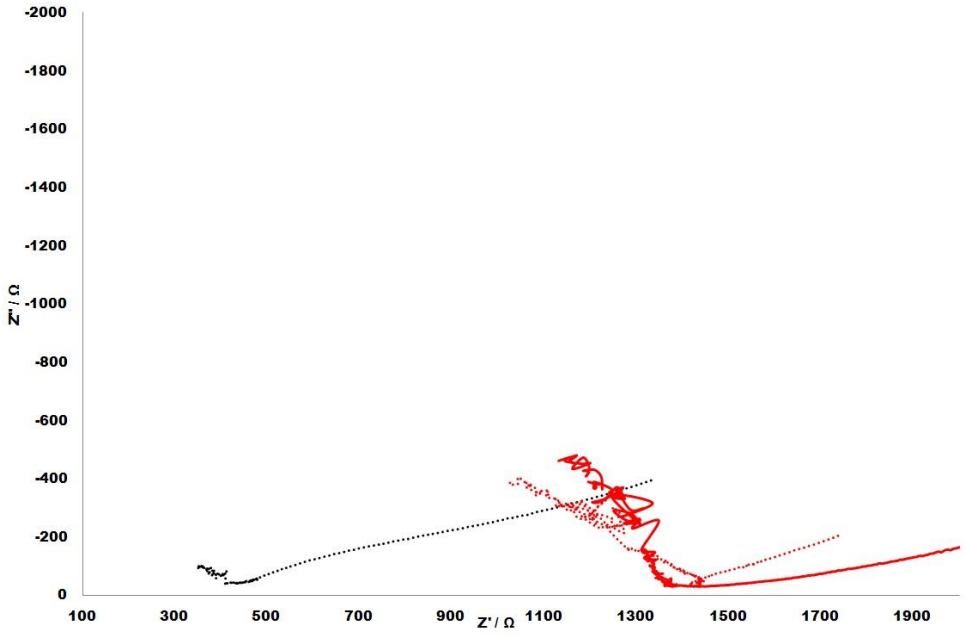

Figure 7.30: Nyquist plots at 130 °C showing the potentiostatic impedance spectrum of m$Nb_2O_5(SO_4)$-NSF (black dots), m$Nb_2O_5(SO_4)$-NSF(110%) (red line), mNb_2O_5-NSF(110%) (red dots)

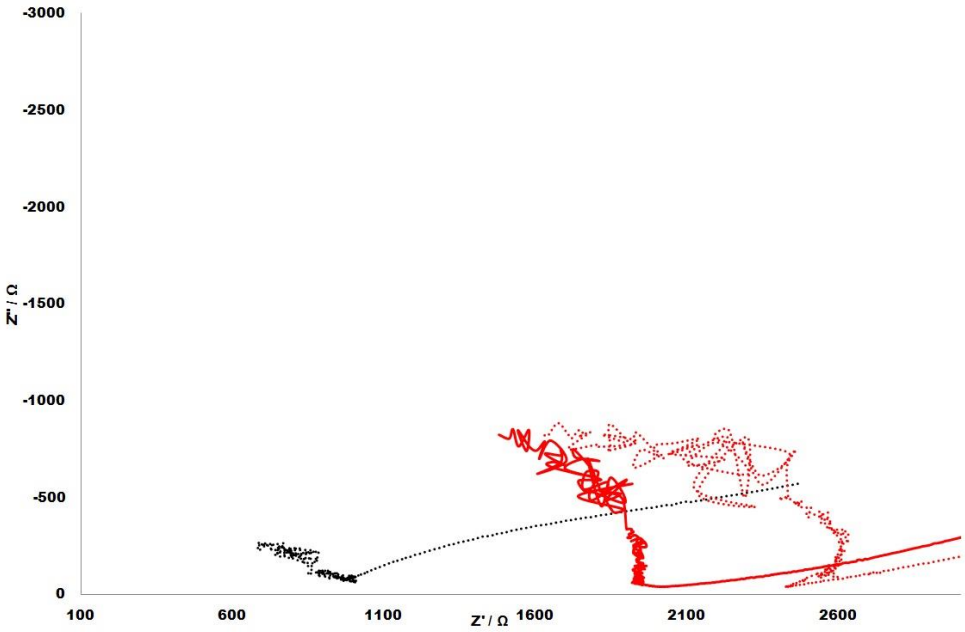

Figure 7.31: Nyquist plots at 140 °C showing the potentiostatic impedance spectrum of $mNb_2O_5(SO_4)$-NSF (black dots), $mNb_2O_5(SO_4)$-NSF(110%) (red line), mNb_2O_5-NSF(110%) (red dots)

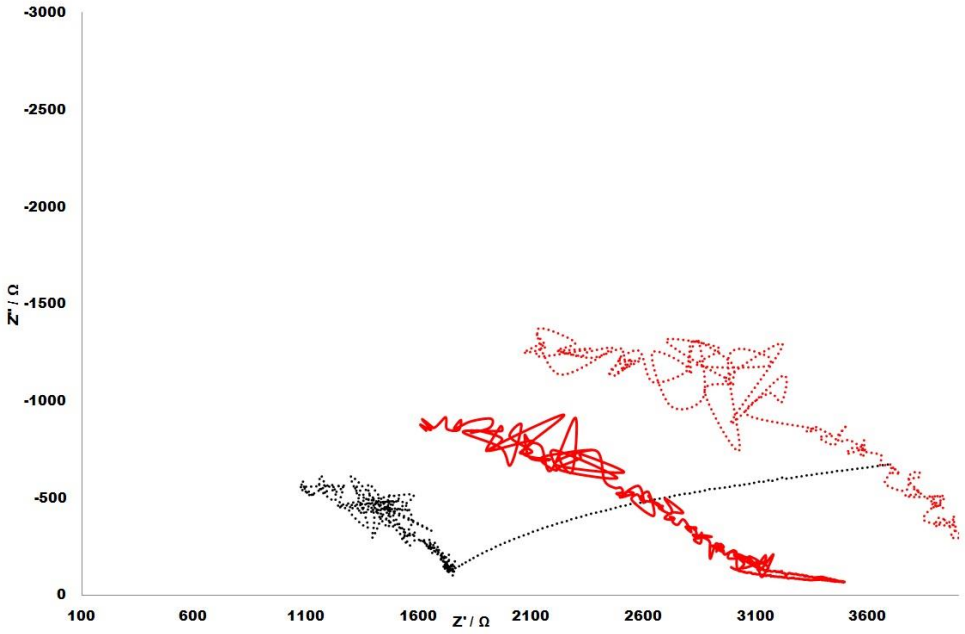

Figure 7.32: Nyquist plots at 150 °C showing the potentiostatic impedance spectrum of $mNb_2O_5(SO_4)$-NSF (black dots), $mNb_2O_5(SO_4)$-NSF(110%) (red line), mNb_2O_5-NSF(110%) (red dots)

Appendix 4: EIS experimental setup.

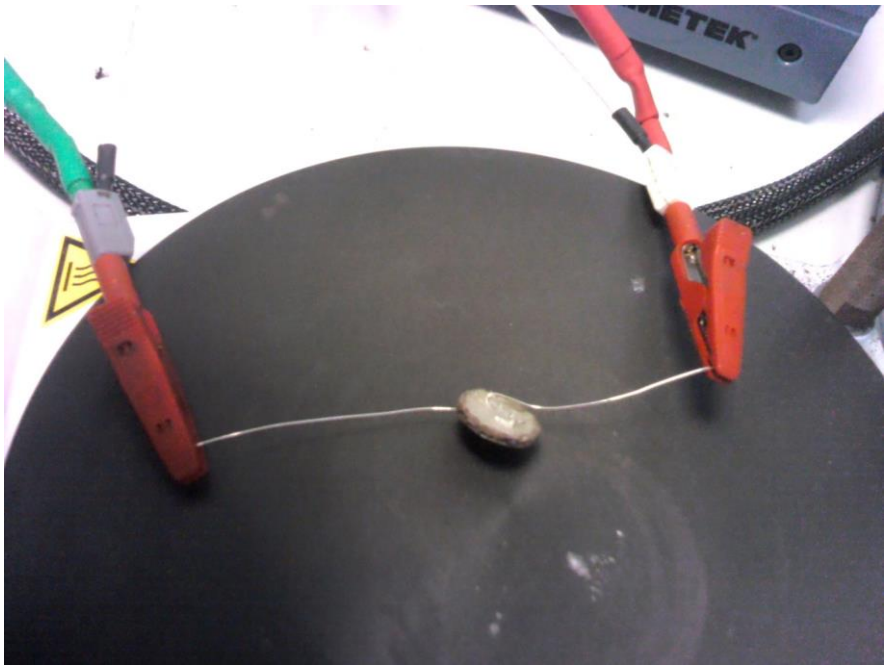

Figure 7.33: Cell set up using the two probe technique. The working and sense electrode are on one side, the counter and reference electrode are on the other

Appendix 5: Copyright forms

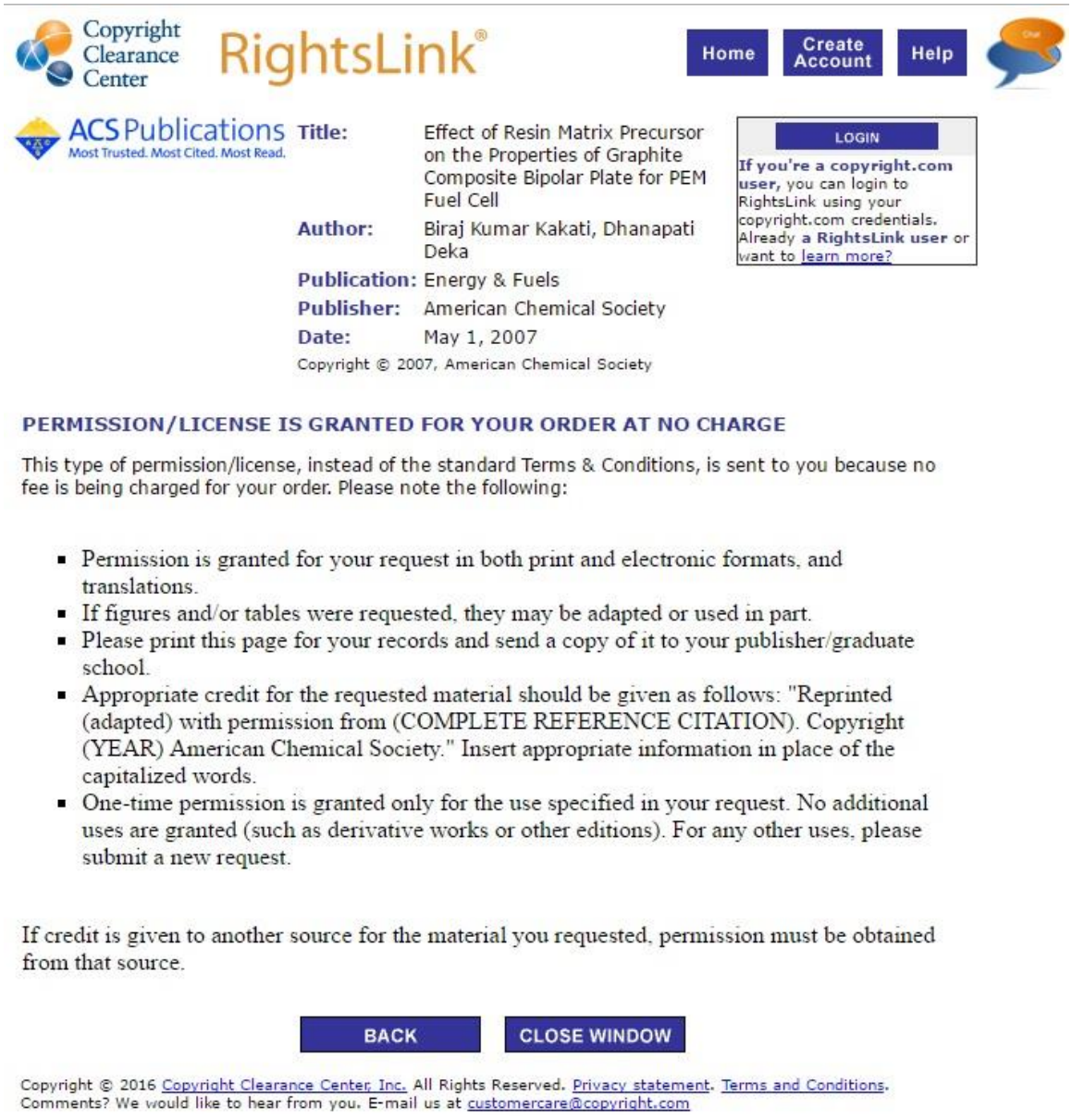

Copyright Clearance Center RightsLink®

Home | Create Account | Help

ACS Publications
Most Trusted. Most Cited. Most Read.

Title: Effect of Resin Matrix Precursor on the Properties of Graphite Composite Bipolar Plate for PEM Fuel Cell

Author: Biraj Kumar Kakati, Dhanapati Deka

Publication: Energy & Fuels

Publisher: American Chemical Society

Date: May 1, 2007

Copyright © 2007, American Chemical Society

LOGIN

If you're a copyright.com user, you can login to RightsLink using your copyright.com credentials. Already a RightsLink user or want to learn more?

PERMISSION/LICENSE IS GRANTED FOR YOUR ORDER AT NO CHARGE

This type of permission/license, instead of the standard Terms & Conditions, is sent to you because no fee is being charged for your order. Please note the following:

- Permission is granted for your request in both print and electronic formats, and translations.
- If figures and/or tables were requested, they may be adapted or used in part.
- Please print this page for your records and send a copy of it to your publisher/graduate school.
- Appropriate credit for the requested material should be given as follows: "Reprinted (adapted) with permission from (COMPLETE REFERENCE CITATION). Copyright (YEAR) American Chemical Society." Insert appropriate information in place of the capitalized words.
- One-time permission is granted only for the use specified in your request. No additional uses are granted (such as derivative works or other editions). For any other uses, please submit a new request.

If credit is given to another source for the material you requested, permission must be obtained from that source.

BACK | CLOSE WINDOW

Copyright © 2016 Copyright Clearance Center, Inc. All Rights Reserved. Privacy statement. Terms and Conditions.
Comments? We would like to hear from you. E-mail us at customercare@copyright.com

Figure 7.34: Permission to reproduce a figure from *Energy Fuels* 21, 1681-1687 (2007), for Figure 1.4 in Chapter 1

License Number	3977560815975
License date	Oct 28, 2016
Licensed Content Publisher	John Wiley and Sons
Licensed Content Publication	Journal of Polymer Science Part A: Polymer Chemistry
Licensed Content Title	The morphology in nafion perfluorinated membrane products, as determined by wide- and small-angle x-ray studies
Licensed Content Author	T. D. Gierke,G. E. Munn,F. C. Wilson
Licensed Content Date	Nov 1, 1981
Licensed Content Pages	18
Type of use	Dissertation/Thesis
Requestor type	University/Academic
Format	Electronic
Portion	Figure/table
Number of figures/tables	1
Original Wiley figure/table number(s)	Fig 1
Will you be translating?	No
Title of your thesis / dissertation	Synthesis and Characterisation of proton conducting composite materials resilient to dehydration at elevated temperatures
Expected completion date	Jan 2017
Expected size (number of pages)	240
Requestor Location	Jonathan P Turley AW110, Upper Glyntaff Campus University of South Wales Cemetery Road Pontypridd, Mig Glamorgan CF37 4BD United Kingdom Attn: Jonathan P Turley
Publisher Tax ID	EU826007151
Billing Type	Invoice
Billing address	Jonathan P Turley AW110, Upper Glyntaff Campus University of South Wales Cemetery Road Pontypridd, United Kingdom CF37 4BD Attn: Jonathan P Turley
Total	0.00 GBP

Figure 7.35: Permission to reproduce a figure from *J. Polym. Sci. Polym. Phys. Ed.* 19, 1687-1704 (1981), for Figure 1.6 in Chapter 1

License Number	3977570047317
License date	Oct 28, 2016
Licensed Content Publisher	Nature Publishing Group
Licensed Content Publication	Nature Materials
Licensed Content Title	Parallel cylindrical water nanochannels in Nafion fuel-cell membranes
Licensed Content Author	Klaus Schmidt-RohrandQiang Chen
Licensed Content Date	Jan 1, 2008
Licensed Content Volume	7
Licensed Content Issue	1
Type of Use	reuse in a dissertation / thesis
Requestor type	academic/educational
Format	electronic
Portion	figures/tables/illustrations
Number of figures/tables/illustrations	1
High-res required	no
Figures	2
Author of this NPG article	no
Your reference number	
Title of your thesis / dissertation	Synthesis and Characterisation of proton conducting composite materials resilient to dehydration at elevated temperatures
Expected completion date	Jan 2017
Estimated size (number of pages)	240
Requestor Location	Jonathan P Turley AW110, Upper Glyntaff Campus University of South Wales Cemetery Road Pontypridd, Mig Glamorgan CF37 4BD United Kingdom Attn: Jonathan P Turley
Billing Type	Invoice
Billing address	Jonathan P Turley AW110, Upper Glyntaff Campus University of South Wales Cemetery Road Pontypridd, United Kingdom CF37 4BD Attn: Jonathan P Turley
Total	0.00 USD

Figure 7.36: Permission to reproduce a figure from *Nat. Mater* 7, 75-83 (2008), for Figure 1.7 in Chapter 1

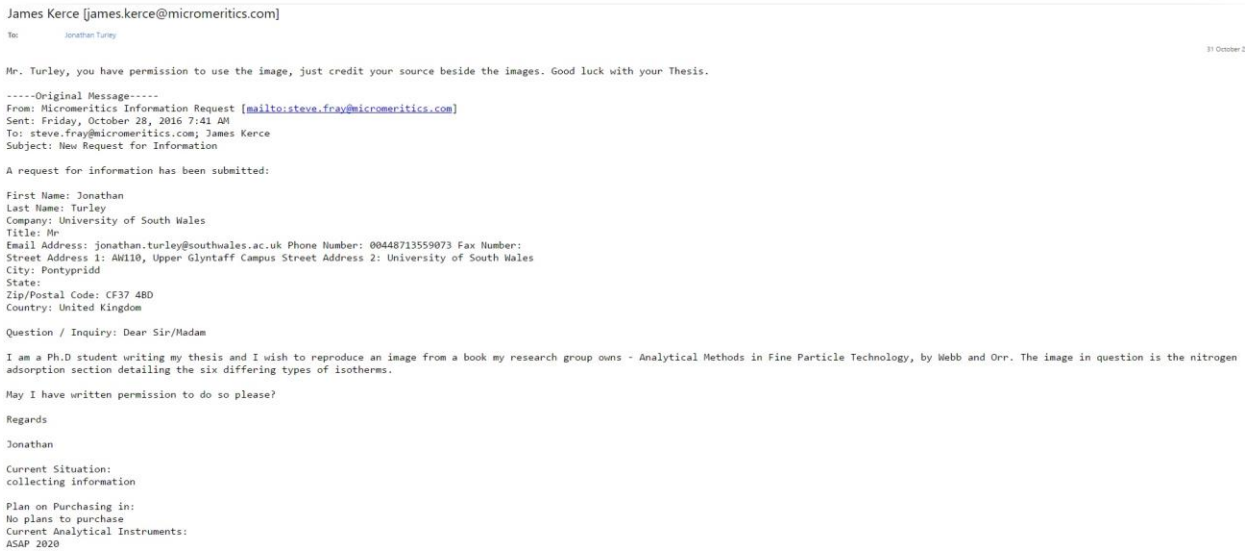

James Kerce [james.kerce@micromeritics.com]

To: Jonathan Turley

31 October 2

Mr. Turley, you have permission to use the image, just credit your source beside the images. Good luck with your Thesis.

-----Original Message-----
From: Micromeritics Information Request [mailto:steve.fray@micromeritics.com]
Sent: Friday, October 28, 2016 7:41 AM
To: steve.fray@micromeritics.com; James Kerce
Subject: New Request for Information

A request for information has been submitted:

First Name: Jonathan
Last Name: Turley
Company: University of South Wales
Title: Mr
Email Address: jonathan.turley@southwales.ac.uk Phone Number: 00448713559073 Fax Number:
Street Address 1: AW110, Upper Glyntaff Campus Street Address 2: University of South Wales
City: Pontypridd
State:
Zip/Postal Code: CF37 4BD
Country: United Kingdom

Question / Inquiry: Dear Sir/Madam

I am a Ph.D student writing my thesis and I wish to reproduce an image from a book my research group owns - Analytical Methods in Fine Particle Technology, by Webb and Orr. The image in question is the nitrogen adsorption section detailing the six differing types of isotherms.

May I have written permission to do so please?

Regards

Jonathan

Current Situation:
collecting information

Plan on Purchasing in:
No plans to purchase
Current Analytical Instruments:
ASAP 2020

Figure 7.37 Permission to reproduce a figure from Analytical Methods in Fine Particle Technology (2008), Figure 1.12 in Chapter 1